ESTABLISHING PERMANENT CURL/WARP TEMPERATURE GRADIENT IN JOINTED PLAIN CONCRETE PAVEMENTS

by

Somayeh Nassiri

BS in Civil Engineering, University of Tabriz, Iran, 2004

MS in Civil Engineering, University of Tehran, Iran, 2007

Submitted to the Graduate Faculty of

The Swanson School of Engineering in partial fulfillment

of the requirements for the degree of

Doctor of Philosophy

University of Pittsburgh

2011

UNIVERSITY OF PITTSBURGH

SWANSON SCHOOL OF ENGINEERING

This dissertation was presented

by

Somayeh Nassiri

It was defended on

March 25, 2011

and approved by

Dr. Donald Janssen, Associate Professor, Department of Civil and Environmental Engineering, University of Washington

Dr. Jeen-Shang Lin, Associate Professor, Department of Civil and Environmental Engineering, University of Pittsburgh

Dr. John Brigham, Assistant Professor, Department of Civil and Environmental Engineering, University of Pittsburgh

Dissertation Director: Dr. Julie Vandenbossche, Assistant Professor, Department of Civil and Environmental Engineering, University of Pittsburgh

ESTABLISHING PERMANENT CURL/WARP EFFECTIVE TEMPERATURE GRADIENT IN JOINTED PLAIN CONCRETE PAVEMENTS

Somayeh Nassiri, PhD

University of Pittsburgh, 2011

The concrete slab in a pavement structure curls due to a temperature gradient and warps in the presence of a drying shrinkage gradient. The curling is upward (downward) when the slab is cooler (warmer) at the top than the bottom. Warping is consistently upward because the slab is more susceptive to drying at the top. Since the slab is not free to curl, tensile stresses form in the slab. These stresses when combined with traffic loadings can result in cracking of the slab. Slabs do not remain flat in the absence of daily gradients. This is because of the temperature/moisture gradient that exists in the slab at the zero-stress time. Zero-stress time occurs after the placement of the slab, during curing and following final set time. The gradients at the zero-stress time, known as built-in or permanent temperature gradients, lock into the slab and either decrease or increase the curling due to the transient gradients. One more factor that influences the future shape of the slab is the permanent warp gradient. A portion of the drying shrinkage in drier seasons can reverse in wet seasons, known as reversible drying shrinkage. Permanent warp is due to the irreversible portion of the drying shrinkage, which progressively increases as the concrete ages and eventually reaches a plateau. This study puts forward a procedure, including three tasks, to establish realistic values for permanent curl/warp in the slab. Task 1 includes identifying the zero-stress time in the slab. This is performed by using the data from four different instrumented

pavement structures in Western Pennsylvania. Task 2 focuses on establishing the built-in temperature gradient based on the measured temperature. As part of this task, a computer temperature model is developed to predict the temperature within the pavement based on the ambient conditions and the heat of hydration. Task 3 focuses on estimating the permanent warp in the slab. This is achieved by using long-term strain measurements in an instrumented pavement section in Pennsylvania, as well as instrumented pavements sections in Minnesota. The drying shrinkage development is also predicted by using a relative humidity model. The difference between the predicted and measured drying shrinkage is attributed to the effects of creep and base restraints.

TABLE OF CONTENTS

LIST OF TABLES

LIST OF FIGURES

ACKNOWLEDGMENTS

I gratefully acknowledge the endless effort of my advisor, Dr. Julie Vandenbossche, who patiently walked me through the rough path of conducting research over the past three and a half years. Along the path, she taught me how to analyze, read and write. I also learned from her that every small phenomenon is worth analyzing and there is always a way to explain the cause.

I should also thank Dr. Don Janssen, one of my committee members, who devoted a great amount of time to deeply investigate and analyze the field data for this study. His thoughts and sharp observations helped me better comprehend the nature of the data.

The time and effort of the other members of the PhD committee, Dr. Jeen-Shang Lin and Dr. John Brigham, is also appreciated gratefully. I am thankful to both these professors for the guidance they provided toward developing the two numerical models implemented in this study.

The financial support for performing a major portion of this study came from the Pennsylvania Departments of Transportation (PennDOT) through Project Work Order 13 Contract # 510601.

I would also like to sincerely thank my colleagues at the University of Pittsburgh who helped with the extensive field work involved with this study. This includes graduate students, F. Mu, M. Barman, K.A. Gatti, L.C. Ramirez, M.A. Geary and T.S. Adams. I would also like to express my thanks to Mr. Tom Burnham, who provided me with a large database of strain

measurements from the Minnesota Road Research Facility (MnROAD) in a very short period of time.

My endless gratitude is also extended to my family, my mom, dad and brother, who remained patient and supportive the entire time of my study, even though we have been separated by a great distance. A special acknowledgment of appreciation goes to my beautiful fiancé, Dave, who has been an endless source of support, energy, motivation and joy, during the past two years.

This work is dedicated to the "Green Movement" in Iran and all the young men and women across the world, who selflessly devote their lives, time and energy to putting an end to human right violations, dictatorship and censorship. I deeply hope and wish for a better future with freedom of speech, fare elections and real democracy for Iranians and other suffering nations.

1.0 CHAPTER 1- OBJECTIVES

1.1 INTRODUCTION TO THE CHAPTER

The first chapter of this dissertation focuses on defining the main objectives of this doctoral study. The motivation behind the research and the significance of the study will also be elaborated in this chapter. In doing so, some basic concepts, terminologies and phenomena prevalent in Portland cement concrete (PCC) pavement structures need to be introduced and discussed initially. A discussion of the causes and factors influencing these phenomena will also be provided. Primary objectives and motivations of this research will be discussed following the basic concepts.

1.2 BASIC CONCEPTS

1.2.1 Transient Curling and Warping in Concrete Slabs

It has been very well established that PCC slabs tend to curl either upward (slab corners lifted up) or downward (slab middle area lifted up), instead of remaining flat (Armaghani, Larsen et al. 1987; Yu, Khazanovich et al. 1998). When a negative temperature gradient is present in the slab,

the slab contracts at the top more than the bottom and therefore curls upward. A negative temperature gradient forms in the slab when the temperature at the top of the slab is lower than that of the bottom of the slab. This condition typically occurs at night. This is presented in Figure 1-1(a). In this case, the slab loses support from the base layer at the edges and the self-weight of the slab exerts tensile stresses at the top of the slab. This tensile stress is highlighted in Figure 1-1(a) by the red arrow.

On the other hand, when a positive temperature gradient (temperature at the top of the slab is higher than the one at the bottom, usually during the day time) exists in the slab, the slab expands more at the top in comparison to the bottom and therefore curls downward. This is the case presented in Figure 1-1 (b). In this case, support is lost near the center of the slab and the self-weight of the slab exerts tensile stress near the bottom of the slab. See the location of the red arrow shown Figure 1-1 (b), which identifies the location of the critical tensile stress.

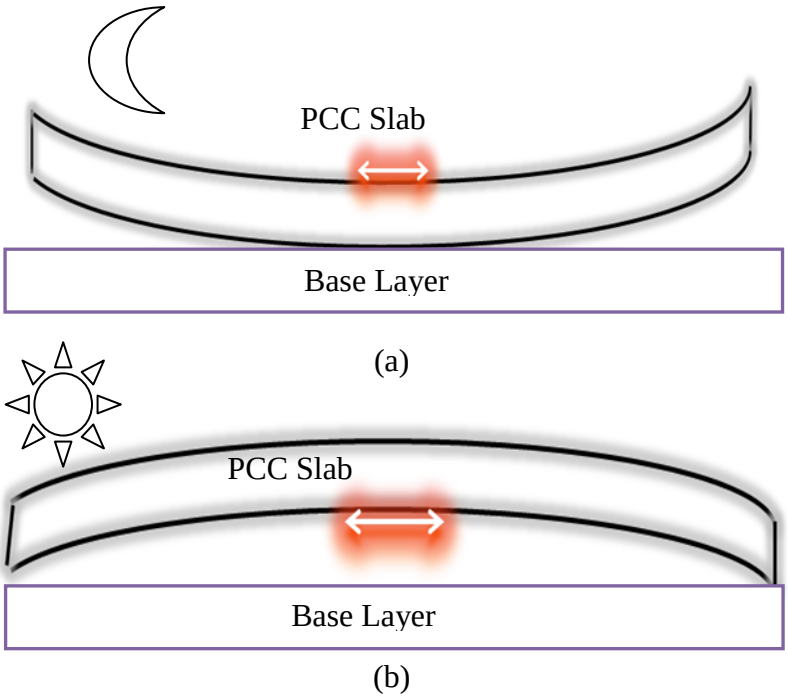

Figure 1-1. (a) Upward curvature of the slab with tensile stresses at the top; (b) Downward curvature of the slab with tensile stresses at the bottom.

The slabs also warp when non-uniform drying shrinkage across the slab depth occurs. The non-uniformity is results from the slab is more susceptible to drying in the upper two inches (Janssen 1986), since it is exposed to the atmosphere. At the bottom, the slab remains mostly saturated at all times. This drying shrinkage gradient produces a curling moment in the slab, referred to as warping. See Figure 1-2.

Part of the drying shrinkage that develops in the PCC slab over time is irreversible but there is also a reversible portion that fluctuates with the ambient relative humidity. The irreversible shrinkage causes permanent warping, while the reversible shrinkage causes seasonal variation in warping (ARA Inc. ERES Consultants Division 2004).

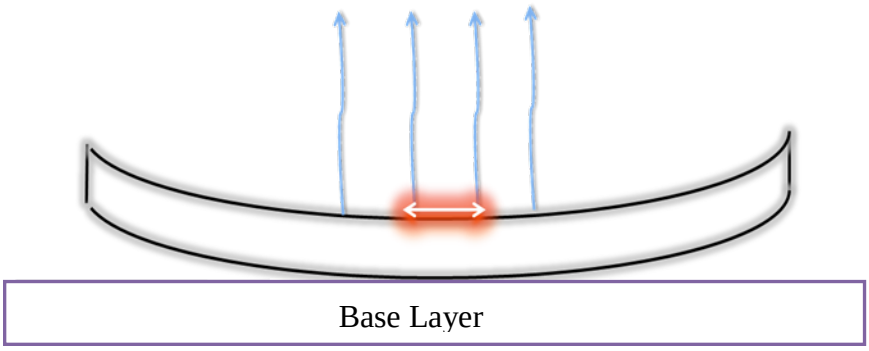

Figure 1-2. Slab warping due to more drying at the surface than bottom.

1.2.2 Permanent Curl/Warp Effective Temperature Gradient

Transient temperature and drying shrinkage gradients influence the shape of the slab, as discussed previously. Another factor that influences the shape of the slab is referred to as the permanent curl/warp effective temperature gradient $\Delta T_{curl/warp}$. This factor is a linear temperature gradient consisting of three major components: the linear temperature gradient equivalent to the built-in temperature/moisture gradient, $\Delta T_{built\text{-}in}$, the linear temperature gradient equivalent to the irreversible drying shrinkage gradient, ΔT_{shri} and the linear temperature gradient equivalent to the creep relaxation ΔT_{creep}. See Equation 1-1. Each of these three factors will be discussed in the following sections, starting with the built-in temperature/moisture gradient.

$$\Delta T_{curl/warp} = \Delta T_{built-in} + \Delta T_{shri} - \Delta T_{creep} \qquad (1\text{-}1)$$

1.2.2.1 Built-in Temperature/Moisture Gradient ($\Delta T_{built\text{-}in}$)

In general, the built-in temperature/moisture gradients are the gradients that exist in the slab at the zero-stress time. Zero-stress time, TZ, is a time after the placement of the concrete slab, during curing and following final set time, when no stresses exist in the slab. This concept will be expanded upon in the next chapter of this study. The $\Delta T_{built\text{-}in}$ in the slab is a significant parameter, since it influences the future shape of the slab. The $\Delta T_{built\text{-}in}$ that locks in the slab at TZ causes the slab to curl instead of remaining flat when the slab is in a zero transient gradient condition (Rao and Roessler 2005).

The effects of a moisture gradient at TZ on the future shape of the slab can in fact be ignored. A previous study (Wells, Phillips et al. 2006) revealed that the slabs are fully saturated during the period of hardening based on humidity measurements in the slab (first few days after placement of the slabs).

1.2.2.2 Irreversible Drying Shrinkage Gradient (ΔT_{shri})

The third component of $\Delta T_{curl/warp}$, as presented in Equation 1-1, is the irreversible differential drying shrinkage. The level of the irreversible drying shrinkage in the slab eventually stabilizes as the slab ages. It has been shown that only 20 to 25 percent of the 20-year drying shrinkage of concrete can be realized in 2 weeks, 50 to 60 percent in 3 months and 75 to 80 percent in one year (Mehta 1986). Overall, it is believed that at least four to five years is required to reach the ultimate drying shrinkage (Burnham and Koubaa 2001). The linear temperature gradient equivalent to the nonlinear long-term irreversible drying shrinkage gradient across the slab depth is the third component of the permanent curl/warp effective temperature gradient.

1.2.2.3 Effect of Creep (ΔT_{creep})

The last component of the permanent curl/warp effective temperature gradient is the effect of the relaxation due to creep. The time-dependent increase of strain in hardened concrete subjected to sustained stress in excess of shrinkage is defined as creep. The causes of creep in concrete are complex. It is generally agreed though, that moisture movements together with the non-linearity of the stress-strain in concrete, especially when the stress is higher than 30 to 40 percent of the ultimate strength, can be among the causes of creep relaxation in the concrete (Mehta 1986). Relaxation can negate the effects of $\Delta T_{curl/warp}$ over time. This relaxation can occur in form of both the early-age creep, which affects the $\Delta T_{built\text{-}in}$ and the long-term creep, which influences the ΔT_{Shri}.

1.3 RESEARCH OBJECTIVE

The main objective of this study is to put forward a practical and simple procedure to estimate realistic values for permanent curl/warp temperature gradient in jointed plain concrete pavements (JPCPs). In defining this parameter, effects of all three components, $\Delta T_{built\text{-}in}$, ΔT_{shri} and ΔT_{creep}, will be addressed.

JPCPs can be constructed featuring different designs (structure and restraints) and PCC mixture properties. They can also be exposed to different climatic conditions depending on their geographical location and the time of paving. The objective of this study is to provide an

estimate of the permanent curl/warp effective temperature gradient for JPCPs for a range of design features and PCC mixtures constructed in different climatic regions.

1.4 MOTIVATION AND RESEARCH SIGNIFICANCE

1.4.1 Tensile Stresses in Concrete Slabs

As discussed earlier, permanent curl/warp temperature gradient either increases or decreases the effects of transient temperature/moisture gradients in the slab. The combined effects of the transient and permanent gradients define the final shape of the slab. When curled upward, some slabs do not contact the sub-layer for several feet along either side of the joints. This can result in high deflections and pumping due to loss of support (Vandenbossche 2003; Rao and Roessler 2005).

Additionally, as explained in Section 1.2.1, when curled upward (downward), the self-weight of the slab exerts tensile stresses at the top (bottom) of the slab. Together with heavy traffic load repetitions at critical locations in each case, these stresses can result in increased fatigue damage with eventual cracking and a drop in the serviceability of the pavement section. The critical location for traffic loading in the presence of a negative temperature gradient, resulting in top-down cracking, is shown in Figure 1-3 (a). The critical traffic loading position when a positive temperature gradient is present in the slab, resulting in bottom-up cracking, is presented in Figure 1-3 (b).

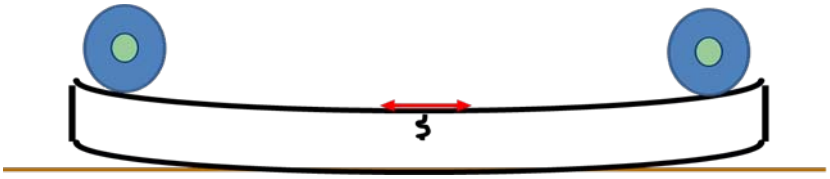

(a)

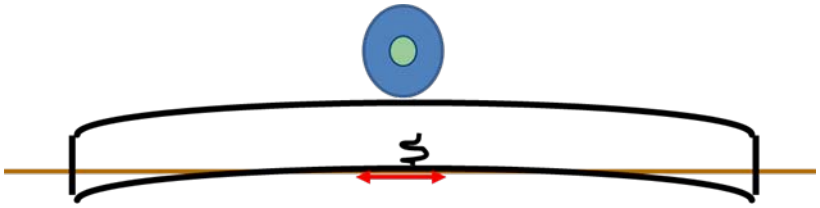

(b)

Figure 1-3. Critical locations for traffic loading resulting in (a) top-down and (b) bottom-up cracking.

In 2002, a study was performed on several newly-constructed JPCP sections in Pennsylvania to identify the probable causes of the top-down cracking (Beckemeyer, Khazanovich et al. 2002). Results from this study showed that the top-down cracking was caused by a combination of excessive upward slab curling, loss of slab support (slab lift-off), and repeated heavy-truck loadings. The built-in slab curling was also found to be a major contributor to the observed top-down cracking.

1.4.2 A Design Input in the New Design Guide

The permanent curl/warp effective temperature gradient is one of the many design inputs required by the Mechanistic-Empirical Pavement Design Guide (MEPDG.) The new design guide uses a mechanistic-empirical approach to predict the amount of cracking and faulting that can occur in the slab over its design life. In doing so, the design software requires more than 100 design inputs to be defined accurately. Departments of transportations (DOT s) across the nation

are taking steps towards replacing the American Association of State Highway and Transportation Officials 1993 (AASHTO 1993) empirical pavement design guide, currently being used, with the MEPDG.

A comprehensive parametric study was performed as part of a research project supported by the Pennsylvania Department of Transportation (PennDOT) to evaluate the sensitivity of each design input to the performance predicted by the MEPDG (Nassiri, Ramirez et al. 2009; Nassiri, Vandenbossche et al. 2009). This study revealed that the $\Delta T_{curl/warp}$, in fact, has a significant influence on the faulting and fatigue cracking predicted using the MEPDG.

Figure 1-4 and Figure 1-5, extracted from this study, show the sensitivity of the predicted faulting and cracking to different variables included in the study, respectively. Based on Figure 1-4, varying the value of this parameter from 0 °F to –10 °F and –20 °F, results in significant changes in the predicted faulting. The larger negative temperature difference results in larger curling of the slab corners and hence an increase in deflections. Higher deflections increases the potential for faulting.

Figure 1-5 shows the effects of this variable on the transverse cracking predicted by the MEPDG. Based on Figure 1-5, some changes are seen in the predicted transverse cracking, when changing the values of this parameter, especially when changed from –10 °F to 0 °F.

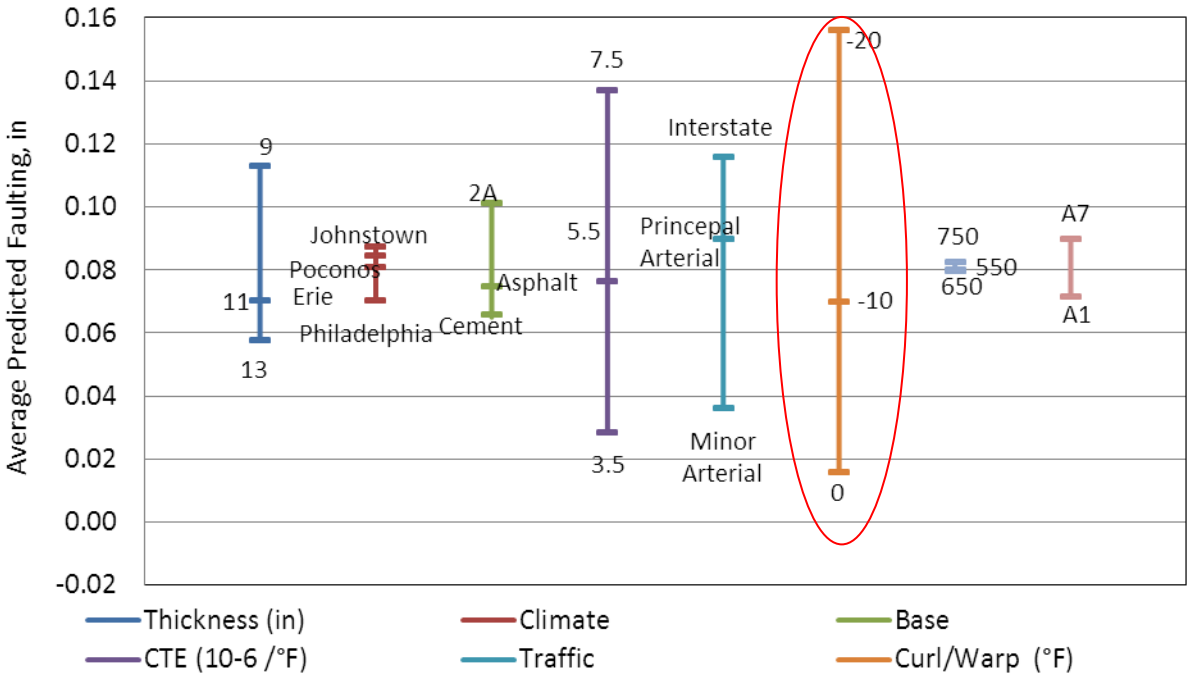

Figure 1-4. Sensitivity of different variables to mean joint faulting (Nassiri, Vandenbossche et al. 2009).

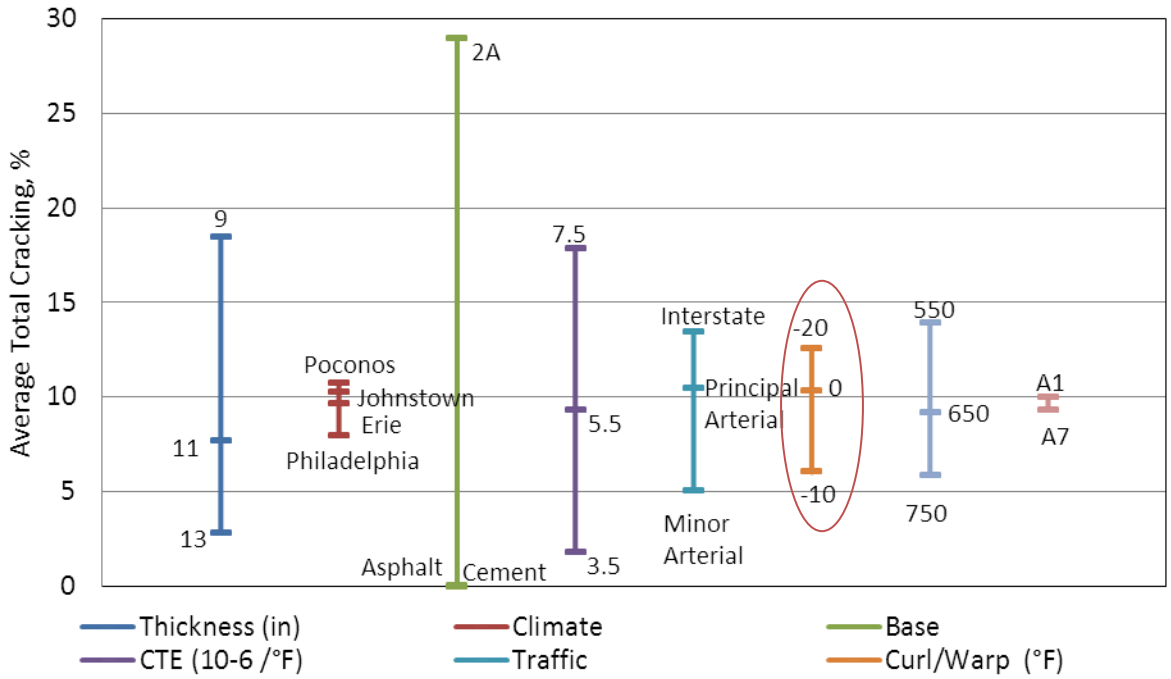

Figure 1-5. Sensitivity of different variables to transverse cracking (Nassiri, Vandenbossche et al. 2009).

Another sensitivity study performed at Iowa State University also included permanent curl/warp as one of the variables in their study (Coree 2005). A larger range of variation was considered for this variable in the Iowa study. Figure 1-6, shows the effects of permanent curl/warp on the transverse cracking predicted by the MEPDG. Based on this figure, changing the value of this parameter from –10 °F (the default value in the design software) to 0 °F, –20 °F and –30 °F can result in significantly high predicted transverse cracking.

The effects of permanent curl/warp effective temperature gradient on the faulting predicted using the MEPDG were also investigated in the Iowa study. This is presented in Figure 1-7. This figure also shows that higher faulting is predicted for larger negative temperature differences.

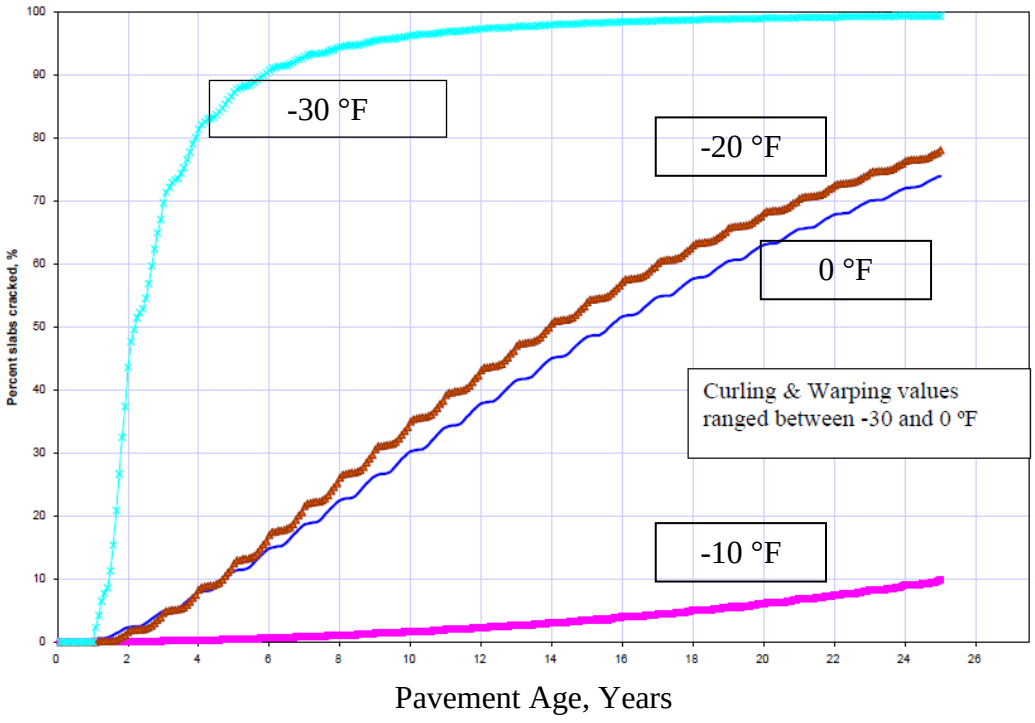

Figure 1-6. Sensitivity of the transverse cracking to permanent curl/warp (Coree 2005).

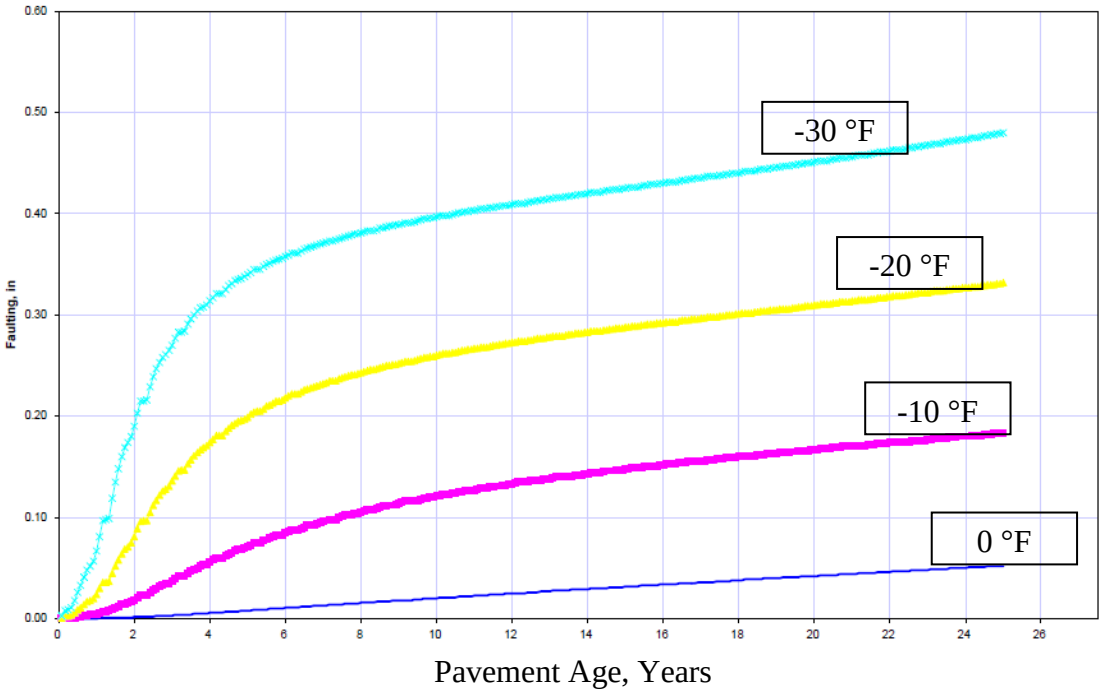

Figure 1-7. Sensitivity of the predicted faulting to permanent curl/warp (Coree 2005).

The above studies show that the distress predicted by the MEPDG strongly depends on the value of the permanent curl/warp effective temperature difference. Currently, a default value of –10 °F is used in the design software for the permanent curl/warp effective temperature difference between the top and the bottom of the slab. This indicates that an equivalent temperature difference of +10 °F is present in the slab. This value was obtained through optimization of the MEPDG empirical cracking model using a database populated with data from pavement sections across the United States. This variable, although changeable when using the design software, is recommended in the design guide documentation to be kept as the default value, unless locally calibrated values are available (ARA Inc. ERES Consultants Division 2004).

A study performed at the University of Pittsburgh (Gutierrez 2003) showed that the MEPDG tends to more accurately predict the distresses for a pavement section, when the permanent effective temperature difference is defined as –10 °F. This conclusion was drawn based on the comparisons made between the MEPDG-predicted performance for test sections at the Minnesota Road Research Facility (MnROAD) and the performance history data available for these test sections.

The 2003 study was extended in another study (Vandenbossche, Mu et al. 2010) to include the effects of climatic conditions, traffic and slab thickness on the built-in gradient required to minimize the cracking predicted using the MEPDG for JPCPs. This study also provided an evaluation to determine whether changes in the default value for the permanent curl/warp effective temperature gradient produces significant changes in the MEPDG-predicted transverse cracking. It was concluded based on the analysis that the most reasonable MEPDG performance prediction for pavements with typical traffic patterns in most environments is obtained by using the MEPDG-recommended default value of –10 °F, since calibration was performed using this value.

As mentioned earlier, various factors such as the pavement structure, external restraints, PCC mixture and climatic conditions during paving can affect the value of this parameter. Therefore, the magnitude of the permanent curl/warp temperature difference can deviate significantly from –10 °F in individual pavement sections (Rao 2005). This parameter should be defined and used in the local calibration process so that more accurate predictions of pavement performance can be achieved.

1.4.3 Previous Studies on Establishing Permanent Curl/Warp Temperature Gradient

Characterization and quantification of the permanent curl/warp in concrete slabs is a difficult task to perform (Yu, Khazanovich et al. 1998). This is due to the numerous influential variables that are involved with establishing this parameter. Some researchers in the past have identified the significance of the permanent curling in PCC slabs and have focused on characterizing its magnitude. These approaches include backcalculating this parameter for in-service pavement sections. This was pursued by using a combination of the finite element method (FEM), mostly by using ISLAB2000 (Khazanovich 1994), and methods, such as surface profile measurements, using a Dipstick (Yu, Khazanovich et al. 1998; Rao, Barenberg et al. 2001; Schmidt 2001; Wells, Phillips et al. 2006) and falling weight deflectometer (FWD)/heavy weight deflectometer (HWD) testing (Vandenbossche 2003; Rao 2005). Some others have performed the American Society for Testing and Materials (ASTM) C 403 "Standard Test Method for Time of Setting of Concrete Mixtures by Penetration Resistance" (ASTM C 403 1999) together with temperature measurements in the slab (Mahboub, Liu et al. 2004; Jeong and Zollinger 2005; Hansen, Wei et al. 2006; Wells, Phillips et al. 2006; Asbahan 2009). Another study focused on quantifying the built-in temperature gradient in the slabs through the use of static strain gages. The built-in temperature gradient in this study was defined at a time corresponding to when expansion/contraction is measured with changes in temperature in the slab (Wells, Phillips et al. 2006).

These methods are very costly and require extensive field measurements and data collection efforts. As a result, very limited data is available on the permanent curl/warp and how different variables influence it. The information available on this parameter is limited to a

handful of research studies, mentioned above. More effort is required in developing a practical and theoretical procedure that can be applied to all JPCP sections, to realistically estimate the permanent curl/warp gradients in the slab.

1.5 RESEARCH APPROACH

As described in Section 1.3, the main objective of this study is to provide an appropriate estimate of the permanent curl/warp gradient in JPCPs. This includes JPCP sections with different construction dates/locations, design and PCC mixtures. To achieve this goal, it is essential to consider the combined effects of the irreversible drying shrinkage gradient (ΔT_{shri}) and the long-term relaxation creep (ΔT_{creep}), as well as the $\Delta T_{built\text{-}in}$ and early-age creep. This work includes three major modules, which focus on establishing: 1- zero-stress time 2- the $\Delta T_{built\text{-}in}$ and 3-the ΔT_{shri} in the slabs. The different modules to be included in the proposed work are presented graphically in the form of a flow chart in Figure 1-8.

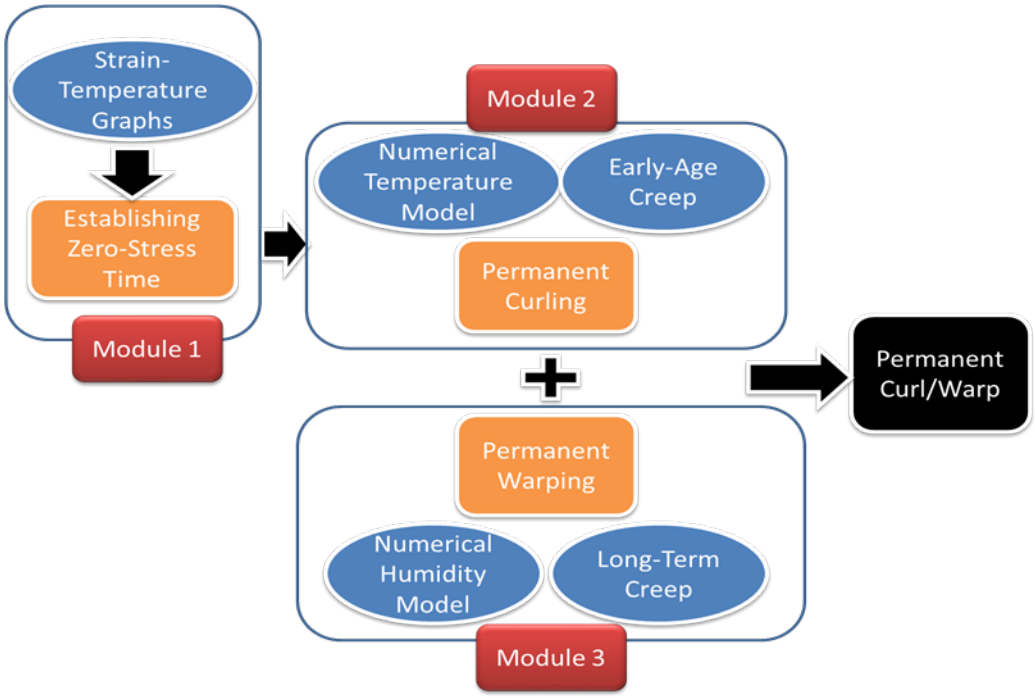

Figure 1-8. Schematic presentation of different modules incorporated into the study.

To establish TZ in the slabs, Module 1 in Figure 1-8, a total number of 36 PCC slabs in four different pavement sections were instrumented with vibrating wire (VW) static strain gages. The TZ in each slab will be established based on the variation in strain with respect to changes in temperature in each slab. The degree of hydration reached in each slab at TZ, "critical degree of hydration," will also be estimated for each project. The critical degree of hydration can then be used to identify TZ in other slabs with the same design features as the four instrumented projects in this study.

To establish $\Delta T_{built\text{-}in}$, Module 2 in Figure 1-8, the temperature measured using thermocouples installed at various depths and location of the slabs will be used. To be able to extend this work to other projects, a numerical temperature model will be developed as part of Module 2. This model considers the effects of the ambient climatic data such as temperature,

relative humidity, wind speed and solar radiation and also the heat generated by the hydration of the cement to predict the temperature variation within the pavement structure. The model is able to predict the temperature in the slab upon placement and for as long as the climatic data is available. The accuracy of the predictions of the model will be validated by using PCC temperature measurements in the field from the four instrumented pavement sections. The predictions from this model can be used to establish the $\Delta T_{built\text{-}in}$ in the PCC slabs beyond the four instrumented projects.

To establish ΔT_{shri} , Module 3 in Figure 1-8, the development of drying shrinkage over a duration of minimum of five years will be established based on measured strains in a 6-year old instrumented test section in Western Pennsylvania. This study will be combined with the results from another study performed in 2001 that used the same approach to establish drying shrinkage in five different pavement designs located at MnROAD.

Once again, to extend this analysis to pavement designs beyond those that are currently instrumented; a numerical model will be developed to predict the internal relative humidity of the concrete across the depth of the slab over time. The accuracy of this model will be investigated based on the relative humidity measurements in the slabs for the test section. The results from the computer model will be used to establish the $\Delta T_{shri.}$ The predicted drying shrinkage will be corrected for the possible effect of long-term creep and also the restraining factors, such as friction with the base and dowel/tie bars, on the development of drying shrinkage. This will be accomplished based on the divergence of the predicted drying shrinkage from the measured drying shrinkage in the slab.

1.6 STRUCTURE OF THE DISSERTATION

This work is comprised of a total of eight chapters. A brief description of each of the remaining chapters is provided below.

- CHAPTER 2: a literature review is provided on each of the three components of permanent curl/warp temperature gradient, including permanent curling, permanent warping and creep. A definition of each of these parameters is provided and the corresponding influencing variables are discussed. The methods available to estimate each factor is also introduced and discussed in this chapter.
- CHAPTER 3: zero-stress time is established in this chapter for four pavement projects instrumented with strain gages and thermocouples. The critical degree of hydration for JPCPs with 10-, 12- and 14-inch concrete slabs and two different stabilized base materials is established in this chapter.
- CHAPTER 4: the built-in temperature gradient for each of the four instrumented projects is estimated in this chapter. The possible effect of early-age creep is also investigated in this chapter.
- CHAPTER 5: a temperature model to predict the temperature within the pavement structure is developed in this chapter. This model is validated using the thermocouple data from the four instrumented projects.
- CHAPTER 6: the equivalent temperature gradient representing the permanent warping in the slab is established by following two different approaches: developing and employing a numerical humidity model versus measuring the strain due to drying shrinkage in the

slabs for two different test sections. The difference between the results from the two approaches is attributed to long-term creep and the restraining factors against the dying shrinkage, such as friction with the base and dowel/tie bars.

- CHAPTER 7: the final objective of the study is achieved by following the complete procedure to establish the permanent curl/warp effective temperature gradient for slabs constructed throughout commonwealth of Pennsylvania and during the construction season.
- CHAPTER 8: a summary of the conclusions, contributions, recommendations and limitations of the study and suggestions for future work is discussed in this chapter.

2.0 CHAPTER 2-LITERATURE REVIEW

2.1 INTRODUCTION TO THE CHAPTER

This chapter provides a background study on the factors influencing the permanent curl/warp temperature gradient. The complete chapter consists of three major sections, focusing on the three components of the $\Delta T_{curl/warp}$, including $\Delta T_{built\text{-}in}$, ΔT_{shri} and ΔT_{creep}. Concrete properties related to each component, such as final set and zero-stress time, drying shrinkage and creep is also briefly described in each section. A brief review of the existing methods/approaches for defining each of the components of the $\Delta T_{curl/warp}$ will also be discussed.

2.2 BUILT-IN/PERMANENT CURLING TEMPERATURE GRADIENT

The built-in gradient traditionally has been accepted as the temperature gradient present in the slab at the time of final set (Yu and Khazanovich 2001; Beckemeyer, Khazanovich et al. 2002; Schindler, Ruiz et al. 2003; Jeong and Zollinger 2004; Jeong and Zollinger 2005; Rao and Roessler 2005; Wade, Nixon et al. 2010). Final set has been defined as the time when the concrete transforms from a liquid to a rigid state (Pinto 1999; Schindler 2004; Pinto and Schindler 2010). One method that has been widely practiced to establish the times of initial and

final set in concrete is ASTM C403(ASTM C 403 1999). This method correlates the initial and final set times to two arbitrary levels of resistance by the concrete against pressure from penetration of multi-sectional needles. The term "critical degree of hydration" was first defined as the degree of hydration that needs to be reached before any strength gain occurs in concrete (Byfors 1980). This term was later correlated to the initial and final set times established by the ASTM C403 test (Schindler 2004). This critical degree of hydration has been used as the time corresponding to the built-in gradient (McCullough and Rasmussen 1999; Ruiz, Rasmussen et al. 2006). However, the built-in gradient should be defined at zero-stress time (TZ) and not the time of final set established using ASTM C403.

TZ for concrete slabs in the field is a structural property that not only depends on weather conditions, the curing method and the PCC design mixture i.e. cement type, w/cm (water-to-cement) ratio, chemical admixtures and supplementary cementitious materials (SCMs) but other factors that exist in the field. These factors include external restraints such as dowel and ties bars for JPCPs, base type and slab thickness. Construction sequencing can also affect TZ in a concrete slab. For example, if the lane to be paved is being tied to an existing adjacent lane previously constructed, additional restraint is generated against the expansion/contraction of the slab. This can result in a delay in the TZ in the slab. TZ Generally occurs after final set and when the concrete has developed sufficient strength to overcome the existing external restraint as well as the friction between the slab and the underlying base.

2.2.1 Factors Influencing TZ

Many variables can influence TZ and consequently $\Delta T_{built\text{-}in}$. These variables include curing method, ambient conditions during curing, such as temperature and relative humidity (RH), dowel and tie bars, slab thickness, base type and PCC mixture properties. These factors will be discussed individually as follows.

Curing Method and Climatic Conditions at the time of Paving

Once placed, the PCC slab is in a constant heat exchange with the atmosphere. This heat exchange occurs in the form of convection, cooling due to evaporation, radiation and irradiation. Different curing methods used at the time of construction, such as a curing compound, plastic sheets or insulation blankets can have an impact on the amount of heat transferred to or from the atmosphere through convection, evaporation and radiation. Therefore, the curing method affects the temperature profile in the slab and thereby the $\Delta T_{built\text{-}in}$. The curing method will also affect the rate of hydration and hence the occurrence of the TZ in the slab.

Depending on the weather conditions present at TZ, either positive or negative temperature gradients can lock into the slab. If the concrete reaches TZ during a hot sunny day, a positive (downward) temperature gradient locks into the slab. While, if TZ occurs during the nighttime, a negative (upward) $\Delta T_{built\text{-}in}$ will lock into the slab. Additionally, the time of the year can affect the magnitude of the gradient. Intuitively, if paving occurs during warmer months (summer), the downward $\Delta T_{built\text{-}in}$ can have larger magnitudes in respect to when the construction occurs in colder months (winter). The effects of the time of paving on $\Delta T_{built\text{-}in}$ will be investigated in more detail in the subsequent chapters.

Climatic conditions at the time of paving also affect TZ in the sense that in the presence of warmer ambient conditions, hydration occurs more quickly and therefore TZ is reached earlier than when the hydration is developed in cold weather conditions. Increasing the curing temperature increases the rate of the reaction between the cement and water, and consequently set time is shortened. This has been previously reported by other researchers (Schindler 2002).

The effects of the curing conditions on TZ can be accounted for by relating the temperature variation in concrete with time. The term "maturity" was for the first time linked to the product of time and temperature [i.e. maturity equals *f* (T×t)] in 1951 by Saul (Byfors 1980).

The assumption is that for any particular mixture, concrete of the same maturity will have approximately the same strength, regardless of the combination of time and temperature leading to the maturity. To be able to establish the maturity, the variation of the temperature in the concrete needs to be measured. Maturity can be established using the following relation:

$$M(t) = \sum (T_a - T_0)\Delta t \qquad (2\text{-}1)$$

where, M = Temperature-time factor at age t, degree-hours

Δt = Time interval, hours

T_a = Average concrete temperature during the time interval Δt, °F

T_0 = Datum temperature below which there is no strength gain, assumed to be equal to -10 °C or 14˚F.

This equation has become known as the Nurse-Saul function. The equivalent age is another approach in defining the time-temperature relationship for concrete. In 1977, the expression presented in Equation 2-2 was suggested for defining the equivalent age (Freiesleben

Hansen and Pederson 1977). This relation is an Arrhenius equation, which relates the chemical reaction in the mixture to temperature.

$$t_e = \sum_{0}^{t} \exp\left(\frac{-E}{R}\left[\frac{1}{273+T_a} + \frac{1}{273+T_r}\right]\right) \quad (2\text{-}2)$$

where, E = Activation energy, J/mol, and

R = Universal gas constant, 8.3144 J/(mol K)

Tr = Assumed as 23 ºC or 73 ºF in North America (Schindler and Folliard 2005).

Byfors studied different maturity functions and showed that the Arrhenius function is best able to account for effects of temperature on the strength gain (Byfors 1980). Additionally, the nonlinear maturity function based on the Arrhenius definition, is considered the most accurate since it better represents the effect of temperature on the strength development over a wide range of temperatures (Carino 1991).

The activation energy (E) in Equation 2-2, defines the temperature sensitivity of the concrete. Typical values for this parameter for different cement types are available in literature. These values are summarized in Table 2-1.

Table 2-1. Activation energy for different cement types (McCullough and Rasmussen 1999).

Cement Type	Activation Energy (J/mol)
I	41,750
IP	41,715
II	39,050
III	44,150
V	36,350

Although convenient, using these typical values for the activation energy does not consider the effect of many factors, including the use of SCMs, such as slag or fly ash, the cement Blaine (fineness) or the amount of free lime (if any used). Schindler in 2005 (Schindler and Folliard 2005), performed a series of semi-adiabatic calorimeter tests on several samples of concrete with different mixture designs. Regression analyses of the results lead to developing a relation for estimating the activation energy that would consider all the above mentioned variables. This relation is provided in Equation 2-3.

$$E = 22{,}100.f_E.P_{C3A}^{0.3}.P_{C4AF}^{0.25}.Blaine^{0.35} \quad (2\text{-}3)$$

where, P_{C3A} = Weight ratio of C_3A in terms of the total cement content

P_{C4AF} = Weight ratio of C_4AF in terms of the total cement content

Blaine = Specific surface area of cement, m^2/kg

f_E = Activation energy modification factor for SCMs, which can be obtained from the following relation:

$$f_E = 1 - 1.05P_{FA}(1 - \frac{P_{FACao}}{0.4}) + 0.4P_{slag} \quad (2\text{-}4)$$

where, P_{FA}= Weight ratio of fly ash out of the total cementitious material content

P_{FACao} = Weight ratio of the Cao content of the fly ash

P_{slag} = Weight ratio of slag out of the total cementitious material content

PCC Mixture Design

Different PCC mixture designs result in different hydration behavior of the concrete and therefore a different TZ. Variables such as the w/cm ratio, the type and amount of chemical

admixtures and the amount, fineness, and composition of the mineral admixtures and cement in the mixture affect the rate of hydration in the concrete. One index that can be used to compare TZ for concrete with the same mixture is the degree of hydration. This is because it has been shown that concrete will set at a specific degree of hydration, if it consists of the same mixture design and materials (Byfors 1980).

The term degree of hydration is intended to provide a measure of how far the reactions between the cement and water have developed. Theoretically, a curve can be defined to represent the hydration process. The relation provided in Equation 2-5 presents a physical interpretation of the degree of hydration, which characterizes the formation of hydration products for a specific concrete mixture over time.

$$\psi = \exp(-\lambda_1(\ln\tau)^{-k_1} \qquad (2\text{-}5)$$

where, ψ = Degree of hydration

τ = Age parameter=$1 + (\frac{t_1}{t_e})$

λ_1, k_1, t_1=Hydration shape and time parameters.

Typical values for the hydration shape and time parameters are available in literature (McCullough and Rasmussen 1999). These values are summarized in Table 2-2.

Table 2-2. Typical values for hydration shape and time parameters.

Cement Type	λ_1	t_1	k_1
I	2.42	2.12	0.85
IP	2.42	2.12	0.85
II	3.16	2.06	1.07
III	3.52	1.1	0.97
V	3.90	2.0	1.29

Another relation available for establishing the degree of hydration is presented below (Freiesleben Hansen and Pederson 1977):

$$\alpha(t_e) = \alpha_u \exp(\frac{\tau}{t_e})^{\beta} \quad (2\text{-}6)$$

where, $\alpha(t_e)$ = degree of hydration;

α_u = Ultimate degree of hydration, defined in Equation 2-7 (Kjellsen, Detwiler et al. 1991)

$$\alpha_u = \frac{1.031.{}^{w}\!/\!_{cm}}{0.194 + {}^{w}\!/\!_{cm}} \quad (2\text{-}7)$$

and τ and β are the hydration time and shape parameters defined in Equations 2-8 and 2-9, respectively (Schindler and Folliard 2005).

$$\beta = 181.4.P_{C3A}^{-0.156}.P_{C3S}^{0.277}.Blaine^{-0.535}.P_{So3}^{-0.5353}.\exp(-0.547P_{slag}) \quad (2\text{-}8)$$

$$\tau = 66.78.P_{C3A}^{-0.154}.P_{C3S}^{-0.401}.Blaine^{-0.804}.P_{So3}^{-0.758}.\exp(2.187.P_{slag} + 9.5P_{FA}.P_{FACao}) \quad (2\text{-}9)$$

Pavement Design Features

Pavement design features, such as PCC slab thickness, use of dowel and tie bars, diameter of dowel bars, type of base material and temperature can influence TZ in the slab. Thicker slabs have to overcome more friction with the base layer due to the resulting increase in weight and can result in a later TZ when compared to thinner slabs placed on the same base type. External restraints, such as dowel bars along the transverse joints and tie bars across the longitudinal joints, might delay TZ in the slab, since more hydration will be necessary to overcome the additional restraint imposed by these design features. Although, this effect was observed to be negligible in a previous study (Asbahan 2009).

The amount of friction with the base also affects TZ by restraining the expansion/contractions of the slab. Slabs placed on a cement treated permeable base (CTPB) or an asphalt treated permeable base (ATPB) can reach TZ later than the same slab placed on a granular base. This is due to the higher friction that is provided by the stabilized base. Furthermore, materials, such as ATPB become less stiff at higher temperatures and hence provide less restraint against deformations of the slab. Possible effects of all these factors need to be considered, when establishing TZ in slabs.

2.2.2 Establishing $\Delta T_{built\text{-}in}$

Temperature distributions across the slab can be measured using thermocouples installed at different depths of the slab. Several field studies have shown that the temperature distribution across the slab depth is not linear (Armaghani, Larsen et al. 1987; Richardson and Armaghani 1987; Mirambell 1990; Yu, Khazanovich et al. 1998). Figure 2-1., is an example of temperatures

measured throughout the depth of a slab on Pennsylvania I-90. The non-linearity of the temperature can be seen in this figure.

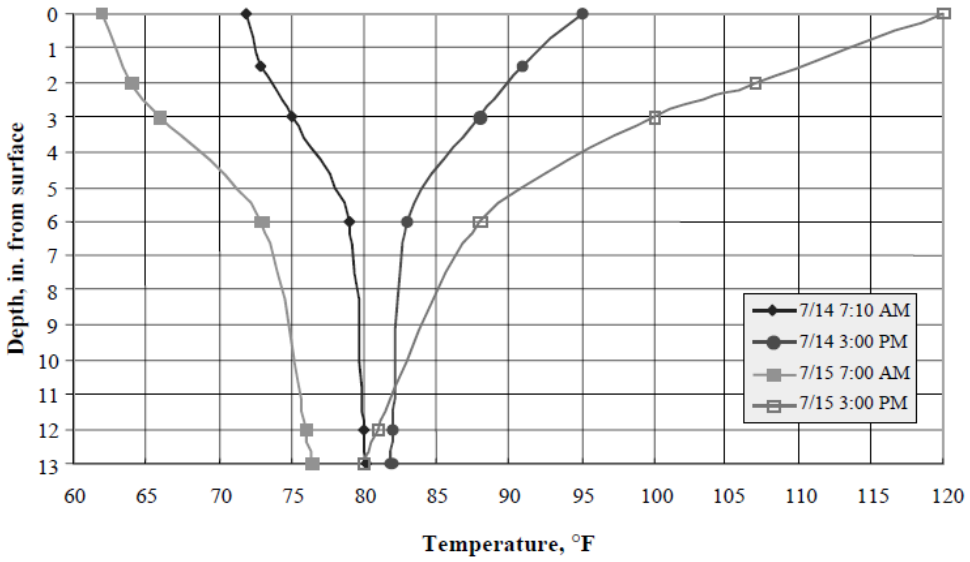

Figure 2-1. Slab temperature profiles measured on Pennsylvania I-90 (Beckemeyer, Khazanovich et al. 2002).

Due to this nonlinearity, the temperature distribution in the slab cannot be accurately quantified through dividing the difference between the measured temperature at the top and bottom of the slab by the distance between them. Therefore, researchers have developed the concept of the equivalent linear temperature gradient (ELTG) (Choubane and and Tia 1992; Zhang, Fwa et al. 2003). This ELTG produces the same curvature as that caused by the nonlinear temperature gradient in the slab. The ELTG can then replace the linear temperature gradient (LTG) used in the solutions developed by Westergaard and Bradbury (Jeong and Zollinger 2005). The ELTG method developed by Janssen and Snyder is elaborated upon herein and will be used to establish $\Delta T_{built\text{-}in}$. The equivalent linear gradient in this method is

established based on a temperature moment concept. The temperature moment can be calculated using the relation provided in Equation 2-10.

$$TM_0 = -0.25\{\sum_{i-1}^{n}[(t_i + t_{i+1})(d_i^2 - d_{i+1}^2)] - 2(d_1^2 - d_n^2)T_{WAT}\} \quad (2\text{-}10)$$

where, t_i = Temperature at location i, °F

d_i = Depth at location i, inch

T_{WAT} = Weighted average temperature, given by Equation 2-11.

$$T_{WAT} = \sum_{i=1}^{n}[\frac{0.5(t_i + t_{i+1})(d_i - d_{i+1})}{(d_1 - d_n)}] \quad (2\text{-}11)$$

The temperature moment can be converted into an equivalent linear gradient by determining the linear gradient that produces the same magnitude of temperature moment as the measured surface profile, using Equation 2-12.

$$ELTG = \frac{-12(TM_0)}{h^3} \quad (2\text{-}12)$$

where, ELTG = Equivalent linear temperature gradient, °F/in

h = Slab thickness, inch

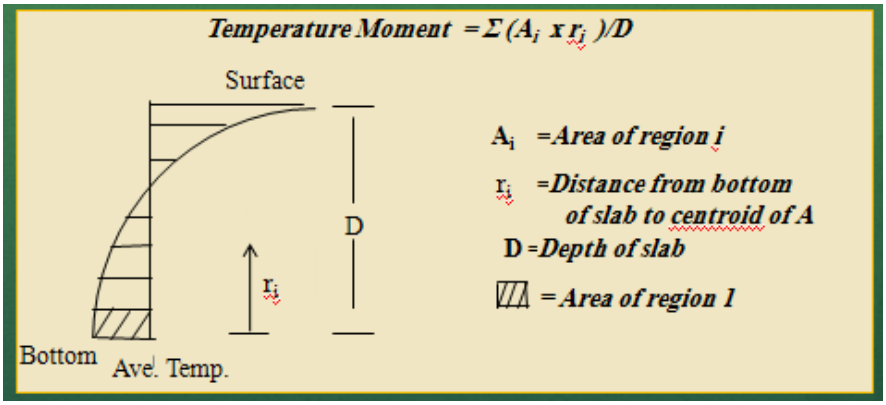

Figure 2-2. Representation of the temperature moment concept in Janssen and Snyder method (Janssen and Snyder 2000).

2.3 PERMANENT WARPING GRADIENT

As discussed previously, a portion of the drying shrinkage that occurs in concrete can be reversed when rewetted. This is known as reversible drying shrinkage. Figure 2-3 shows the typical behavior of concrete through drying/wetting cycles. The irreversible portion of the shrinkage is responsible for permanent warping in concrete slabs, while the reversible portion causes seasonal variation in warping (ARA Inc. ERES Consultants Division 2004). The focus of this section is on the long-term irreversible drying shrinkage used to establish the permanent warping, ΔT_{shri}, in the slab.

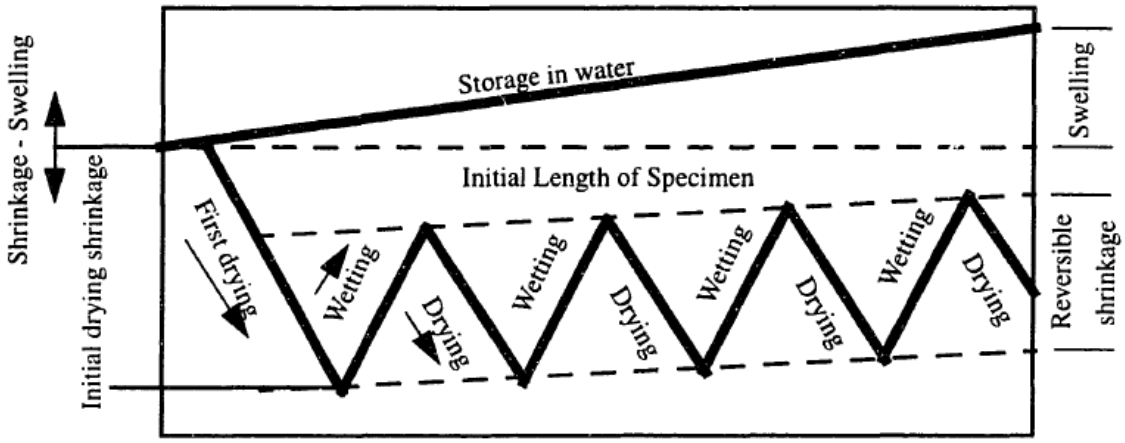

Figure 2-3. Typical behavior of PCC upon drying and rewetting (Neville 1996).

2.3.1 Factors Influencing Drying Shrinkage

Factors affecting permanent warping, ΔT_{shri} , include the age of concrete, size and shape of the section, ambient exposure conditions , PCC mixture design, curing method and the existence and diameter of dowel and tie bars.

Age

Irreversible drying shrinkage in concrete is a property that takes a long period of time to stabilize. The in-situ drying shrinkage was established in a previous study based on measured strains in the slabs (Burnham and Koubaa 2001). Results from this study showed it takes the drying shrinkage 4 or 5 years to reach its maximum value.

Ambient Conditions

The ambient RH affects the rate of the development of irreversible drying shrinkage in the concrete. An increase in the atmospheric RH is expected to reduce the relative rate of moisture flow from the interior to the outer surface of concrete. In drier areas, higher values of irreversible drying shrinkage can be developed in concrete (Mehta 1986). This was shown in a study performed by Bissonntte in 1999. See Figure 2-4.

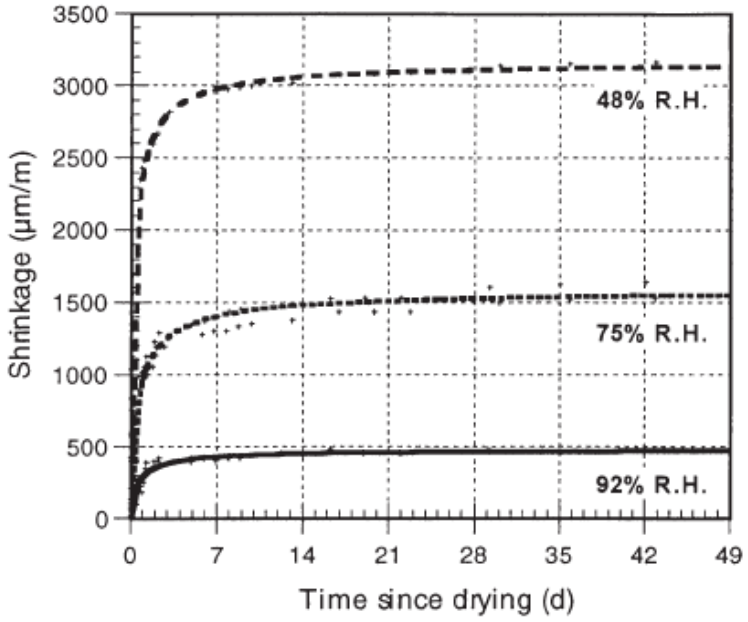

Figure 2-4. Effect of ambient RH on shrinkage (Bissonnette, Pierre et al. 1999).

PCC Mixture Properties

The PCC mixture properties that affect drying shrinkage include w/cm ratio, water and cement content, microstructure of the paste, the use of chemical admixtures and aggregate content, type and top size. The influence of some of these factors on drying shrinkage will be further defined below.

Irreversible drying shrinkage is affected by the porosity of the mixture. One PCC mixture property that affects the porosity in concrete is the w/cm ratio. Researchers have shown that an increase in the water content usually results in an increase in drying shrinkage at later time periods (in excess of 90 days) (Soroka 1979). See Figure 2-5. Mixes with a higher cement content will also experience more shrinkage (Martinez 1998). See Figure 2-5.

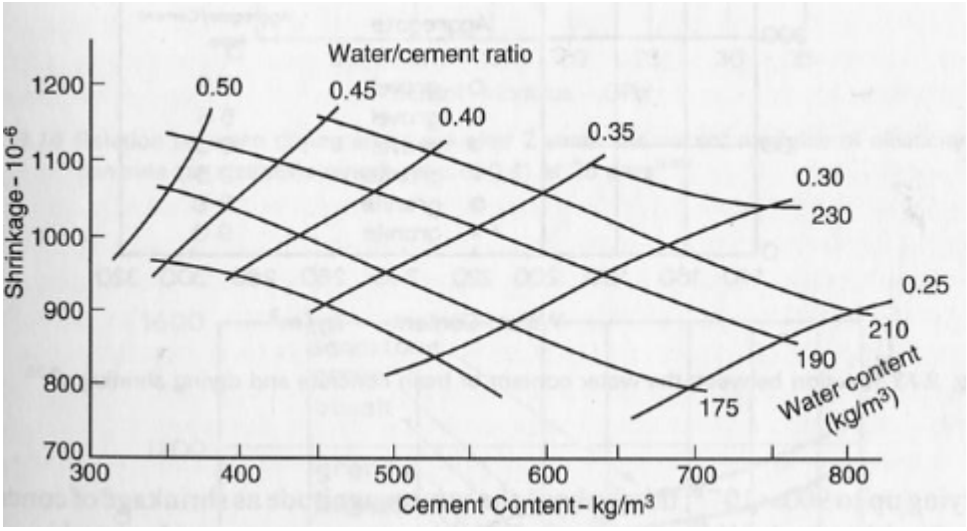

Figure 2-5. Effects of water and cement content on drying shrinkage (Neville 1996).

Another PCC mixture property that affects the drying shrinkage in the concrete is the coarse aggregate. The coarse aggregate in the concrete restrains drying shrinkage. Increasing the amount or stiffness of the coarse aggregate in the concrete can result in less drying shrinkage. See Figure 2-6 for effects of aggregate type. The following relation, developed by Powers based on tests performed on two different aggregates, shows the relation between the drying shrinkage of the paste, Sp, and the drying shrinkage of the concrete, Sc:

$$\frac{Sc}{Sp} = (1-g)^n \qquad (2\text{-}13)$$

where, g = Volume fraction of the aggregate,

n = Varying between 1.2 and 1.7, depending on the stiffness of the aggregate (L' Hermite 1962).

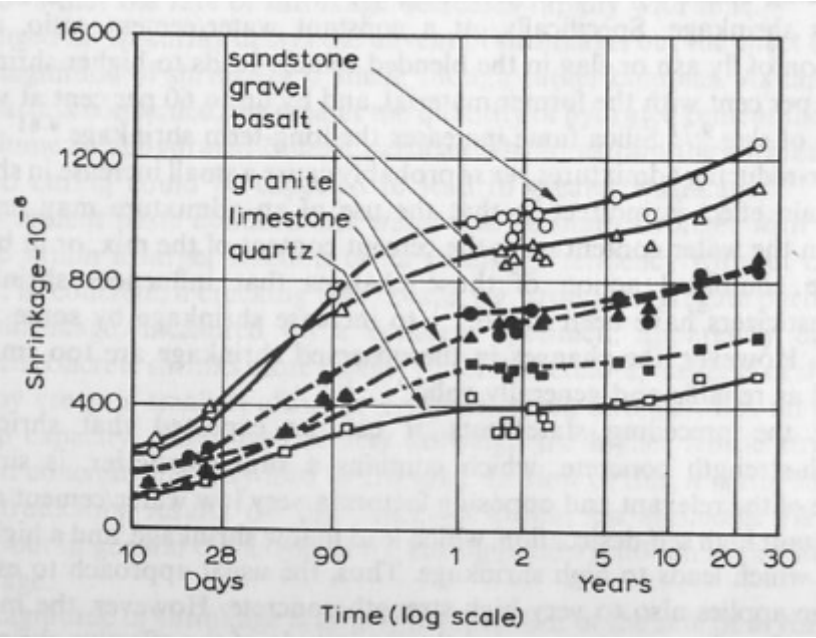

Figure 2-6. Effects of aggregate type on drying shrinkage (Neville 1996).

Mineral admixtures, such as fly ash and blast furnace slag, are commonly used in concrete. In general, mineral admixtures reduce the water demand of the mix and hence can result in less shrinkage.

Slab Thickness

Water transport from the interior of the concrete to the atmosphere is affected by the travel length (Mehta 1986). Therefore, both the thickness and size of the slab can affect the rate of drying shrinkage in the slab.

2.3.2 Available Methods for Establishing ΔT_{shri}

As discussed earlier, due to exposure to the atmosphere, the upper portion of the slab is more susceptive to drying than the bottom. This results in a nonlinear moisture gradient in the slab. However, Westergaard closed-form solutions for estimating curling stresses require a linear temperature gradient. Therefore, there is a need to define a linear temperature gradient equivalent to the nonlinear moisture gradient in the slab.

Previous researchers have defined an ELTG that would cause an equivalent strain in the slab due to the presence of a nonlinear moisture gradient. For instance (Eisenmann and Leykauf 1990) showed that a LTG could be defined using Equation 2-16. This gradient would generate an equivalent moment in a beam section due to the presence of a drying shrinkage gradient.

$$\Delta t = \frac{6t\varepsilon_s(h - h_s)}{\alpha h^3} \qquad (2\text{-}14)$$

where, Δt = Linear temperature gradient, ˚F/in

ε_s = Surface shrinkage,

h = PCC slab thickness, inches

h_s = Maximum depth that shrinkage occurs, about 2 inches

α = Coefficient of thermal expansion (CTE), /°F

The concept of replacing the drying shrinkage gradient across the slab with an ELTG across the slab depth is also employed in the MEPDG. In the MEPDG, the effects of monthly variations on warping are expressed in terms of an equivalent temperature difference and are added to the equivalent linear temperature difference when calculating stresses (ARA Inc. ERES Consultants Division 2004). Equation 2-15 presents the ELTG, representing deviations in warping from the annual average adjusted based on the ambient RH.

$$ETG_{shi} = \frac{3(\varphi.\varepsilon_{su})(S_{hi} - S_{have})h_s(\frac{h}{2} - \frac{h_s}{3})}{\alpha h^3} \quad (2\text{-}15)$$

where, ETG_{Shi} = Equivalent temperature gradient, ˚F/in

φ = Reversible shrinkage factor, fraction of total shrinkage. Based on the MEPDG documentation, a value of 0.5 is recommended for use, unless more accurate information is available,

ε_{su} = Ultimate drying shrinkage based on PCC mixture properties, × 10^6

S_{hi} = Relative humidity factor for month i:

S_{hi} = 1.1 for $RH_a \leq 30$ %

S_{hi} = 1.4 – 0.01 RH_a for 30 % < RH_a < 80 %

S_{hi} = 3.0 – 0.03 RH_a for $RH_a \geq 80$ %

RH_a = Ambient average RH, percent

$S_{h\,ave}$ = Annual average RH factor. Annual average of S_{hi}

The above equation is based on the ultimate drying shrinkage of the concrete. To estimate the temperature difference equivalent at any time after placement, Equation 2-16 from the ACI Committee 209 was used in the MEPDG (ARA Inc. ERES Consultants Division 2004).

$$ETG_{sht} = (\frac{Age}{n + Age})ETG_{shi} \quad (2\text{-}16)$$

where, $ETG_{Sht} = ETG_{Shi}$ at any time t days from PCC placement, °F

Age = PCC age, days since placement

n = Time to develop 50 percent of the ultimate shrinkage strain, days, recommended to be assumed as 35 in the ACI committee 209.

It should be pointed out that the ultimate drying shrinkage in Equation 2-17 can be established based on laboratory test results following the AASHTO T160 protocol, "Standard Method of Test for Length Change of Hardened Hydraulic Cement Mortar and Concrete." The second method for establishing the ultimate drying shrinkage is employing empirical relations that are available for this purpose.

The most widely-used relation is the one developed by Bazant (Bazant and Baweja 2000) that is also incorporated into the MEPDG. This simple empirical model estimates the ultimate drying shrinkage for the PCC based on the mixture design and 28-day compressive strength. The result is corrected for the curing method and the cement type through two factors of C_1 and C_2. This relation is provided in Equation 2-17.

$$\varepsilon_{su} = C_1 C_2 \{26W^{2.1}(f_c')^{-0.28} + 270\} \quad (2\text{-}17)$$

where, ε_{su} = Ultimate drying shrinkage strain, $\times 10^{-6}$

w = Water content for the PCC mix under consideration, lb/ft^3

f'_c = 28-day PCC compressive strength, psi

C_1 = Cement type factor defined as 1.0 for Type I cement, 0.85 for Type II cement, and 1.1 for Type III cement

C_2 = Type of curing factor defined as 0.75 if steam cured, 1.0 if cured in water or 100% RH and 1.2 if sealed during curing (curing compound.)

Another method to estimate a linear temperature gradient equivalent to the drying shrinkage gradient in the slab is based on the RH distribution along the slab depth over time. Measuring RH in concrete goes back to 1940 (Grasley 2003). The internal RH has been measured for concrete previously by the use of psychrometers (Janssen 1986), chilled mirror dew point and dry bulb temperature sensors (Jeong and Zollinger 2005), Sensirion SHT75 relative humidity sensors packed in a plastic tube with a Gore-Tex cap (Grasley and Lange 2004) and other humidity probes (Mccarter, Watson et al. 2001, Parrott 1988; Andrade, Sarría et al. 1999; Loukili, Khelidj et al. 1999; Yang 1999; Altoubat 2000).

Based on the RH distribution in the concrete, the method developed by Mohamed and Hansen (1997) can be followed to establish an equivalent temperature gradient. In this method, a third-degree polynomial function is assumed to represent the humidity difference coefficient throughout the slab depth. The regression coefficients from the polynomial function are used to establish the equivalent linear humidity difference coefficient. This is presented in 2-18 and 2-19 (Jeong and Zollinger 2005).

$$\Delta[1-(RH/100)^3] = A + Bz + Cz^2 + Dz^3 \quad (2\text{-}18)$$

$$\Delta[1-(RH/100)^3]_{eq} = -12\left(\frac{Bh}{12} + \frac{Dh^3}{80}\right) \quad (2\text{-}19)$$

where, $\Delta[1-(RH/100)^3]_{eq}$ = Equivalent linear humidity difference coefficient,

z = Coordinate defined as zero at mid-depth of the slab, where upward is negative and downward is positive,

A, B, C, D = Regression coefficients,

h = Thickness of the concrete slab, inch

The moisture strain is defined as the product of the equivalent linear humidity difference coefficient and the ultimate drying shrinkage of the PCC (Jeong and Zollinger 2005). The relation is provided in Equation 2-20.

$$\varepsilon_M = -\varepsilon_\infty \Delta\left[1-\left(\frac{RH}{100}\right)^3\right]_{eq} \quad (2\text{-}20)$$

where: ε_M = Moisture strain,

ε_ω = Ultimate drying shrinkage strain.

The equivalent linear temperature difference can then be defined by simply dividing the drying strain by the CTE of the concrete (α_c), as presented in the following relation.

$$ELG = \frac{-\varepsilon_\infty \Delta[1-\frac{RH}{100}]_{eq}^3}{\alpha_c} \quad (2\text{-}21)$$

2.4 LONG-TERM AND EARLY-AGE CREEP

The response of an elastic material to constant loading would be a constant instantaneous deformation. Concrete, on the other hand, shows an instantaneous and also a viscous flow under suddenly applied and then maintained loads (Westman 1999). The instantaneous elastic and the creep strain under a constant stress are distinctly presented in Figure 2-7.

Creep strain shown in Figure 2-7 is known as the basic creep. Basic creep in concrete occurs in constant moisture and temperature conditions. This parameter is established in the laboratory by performing tests on sealed concrete specimens. When allowed to dry, however, another type of creep comes into play, referred to as the drying creep (Pfeiffer and Tanabe 1993). Drying shrinkage, basic creep and drying creep are presented all together in Figure 2-11.

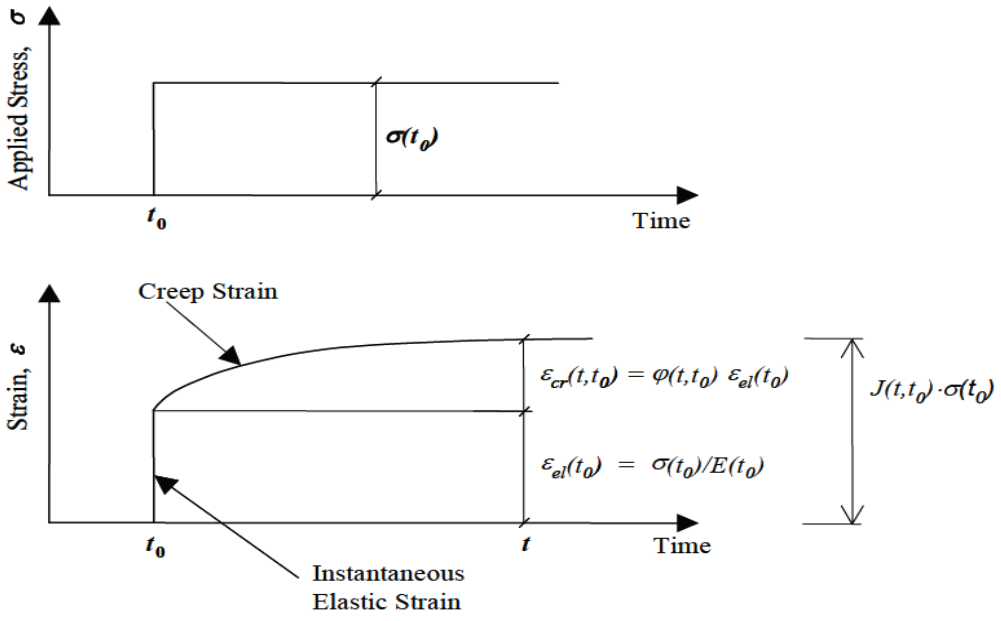

Figure 2-7. Instantaneous strain and creep over time (Ruiz, Rasmussen et al. 2006).

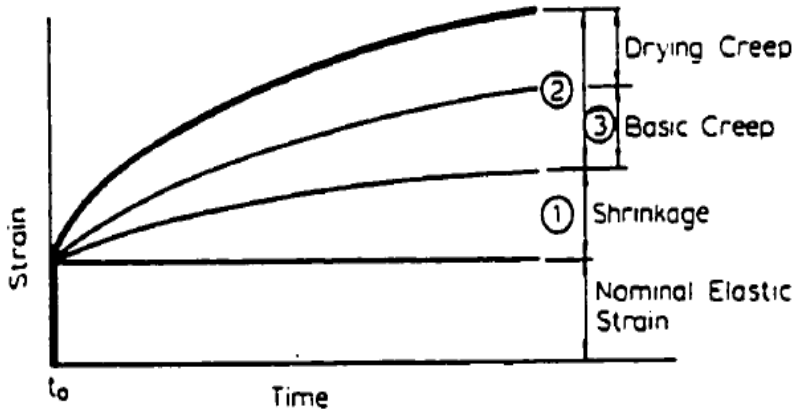

Figure 2-8. Presentation of basic and drying creep with respect to drying shrinkage (Neville 1996).

2.4.1 Factors Influencing Creep

Drying shrinkage and creep in concrete are considered interrelated phenomena. This is because of the similar factors that influence the two phenomena. Influencing factors regarding creep in the concrete, including age and duration of loading, state of loading, the ambient conditions and the PCC mixture, are further discussed below.

Age and Time of Loading

For a constant stress, the total amount of creep increases with time at a decreasing rate (Neville 1970). Furthermore, more creep occurs in specimens that are loaded at earlier ages.

State of Loading

Generally, creep is investigated in compression. This is because concrete is generally designed to carry compressive loads and also because compressive creep tests are the easiest ones to perform. However, concrete in pavement structures, are subjected to tension and flexural

loadings. The number of studies that have focused on tensile creep is very limited and the results are somewhat contradictory. For instance, some conclude that the magnitude of creep in tension is the same as that in compression (Neville 1970). This discussion will be expanded upon later in this chapter.

Ambient Conditions

More creep is seen at higher temperatures (Mehta 1986; Persson 1998). Results of a creep test performed on samples at a stress-strength ratio of 70 percent at different temperatures are shown in Figure 2-9. It has also been shown that concrete stored at higher temperatures before loading will exhibit more creep than concrete stored at lower temperatures (Neville 1970).

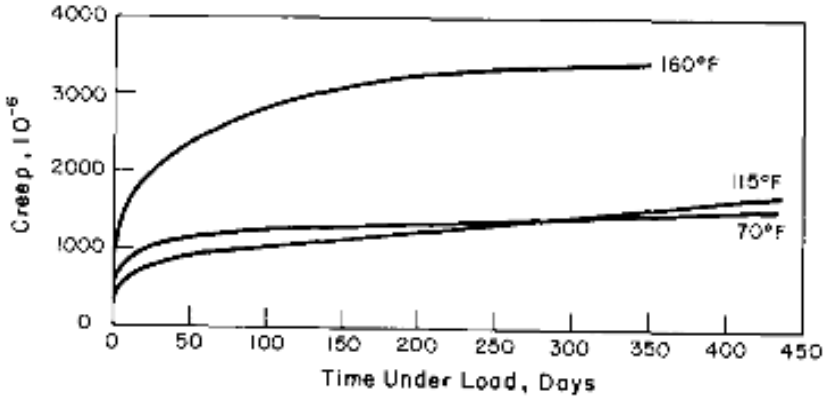

Figure 2-9. Effects of temperature on creep (Nasser and Neville 1966).

Another study performed at the University of Washington shows curvature in beam specimens under constant flexural loading increases with an increase in temperature. This increase was proportional to the amount the temperature was increased above a base temperature of 20°C (Taflin 2001).

The ambient RH the concrete is exposed to has the same effect on creep as it does on drying shrinkage (Mehta 1986). The drying concrete creeps at a higher rate and achieves a higher ultimate creep than concrete which remains wet (Neville 1970). The effects of the ambient RH on creep are presented in the following figure.

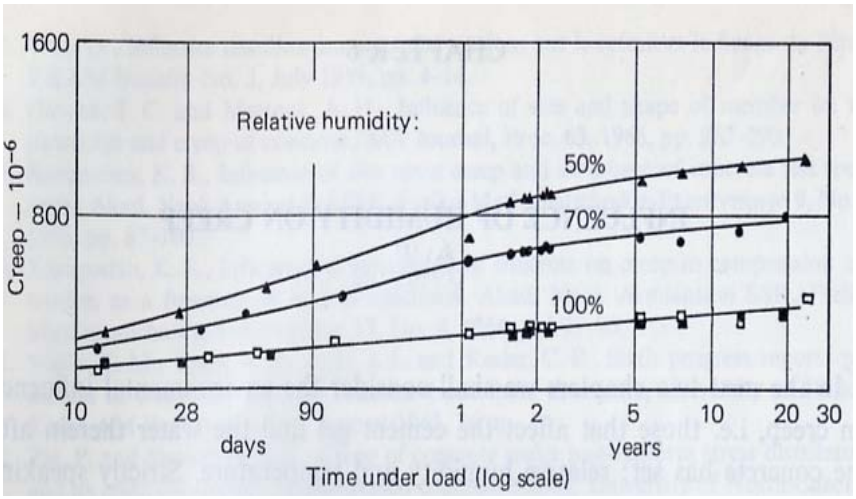

Figure 2-10. Effects of the ambient RH on creep in concrete (Neville 1970).

PCC Mixture Properties

Creep in concrete occurs in the hydrated cement paste (Neville 1996). The unhydrated cement particles and the coarse aggregate, however, restrain the creep in the paste. Therefore, creep, similar to drying shrinkage, depends on the volumetric content, gradation, maximum size and stiffness of the coarse aggregate. The following relation shows the relation between the ratio of creep of the paste, Cp, to creep of concrete, c, (Neville 1964):

$$\log\frac{Cp}{c} = \alpha \log\frac{1}{1-g-u} \qquad (2\text{-}22)$$

$$\alpha = \frac{3(1-\mu)}{1+\mu+2(1-2\mu_a)\frac{E}{Ea}} \quad (2\text{-}23)$$

here, c = Creep of concrete,

g = Volumetric content of aggregate,

u = Volumetric content of unhydrated cement,

μa = Poisson's ratio of aggregate,

μ = Poisson's ratio of surrounding material (concrete),

Ea = Modulus of elasticity of aggregate,

E = Modulus of elasticity of concrete.

Another mixture property that can influence creep is the cement type. Different cement types can result in different concrete strengths at the time of loading and therefore different levels of creep. For a given age of loading, creep increases in magnitude for concrete made with different types of cement based on the following order: Type III, Type I and Type IV (Neville 1970).

2.4.2 Available Models for Establishing Creep

As seen in Figure 2-7, strain under constant loading has two parts: the elastic strain and creep. The elastic strain is defined as follows:

$$\varepsilon_{el}(t_0) = \sigma(t_0)/E(t_0) \quad (2\text{-}24)$$

$E(t_0)$, also known as E_0 or E_{eff} , in Equation 2-24 is known as the asymptotic modulus of elasticity at t_0 and can be defined as shown in Equation 2-25 (Ruiz, Rasmussen et al. 2006):

$$E_0 = 1.5\, E_{28} \tag{2-25}$$

Or as in Equation 2-26 (Gilbert 1988):

$$E_0 = 1000\, f_c \tag{2-26}$$

where, f_c = The 28-day compressive strength of concrete, MPa

The magnitude of the creep that develops in concrete is usually defined in terms of the creep coefficient $\varphi(t,t_0)$ (Gilbert 1988). The creep coefficient is defined in the following relation. This is also presented in Figure 2-7.

$$\varphi(t,t_0) = \frac{\varepsilon_{cr}}{\varepsilon_{el}} \tag{2-27}$$

Creep compliance used by many researchers to describe the creep behavior is defined in terms of the total strain ε_t and the sustained stress applied at t_0. See the relation below.

$$\varepsilon(t,t_0) = J(t,t_0)\sigma(t_0) \tag{2-28}$$

$J(t,t_0)$ can also be defined in terms of the creep coefficient:

$$J(t,t_0) = \frac{1+\varphi(t,t_0)}{E(t_0)} = \frac{1}{E_{eff}} \tag{2-29}$$

The compliance function, including both instantaneous and creep strain, can be defined as follows:

$$J(t,t_0) = \frac{1}{E_0} + C_0(t,t_0) \qquad (2\text{-}30)$$

$C_0(t,t_0)$ in Equation 2-30 is the creep compliance function.

The creep discussed above is the creep that occurs in the concrete when there is no moisture exchange between the concrete and the atmosphere, hygral equilibrium (Westman 1999). Drying, on the other hand, affects creep in the concrete. Simultaneous drying shrinkage increases the magnitude of creep in compression and negates the effects of creep in tension. Drying together with compressive creep is presented in Figure 2-11. Strains due to drying are usually superimposed on the strains due to compressive creep.

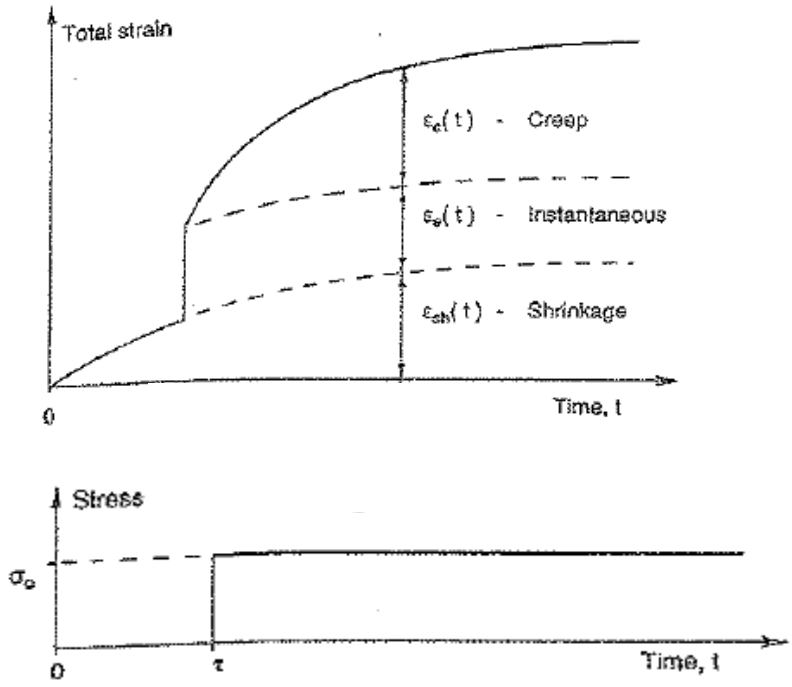

Figure 2-11. Instantaneous, creep and drying strain over time (Gilbert 1988).

The final compliance function including the drying strains can be defined as follows:

$$J(t,t_0) = \frac{1}{E_0} + C_0(t,t_0) + C_d(t,t_0,t') \tag{2-31}$$

where, t' = Time that drying starts, days

Many researchers have focused on defining relations that would best define the creep compliance functions. Most of these relations were calibrated based on compressive creep laboratory tests. The most popular creep compliance function is the one developed by Bazant. The Double-Power Law was developed more than two decades ago and is presented in Equation 2-31 (Bazant and Panula 1978).

$$J(t,t') = \frac{1}{E_0} + \frac{1}{E_0}(t'^{-m} + a)(t - t')^n \qquad (2\text{-}32)$$

Where φ_1, m, α and n are material parameters depending on strength, w/cm ratio, cement type etc. The Double-Power Law was later extended to the Triple-Power Law in which the long-term creep is described more accurately (Bazant and Chern 1985):

$$J(t,t') = \frac{1}{E_0} + \frac{1}{E_0}(t'^{-m} + a)[(t - t')^n - B(t,t',n)] \qquad (2\text{-}33)$$

In this relation, the five material parameters have the same values as in the Double-Power Law. B(t, t', n) is a binomial integral, which can be simulated by various power series or by step-by-step integration interpolated from a table of values provided in the reference.

The Double and Triple-Power Law are not calibrated for early-age (t_0 less than 2 days). Tests performed by Emborg (Emborg 1989) revealed that the Triple-Power Law is not able to capture creep at early-ages. This is shown in Figure 2-13. Two issues are noticeable in this figure: 1. the instantaneous strain predicted by the model is lower than the test results and 2. for early-age loading, the creep strain does not fit the test results as well as later loadings. Therefore, Triple-Power Law was extended in 1989 for early-age loading by Emborg. It was later modified and finalized by Westman in 1999. Two factors of $\psi_1(t_0)$ and $\psi_2(t, t_0)$ were added to the old model to account for the two limitations discussed above. The extended Triple-Power Law is as follows:

$$J(t,t') = \frac{1}{E_0} + \frac{1}{E_0}(t'^{-m} + a)[(t - t')^n - B(t,t',n)] + \frac{\psi_1}{E_0} + \frac{\psi_2}{E_0} \qquad (2\text{-}34)$$

$$\psi_1(t_0) = \gamma_1 (\frac{t_1 - t_0}{t_1 - t_s})^{a_1} \quad (2\text{-}35)$$

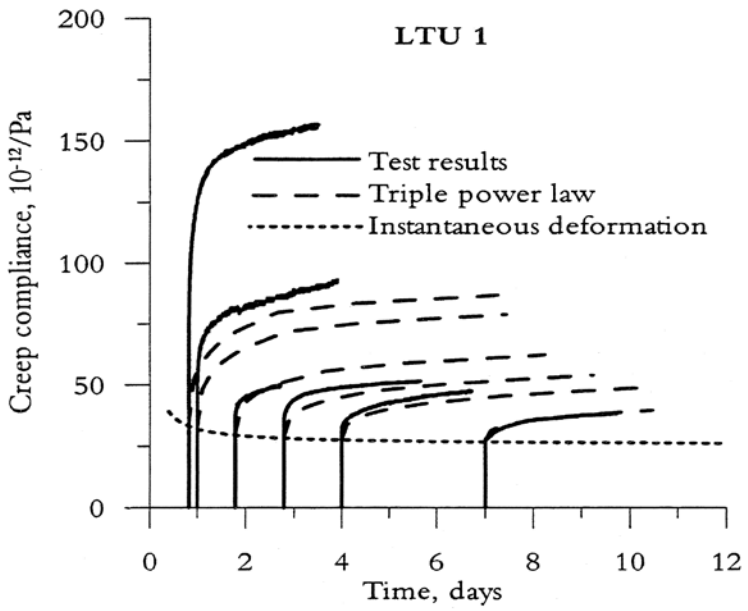

Figure 2-12. Examples of calculation using Triple-Power Law versus the test results (Westman 1999).

$$\psi_2(t, t_0) = \gamma_1 [1 - \exp(-(\frac{t - t_0}{t_2})^{a_2}](\frac{t_1 - t_0}{t_1 - t_s})^{a_2} \quad (2\text{-}36)$$

where, t_0 = Equivalent age when the load is applied, days

t_s = Apparent time at final set, days

t_1, t_3 = Time limits for adjustments at early ages

t_2, a_2 = Parameters for the development of the time function, days

γ_1 = Initial value of $\psi_1(t_0)$ at t_0=ts,

γ_2 = Initial value of $\psi_2(t, t_0)$ at t_0=ts,

a_1 = Parameter modifying the shape of $\psi_1(t,t_0)$

a_3 = Parameter modifying the end value of $\psi_2(t,t_0)$

The effects of $\psi_1(t_0)$ and $\psi_2(t,t_0)$ on the predictions obtained using the Triple-Power Law is presented in Figure 2-13.

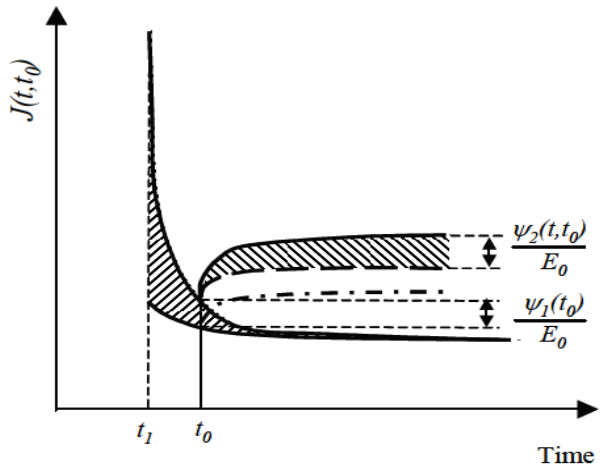

Figure 2-13. Effects of $\psi_1(t_0)$ and $\psi_2(t,t_0)$ on the creep compliance over time.

As mentioned earlier, the majority of the work performed on creep has been focused on loading in compression. However, detailed knowledge about tensile creep behavior at early ages due to shrinkage and thermal stresses is also essential (Ostergaard, Lange et al. 2001). The relation between tensile and compressive creep is somewhat unknown, especially at high stress-levels (Westman 1999). Performing creep tests in tension are in general more difficult than loading in compression. Most researchers in the past have assumed that compression and tensile creep are of the same order of magnitude (Gilbert 1988; Westman 1999).

In 1994, a study was performed that included early-age creep tests both under compressive and tensile loading (Umehara, Uehara et al. 1994). Tensile loading was carried out after compressive loading. In this study, relations were developed for early-age tensile and compressive creep compliance functions. Tensile creep compliance was defined as Equation 2-39 while compressive creep is defined in Equation 2-40. These relations, however, only represent the creep phenomena under limited testing conditions. Therefore, they need to be corrected for effects of temperature, load magnitude and the age at which the load is applied. These relations are presented below starting with the relation for the effects of temperature:

$$J_t(t) = \{28.74(1-e^{-0.801t}) + 8.13(1-e^{-45.38t}) + 7.46t\} \times 10^{-6} \quad (2\text{-}37)$$

$$J_c(t) = \{26.96(1-e^{-24.7t}) + 71.99(1-e^{-0.575t})\} \times 10^{-6} \quad (2\text{-}38)$$

where, J = Creep compliance, mm^2/N

t = Duration of loading, days

$$\Phi_c(T) = 0.0112T + 0.552 \quad (2\text{-}39)$$

where, T = Temperature, °C

The effects of the duration of the compressive loading are considered by the following relation:

$$\xi_c(\tau) = -0.307 \log \tau + 1.0 \quad (2\text{-}40)$$

where, τ = Concrete age when the load is applied, day

The structural formula for compressive creep is defined as:

$$J_c = \xi_c(\tau).\Phi_c(T).J'_c(t) \quad (2\text{-}41)$$

The structural formula for tensile creep is defined as:

$$J_t = \xi_t(\tau).\Phi_t(T).\delta_t(\sigma).J'_c(t) \quad (2\text{-}42)$$

where, $\delta_t(\sigma)$ = Represents the influence of intensity of the compressive stress:

$$\delta_t(\sigma) = 0.017\sigma + 0.701 \quad (2\text{-}43)$$

$\xi_t(\tau)$ = Represents the influence of period of compressive loading:

$$\xi_t(\tau) = -1.0107 \log \tau + 1.538 \quad (2\text{-}44)$$

where, τ = Period of compressive loading, days

$\emptyset_t(T)$ = Represents the influence of temperature:

$$\Phi_t(T) = 0.0257T + 0.487 \quad (2\text{-}45)$$

This study, although very beneficial, is limited in several ways. One of the limitations is that the tests are performed only on specimens cast from one concrete mixture. Therefore, the influence of the PCC mixture properties, such as the w/cm ratio or aggregate type and amount, are not accounted for in this study. The PCC mixture design used in the study is provided in Table 2-3. Additionally, the tensile creep is defined only as a function of the magnitude and duration of compressive loading, since all tensile creep tests were performed proceeding compressive creep loadings.

Table 2-3. PCC mixture properties used in the study (Umehara, Uehara et al. 1994).

		Composition (kg/m^3)			
w/cm Ratio	Air (%)	Water	Cement	Sand	Gravel
56	4.0	157	281	835	1010

In another study performed at the University of Illinois (Altoubat and Lange 2001), tensile creep tests were performed on two normal concrete (NC) mixtures with w/cm ratios of 0.4 and 0.5. The PCC mixture design is provided in Table 2-4 for both mixtures. In this study, the effects of sealing versus moist curing to prevent drying shrinkage is also analyzed. This study concludes that in order to completely isolate the basic tensile creep from drying shrinkage; samples need to be moist cured instead of sealed.

Table 2-4. PCC mixture properties used in the study (Altoubat and Lange 2001).

Constituent (kg/m^3)	NC-0.4	NC-0.5
Coarse Aggregate	925.8	925.8
Fine Aggregate	741.8	741.8
Cement	480	421.4
Water	192.0	210.7
Water-Reducing Admixture (ml/m^3)	565.1	--

This study uses the solidification theory to model the basic creep observed in the tests. The relation provided in Equation 2-46 fits the concrete mixtures tested in this study but may not provide an optimal fit for other concretes.

$$\varepsilon_{cr} = \frac{\sigma}{\nu(t)}[A_1(1-e^{-0.01(t-t_0)} + A_2(1-e^{-0.1(t-t_0)}] \quad (2\text{-}46)$$

where, $A_i = 1/E_i$, and is a constant for the i^{th} unit of the Kelvin chain

t = Age of concrete, days

t_0 = Age of concrete at time of loading, days

$v(t)$ = Volume fraction growth, defined as:

$$\frac{1}{v(t)} = \left(\frac{\lambda_0}{t}\right)^m + \alpha \qquad (2\text{-}47)$$

where, m and a = Empirical constants

λ_0 = Assumed as 24 when the age is expressed in hours

The model parameters were established for the two PCC mixtures as provided in Table 2-5.

Table 2-5. Values for the empirical constants in the creep model for the two PCC mixtures used in the study (Altoubat and Lange 2001).

Mixture	A_1	A_2	m	α
NC-0.4	103.45	357.07	5.5276	0.0852
NC-0.5	43.75	32.19	1.8868	0.5678

These factors were established using an incremental analysis and therefore are only valid for the same materials and loading conditions (Altoubat 2000). Another study performed at the University of Washington focused on investigating flexural creep in concrete (Taflin 2001). This study investigates the effect of different temperature levels during loading and also different stress/strength ratios on creep observed in 7-day old beams. The duration of the flexural loading is 24 hours and the temperature considered include 20-, 35- and 50 °C. Different levels of stress/strength ratios include 20-, 40-, 60- and 80 percent. The PCC design mixture used to cast the samples is provided in Table 2-6.

Table 2-6. Concrete mix design used in the University of Washington study (Taflin 2001).

Parameter	Quantity (kg/m^3)
Coarse Aggregate (8-16mm)	774
Fine Aggregate (0-8mm)	1048
Cement	343
Water	148
W/C ratio	0.43

The measured creep is presented in terms of curvature. A general relation is developed based on the 24-hour curvature and the stress/strength ratio for one test performed on the mixture at 20 °C. This relation, provided in Equation 2-48, can be used to estimate creep at any desired stress level and temperature.

$$K_{cr\_n} = S_n\left(\ln(\ln(t_n + e))\right)\left[CT_n - \left(\frac{(K_{cr20})(S_{20})}{\ln(\ln(t_{20} + e))}\right) - CT_{20}\right] \quad (2\text{-}48)$$

where, K_{cr_n} = Creep curvature at any stress, temperature and time for new mix

S_n = Desired stress/strength ratio (%) for new mix

t_n = Desired time (hours) for new mix

C = Slope constant ($3x10^{-7}$)

T_n = Desired temperature (°C) for new mix

K_{cr20} = 24-hour creep curvature for single test on new mix at 20°C

t_{20} = 24-hours (end time for single test on new mix)

T_{20} = 20°C (temperature for single test on new mix)

S_{20} = Stress/strength ratio used in single test on new mix at 20°C

This study is very beneficial since the major mode of loading in pavement structures is flexure. The study can be extended to include the effects of time of loading and also different PCC mixture designs on the measured creep.

The following conclusions can be drawn from the brief review provided in this section on creep studies discussed above: The number of studies that have focused on early-age tensile creep in concrete is very limited. The studies need to be expanded to include a larger range PCC mixture designs and loading conditions.

2.4.3 Effects of Creep on $\Delta T_{curl/warp}$ in JPCPs

A very limited number of studies are available that have focused on investigating the changes in the permanent curl/warp due to creep over the years. Establishing the effects of creep on the permanent curl/warp gradients in concrete slabs over the years is very complex due to the fluctuating magnitude and state of stress in the slab.

Studies performed in 2001 (Rao, Barenberg et al. 2001; Schmidt 2001), evaluated the changes in the built-in gradient for a concrete pavement in Mankato, MN over a duration of two years. The test section consists of an 8-inch thick PCC slab on an unstabilized base. Curling of the corner of the slabs with respect to the interior of the slabs was established by the use of a Dipstick profiler. This was performed at ages within 24 hours after paving as well as 3, 15 and 40 days and2 years after paving. The FEM was used to predict the curvature of the slab due to measured temperature gradients. The difference between the measured curvature and the FEM

predicted values were attributed to the built-in temperature gradient plus shrinkage and creep and is introduced as the equivalent gradient.

Based on this study, the equivalent gradient is reduced by 33 percent from age 3 to 15 days. This value increases by 50 percent between the ages of 15 and 40 days due to drying shrinkage. The final profile measurement taken at an age of two years showed that the equivalent temperature gradient dropped by 20 percent from that established at 40 days. This drop in the value of the equivalent temperature gradient was attributed to the effect of creep in the slab. The final value for the equivalent temperature gradient established two years after paving was -4.6 °F/in.

In the regards to this study, it should be noted that: 1-The deflections of the corners with respect to the center of the slab have been defined as the curvature of the slab. Also a benchmark was not used to establish the actual elevations of the slab and so the mid-slab was selected as the point of rotation of curvature for the relative elevations.; 2-The use of a benchmark for establishing the actual elevations based on the relative elevations provided by the Dipstick, has shown that the point of rotation is a fair distance away from the center of the slab and is closer to the slab edge. (Vandenbossche, 2003); 3-The accuracy of ISLAB in modeling the restraint and support conditions in the slab is limited.

3.0 CHAPTER 3-ESTABLISHING ZERO-STRESS TIME

3.1 INTRODUCTION

In order to be able to establish the built-in temperature gradient in the slab, the zero-stress time, TZ, needs to be determined first. One approach that can be followed for this purpose was developed in a previous study (Wells, Phillips et al. 2006) and is based on the changes seen in the measured strain with respect to the temperature variation in the slab. In the current study, this method will be applied to four different pavement sections located in Pennsylvania that were instrumented with VW static strain gages. In an effort to establish TZ for other PCC slabs beyond the four projects in this study, the degree of hydration at TZ, the critical degree of hydration, is also established for each of the four pavement sections. The idea is that TZ for any PCC slab, with the same design represented by each of the four instrumented projects, can be established based on the critical degree of hydration established for that design.

The geographical location, time of construction and design features for the four projects is summarized in Table 3-1. In this table, the projects are organized based on the material used to construct the base. The first two projects with the ATPB form the first group, and the second two projects with the CTPB make up the second group of pavement structures. Projects 1, 2 and

4, which were parts of Sections B09 and B10 on State Route 22, are presented in red in Figure 3-1. The approximate location of all four projects is presented on another map in Figure 3-2.

First a brief description of the instrumentation procedure and equipment is provided. It should be noted that the method and equipment used in the instrumentation is the same for all four projects. Following the section on the instrumentation, each instrumented project will be introduced individually. Three major topics will be covered for each project: "design features and PCC mixture design", "fresh and hardened concrete properties" and lastly "establishing TZ."

Table 3-1. Location and time of paving for four projects instrumented in this study.

Project No.	Geographic Limits	Test Section Stationing	Pavement Structure	County	Date of Construction
1	SR 22 (B09) from PA 982 to Auction Barn Rd T-968	From 1136+50 to 1147+60- Westbound	JPCP- 12" PCC/4" ATPB/ 6" 2A Subbase	Westmoreland, Pennsylvania	09/02/2009
2	SR 22 (B09) from PA 982 to Auction Barn Rd T-968	From 1115+00 to 1101+65- Eastbound	JPCP- 12" PCC/4" ATPB/ 6" 2A Subbase	Westmoreland, Pennsylvania	5/10/2010
3	SR 22 (B10) from Auction Barn Rd T-968 to Indiana County Line	From 939+60 to 955+15- Westbound	JPCP- 14" PCC/4" CTPB/6" 2A Subbase	Westmoreland, Pennsylvania	10/8/2009
4	US 22 from T-724/T-910 to SR 2024	From 377+96 to 399+45- Westbound	JPCP- 10" PCC/4" CTPB/6" 2A Subbase	Indiana, Pennsylvania	4/29/2010 and 4/30/2010

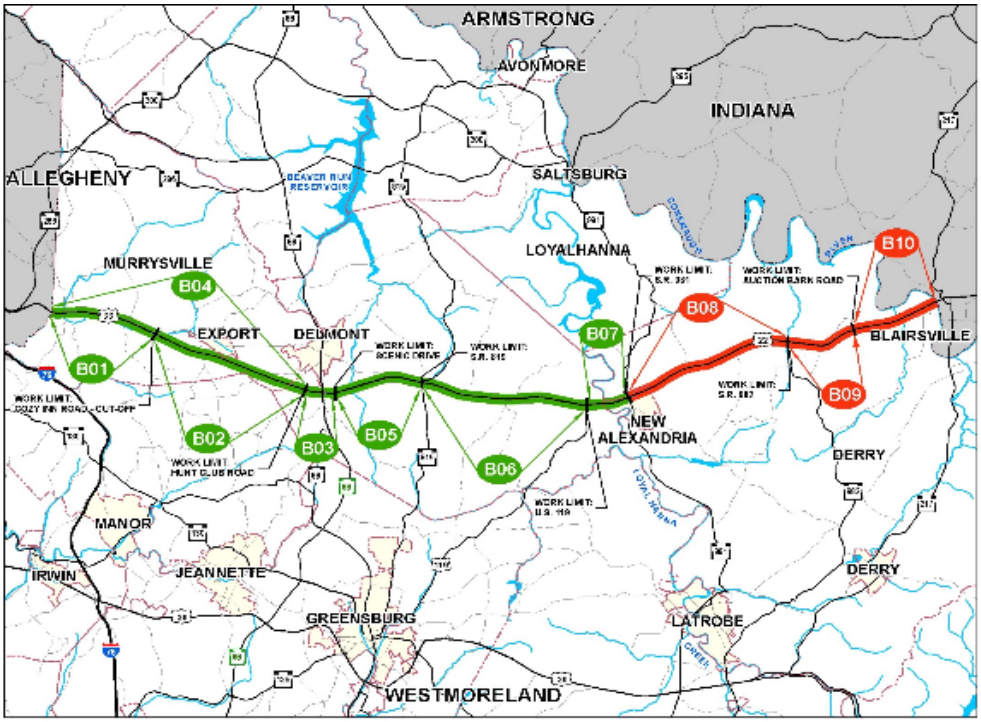

Figure 3-1. Renew 22 project construction sections, (www.renew22.com, Feb. 2011).

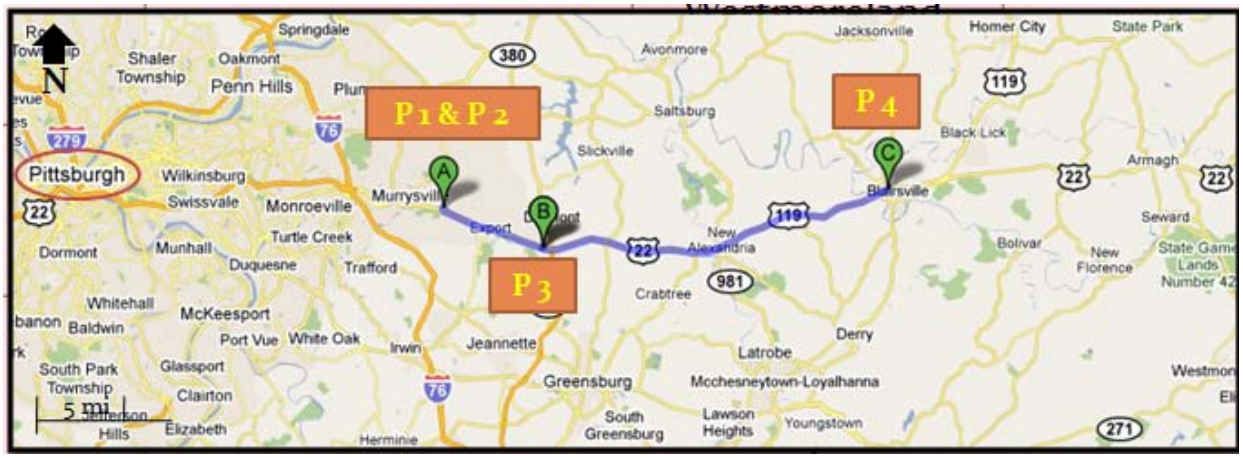

Figure 3-2. Location of the four instrumented projects on the map with respect to Pittsburgh http://maps.google.com/maps.

3.2 INSTRUMENTATION

3.2.1 Instrumentation Layout

The four pavement structures listed in Table 3-1 were instrumented with two different sensors at different locations and depths. The sensors were installed in clusters of three slabs referred to as a "cell." For each project, a total of three cells were paved at different times of the day. Figure 3-3 shows the layout of the cells within each test section. Each cell consisted of 3 consecutive slabs (A, B and C); with each cell paved at a different time throughout the day. Cell 1 for each project was located with the anticipation that it would be paved in the morning. Cell 2 was located so that it would be paved at approximately noon and Cell 3 was located to target a section of the pavement that would be paved later in the afternoon.

Each cell contained two types of sensors, including VW static strain gages and thermocouples. Approximate locations of the sensors within each slab in each cell can be found in the schematic provided in Figure 3-4.

As Figure 3-3 shows, the sensors were installed in each cell and wired to the datalogging equipment. Data was collected at 15-minute intervals for each sensor for a duration of between three to six days after paving. This duration of time varied for each project depending on the day the shoulders were scheduled to be paved (at this time, the datalogging equipment needed to be removed from the shoulder area).

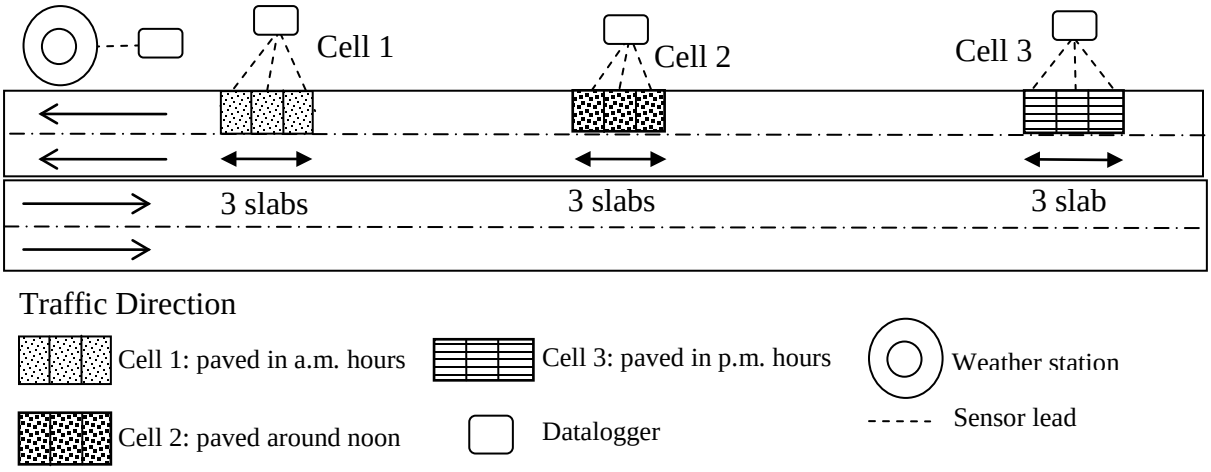

Figure 3-3. Schematic layout of the three cells instrumented in each project.

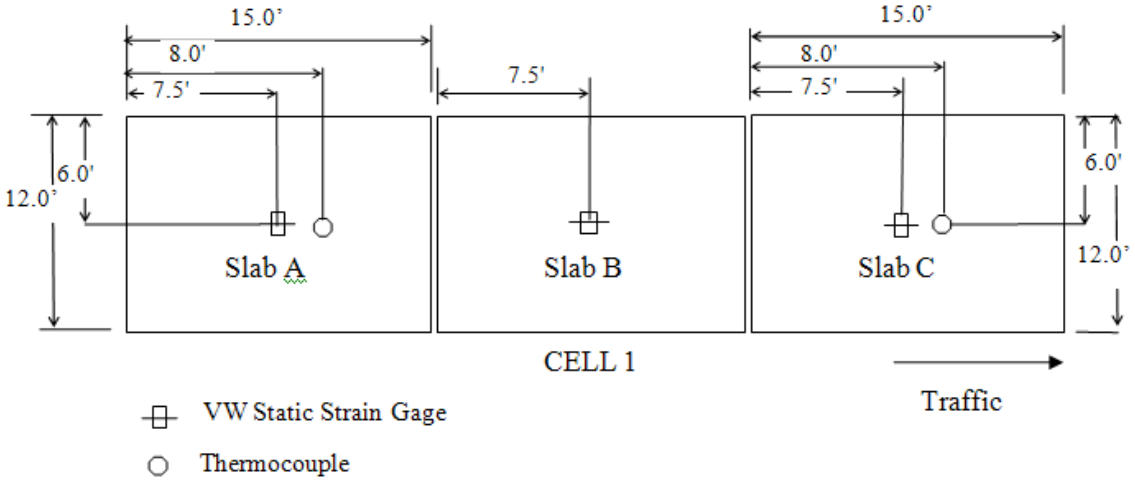

Figure 3-4. A typical slab instrumentation layout for the cells in each project.

Within each slab, two VW static strain gages were installed at mid-slab. Two thermocouple trees were also installed at the middle of Slab A and at the middle of Slab C within each cell. The approximate locations of the sensors are schematically presented in Figure 3-5. In each slab, one VW static strain gage was installed approximately one inch from the surface of the slab and another one approximately one inch from the surface of the base layer. Figure 3-5

presents a schematic cross section of a pavement with VW gages at the top and bottom of the slab.

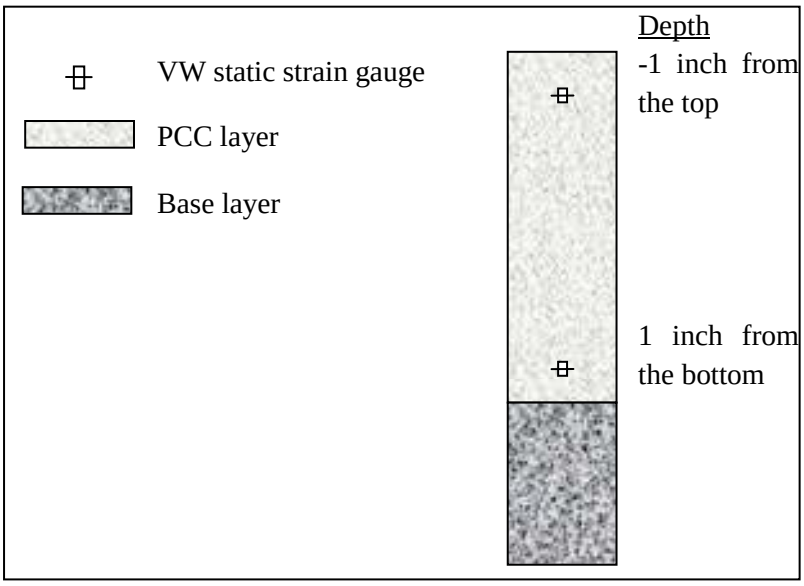

Figure 3-5. Location of the VW static strain gages across the depth of the pavement.

Thermocouples were also installed at various depths of the slabs. The approximate locations of the thermocouples in a 12-inch slab are presented in Figure 3-6, as an example. The exact depth from the slab surface was established for each sensor through pre- and post-paving surveys performed on each project.

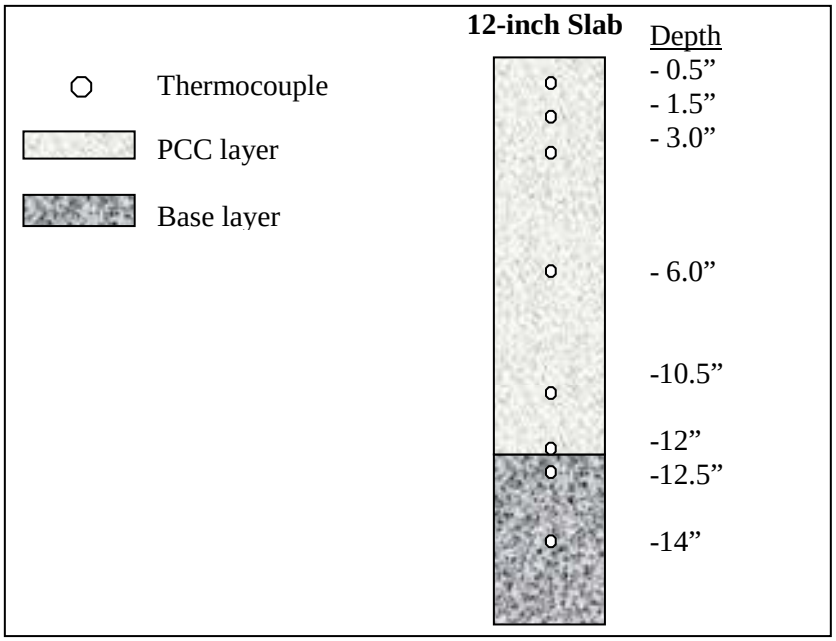

Figure 3-6. Location of the thermocouples along the depth of the pavement structure.

3.2.2 Instrumentation Equipment

The sensors used for the instrumentation of the projects, as mentioned in the previous section, included VW static strain gages and thermocouples. A datalogging system was used to collect the data in each cell. Additionally a weather station was assembled at the site for each project to collect and record the ambient conditions. A brief description on each will be provided as follows, starting with the VW static strain gages.

3.2.2.1 VW Static Strain Gages

Model 4200 VW concrete embedment strain gages manufactured by Geokon were used to measure strain in the concrete slabs for each project. The accuracy of the gage is reported as

±0.5 με by the manufacturer (Geokon 2010). The gages operate on the vibrating wire principle.

As seen in Figure 3-7 (a), the gage consists of a steel wire, which is pulled and tensioned inside a hollow metal tube. When the gage is embedded in concrete and concrete deformations take place, these end blocks move relative to one another. The movement of these end blocks influences the degree of tension in the steel wire. This tension in the wire is quantified by an electromagnetic coil, which measures the wire's resonant frequency of vibration upon being plucked. The gage is also equipped with a thermistor (see Figure 3-7 (a)) so that corrections can be made for changes in the length of the wire due to temperature. Figure 3-7 (b) shows a picture of a VW strain gage.

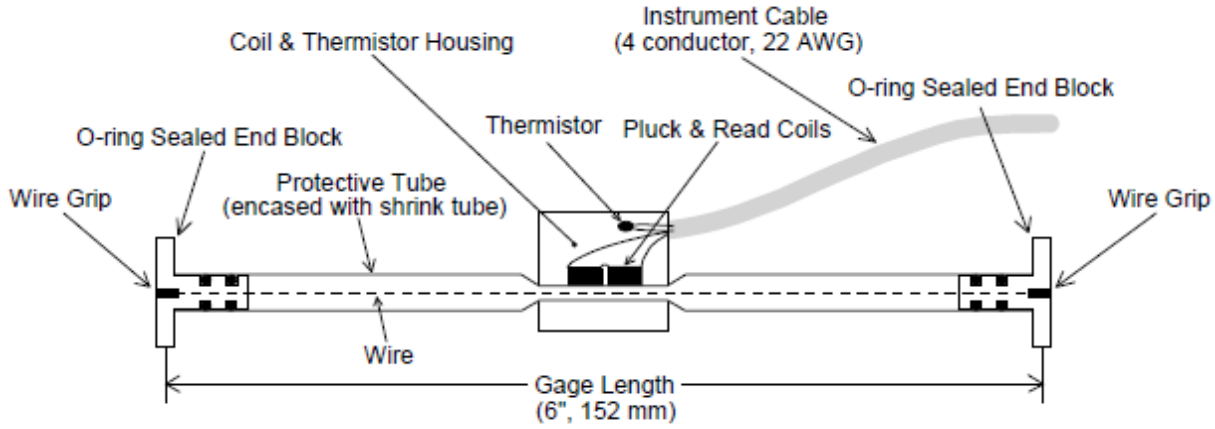

(a)

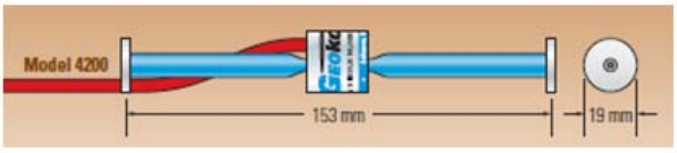

(b)

Figure 3-7. Schematic of a VW Model 4200 static strain gage (Geokon 2010).

To install the gages in the field, each set of two gages was fixed to two wooden dowels at each end by using wire ties. To plant the wooden dowels in the base layer, two holes were drilled in the base layer using a hammer drill. Special care was taken to make sure the gages were installed parallel to each other. Figure 3-8 shows two gages installed in the CTPB layer.

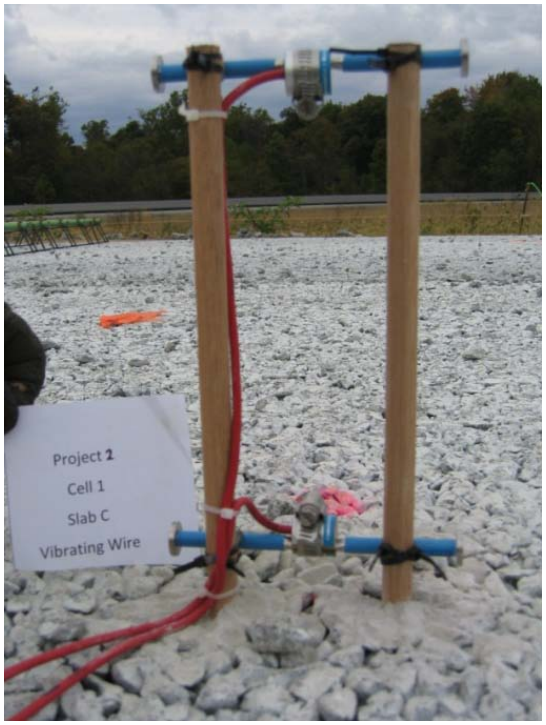

Figure 3-8. Installation of the VW static strain gages in Project 2.

3.2.2.2 Thermocouples

Early-age temperature changes in the slabs were measured by utilizing Type T thermocouple wire from the Omega Engineering. The operating principle of a thermocouple is that when two dissimilar metals, copper and constantan in the case of a Type T thermocouple, are in contact, they form a small but unique voltage. Since this voltage changes in an approximately linear

manner with changes in temperature, a relationship can be established between the two. This relationship can be used to measure the temperature.

In order to get the temperature measurements at the desired depths throughout the slab, thermocouple wire ends were fixed to wooden dowels at different depths using wire ties. These dowels were then inserted down into the base so that the thermocouples could measure the temperature at the desired depths of the pavement structure. Figure 3-9 presents pictures of two thermocouple trees installed at two different projects. The picture on the right is a project with a ATPB and the picture on the left is a project with a CTPB.

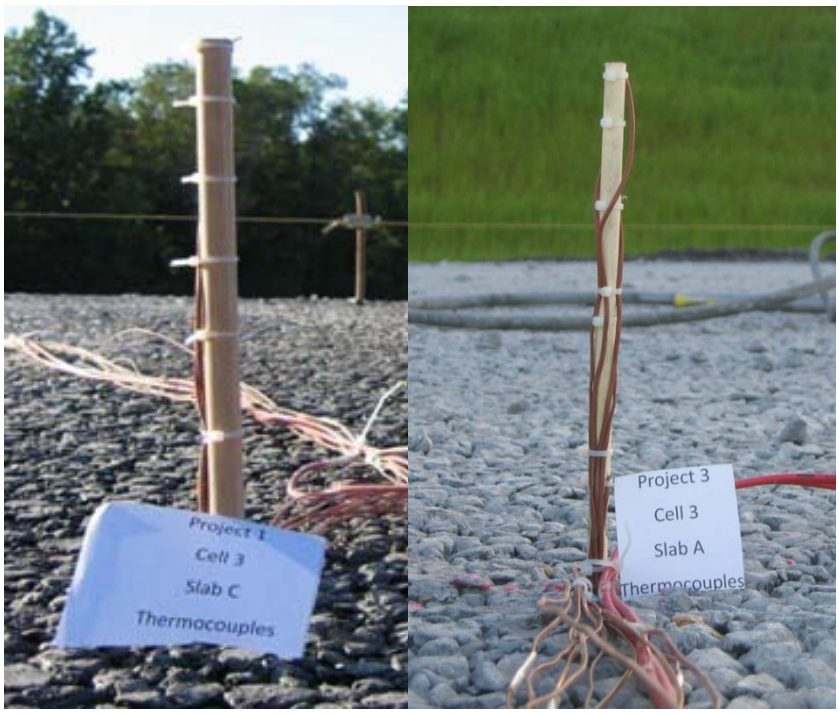

Figure 3-9. Installation of a thermocouple tree, on the left in a ATPB layer and on the right in a CTPB layer.

It is noteworthy that during the paving of the slabs for each project, great care was taken to protect the sensor installations from the damage due the paving process. Prior to the passing

of the paver, fresh concrete was carried from the paver to the sensors using wheelbarrows. Note the top picture in Figure 3-10. The concrete was then mounded (bee hived) around each sensor installation by hand and then consolidated using a flexible shaft vibrator. This process is shown in Figure 3-10.

(a)

(b)

Figure 3-10. (a) Protecting the sensor installations from the pass of the paver; (b) Concrete mounded on top of the already installed sensors before passage of the paver.

3.2.2.3 Weather Station

A weather station was also installed at the site of each project so that the major meteorological factors could be monitored throughout the data collection period. The weather station was used to monitor the ambient temperature, relative humidity, wind velocity and direction, precipitation, and solar radiation.

At the site for each project, the weather station was located sufficiently close to the pavement to be representative of the ambient environment under which the concrete sets, while still being an acceptable distance away from any obstructions such as buildings or trees. Figure 3-11 shows a schematic view of the weather station used in this study.

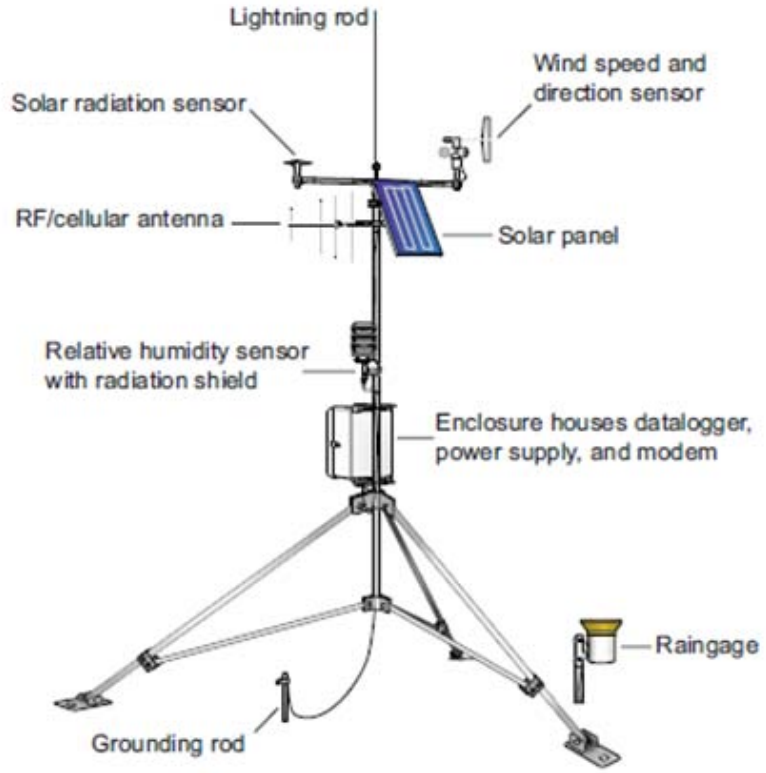

Figure 3-11. Schematic view of the weather station used at the site for each project, *(http://www.campbellsci.com/documents/solution-brochures/climate.pdf, Sept. 2009)*

3.2.2.4 Datalogging Systems

Data from the sensors was collected and stored on a Campbell Scientific CR1000 datalogger at every 15-minute interval. Figure 3-12 shows a picture of a CR1000 datalogger. Additional components used to read the data from the sensors include Campbell Scientific AVW200 vibrating wire interfaces and Campbell AM16/32B relay multiplexers for the VW gages and Campbell Scientific AM25T multiplexors for the thermocouples. This equipment expands the number of channels that can be wired to the datalogging equipment, allowing for up to 32 VW and 25 thermocouples to be wired to a single datalogger.

Figure 3-12. A picture of a CR1000 datalogger and power.

3.3 PROJECT 1- WESTBOUND OF SECTION B09 ON SR 22,

The instrumentation process described in the above section was followed for every project. The data from the sensors is utilized to establish TZ and subsequently $\Delta T_{built\text{-}in}$ for each slab. Prior to evaluating and analyzing the data for each project, a complete description of the project location, design features and concrete mixture design is presented.

3.3.1 Project 1-Location and Characteristics

Paving took place on the morning of September 2, 2009 beginning at approximately 7:30 AM. The roadway is a JPCP with 15-ft transverse joint spacing and 12-ft wide lanes. No. 5 epoxy-coated tie bars, were placed every 30 inches along both the lane/shoulder and centerline joints. Epoxy-coated 1.5-inch diameter, 18-inch long dowel bars were spaced every 12 inches along the transverse joints.

The first three slabs (Cell 1) in this project were paved at approximately 8:00 AM, slabs in Cell 2 were paved around 10:15 AM and the last cluster of slabs in Cell 3 were paved at approximately 11:30 AM. The time of paving for each cell was exceptionally close for this project. Even though the location of each cell was established based on discussions with the contractor, the unpredictability of the paving production rate on the day of paving resulted in paving all three cells at similar times of the day.

The design thickness for the PCC layer was 12 inch. Surveying before and after the paving revealed that the finished thickness of the slab varied between 11.75- and 12.5 in. The average thickness for each cell in this project is shown in Figure 3-13.

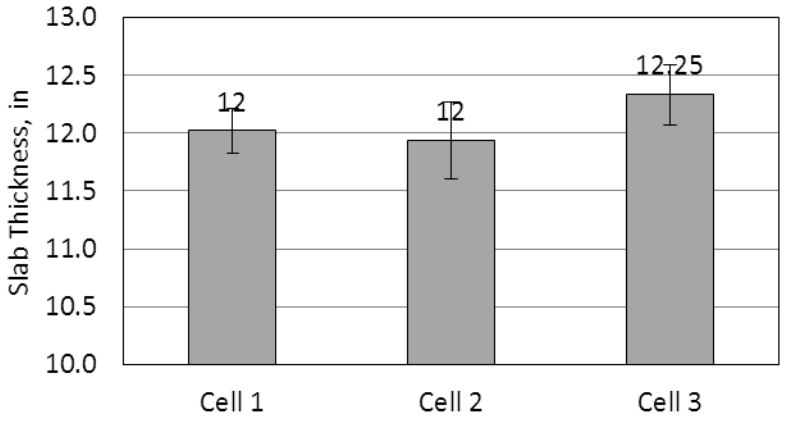

Figure 3-13. Variability of the as-built slab thickness in different cells for Project 1.

The PCC for this project was produced by Golden Triangle Construction Co. Inc. at a plant located approximately 4 miles west of the project site. Concrete was delivered to the site via tri-axle trucks. The two westbound lanes were paved in one pass. The shoulders were scheduled to be paved within one week after the paving of the mainline. After finishing and

transverse tinning, a curing compound was applied to the surface. Sawing of the joints began at approximately 4:30 PM on the paving day. The joints were sawed to a depth of 1/3 the slab thickness.

The PCC mixture used to pave each cell based on the design sheet provided by the batch plant on the paving day is provided in Table 3-2. The mix water came from an on-site well. The air entrainment and water reducing admixtures were supplied by Euclid Chemical Co. located in Cleveland, Ohio. The air entraining admixture was AEA-92 and Eucon WR was the water reducer agent. The coarse aggregate met a AASHTO No. 57 gradation and consisted primarily of limestone and the fine aggregate met PennDOT Specification Type A. Gradations for the fine and coarse aggregates can be found in Table 3-3 and Table 3-4 respectively.

Table 3-2. Paving PCC mixture for Project 1.

Material	Specific Gravity	Absorption (%)	Batch Weight (lb/yd^3)		
			Cell 1	**Cell 2**	**Cell 3**
Cement-Type I	3.15	N/A	500	500	500
Fly Ash-Class C	2.65	N/A	88	88	88
Fine Aggregate	2.62	1.24	1334	1322	1302
Coarse Aggregate	2.68	0.52	1857	1853	1857
Water Content	1	N/A	160	175.3	172.3

Table 3-3. Gradation of the fine aggregate used for the PCC for Project 1.

Fine Aggregate	
Sieve Size	Percent Finer
3/8"	100
#4	98
#8	76
#16	60
#30	50
#50	28
#100	9

Table 3-4. Gradation of the coarse aggregate used for the PCC for Project 1.

Coarse Aggregate - Limestone	
Sieve Size	Percent Passing
1 ½"	100
1"	97
½"	42
#4	4
#8	2

Type I cement manufactured by Armstrong Cement & Supply in Cabot, Pennsylvania was used on this project. The cement composition based on the mill sheet is summarized in Table 3-5. Class C fly ash from Essroc Materials Inc.-Joppa power plant was also used in the PCC. The fly ash was tested by the producer and had the chemical composition summarized in Table 3-6.

Table 3-5. Composition of the cement used for the PCC for Project 1.

Component	Value (%)	Specification
SiO_2	20.2	-
Al_2O_3	5.3	-
Fe_2O_3	4.3	-
CaO	64.4	-
MgO	1.0	6.0-Max
SO_3	2.95	C-1038-Max
C_3S	59	3.0-Max
C_3A	6.7	0.75-Max
Alkalis	0.55	-
Loss of Ignition	0.90	-
Insoluble Res.	0.32	-
Physical Data		
Blaine (cm^2/gm)	3800	2800-Min

Table 3-6. Composition of the fly ash used for the PCC for Project 1.

Component	Value (%)
Silica, SiO_2	35.87
Aluminum Oxide, Al_2O_3	21.44
Ferric Oxide, Fe_2O_3	6.01
Sulfur Oxide, SO_3	1.51
Calcium Oxide, Cao	25.74
Magnesium oxide, MgO	5.22
Available Alkalis	1.3

The PCC slab was placed on top of a 4-inch ATPB layer, which was over a subbase (separator) layer. The mixture design for the ATPB is provided in Table 3-7. The gradation of the open-graded aggregate used for the ATPB is provided in Table 3-8. A view of the base layer with dowel baskets fixed in place can be seen in Figure 3-14. A 6-inch granular subbase layer meeting PennDOT Class 2A material was placed on top of the fill material. The gradation for the 2A subbase layer material can be found in Table 3-9.

Table 3-7. Mixture design for the ATPB, Project 1.

Material Type	Material Class	Percent in Mix	Bulk Specific Gravity	Absorption
Coarse Aggregate	A57	78.8	2.665	0.52
Coarse Aggregate	A8	6.8	2.652	0.53
Fine Aggregate	B3M	11.8	2.617	1.14
Binder	PG 64-22	2.5	1.028	--

Table 3-8. Gradation of the aggregate used in the ATPB, Project 1.

Sieve Size	Percent Finer
1 ½"	100
1"	99
½"	56
No. 4	17
No. 16	9
No. 200	2.5

Figure 3-14. View of the base layer and the dowel baskets, one day prior to paving.

Table 3-9. Gradation of the 2A subbase material, Project 1.

Sieve Size	Test 1	Test 2	Test 3	PennDOT Limits
	Percent Finer	Percent Finer	Percent Finer	
2"	100	100	100	100
3/4"	73	73	71	52-100
3/8"	46	47	42	36-70
#4	32	30	26	24-50
#16	17	17	14	10-30
#200	2	2	2	$\leq$ 10

3.3.2 Fresh and Hardened Concrete Properties-Project 1

The fresh concrete properties measured in the field included air content, slump, unit weight and the w/cm ratio. The air content was measured using a pressure meter in accordance with ASTM C231. Concrete slump was measured following ASTM C143/C 143M. The w/cm ratio of the concrete mix was determined using the microwave oven water content test (AASHTO T318-93). As part of this procedure, the concrete unit weight was also determined based on ASTM C138. Depending on the available time in the field, some tests were able to be repeated for the PCC used to pave each cell. The test results for the PCC used for each cell in Project 1 are summarized in Table 3-10.

Table 3-10. Fresh concrete test results measured at the site of Project 1.

Concrete Property	Cell 1			Cell 2			Cell 3		
	High	Low	Ave.	High	Low	Ave.	High	Low	Ave.
Slump (in)	2.0	1.5	1.67	1.5		1.5	1.5		1.5
Entrained Air (%)	6.5	6.0	6.25	6.0	4.5	5.25	6.5		6.5
Unit weight (lbs/ft^3)	152			153	151	152	-	-	-
w/cm Ratio	0.41			0.48	0.47	0.475	0.49	0.45	0.47

The times of initial and final set of the PCC mixture were determined under field conditions in accordance with ASTM C403 "Standard Test Method for Time of Setting of Concrete Mixtures by Penetration Resistance." The mortar was obtained by sieving the PCC and was placed in three 6-in cubic specimens. The results of the test for each sample can be found in Table 3-11. The test results, in terms of the penetration resistance pressure versus time are also presented in Figure 3-15. In order to be able to establish maturity at the time of set, the temperature of one of the samples was measured during the test. The maturity was established using the Nurse-Saul relation as presented in Equation 2-1. The estimated maturity at initial and final set time is also reported in Table 3-11. These values will be used later to establish the initial and final set times in slabs.

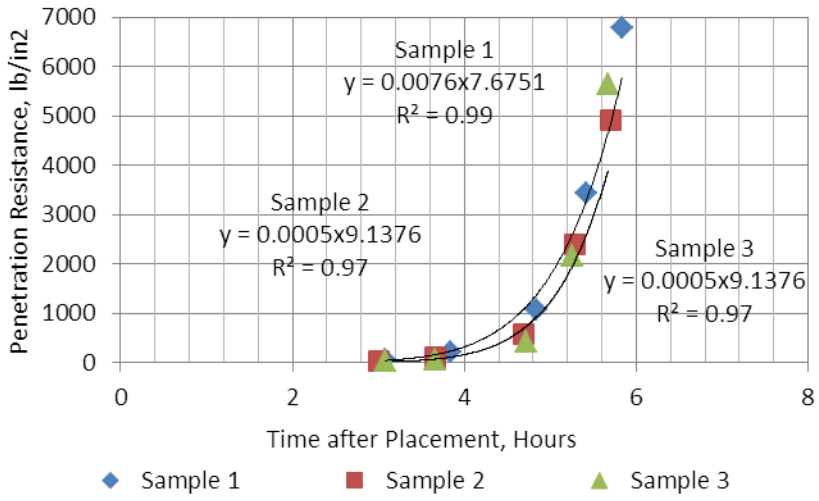

Figure 3-15. Penetration resistance over time for three samples cast from the PCC used for Project 1.

Table 3-11. Results from the penetration test for samples from the PCC used for Project 1.

	Penetration Resistance (psi)	Time (Hours)				
		Sample 1	Sample 2	Sample 3	Average	Maturity (°F-Hours)
Initial Set	500	4.2	4.5	4.5	4.5	372
Final Set	4,000	5.6	5.7	5.7	5.7	535

Concrete specimens were cast in the field for characterizing the concrete hardened properties. See Figure 3-16. Prisms and cylinders were cast and cured in accordance with ASTM C31/AASHTO T 126 and then transported to the Pavement Mechanics and Materials Laboratory (PMML) at the University of Pittsburgh for curing and testing. Tests included characterization of the elastic modulus (E_c), compressive strength (f_c) and modulus of rupture (MR). The age of the specimens at testing included 1-, 3-, 14-, 28- and 90-day. Only the 28-day test results are provided here but addition information on this can be found elsewhere (Nassiri and Vandenbossche 2010).

Figure 3-16. Concrete specimens cast for material characterization at Cell 2, Project 3.

Table 3-12. Hard concrete properties established in the laboratory at 28-days for the PCC used for Project 1.

Property	Cell 1	Cell 2	Cell 3	Mean	Standard Deviation
E_c (psi)	5.35E+06	4.95E+06	4.70E+06	5.00E+06	300,000
υ	0.24	0.19	0.22	0.22	0.03
f_c (psi)	5790	5730	4810	5440	550
MR (psi)	925	950	780	885	90

The coefficient of thermal expansion (CTE) of the PCC was also established for each cell in each project. This was achieved through the use of VW static strain gages. The gages were installed in cylindrical molds prior to casting the samples. The test for measuring the CTE values was based on a modified version of the AASHTO TP60 procedure. This modification consisted of using a VW strain gage to measure changes in length with changes in temperature instead of a linear variable deflection transducer. A total of three cylinders (one from each cell)

were cast in the field for Project 1. The CTE measured for the concrete used to pave Project 1 are provided in Table 3-13.

Table 3-13. Measured CTE for the PCC used in Project 1.

Cell Number	CTE (με/ºF)	Mean of CTE (με/ºF)	Standard Deviation (με/ºF)
1	5.1	5.1	0.04
2	5.1		
3	5.0		

Drying shrinkage was another property of the concrete that was established in the laboratory. Three 4×4×11¼-in prismatic specimens with gage studs were cast in the field, one from the mixture used to pave each cell. The length change of each specimen was measured in the laboratory based on AASHTO T 16/ASTM C 157 at 4-, 7-, 14-, 28-, 56-, 112-, 224-, and 448 days. The drying shrinkage specimens were transported to the PMML at the University of Pittsburgh and moist cured. They were demolded at the age of $23\,{}^{1}/_{2} \pm {}^{1}/_{2}$ hours after the addition of water to the cement during the mixing operation. After the initial comparator reading was taken immediately upon demolding, the specimens were stored in a lime-saturated water bath until they reached the age of 28 days, including the time period in the molds. After this period, the specimens were transported to the drying shrinkage environmental room with a constant temperature of 73 ± 3 ºF and a relative humidity of 50 ± 3 percent. The length change of each specimen was measured at different time intervals.

Unfortunately, only two of the three samples cast could be used because the gage studs for one specimen were damaged during the demolding process. The drying shrinkage measured

for these two samples is presented in Figure 3-17. The ultimate value obtained is 408 με and 462 με for Cell 1 and 2, respectively. This result measured for the samples taken from each cell corresponds to the w/cm ratios measured in the field as 0.41 for Cell 1 and 0.47 for Cell 2.

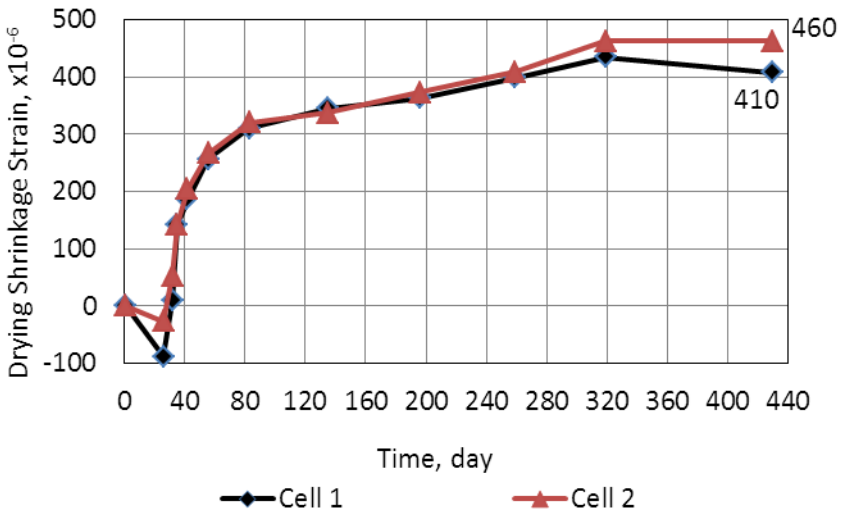

Figure 3-17. Measured PCC drying shrinkage strain based on ASTM C 157, Project 1.

3.3.3 Establishing TZ-Project 1

The variation in the measured strain in the fresh concrete with respect to the changes in its temperature is used in this study to establish TZ for each concrete slab. To measure the strain and the temperature in the slabs, VW static strain gages were installed in the slabs prior to paving.

The measurements from the VW gages were used to establish the zero-stress time in the concrete. Strain measurements in several fresh concrete slabs showed that while the concrete is still fresh, the strain measurements with respect to temperature are erratic. Also strain measurements between the final set and TZ with respect to changes in temperature are

negligible. However, at TZ, the two end blocks of the metal tube are fully restrained by the concrete and start to move as the concrete expand/contract and therefore the gages measurements reflect strain changes in the concrete. At this point, a transition can be identified from the negligible strain measurements to smooth changes in strain with respect to temperature. This transition point is recognized as TZ in slabs. The length changes in the wire due to temperature changes needs to be isolated from the readings. This is performed by using the following relation (Geokon 2010):

$$\varepsilon_{total} = (R_1 - R_0)\, B + (T_1 - T_0) \times \alpha_s \qquad (3\text{-}1)$$

where, ε_{total}= Strain in concrete, με

R_0 = Raw strain at time 0 (concrete raw strain at final set time)

R_1 = Raw strain at time 1

T_0 = Temperature at time 0 (concrete temperature at final set time)

T_1 = Temperature at time 1

α_s = CTE of the steel wire in the gage = 6.78 με/°F

B = Batch calibration factor defined as 0.97 by the manufacturer.

The strain measurements recorded with respect to temperature are highlighted in Figure 3-18. This figure presents an example strain-temperature graph generated using the data measured by the VW gage installed at the top of Slab A in Cell 1, Project 1. Strains in this figure were determined using Equation 3-1. In order to define R_0 and t_0 in this equation, the final set time for Project 1 was defined as the time the slab reached the maturity of 535 °F-Hours, as established by the penetration test discussed in Section 3.3.2. The temperature and strain corresponding to this time was used to define T_0 and R_0 in Equation 3-1.

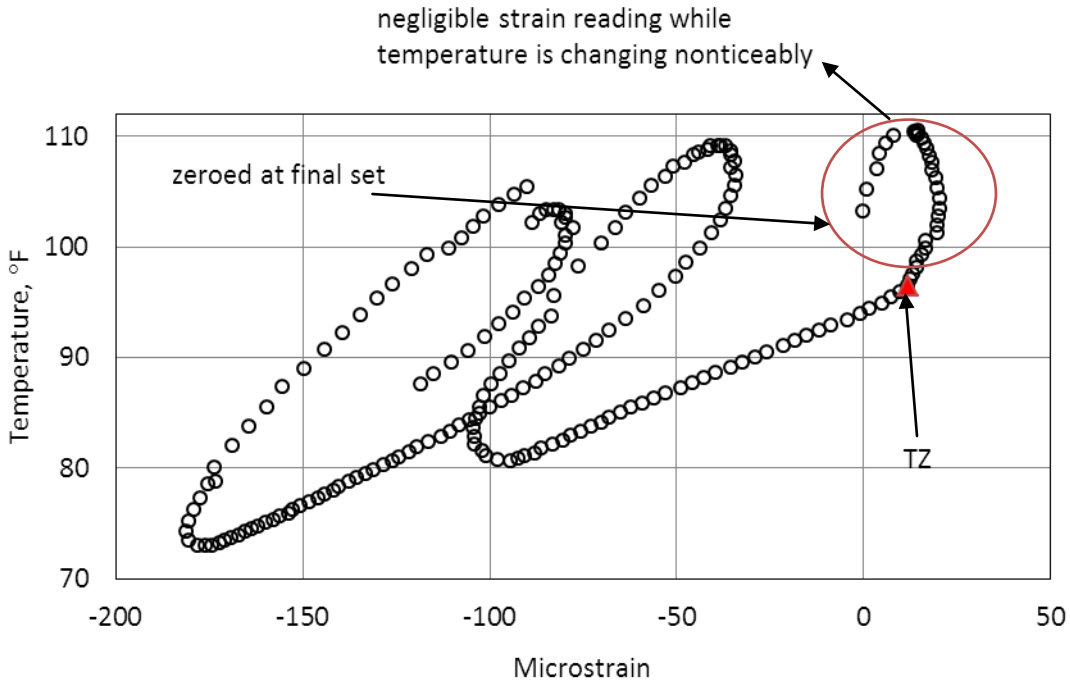

Figure 3-18. An example measured strain versus temperature for a concrete slab.

The same graphs were produced for all instrumented slabs in Project 1, using measurements from the VW gages installed at the top and bottom of the slabs. Three slabs were instrumented in each cell and there were three cells within each project. Therefore, a total number of 18 strain-temperature graphs were produced for each project. These graphs are provided in Figure 3-19 to Figure 3-36. TZ is identified in each figure by a red triangle. Furthermore, a summary of the time of placement, final set and TZ are provided in two tables, one for the top gages and one for the bottom gages, in each cell. This is provided in Table 3-15 to Table 3-19.

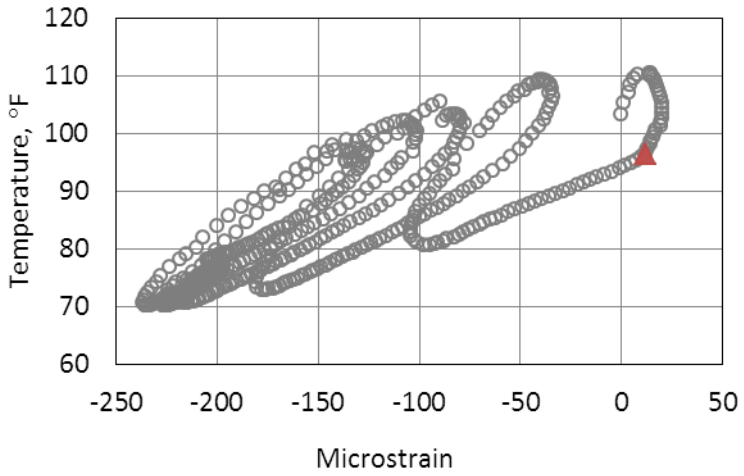

Figure 3-19. Strain/temperature changes measured by VW 1, at the top of Slab A, Cell 1, Project 1.

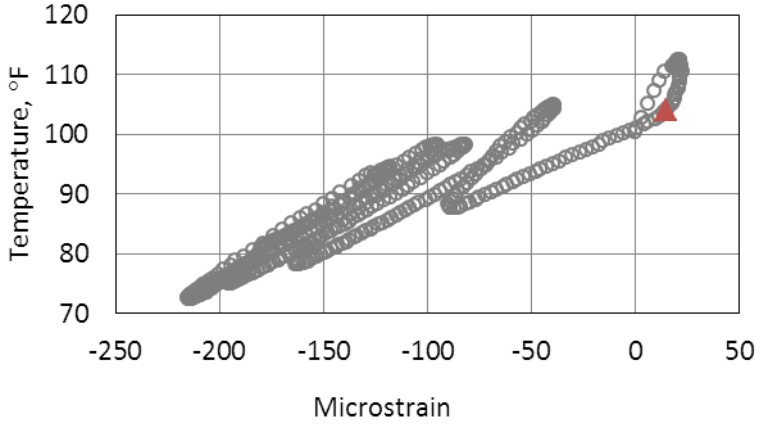

Figure 3-20. Strain/temperature changes measured by VW 3, at the top of Slab B, Cell 1, Project 1.

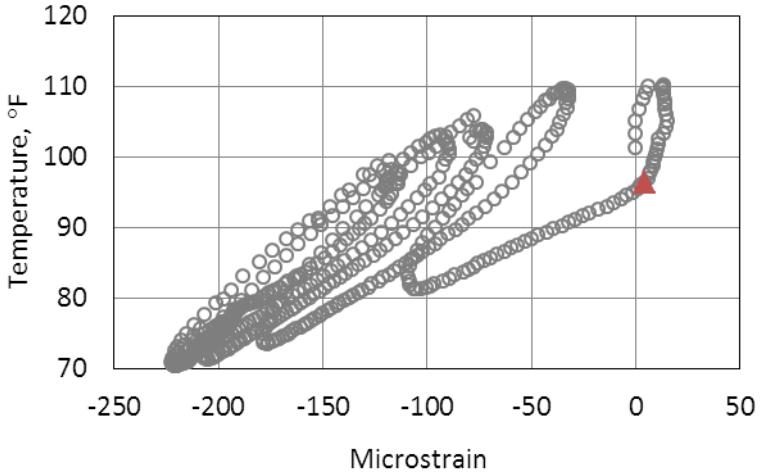

Figure 3-21. Strain/temperature changes measured by VW 5, installed at the top of Slab C, Cell 1, Project 1.

Table 3-14. Final set and TZ for top of slabs in Cell 1, Project 1[1].

Slab	Time of Placement	Time of Final Set	TZ
A	8:00 AM	2:45 PM	10:45 PM
B	8:00 AM	2:45 PM	10:45 PM
C	8:00 AM	2:45 PM	11:00 PM

[1] Time of final set was established based on the penetration test and TZ was established based on measurements by the VW static strain gages.

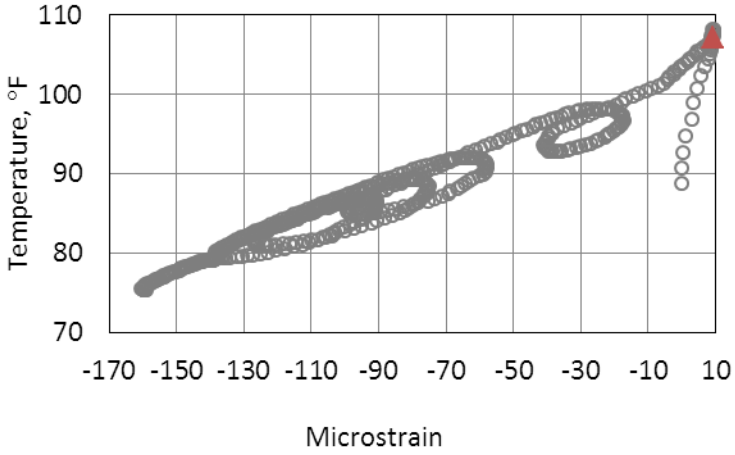

Figure 3-22. Strain/temperature changes measured by VW 2, at the bottom of Slab A, Cell 1, Project 1.

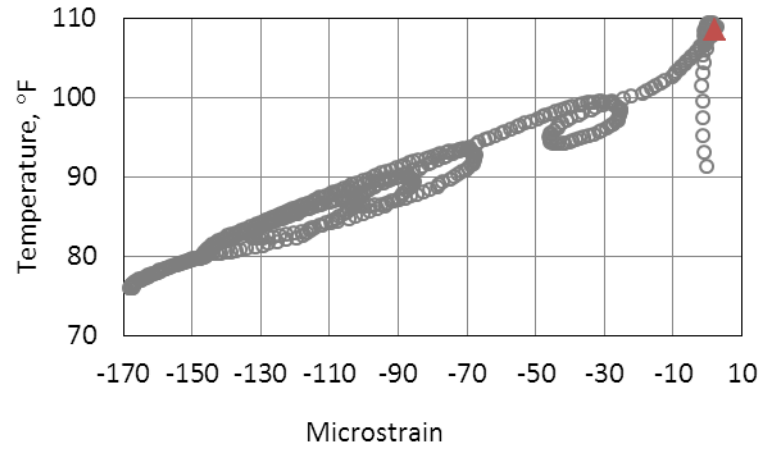

Figure 3-23. Strain/temperature changes measured by VW 4, at the bottom of Slab B, Cell 1, Project 1.

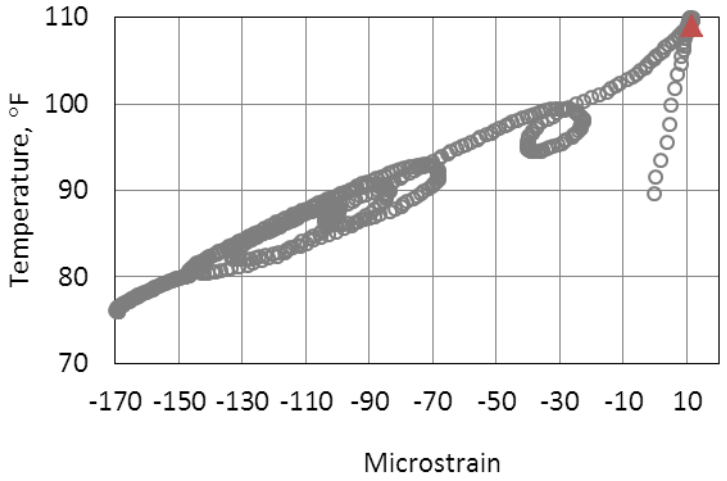

Figure 3-24. Strain/temperature changes measured by VW 6, at the bottom of Slab C, Cell 1, Project 1.

Table 3-15. Final set and TZ for bottom of slabs in Cell 1, Project 1.

Slab	Time of Placement	Time of Final Set	TZ
A	8:00 AM	3:30 PM	11:15 PM
B	8:00 AM	3:30 PM	11:15 PM
C	8:00 AM	3:30 PM	11:15 PM

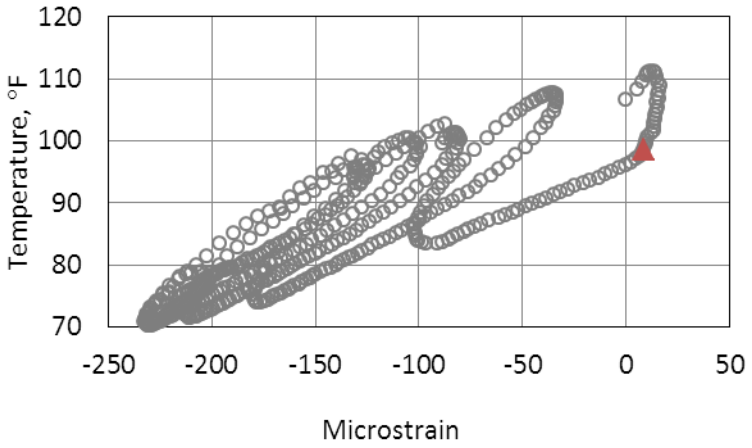

Figure 3-25. Strain/temperature changes measured by VW 1, at the top of Slab A, Cell 2, Project 1.

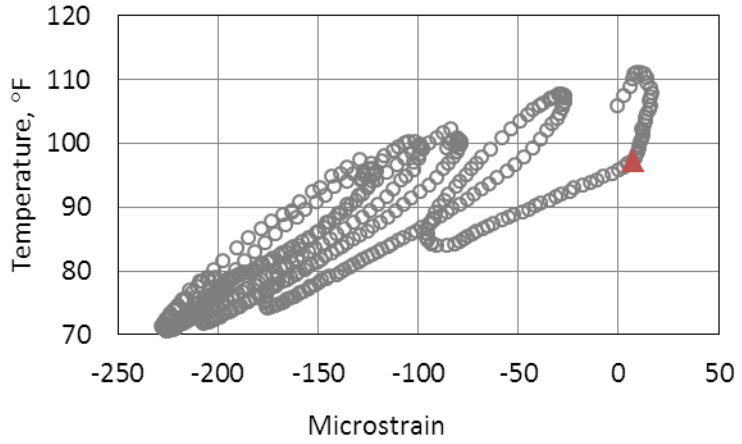

Figure 3-26. Strain/temperature changes measured by VW 3, at the top of Slab B, Cell 2, Project 1.

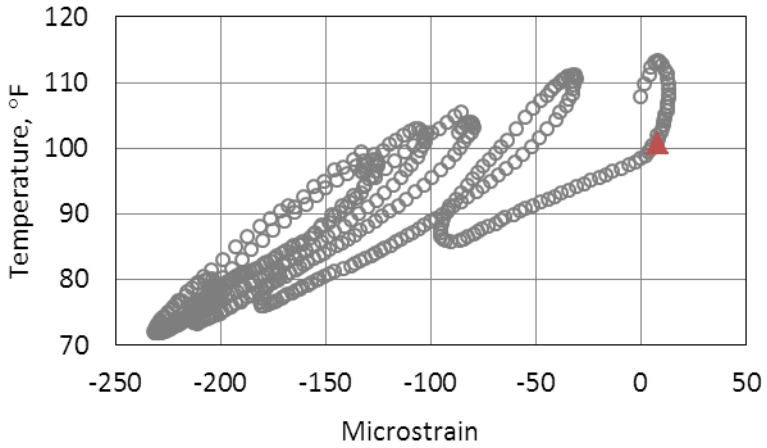

Figure 3-27. Strain/temperature changes measured by VW 5, at the top of Slab C, Cell 2, Project 1.

Table 3-16. Times of final set and zero stress for top of slabs in Cell 2, Project 1.

Slab	Time of Placement	Time of Final Set	TZ
A	10:15 AM	4:30 PM	11:15 PM
B	10:30 AM	4:30 PM	11:15 PM
C	10:30 AM	4:30 PM	11:15 PM

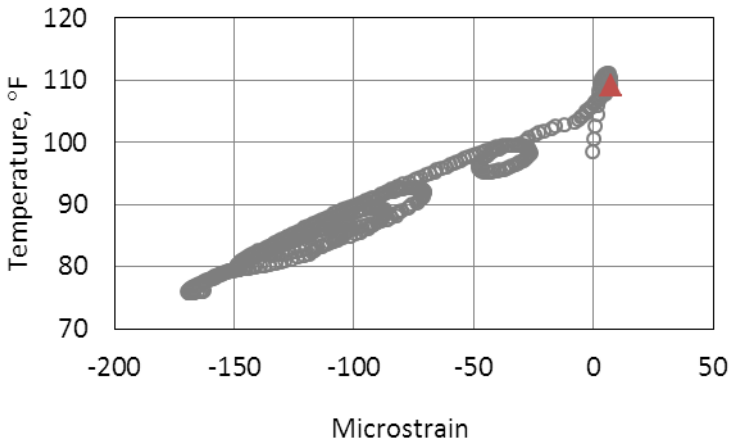

Figure 3-28. Strain/temperature changes measured by VW 2, at the bottom of Slab A, Cell 2, Project 1.

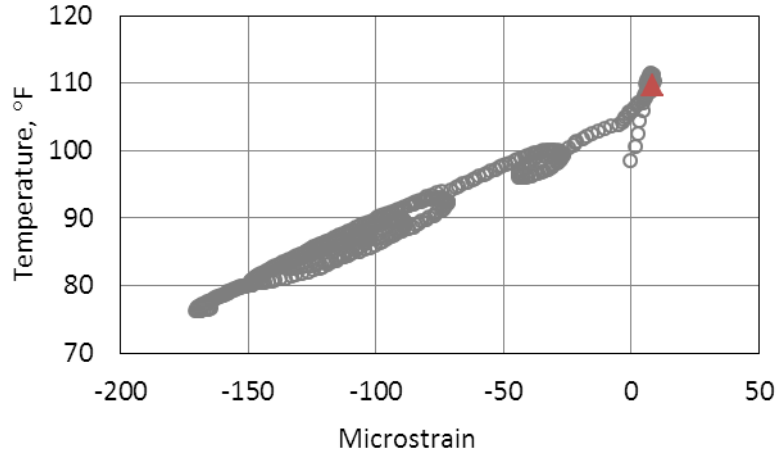

Figure 3-29. Strain/temperature changes measured by VW 4, at the bottom of Slab B, Cell 2, Project 1.

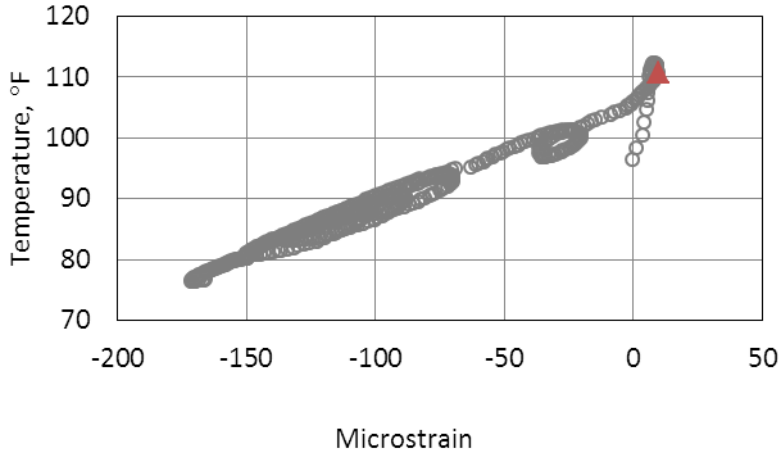

Figure 3-30. Strain/temperature changes measured by VW 6, at the bottom of Slab C, Cell 2, Project 1.

Table 3-17. Final set and TZ for bottom of slabs in Cell 2, Project 1.

Slab	Time of Placement	Time of Final Set	TZ
A	10:15 AM	5:00 PM	12:30 AM
B	10:30 AM	5:00 PM	12:30 AM
C	10:30 AM	5:00 PM	12:30 AM

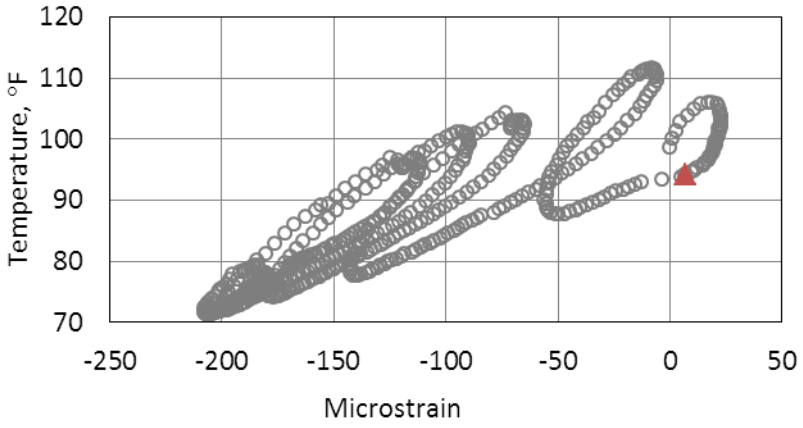

Figure 3-31. Strain/temperature changes measured by VW 1, at the top of Slab A, Cell 3, Project 1.

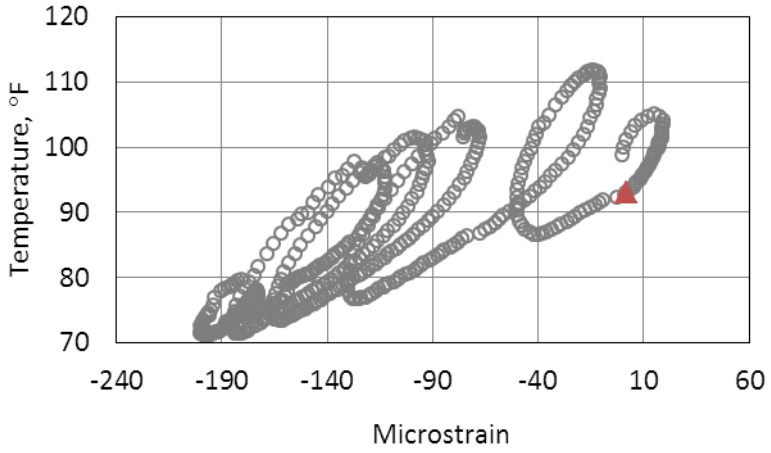

Figure 3-32. Strain/temperature changes measured by VW 3, at the top of Slab B, Cell 3, Project 1.

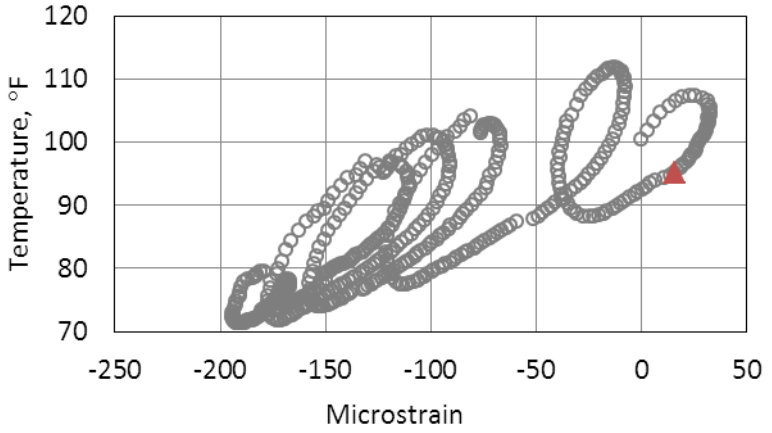

Figure 3-33. Strain/temperature changes measured by VW 5, at the top of Slab C, Cell 3, Project 1.

Table 3-18. Final set and TZ for top of slabs in Cell 3, Project 1.

Slab	Time of Placement	Time of Final Set	TZ
A	11:45 AM	6:00 PM	4:00 AM
B	11:45 AM	6:00 PM	4:00 AM
C	11:45 AM	6:00 PM	4:00 AM

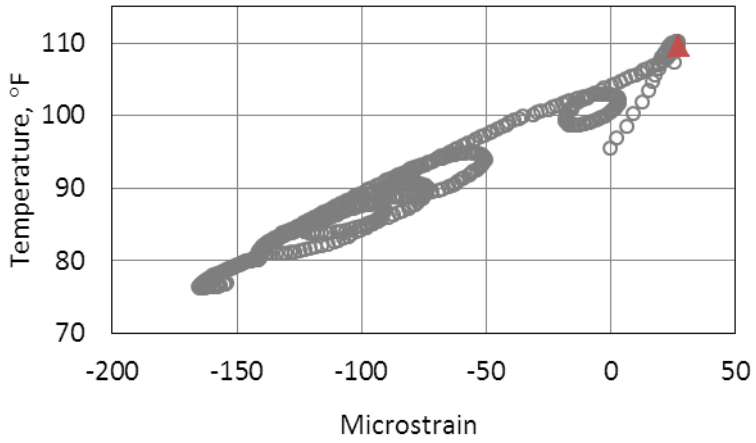

Figure 3-34. Strain/temperature changes measured by VW 2, at the bottom of Slab A, Cell 3, Project 1.

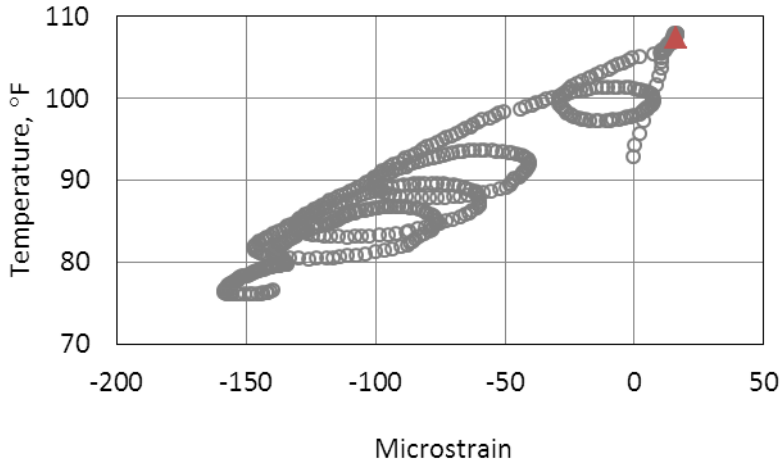

Figure 3-35. Strain/temperature changes measured by VW 4, at the bottom of Slab B, Cell 3, Project 1.

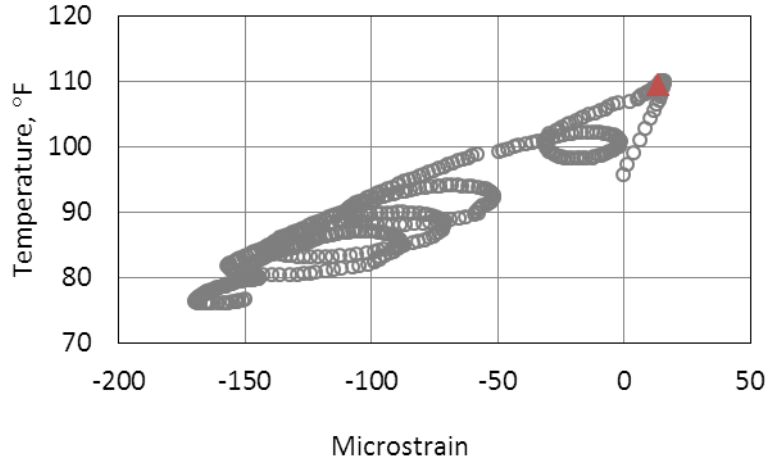

Figure 3-36. Strain/temperature changes measured by VW 6, at the bottom of Slab C, Cell 3, Project 1.

Table 3-19. Final set and TZ for bottom of slabs in Cell 3, Project 1.

Slab	Time of Placement	Time of Final Set	TZ
A	11:45 AM	6:00 PM	1:30 AM
B	11:45 AM	6:00 PM	1:30 AM
C	11:45 AM	6:00 PM	1:30 AM

Discussions Regarding the Strain-Temperature Behavior in the Slabs

When comparing the strain-temperature hysteresis at the top of the slabs, seen in Figure 3-19 to Figure 3-21 for Cell 1, and Figure 3-25 to Figure 3-27, for Cell 2 and Figure 3-31 to Figure 3-32 for Cell 3, to the strain-temperature hysteresis at the bottom of the same slabs, it is noticed that the strain changes with respect to temperature is in the clock-wise direction at the top of the slabs; while a counter clock-wise trend is seen in the strain changes for the bottom of the slabs. This behavior is consistent in all slabs in all three cells.

To investigate this issue further, the strain-temperature data from another test section instrumented and constructed in August of 2004 in Murrysville, Pennsylvania was used. This section includes an additional VW static strain gage installed at approximately mid-depth of the slabs. These gages are located at the corners of the slabs and are installed in three directions (longitudinal, transverse and diagonal). This test section included two cells, each consisting of three consecutive 12-inch thick slabs. The slabs for one cell feature 1.5-inch diameter dowel bars and No. 5 tie bars. The slabs in the other cell do not include dowel or tie bars.

The strain-temperature measurements at three different depths in the longitudinal direction and at the corner of Slab A at the shoulder side, in the undoweled slabs, are provided in Figure 3-37 to Figure 3-39. The strain-temperature measurements in the other two slabs in this cell exhibited the exact same behavior as the ones for Slab A. Furthermore, the strain-temperature measurements at the same location/direction in the slabs in the doweled cell showed the same behavior as the one provided in Figure 3-37 to Figure 3-39 and therefore are not provided here to avoid repetition.

First, as seen in Figure 3-37 to Figure 3-39, it is noticed that the strain-temperature changes at the top of the slab do not form complete and distinct hysteresis loops as the ones previously observed for Project 1. As seen Figure 3-38 and Figure 3-39, at mid-depth and the bottom of the slab, on the other hand, distinct hysteresis loops are generated. The strain-temperature hysteresis seen in Figure 3-37 to Figure 3-39, show different trends at the top in comparison to the mid-depth and the bottom of the slabs. The hysteresis is clock-wise for the top measurements and is counter clock-wise for the mid-depth and bottom measurements.

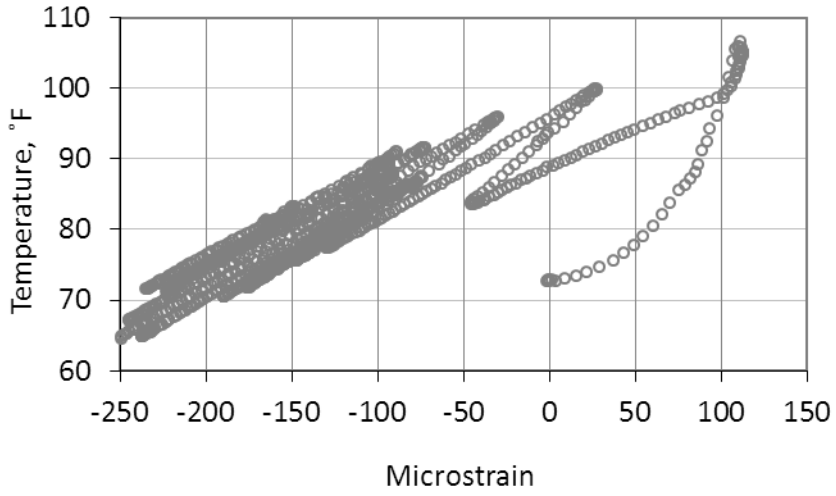

Figure 3-37. Strain/temperature changes measured by VW 16, installed at 2.3 inch of Slab A, undoweled slabs, SR 22 Project.

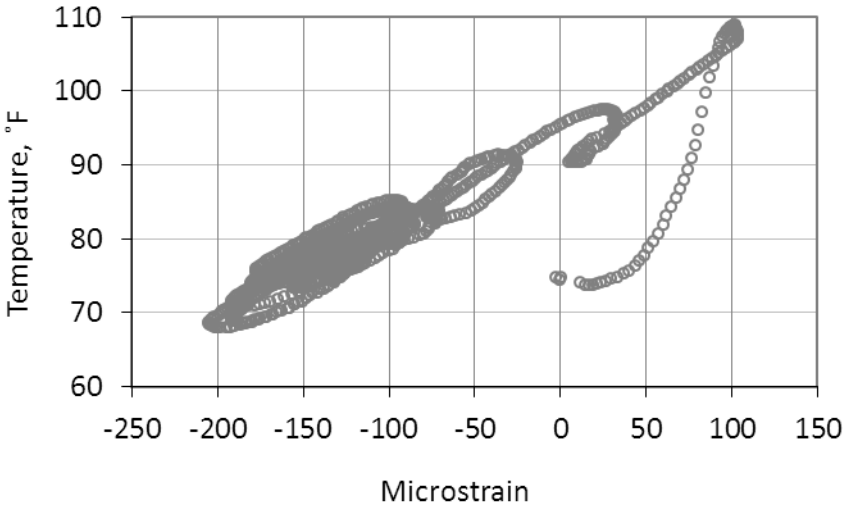

Figure 3-38. Strain/temperature changes measured by VW 19, installed at 6.2 inch of Slab A, undoweled slabs, SR 22 Project.

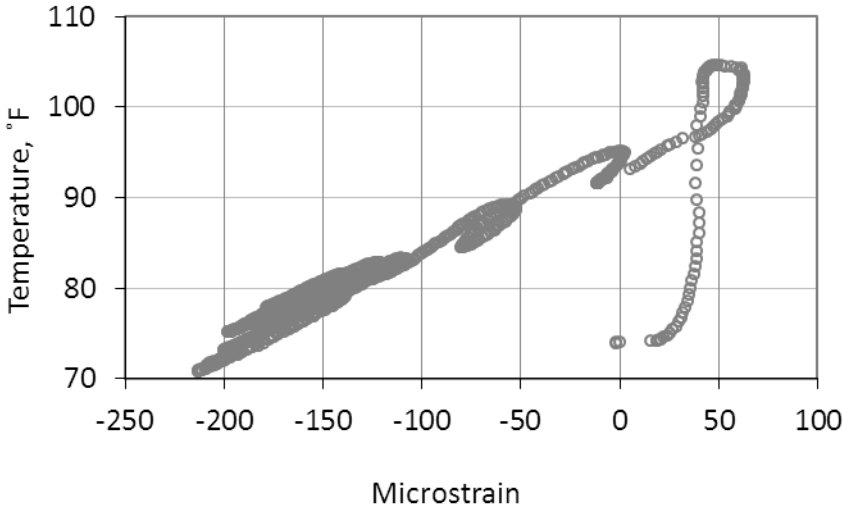

Figure 3-39. Strain/temperature changes measured by VW 22, installed at 11.7 inch of Slab A, undoweled slabs, SR 22 Project.

The same behavior was observed for the strain-temperature hysteresis in the diagonal direction; while, a different trend was observed for the strain measurements in the transverse direction. The changes in the measured strain with respect to temperature in this direction were

counter clock-wise at the top and at the mid-depth, while they were clockwise at the bottom in all the slabs. No certain judgment could be made regarding the cause of this behavior based on these observations.

Another interesting point about the strain-temperature graphs presented in Figure 3-19 to Figure 3-36 is the changes observed in the CTE of the slab over the first two days after construction. For instance, as seen in Figure 3-19, the slope of the strain-temperature line is noticeably lower prior to the first strain-temperature loop (the first night after construction) when compared to the line for the second strain-temperature loop (the second night after the construction of the slab.) The slope remains almost constant after the second loop over time. This simply implies that the CTE of the slab is the highest during the first 24 hours after the construction. The same behavior is observed for the strain-temperature measurements at the top of the slabs in Cells 2 and 3. Based on this observation, it appears that the CTE of fresh concrete decreases as the hydration progresses. This behavior is most likely demonstrating the gradual increase in stiffness of the concrete and not an actual change in the CTE of the mix.

The next discussion on the strain-temperature graphs provided in Figure 3-19 to Figure 3-36 is in regards to the effect of the base on the strain in the slab. Based on Figure 3-23, as the temperature decreases from the peak temperature, initially small and later rather large compressive strains are observed at the bottom of the slab. As the temperature continues to drop from about 95 °F to 93 °F, no change is seen in the measured strain. As the temperature starts to increase, a significant increase is noticed in the strain (up to temperature of about 96 ° F). After this point, surprisingly, a decrease is seen in the strain at the bottom as the temperature continues to increase from 96 °F to 98 °F. This pattern appears to continue for the remaining temperature cycles. To explain this unusual trend seen in the strain-temperature behavior at the bottom of the

slabs, the strain was plotted with respect to time. The measured strain at the top and the bottom of Slab A in Cell 1 is provided in Figure 3-48 together with the weighted average temperature of the slab.

It is very interesting to notice that the strain at the top of the slab responds almost immediately to the temperature changes in the slab (the high and low spikes in strain occur at the same time as the temperature spikes). At the bottom, on the other hand, a delay of approximately four hours is seen between the strain and temperature spikes. This behavior of the slab at the bottom is attributed to the restraints provided by the base layer against the expansion and contraction of the slab. It is also noticed that the delay decreases as hydration progresses and the slab ages. This could be due to the overall increase in the stiffness of the slab.

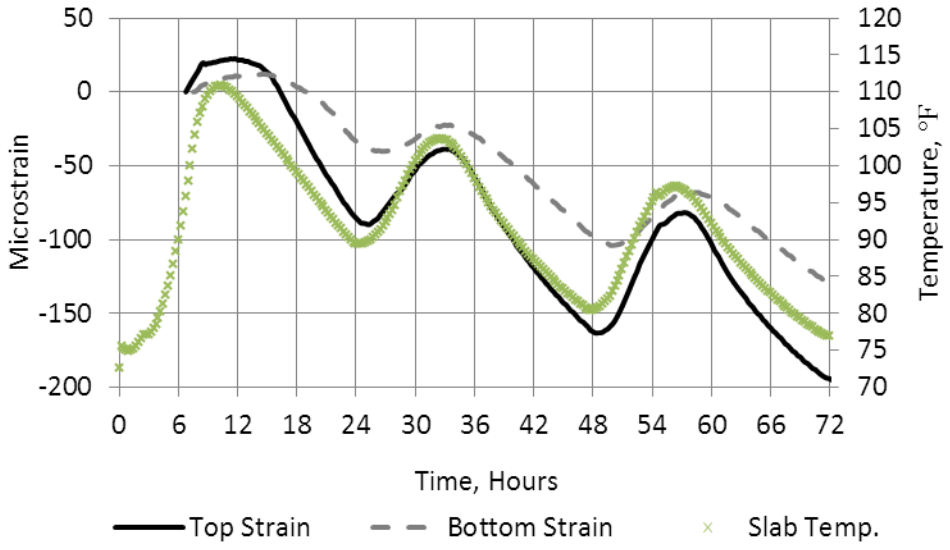

Figure 3-40. Strain measured over time in the slab at the top and bottom of Slab A, Cell 1, Project 1.

The effect of the stabilized base layer on the measured strain in the slab was investigated in the previous section. It is attempted in this section to establish the location of the neutral axis in the slab based on the strain-temperature behavior in the slabs.

As discussed previously, clock-wise hysteresis strain-temperature loops are prevalent at the top of the slabs and counter-clock-wise loops were observed in the strain-temperature behavior at the bottom of the slabs. The location of the neutral axis in the slab is established at the depth at which the strain-temperature behavior of the slab would show no hysteresis loops. The procedure is described graphically in Figure 3-41. As seen in the Figure 3-41 (a), for every strain-temperature loop, first, the length of the loop is established. Second, the width of the loop is established using the temperature corresponding to the top and bottom mid-loop points (ΔT in Figure 3-41). ΔT is established following the same procedure for the bottom of the slab, as depicted in Figure 3-41 (b).

The top ΔT together with the top gage location and the bottom ΔT along with the bottom gage location in the slab are used to produce the line shown in Figure 3-50. The location of the neural axis is defined as the depth that corresponds to zero-width loop. This is presented graphically in Figure 3-50.

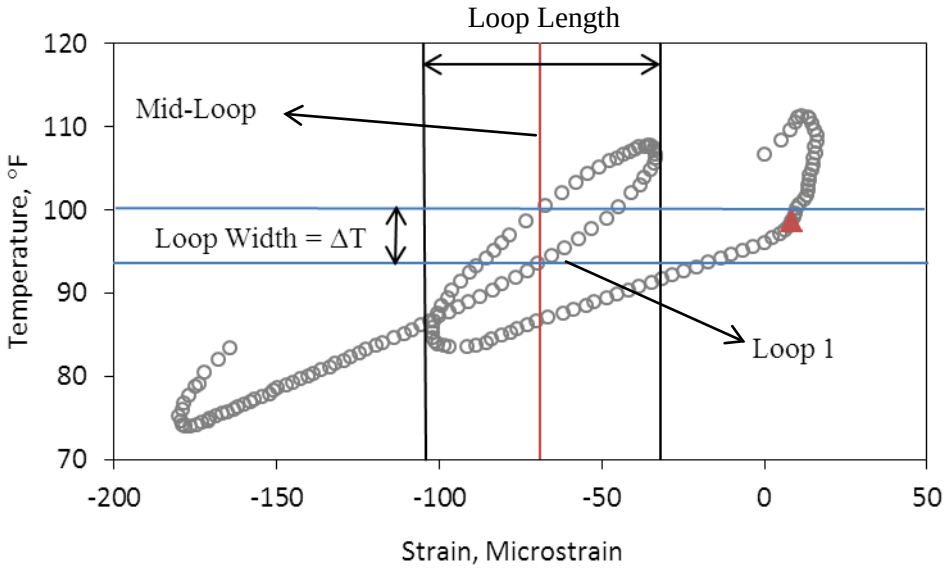

(a)

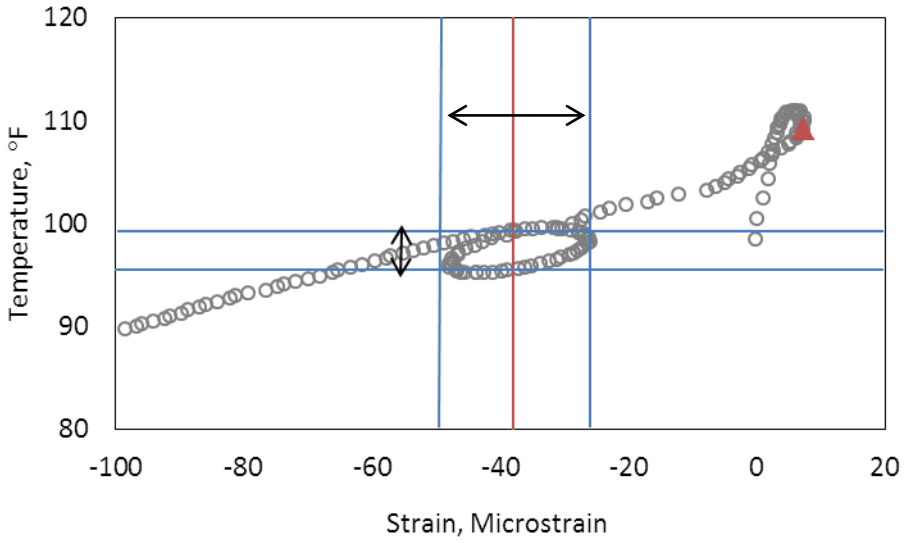

(b)

Figure 3-41. Establishing the neutral axis location for Slab A, Cell 1, Project 1, strain-temp. measured (a) at the top (b) at the bottom.

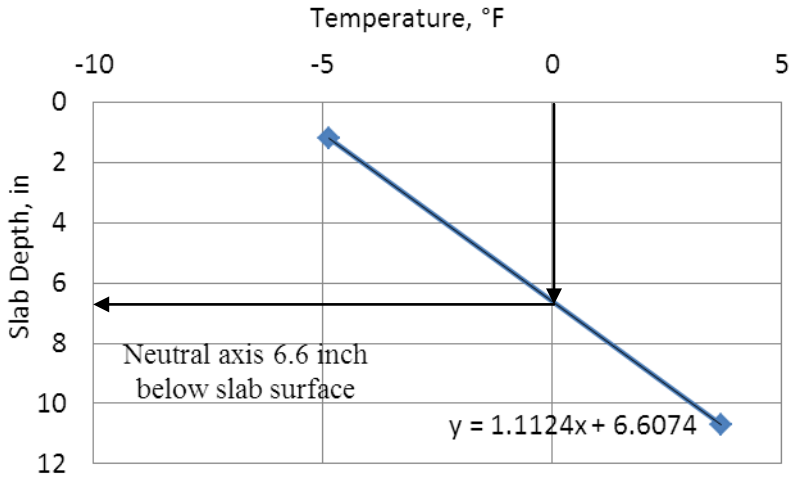

Figure 3-42. Establishing the location of the neutral axis in the slab depth.

The same procedure was followed for all four loops seen at the top and bottom of Slab A on each cell to establish the location of the neutral axis in the slab. The subsequent result is presented in Figure 3-46 in terms of percent of slab thickness. It is interesting to notice in Figure 3-46 that the location of the neural axis is between 60 and 65 percent of the slab thickness for Cells 1 and 3, while it is almost at mid-depth in Cell 2. As will be discussed more in detail in the future section of the dissertation, the temperature of the ATPB layer was generally higher at Cell 2 compared to the temperature of the base for Cells 1 and 3. This is because Cell 2 was constructed during the hot hours of the day. The higher temperature of the ATPB could result in fewer restraints against the deformations of the slab and thereby affecting the location of the neutral axis.

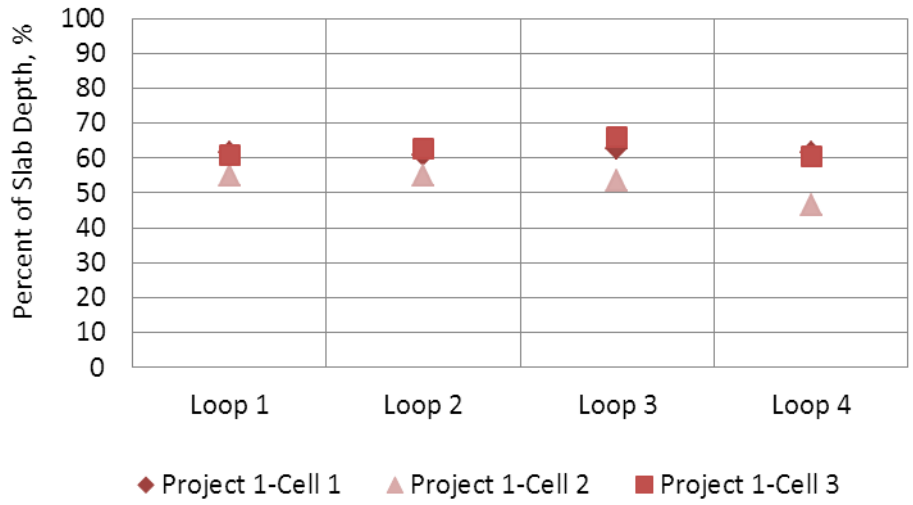

Figure 3-43. Location of the neutral axis in terms of percent slab thickness for three cells in Project 1.

Discussion of the TZ Established for Three Cells

Based on Table 3-15 to Table 3-19, the slabs in Cell 1 reached TZ within 13 to 14.75 hours while this time is between 12.75 and 14.25 hours for Cell 2 and 13.75 to 16.25 hours for Cell 3. The curing temperature of the concrete is a key variable having a significant effect on the rate of hydration (Schindler 2004). Therefore, the ambient conditions measured at the site for Project 1 can be used to explain the late TZ seen for Cell 3 in comparison to the other two cells. The ambient temperature and solar radiation measured over the first 24 hours after paving of Cell 1 are presented in Figure 3-44. As seen in Table 3-18 and Table 3-19, final set time in Cell 3 does not occur until 6:00 pm. This time corresponds to the time equal to 10 hours in Figure 3-44. At this point, both temperature and solar radiation are starting to drop. The late TZ observed in Cell 3 can be a result of the falling air temperature in the late afternoon.

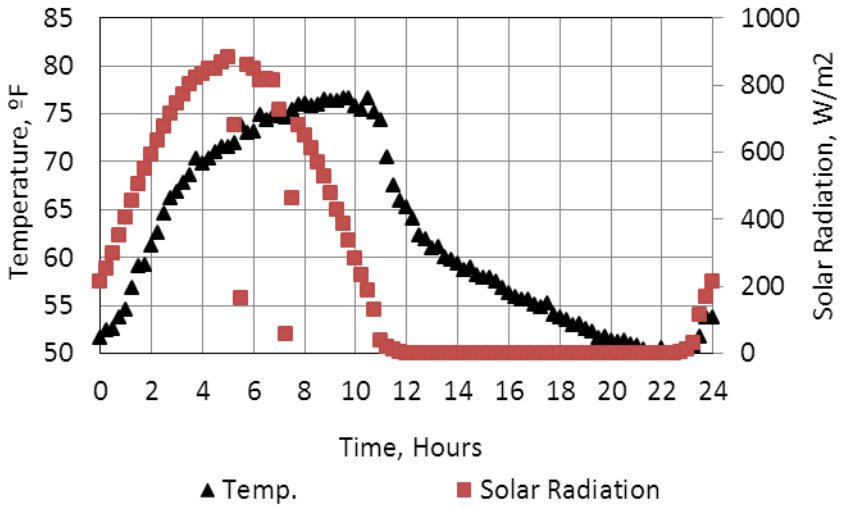

Figure 3-44. Ambient temperature and solar radiation measured at the site for Project 1.

TZ and final set time in each cell with respect to temperature changes at the top and bottom of the slabs are presented in Figure 3-45 for a duration of 24 hours after construction. Based on this figure, the final set time for all slabs occurred before the peak temperature and TZ took place after this point.

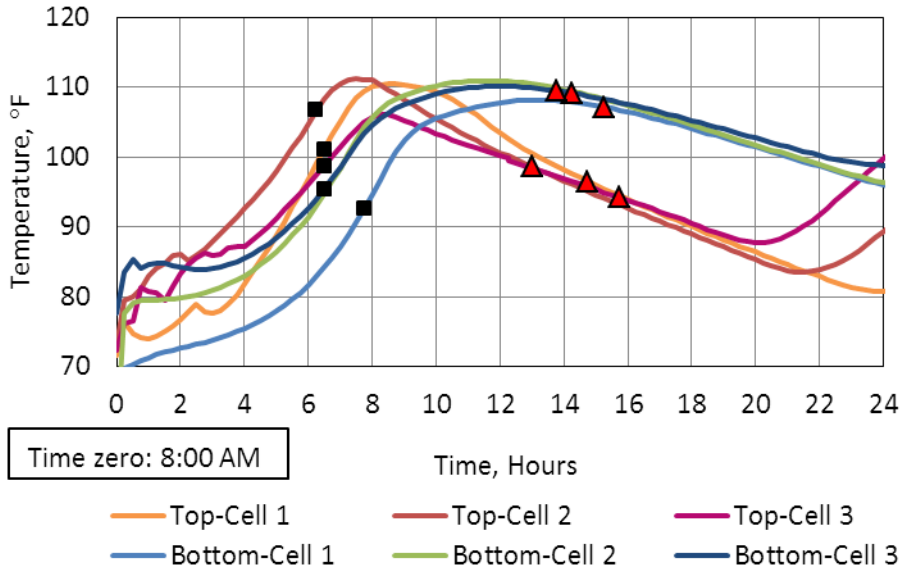

Figure 3-45. Final set and TZ presented on the temperature-time graphs for the 3 cells in Project 1.

To account for varying ambient and therefore curing condition for each cell resulting from paving at different times, the equivalent age concept was employed. This parameter was estimated over time by incorporating the temperature measurements in the slab obtained by the thermistor within the VW gages into Equation 2-2. The estimated equivalent age at TZ for the top and the bottom of each slab is provided in Table 3-20. The data in Table 3-20 shows that, as expected, the equivalent age at TZ in all slabs is very similar. Slight variations observed from cell to cell can be due to inconsistencies in the PCC mixture. This discussion will be expanded upon in the next section.

Table 3-20. Equivalent age at TZ for all slabs in Project 1.

	Equivalent Age at TZ (Hours)								
	Cell 1			Cell 2			Cell 3		
	Slab A	Slab B	Slab C	Slab A	Slab B	Slab C	Slab A	Slab B	Slab C
Top Gage	33.2	35.7	33.4	31.7	31.5	32.9	35.4	34.5	36.5
Bottom Gage	31.2	32.4	32.3	34.6	35.0	35.6	33.8	31.5	32.7

TZ is the time that the concrete has gained sufficient strength/stiffness to overcome the restraint preventing the slab from expanding/contracting with changes in temperature. The degree of restraint is a function of the design features of the pavement, such as restraint between the slab and the base, the presence of dowel and tie bars, etc. It is also a function of the construction sequencing. For example, if the lane to be paved is being tied into an existing adjacent lane previously constructed, additional restraint can be present. In an effort to predict the TZ for pavements beyond the four instrumented sections, the concrete stiffness at TZ must be defined for the range of design (restraint) features commonly encountered.

Since early age stiffness is difficult to measure but it equates well to degree of hydration, it is easier to establish TZ at a defined degree of hydration for each set of design features. The primary design feature to be evaluated is the effects of the restraint due to the base type (ATPB vs. CTPB). The degree of hydration concept was discussed in Section 2.3.2. Schindler's hydration models were used in this study to estimate the degree of hydration over time in each of the slabs. The inputs required by the hydration model and their corresponding values are summarized in Table 3-21. Again, the cement composition was obtained from the cement mill sheet, provided in Table 3-5, and the w/cm ratio of the PCC mixture was measured in the field by performing the microwave oven water content test. Using the input data from Table 3-21, the hydration shape and time parameters and the ultimate degree of hydration was obtained for the PCC mixture used for Project 1. The result is provided in Table 3-32. The corresponding relations for estimating each parameter was discussed earlier in Section 2.2.2.

Table 3-21. Inputs used to estimate the degree of hydration, Project 1.

Parameter	Value
P_{C3S} (%)	59
P_{C3A} (%)	6.7
P_{SO3} (%)	2.95
w/cm Ratio for Cell 1	0.41
w/cm Ratio for Cell 2 and 3	0.47

Table 3-22. Hydration parameters and the ultimate degree of hydration, Project 1.

Parameter	Value
T	22.26
B	0.63
Ultimate Degree of Hydration- Cell 1	0.70
Ultimate Degree of Hydration- Cell 2 and 3	0.73

The input data from Table 3-32 and also the equivalent age values estimated for each slab over time were used to establish the degree of hydration over time in each slab. The hydration over time at the top of the slab for Cell 1 is presented in Figure 3-46. The estimated degree of hydration at TZ, known as the critical degree of hydration, in each slab is summarized in Table 3-23. This information is also presented in the form of a bar graph in Figure 3-47.

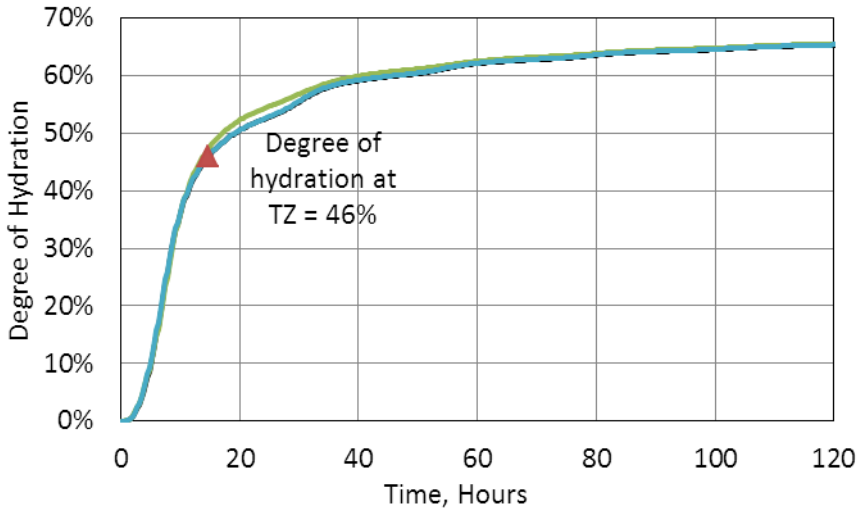

Figure 3-46. Degree of hydration based on top gages for slabs in Cell 1, Project 1**.**

Table 3-23. Critical degree of hydration for all the slabs in Project 1.

	Critical Degree of Hydration								
	Cell 1			Cell 2			Cell 3		
	Slab A	Slab B	Slab C	Slab A	Slab B	Slab C	Slab A	Slab B	Slab C
Top Gage	0.46	0.47	0.46	0.47	0.47	0.48	0.49	0.49	0.49
Bottom Gage	0.45	0.46	0.45	0.49	0.49	0.49	0.48	0.47	0.48

According to Table 3-23, slight variation of approximately 1 percent is seen in the critical degree of hydration established for the top of the slab in comparison to the bottom of each slab.

This variation can be explained by considering the precision of the methodology that was used to establish TZ. When using strain-temperature graphs to establish TZ (the method used in this study), the period of plus/minus one half hour appears to be the possible source of the error in establishing TZ. This period of time was established based on the evaluation of TZ established in every graph for each gage in all four projects. The strain and the temperature data used to produce the strain-temperature graphs were automatically collected at 15-minute intervals. As a result of this collection interval, the data points used to generate the strain-temperature graphs are very close together, as seen in Figure 3-19 to Figure 3-36. When establishing TZ visually on a figure similar to the ones presented in Figure 3-19, this point can be determined only approximately since any neighboring point with the same trend in behavior can also be recognized as TZ. This variation of plus/minus one half hour in TZ will subsequently result in some variation in the equivalent age and the degree of hydration at TZ. This possible variation in the degree of hydration at TZ can sometimes be as high as 2 percent.

The results presented in Figure 3-47 clearly reflect the effects of the varying water content in the PCC mixture used in the 3 different cells. According to Table 3-2, the water content for the PCC mixture used in Cell 1 based on the "Concrete Design Sheet" was 160 lb/yd^3 while this value was as high as 175 lb/yd^3 and 172 lb/yd^3 in Cell 2 and Cell 3, respectively. It is noteworthy that the cement content was the same for all of the cells. The microwave oven test showed the same trend in the w/cm ratio for the three cells. Based on these results, the w/cm ratio in Cell 1 was equal to 0.41 while it was estimated as 0.47 in Cells 2 and 3. The higher amount of water in Cell 2 and 3 in comparison to Cell 1 can explain the higher degree of hydration reached at TZ in these two cells. Additionally, a slightly higher degree of hydration in Cell 3 with respect to Cell 2 could again be due to a slightly higher water content in Cell 3. This

agrees with findings in past literature that for setting to occur, more hydration products must develop at higher w/cm ratios (Schindler 2004).

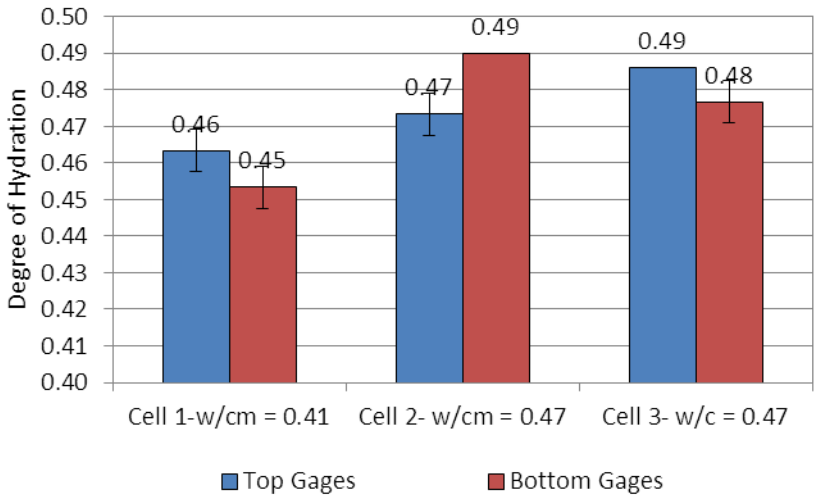

Figure 3-47. Average degree of hydration at TZ for three cells in Project 1.

It is interesting to note that although the same amount of water was used in the PCC mixture for both Cells 2 and Cell 3, a lower critical degree of hydration is seen at the bottom of Cell 3. To explain this behavior the temperature of the base at TZ was investigated.

It is known that one of the restraints against the slab expansion/contractions during hydration is the restraint provided by the base layer through friction. The base for Project 1 was an ATPB. The material properties for hot mix asphalt, particularly stiffness, can be affected by its temperature. This layer, when colder and therefore stiffer, can provide more restraint against the movements of the freshly-placed PCC slab. Temperature variation in the ATPB layer with respect to the weighted average temperature across the slab was investigated for each cell during TZ. This is presented in Figure 3-48. From this figure, the base temperature can be considered the same in all of the cells. This temperature is almost the same in Cells 2 and 3 while it is 2

degrees warmer in Cell 1. Another source of restraint could be the opposite trends (expansion vs. contraction) in the temperature variation for the slab in comparison to that of the base.

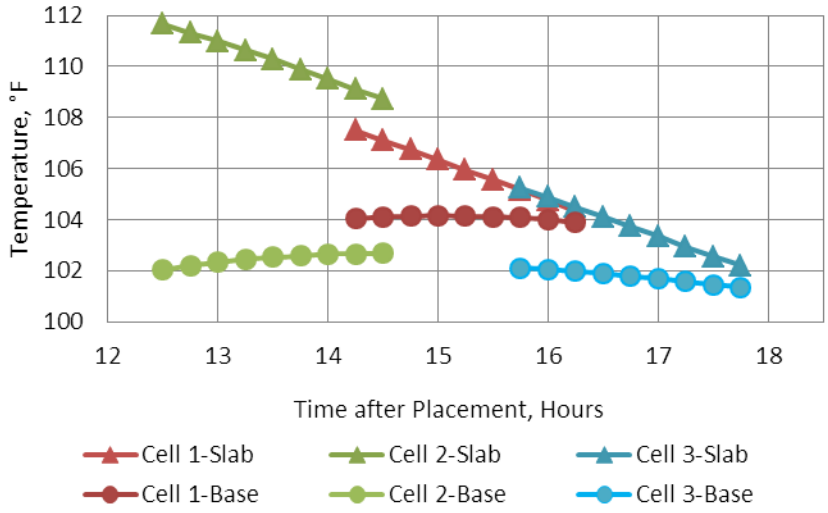

Figure 3-48. Base and slab temperature variation at TZ for each cell, Project 1.

When considering the trend of temperature change in Figure 3-48 for the base layer in each cell, it can be concluded that the temperature of the base is almost constant at TZ in all the cells. Therefore, the base temperature does not appear to be influencing TZ reached in the slabs and does not need to be considered.

Overall, it can be concluded that the critical degree of hydration varied between 0.46 and 0.49 at the top and from 0.45 to 0.48 at the bottom of the slabs for Project 1.

3.4 PROJECT 2-EASTBOUND OF SECTION B09 ON SR 22,

3.4.1 Project 2-Location and Characteristics

The next project instrumented was the eastbound lanes for the section referred to above as Project 1. The eastbound lanes included a pavement structure with the same design as the westbound lanes (Project 1.) As discussed previously, this design included a 12-inch PCC slab with a 4-inch ATPB layer over a 6-in 2A subbase layer.

Construction of the eastbound lanes, started approximately one year after the westbound lanes were constructed. Instrumentation of Project 2 was performed on May 7, 2010. The paving of the section started at 6:00 AM, Monday May 10, 2010 at stationing 1118+00. Paving ended at about 6:00 PM around stationing 1102+00. Cell 1 was located at stationing 1115+45 to 1115+00 and was paved at about 7:30 AM, Cell 2 was located at stationing 1106+2.5 to 1105+57.5 and was paved at about 2:30 PM and Cell 3 was located at stationing 1102+00 to 1101+65 and was paved at 4:45 PM.

The new pavement structure is a JPCP with a transverse joint spacing of approximately 15 ft. Some slabs at the location of Cell 2 had a shorter joint spacing ranging between 11 and 12 ft. The joint spacing was constructed to match with the joint spacing of the existing lane.

The design thickness for the PCC layer was 12 inch. Pre- and post-construction surveying at each cell revealed the as-built thickness of the PCC layer as provided in Figure 3-49. In this figure, each bar represents the mean thickness for the 3 slabs in each cell. The error bars indicate one standard deviation above and below the mean.

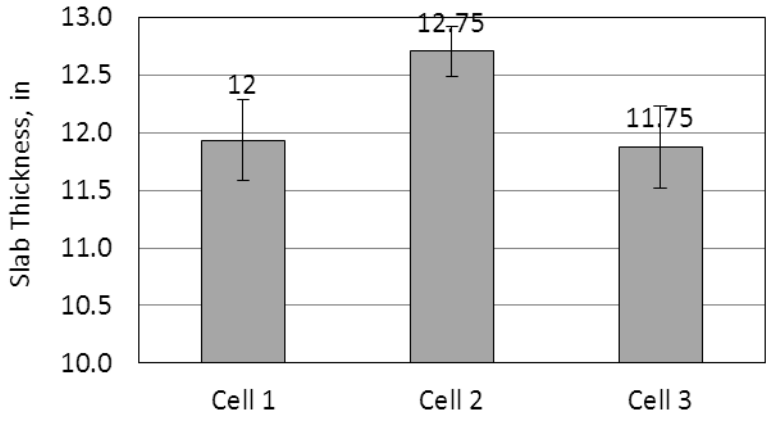

Figure 3-49. Average slab thickness for each cell instrumented in Project 2.

PennDOT Class AA-500 concrete was used for this project. This means the concrete mixture included 500 lb/yd^3 cementitious material. Similar to Project 1, the concrete for this project was produced by Golden Triangle Construction Co. Inc. at a batch plant located in New Alexandria, Pennsylvania. A summary of the mixture design can be found in Table 3-24 for each cell. The cementitious material included Type I cement manufactured by Armstrong Cement & Supply in Cabot, Pennsylvania, and 15 percent Class C fly ash, from Mineral Resources, Rush Island, Leetsdale, Pennsylvania.

The mix water was from an on-site well. Air entrainment and water reducing admixtures supplied by Euclid Chemical Co. located in Cleveland, Ohio were also used. AEA-92 was used as the air entraining admixture and Eucon WR was used as the water reducing agent.

Table 3-24. Mixture design for the PCC used for each cell in Project 2.

Material	Specific Gravity	Absorption (%)	Batch Weight (lb/yd^3)		
			Cell 1	**Cell 2**	**Cell 3**
Type I-Cement	3.15	n/a	500	500	500
Fly Ash-Class C	2.65	n/a	88	88	88
Fine Aggregate	2.62	1.24	1316	1285	1302
Coarse Aggregate	2.68	0.52	1860	1860	1853
Water Content	1	n/a	150	163	172

The coarse aggregate met the AASHTO No. 57 gradation specification and consisted primarily of limestone and the fine aggregate meeting PennDOT Specification Type A sand. The gradations for the fine and the coarse aggregate can be found in Table 3-25 and Table 3-28, respectively. The cement type and composition are significant factors that affect the time of set of the concrete. The composition of the cement based on the manufacturer's mill sheet is summarized in Table 3-27. The composition for the fly ash is also provided in Table 3-28.

The mixture design for the ATPB layer and the gradation for the subbase were the same as that used in Project 1. This information was provided in Section 3.3.1 and is not presented here to avoid repetition.

Table 3-25. Gradation of fine aggregate used in the PCC, Project 2.

Fine Aggregate	
Sieve Size	Percent Finer
3/8"	100
#4	99
#8	77
#16	59
#30	48
#50	25
#100	6

Table 3-26. Gradation of coarse aggregate used in the PCC, Project 2.

Coarse Aggregate - Limestone	
Sieve Size	Percent Finer
1 ½"	100
1"	97
½"	42
#4	4
#8	2

Table 3-27. Composition of the cement used in the PCC mixture for Project 2.

Chemical Data		
Component	Value (%)	Specification
SiO_2	20.1	-
Al_2O_3	5.35	-
Fe_2O_3	4.4	-
CaO	63.4	-
MgO	1.0	6.0-Max
SO_3	2.85	C-1038-Max
C_3S	54.9	3.0-Max
Alkalis	0.53	-
Loss of Ignition	1.20	-
Insoluble Res.	0.30	-
Physical Data		
Blaine (cm^2/g)	3580	2800-Min 4000-Max

Table 3-28. Composition of the fly ash used for Project 2.

Component	Value (%)
Silica, SiO_2	37.58
Aluminum Oxide, Al_2O_3	20.82
Ferric Oxide, Fe_2O_3	5.58
Sulfur Tri Oxide, SO_3	0.99
Calcium Oxide, Cao	25.74
Magnesium oxide, MgO	4.89
Available Alkalis	1.13

3.4.2 Fresh and Hardened Concrete Properties-Project 2

During paving, fresh concrete properties such as slump, w/cm ratio, entrained air, and time of set were measured by the research team at each cell. Table 3-29 provides the tests results for the fresh PCC. It should be noted that due to several mechanical issues with the paver, the rate of paving was significantly slower than originally planned. Due to delays in paving, the sensors installation for Cell 3 had to be moved from the original location to a location closer to the paver within one hour prior to paving of the cell, so that the section could be paved on the same day as Cells 1 and 2. Because of this last minute change, sufficient time was not available to perform the w/cm ratio testing for Cell 2.

Table 3-29. Fresh concrete properties measured at the site for Project 2.

Property	Measured								
	Cell 1			Cell 2			Cell 3		
	High	Low	Ave.	High	Low	Ave.	High	Low	Ave.
Slump (in)	1.75			1.25			1.25		
Air (%)	6.0			5.75			6.0		
w/cm Ratio	0.49	0.42	0.455	-	-	-	0.49	0.46	0.475
Unit Weight (lb/ft^3)	148	145	146.5	151	149	150	149	147	148

The time of initial and final set was established according to ASTM C403. In order to do so, three mortar samples were prepared from one batch of concrete from Cell 1. Similar to the previous project, to establish the maturity at the set time, the temperature variation in each concrete sample was measured throughout the test using thermocouples. The results from the test are summarized in Table 3-30. Figure 3-50 shows the penetration resistance pressure

readings over time for the three samples. The average final set time for the three samples was estimated at 7 hours and 20 minutes.

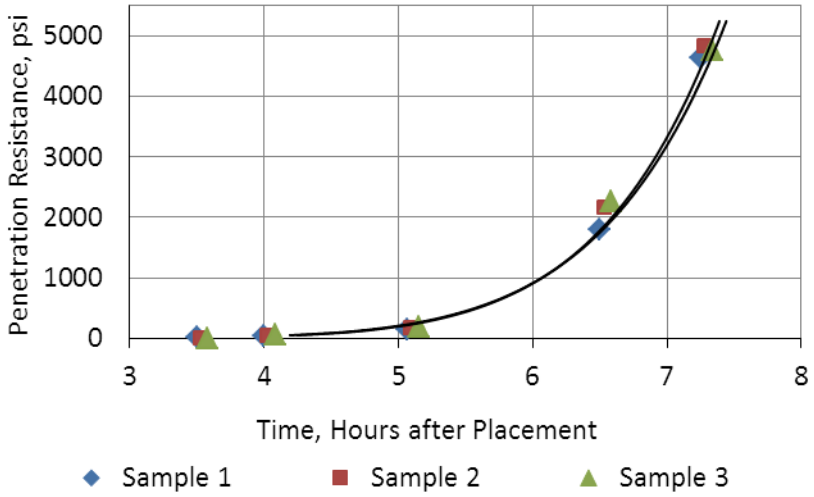

Figure 3-50. Penetration resistance over time for the three mortar samples, Project 2.

Table 3-30. Initial and final set times based on the penetration test, Project 2.

Sample Number	Time of Initial Set (Hours)	Time of Final Set (Hours)	Maturity (°F-Hours)
1	5.7	7.6	428
2	5.6	7.2	378
3	5.6	7.2	373
Average	5.6	7.3	393

Mechanical and thermal properties of the PCC were established by casting PCC specimens in the field for this project. The specimens were then transported to the PMML at the University of Pittsburgh, cured and tested in accordance with the ASTM standards. The result for each test at 28-days is presented in Table 3-31.

Table 3-31. 28-day elastic modulus, compressive strength and Poisson's ratio established in the laboratory for Project 2.

Property	Cell 1	Cell 2	Cell 3	Mean	Standard Deviation
E_c (psi)	5.2 E+06	4.9 E+06	4.95 E+06	5.0 E+06	100,000
υ	0.23	0.21	0.21	0.22	0.01
f_c (psi)	5890	5730	6440	6020	370
MR (psi)	860	725	840	810	75

The CTE of the PCC mixture used for Project 2 was measured following the same procedure described in Section 3.3.2. One sample was cast from the PCC used to pave each cell. The results of the subsequent tests are summarized in Table 3-32.

Table 3-32. Measured CTE for the PCC used for Project 2.

Cell Number	CTE (με/ºF)	Mean (με/ºF)	Standard Deviation (με/ºF)
1	5.2	5.2	0.09
2	5.1		
3	5.3		

The drying shrinkage for the PCC mixture used for Project 2 was established, in accordance with AASHTO T 160/ASTM C 157. A total of three beams were cast, one representing the PCC used in each cell. The embedded studs in the sample from Cell 2 were unfortunately damaged during demolding. The drying shrinkage test results obtained over time and up to 320 days are presented in Figure 3-51. Unfortunately, the sample from Cell 3 was moist cured for a longer period than the duration of 28 days recommended by the standard. A value of 715 με is established as the 320-day drying shrinkage for the sample from Cell 1 and 520 με for the sample cast from PCC in Cell 3, which was not moist cured in accordance with the ASTM standard. No judgments can be made on the PCC mixture design based on the

established drying shrinkage for the two cells due to different curing conditions applied to each sample.

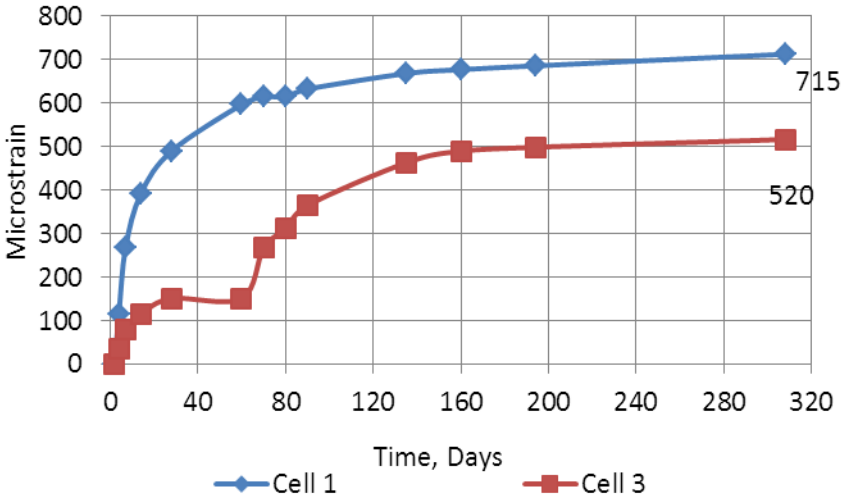

Figure 3-51. Drying shrinkage lab test results for PCC from Cells 1 and 3, Project 2.

3.4.3 Establishing TZ-Project 2

Similar to Project 1, strain and temperature measurements from the VW strain gages in the slabs were used to establish TZ at the top and at the bottom of each slab. These graphs can be found in Figure 3-52 to Figure 3-69. The final set time required for establishing the strain changes in the slabs was established as the time the slabs reached the maturity of about 400 °F-Hours according to the penetration test results. A summary of the time of final set, TZ and placement is also provided for each set of gages at the top and bottom of the slabs in Table 3-33 to Table 3-38.

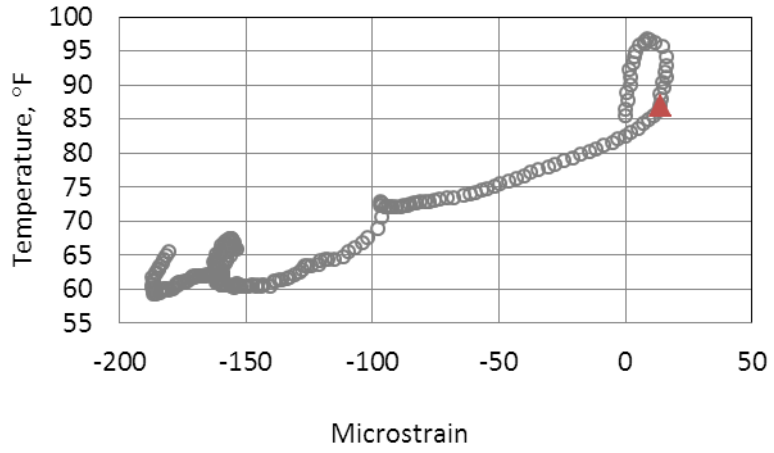

Figure 3-52. Measured strain-temperature at the top of Slab A, Cell 1, Project 2.

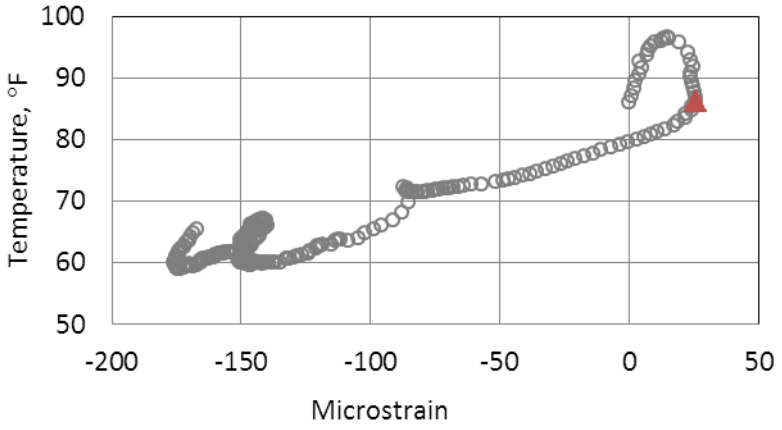

Figure 3-53. Measurements strain-temperature at the top of Slab B, Cell 1, Project 2.

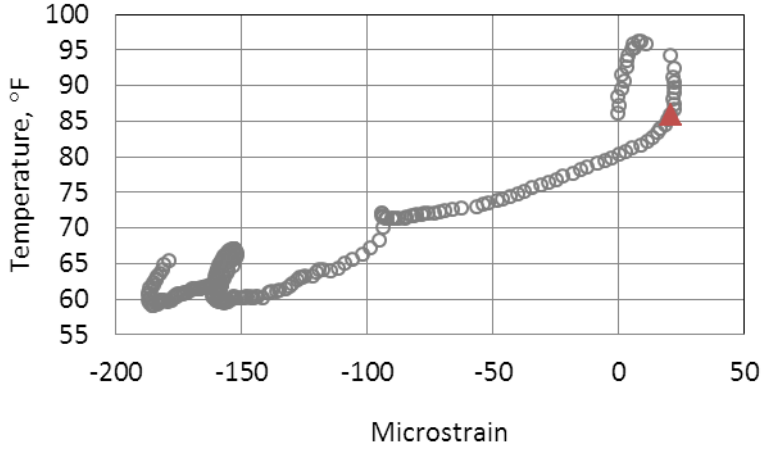

Figure 3-54. Measured strain-temperature at the top of Slab C, Cell 1, Project 2.

Table 3-33. Final set and TZ at the top of Slabs A, B and C Cell 1, Project 2.

Slab	Time of Placement	Time of Final Set	TZ
A	8:15 AM	2:30 PM	8:45 PM
B	8:15 AM	2:30 PM	8:45 PM
C	8:30 AM	2:45 PM	8:45 PM

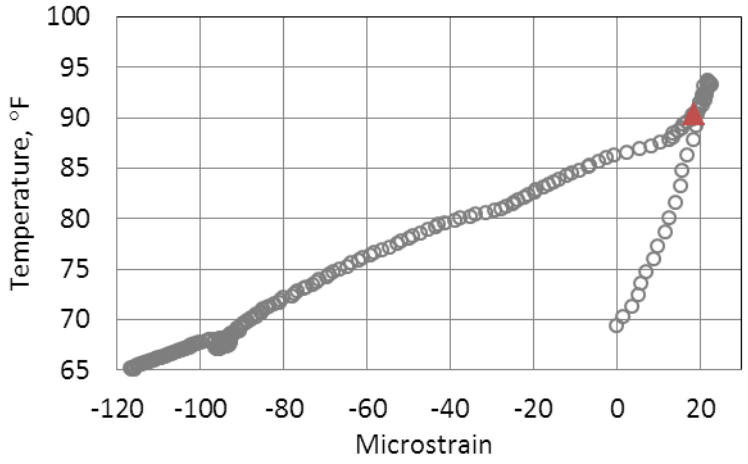

Figure 3-55. Measured strain-temperature at the bottom os Slab A, Cell 1, Project 2.

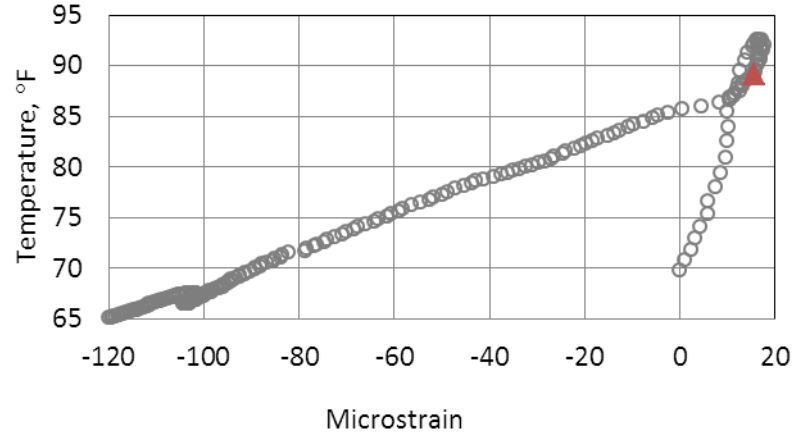

Figure 3-56. Measured strain-temperature at the bottom of Slab B, Cell 1, Project 2.

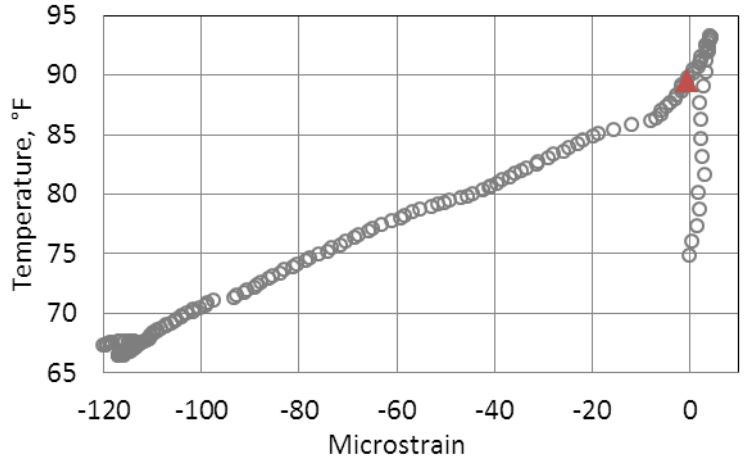

Figure 3-57. Strain-temperature measurements at the bottom of Slab C, Cell 1, Project 2.

Table 3-34. Final set and TZ at the bottom of Slabs A, B and C, Cell 1, Project 2.

Slab	Time of Placement	Time of Final Set	TZ
A	8:15 AM	3:45 PM	1:15 AM
B	8:15 AM	4:00 PM	1:00 AM
C	8:30 AM	4:00 PM	1:15 AM

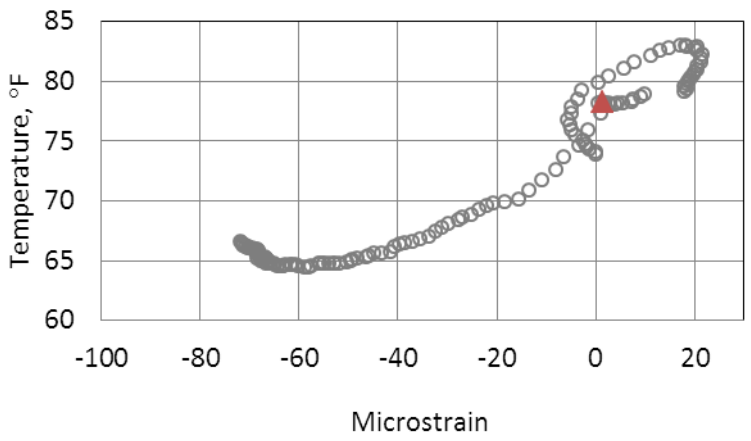

Figure 3-58. Measured strain-temperature at the top of Slab A, Cell 2, Project 2.

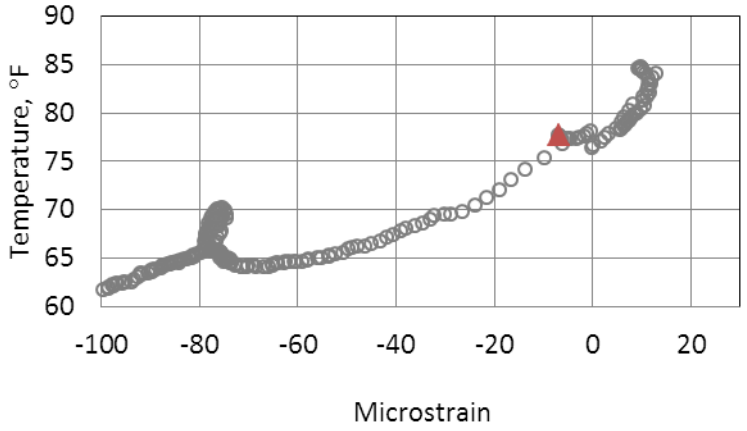

Figure 3-59. Measured strain-temperature at the top of Slab B, Cell 2, Project 2.

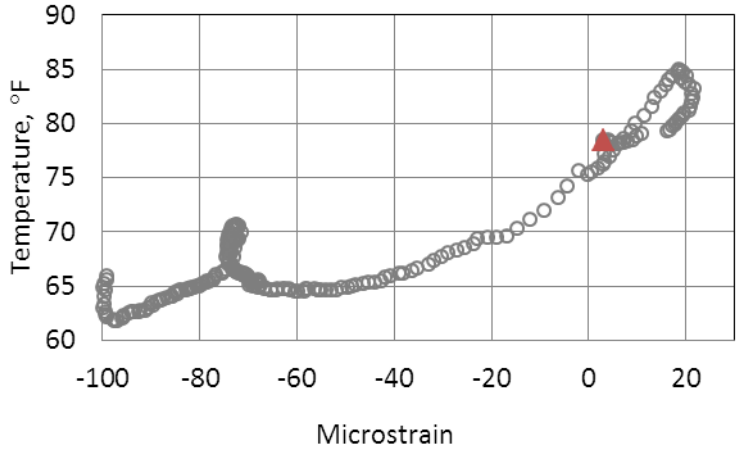

Figure 3-60. Measured strain-temperature at the top of Slab C, Cell 2, Project 2.

Table 3-35. Final set and TZ at the top of Slabs A, B and C, Cell 2, Project 2.

Slab	Time of Placement	Time of Final Set	TZ
A	3:00 PM	8:45 PM	9:30 AM
B	3:00 PM	8:45 PM	9:30 AM
C	3:15 PM	8:15 PM	9:30 AM

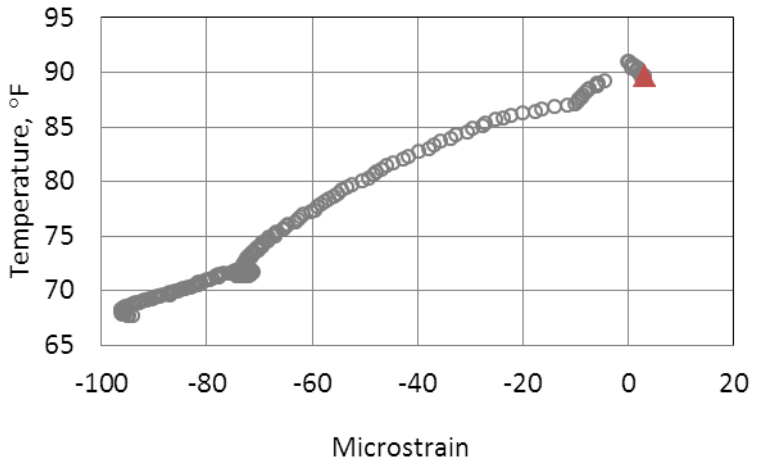

Figure 3-61. Measured strain-temperature at the bottom of Slab A, Cell 2, Project 2.

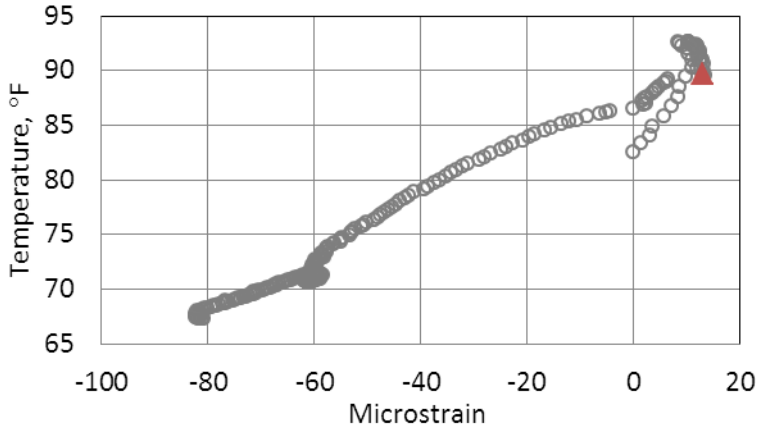

Figure 3-62. Measurements strain-temperature at the bottom of Slab B, Cell 2, Project 2.

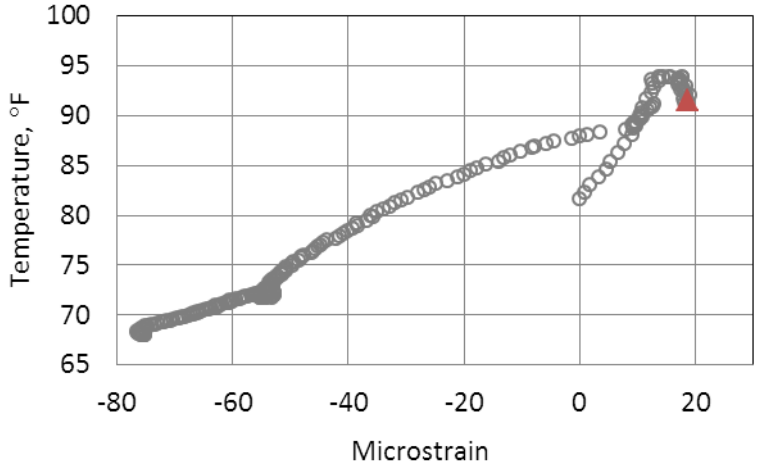

Figure 3-63. Measured strain-temperature at the bottom of Slab C, Cell 2, Project 2.

Table 3-36. Final set and TZ at the bottom of Slabs A, B and C, Cell 2, Project 2.

Slab	Time of Placement	Time of Final Set	TZ
A	3:15 PM	8:20 PM	7:00 AM
B	3:15 PM	8:20 PM	7:00 AM
C	3:15 PM	8:20 PM	7:00 AM

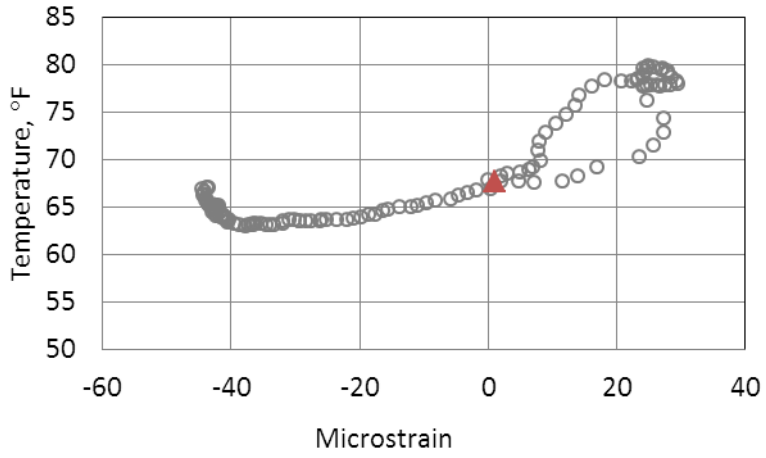

Figure 3-64. Measured strain-temperature at the top of Slab A, Cell 3, Project 2.

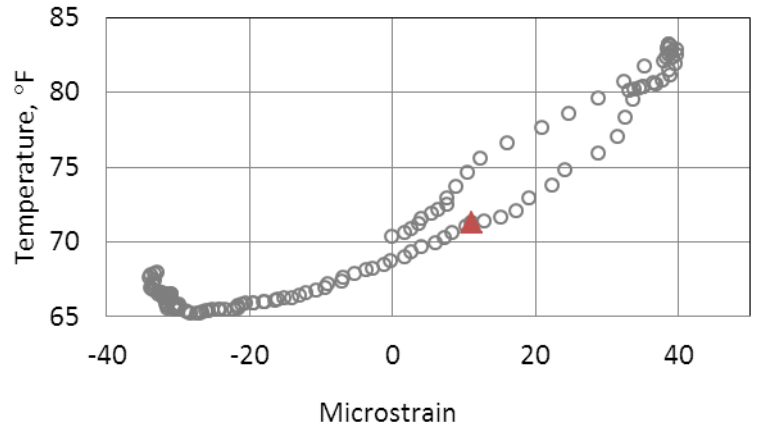

Figure 3-65. Measured strain-temperature at the top of Slab B, Cell 3, Project 2.

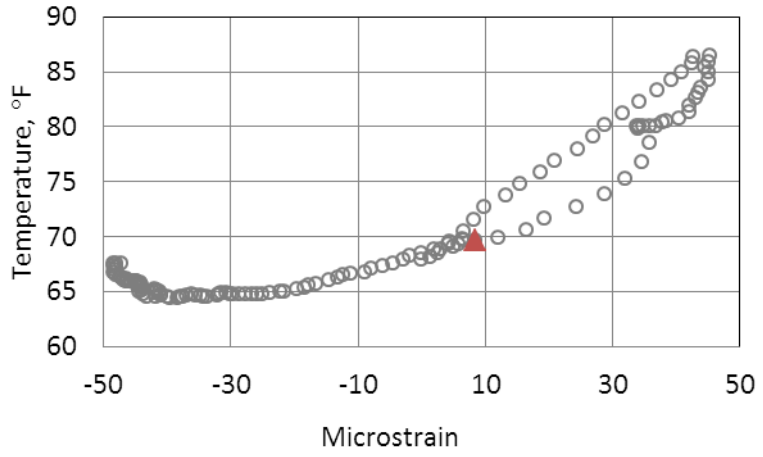

Figure 3-66. Measured strain-temperature at the top of Slab C, Cell 3, Project 2.

Table 3-37. Final set and TZ at the top of Slabs A, B and C, Cell 3, Project 2.

Slab	Time of Placement	Time of Final Set	TZ
A	4:45 PM	11:15 PM	12:15 PM
B	4:45 PM	11:00 PM	12:30 PM
C	4:45 PM	11:15 PM	12:00 PM

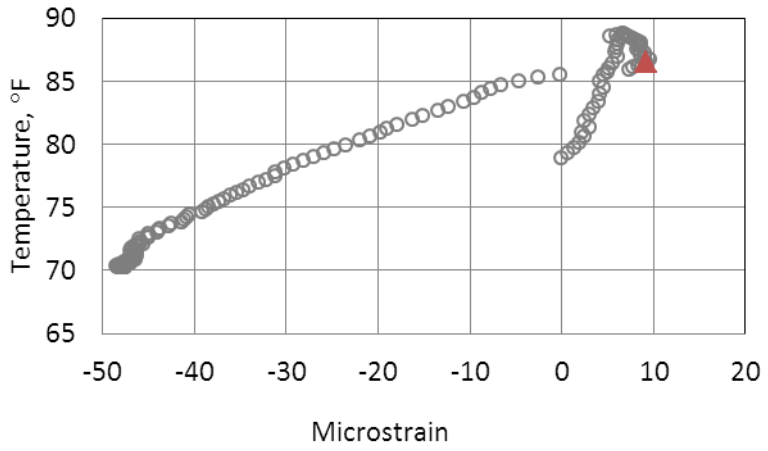

Figure 3-67. Measured strain-temperature at the bottom of Slab A, Cell 3, Project 2.

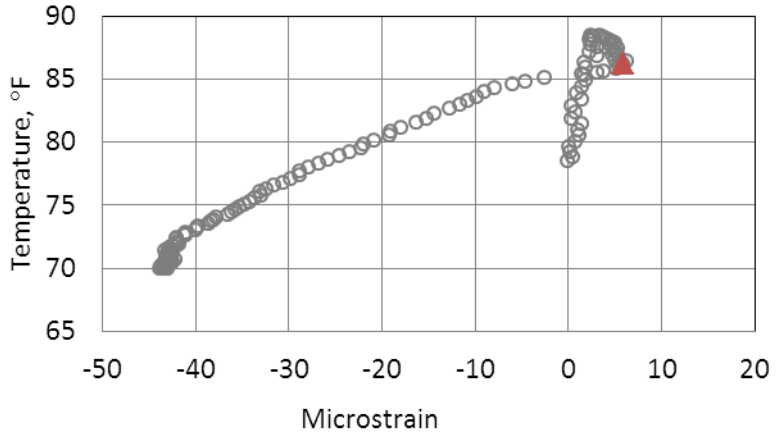

Figure 3-68. Measurements strain-temperature at the bottom of Slab B, Cell 3, Project 2.

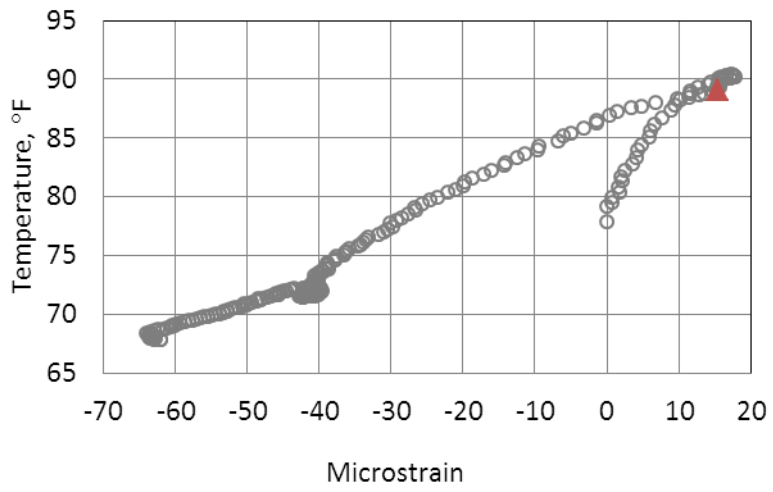

Figure 3-69. Measurements strain-temperature at the bottom of Slab C, Cell 3, Project 2.

Table 3-38. Final set and TZ at the bottom of Slabs A, B and C, Cell 3, Project 2.

Slab	Time of Placement	Time of Final Set	TZ
A	4:45 PM	10:30 PM	9:30 AM
B	4:45 PM	10:30 PM	9:30 AM
C	4:45 PM	10:30 PM	9:30 AM

Based on Table 3-33 to Table 3-38, TZ was reached at 11.5 to 13 hours in Cell 1 and between 16 to 18.75 hours in Cell 2 and at 16.75 to 19.5 hours in Cell 3. To investigate the effects of the ambient temperature on hydration, concrete temperature variation over time was presented for each slab together with the ambient temperature. This is presented in Figure 3-70.

According to Figure 3-70, Cell 1 shows the highest peak temperature and Cell 3 the lowest. This can be explained by considering the ambient temperature changes throughout the construction day. As seen in Figure 3-70, the ambient temperature is rising when slabs in Cell 1 were paved and cured; while it is falling when the slabs in the last cell reach final set time. The peak in the day-time ambient temperature coincides with the heat of hydration in Cell 1 and results in the highest peak temperature observed within the slabs. It is also interesting to note the effect of the base temperature on the hydration at the top versus at the bottom in different cells. In Cell 1, the slab shows a higher peak at the top; while in Cells 2 and 3 the slab shows higher temperatures at the bottom. As seen in Figure 3-70, the slabs are heating up at final set while they are cooling down at TZ, similar to what was observed for Project 1.

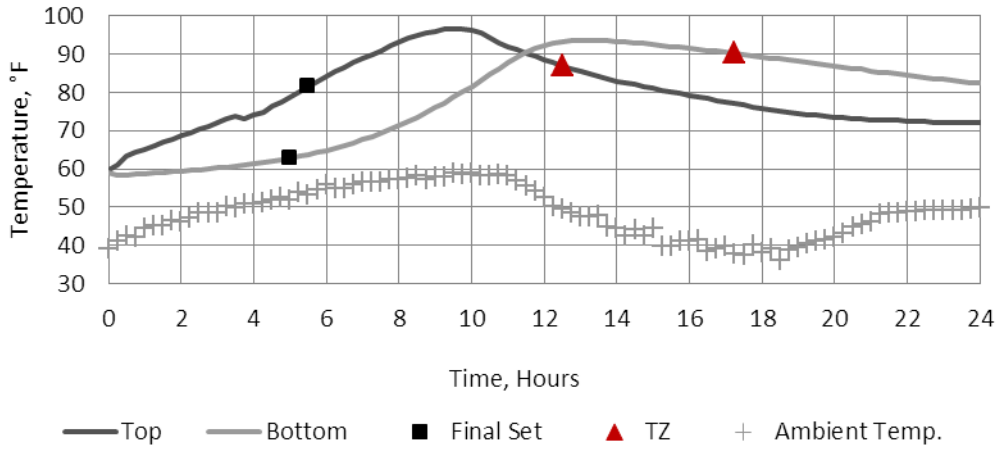

(a)

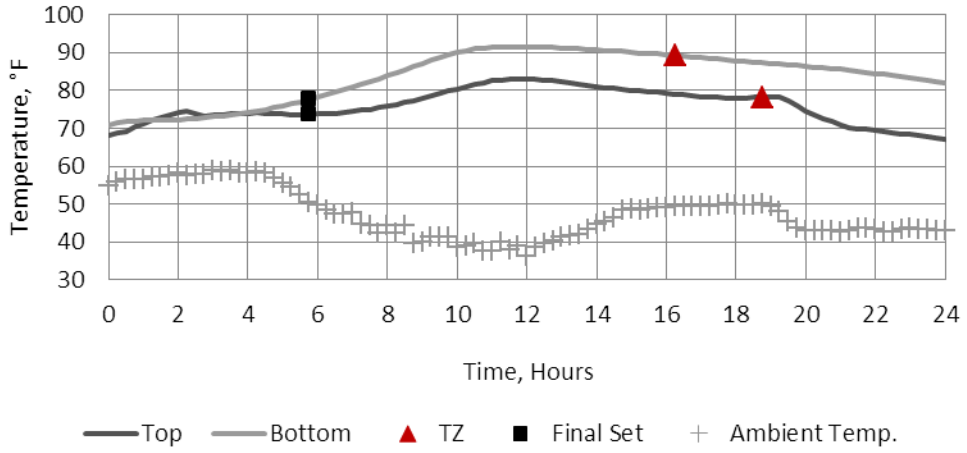

(b)

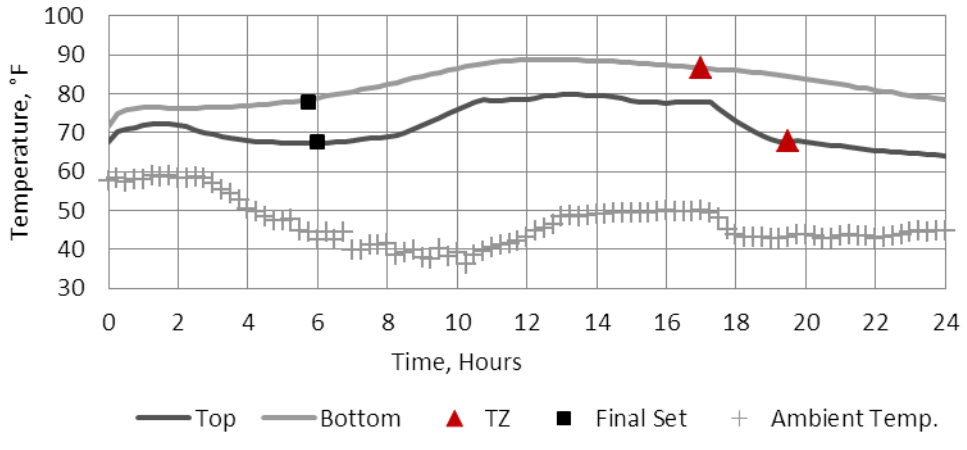

(c)

Figure 3-70. Final and TZ presented with respect to the temperature over time for (a) Cell 1(b) Cell 2 (c) Cell 3.

The equivalent age was estimated over time based on the temperature measurements at the top and bottom of each slab. The equivalent age at TZ for each slab is summarized in Table 3-30.

The degree of hydration was another factor that was estimated for each instrumented slab. The inputs required by the hydration model (Equations 1-6 to 1-10) and their corresponding values are summarized in Table 3-30. The cement composition was obtained from the cement mill sheet, provided in Table 3-27, and the w/cm ratio of the PCC mixture was measured in the field using the w/cm ratio microwave oven test. Using the input data from Table 3-40, the hydration shape and time parameters and the ultimate degree of hydration was estimated for the PCC mix used in each cell. The subsequent results are provided in Table 3-41.

Table 3-39. Equivalent age at TZ for all slabs in Project 2.

	Equivalent Age at TZ (Hours)								
	Cell 1			Cell 2			Cell 3		
	Slab A	Slab B	Slab C	Slab A	Slab B	Slab C	Slab A	Slab B	Slab C
Top Gage	19.6	19.0	18.1	22.9	23.7	23.8	20.9	23.3	22.4
Bottom Gage	21.2	21.0	18.2	24.4	26.8	25.4	25.0	24.7	25.6

Table 3-40. Inputs used to estimate the degree of hydration, Project 2.

Parameter	Value
P_{C3S} (%)	54.9
P_{C3A} (%)	6.8
P_{SO3} (%)	2.85
Average w/cm Ratio for Cell 1	0.455
Average w/cm Ratio for Cell 3	0.475

Table 3-41. Hydration parameters and the ultimate degree of hydration, Project 2.

Parameter	Value
T	24.3
B	0.63
Ultimate Degree of Hydration- Cell 1	0.723
Ultimate Degree of Hydration- Cell 3	0.732

The hydration time and shape factors from Table 3-41 were used to establish the progress of hydration in slabs. The estimated critical degree of hydration is summarized in Table 3-42 for all the slabs instrumented in Project 2. The results are also presented in the form of a bar graph in Figure 3-71.

Table 3-42. Degree of hydration at TZ for all slabs in Project 2.

	Critical Degree of Hydration								
	Cell 1			Cell 2			Cell 3		
	Slab A	Slab B	Slab C	Slab A	Slab B	Slab C	Slab A	Slab B	Slab C
Top Gage	0.33	0.32	0.31	0.37	0.38	0.38	0.35	0.38	0.37
Bottom Gage	0.35	0.35	0.31	0.39	0.4	0.41	0.4	0.39	0.4

The average critical degree of hydration for the top and bottom of each cell in Figure 3-71 shows that slabs reached TZ at a higher degree of hydration at the bottom than at the top. This is the case for all three cells. Furthermore, the effect of a higher water content in the PCC mixture used for Cells 2 and 3 in comparison to Cell 1 is reflected in the results in Figure 3-71. According to the PCC design sheet, the PCC for Cell 1 contained 150 lb/yd^3 water while this value was reported as 163 lb/yd^3 and 172 lb/yd^3 in Cell 2 and 3.

Temperature variation in the base layer over a duration of one hour before and one hour after TZ is presented in Figure 3-72 together with the weighted average temperature in the slab. Based on this figure, the slab is warmer at TZ for Cell 1 with respect to Cells 2 and 3. A warmer ATPB is expected to provide less restraint against expansion/contraction of the fresh concrete. The warmer base in Cell 1 together with the low water content in this cell, as discussed above, can explain the low degree of hydration observed for this cell at TZ.

Overall, the critical degree of hydration for this project was established at between 0.32 and 0.37 at the top and from 0.34 to 0.40 at the bottom of the slabs.

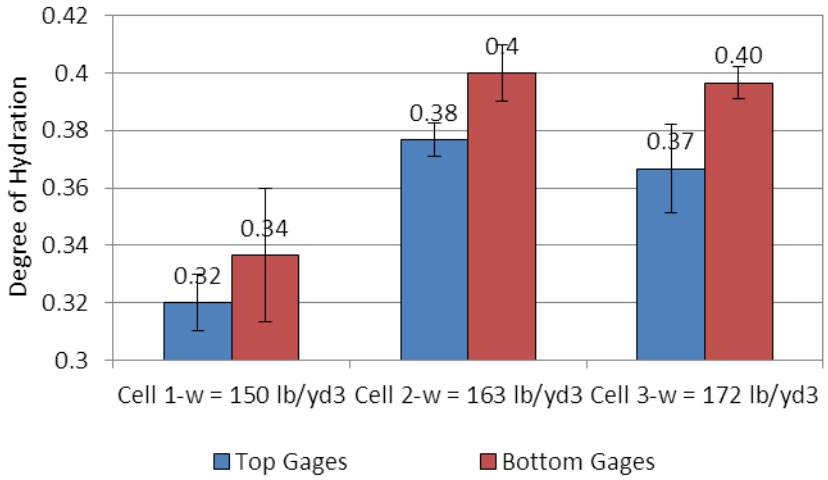

Figure 3-71. Average critical degrees of hydration in the three cells in Project 2.

The two other factors that can influence TZ in the slabs are slab unit-weight and thickness. The slabs in Cell 2 are slightly heavier when compared to the other two cells. Test results in the field showed that the unit weight of the mix in Cell 1 was equal to 146 lb/ft^3, while it was 150 lb/ft^3 in Cell 2 and 148 lb/ft^3 in Cell 3. This slight variation in the unit weight is not expected to affect TZ.

As seen in Figure 3-49, the slabs in Cell 2 are about one inch thicker than in the other two cells. Again, a variation of 1 inch in the slab thickness is not expected to influence TZ significantly. However, the combination of a slightly lower self-weight and thickness plus a lower water content and higher base temperature might explain the lower critical degree of hydration observed for Cell 1.

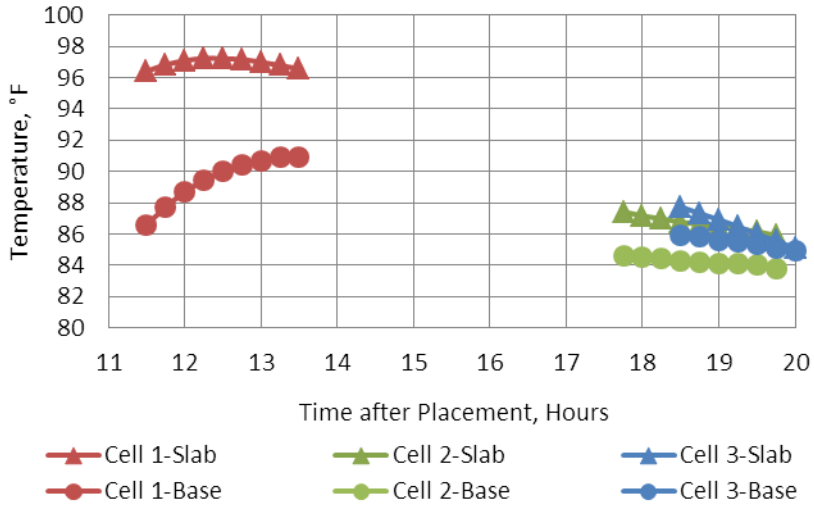

Figure 3-72. Temperature of the slab and the base at TZ for all the cells in Project 2.

3.5 PROJECT 3-SECTION B10 ON SR 22

3.5.1 Project 3-Location and Characteristics

Another section of SR-22, located in the municipality of Blairsville, Westmoreland County, Pennsylvania was selected as the next location. Paving of this section took place on the morning of October 8, 2009, beginning at approximately 7:30 AM.

The test section included nine PCC slabs on the westbound of SR-22. Cell 1 was constructed in the morning at about 9:05 AM, and from stationing 939+60 to 940+05, Cell 2, was constructed at about 12:40 PM and from stationing 948+00 to 948+45 and Cell 3 was constructed in the afternoon from 3:59 PM to 4:10 PM between stationing 954+70 and 955+15.

The design thickness for the PCC layer was 14 inch. Based on a pre- and post-paving survey, the as-built thickness varied significantly between the cells. The average thickness of the slabs for each cell is shown in Figure 3-73.

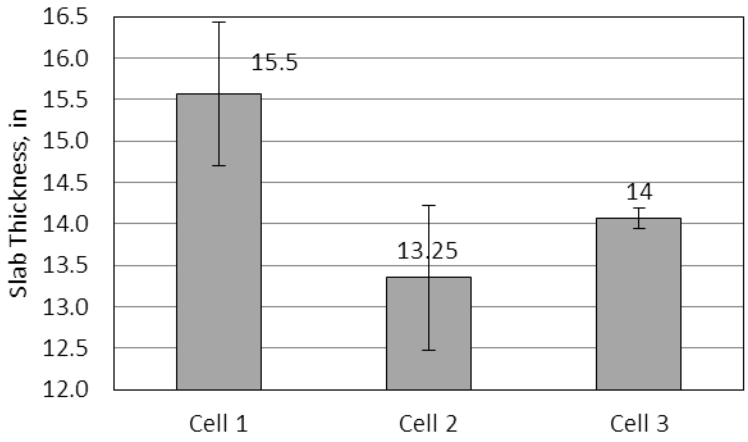

Figure 3-73. Average as-built slab thickness in each cell, Project 3.

The PCC was produced by New Enterprise Stone & Lime Co., Inc. It was mixed at a portable plant located approximately 5 miles east of the project site and was delivered to the site via trucks. Following finishing, a curing compound was applied to the surface. Since it started to rain during the application of the curing compound, slabs were covered with plastic sheets at 4:15 PM. This is shown in Figure 3-74. Sawing of the joints did not begin until the next morning.

Figure 3-74. Slabs covered with plastic sheets due to rain.

The PCC mixture design was obtained from the batch plant on the day of paving. The cementitious materials included Type I cement manufactured by Cemex in Wampum, Pennsylvania and 15 percent Class F fly ash from Headwaters Co.-Hatfield Power Station. The mix water came from the city of Blairsville, Pennsylvania American Water. The air entrainment and water reducing admixtures were supplied by Axim Concrete Technologies of Middlebranch, OH. AE-360 was the air entraining admixture and 1000N was the water reducing agent used. A summary of the mixture design for each cell can be found in Table 3-43. The coarse aggregate met a AASHTO No. 57 gradation and consisted primarily of limestone. The fine aggregate met PennDOT Specification Type A sand. Gradations for the fine and coarse aggregates can be found in Table 3-44 and Table 3-45, respectively.

Table 3-43. PCC mixture design for the concrete used to pave Project 3.

Material	Specific Gravity	Absorption (%)	Batch Weight (lb/yd^3)		
			Cell 1	**Cell 2**	**Cell 3**
Type I Cement	3.15	n/a	550	550	550
Fly Ash-Class F	2.89	n/a	100	100	100
Fine Aggregate	2.62	1.24	1161	1161	1163
Coarse Aggregate	2.68	0.52	1840	1840	1840
Unit Weight (lb/ft^3)	1	n/a	142.6	142.6	142.6
Water Content			175	177.3	177.3

Table 3-44. Gradation of the fine aggregate used in the PCC.

Fine Aggregate	
Sieve Size	Percent Finer
3/8"	100
#4	100
#8	79
#16	62
#30	43
#50	22
#100	6

Table 3-45. Gradation of the coarse aggregate used in the PCC.

Coarse Aggregate - Limestone	
Sieve Size	Percent Finer
1 ½"	100
1"	99
½"	37
#4	5
#8	3

The composition of the cement used in the PCC mix is summarized in Table 3-48. This information was obtained from the cement mill report provided by the plant.

The PCC slab was placed on a 4-inch layer of CTPB. The mixture design for the CTPB is provided in Table 3-47. The gradation of the open-graded aggregate used for the CTPB is shown in Table 3-48. A view of the CTPB with dowel baskets fixed in place can be seen in Figure 3-75. The subbase gradation was the same as that used in previous projects and will not be repeated here.

Table 3-46. Composition of the cement used for Project 3.

Chemical Data		
Component	Value (%)	Specification
SiO_2	19.5	-
Al_2O_3	4.8	-
Fe_2O_3	3.6	-
CaO	52	-
MgO	2.7	6.0-Max
SO_3	2.9	C-1038-Max
C_3S	69	3.0-Max
C2s	12	
C_3A	1	0.75-Max
Alkalis		-
Loss of Ignition	1.9	-
Insoluble Res.	0.43	-
Physical Data		
Blaine (cm^2/g)	4030	2800-Min 4000-Max

Table 3-47. Mixture design for the CTPB, Project 3.

Material	Specific Gravity	Absorption	Weight in the Batch (lb/yd^3)
Cement-Cemex Cement-Louisville, KY	3.15	-	180
Pozzolan- Headwaters Co.-Hatfield Power Station	2.40	-	30
Coarse Aggregate-Hanson Torrance Quarry	2.68	0.52	2292
Mix Water	-	-	84

Table 3-48. Gradation of the aggregate used in the CTPB mixture for Project 3.

CTPB	
Sieve Size	Percent Finer
1 ½"	100
1"	99
½"	44
No. 4	4
No. 8	2

Figure 3-75. CTPB layer with the dowel baskets in place, Project 3.

3.5.2 Fresh and Hardened Concrete Properties

During paving, fresh concrete properties such as slump, w/cm ratio microwave oven, entrained air and time of set tests were measured by the research team at each cell. See Table 3-49 for test results.

Table 3-49. Fresh concrete properties measured at the site for Project 3.

Property	Measured								
	Cell 1			Cell 2			Cell 3		
	High	Low	Ave.	High	Low	Ave.	High	Low	Ave.
Slump (in)	-	-	1.5	-	-	1.25	1	0.75	0.87
Air (%)	-	-	5.5	-	-	5.9	-	-	5.8
w/cm Ratio	0.52	0.46	0.48	0.57	0.46	0.50	0.48	0.45	0.46
Unit Weight (lb/ft^3)	149	149	149	150	151	150.5	151	148	149.5

The times of initial and final set for the PCC mixture were determined under field conditions by performing the penetration test. Thermocouples were placed at the mid depth of each sample to record temperature changes to characterize the maturity for each sample. The results from the tests are summarized in Table 3-50 and Figure 3-79.

Table 3-50. Times of initial and final set based on the penetration test, Project 3.

Sample Number	Time of Initial Set (Hour)	Time of Final Set (Hour)	Maturity (°F-Hour)
1	5.7	7.8	414
2	5.5	7.7	448
3	5.5	7.2	390
Average	5.6	7.6	417.3

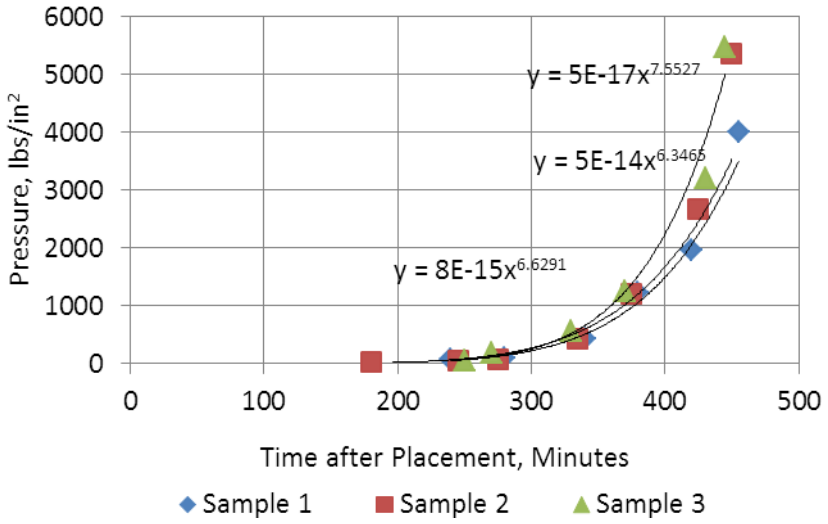

Figure 3-76. Penetration resistance results for the three samples for Project 3.

More than 40 concrete specimens were cast and transferred to the University of Pittsburgh PMML for curing and testing. Results for only 28-day tests are provided in Table 3-51.

Table 3-51. 28-day elastic modulus, compressive strength and Poisson's ratio established in the lab for Project 3.

Property	Cell 1	Cell 2	Cell 3	Mean	Standard Deviation
E_c (psi)	4.05E+06	4.25E+06	4.8E+06	4.4E+06	300,000
υ	0.18	0.2	0.16	0.18	0.02
f_c (psi)	4910	4850	5270	5010	190
MR (psi)	770	715	870	785	65

The CTE of the PCC mixture used for Project 3 was measured following the same procedure described fully in Section 3.3.2. One sample was cast from the PCC used to pave each cell. The results of the subsequent tests are summarized in Table 3-52.

Table 3-52. Measured PCC CTE for all the cells for Project 3.

Cell Number	CTE (με/ºF)	Mean of CTE (με/ºF)	Standard Deviation (με/ºF)
1	5.4	5.3	0.07
2	5.3		
3	5.2		

To establish the drying shrinkage for the PCC mixture used to pave Project 3, a total of six drying shrinkage specimens were cast in the field. For three of the specimens, the drying shrinkage of the PCC mixture was established in accordance to AASHTO T 160/ASTM C 157. According to the dual standard, the samples are required to be wet cured in a lime-saturated water-bath for 28 days. After this period, the samples are transferred to an environmental room with a temperature of 73 ± 3 ºF and relative humidity of 50 ± 3 percent in accordance with the standard.

Unfortunately, out of these three samples, only two were able to be tested, since the studs in the other specimen were damaged. The test results obtained for the two specimens can be found in Figure 3-72. According to the measurements performed in the field, the PCC mixture in Cell 2 had a w/cm ratio of 0.5 while this parameter was established as 0.48 for Cell 1. This slight difference in the w/cm ratio of the two cells does not explain the distinct difference that is seen between the drying shrinkage established for Cell 1 in comparison to Cell 2. Based on the test results for the past two projects, the high results obtained for the sample from Cell 2 are highly unlikely to be representative of the drying shrinkage of the mixture. The value of 600 με established for the sample from Cell 1 in Figure 3-77 is most likely more representative of the ultimate drying shrinkage of the PCC used to pave this project.

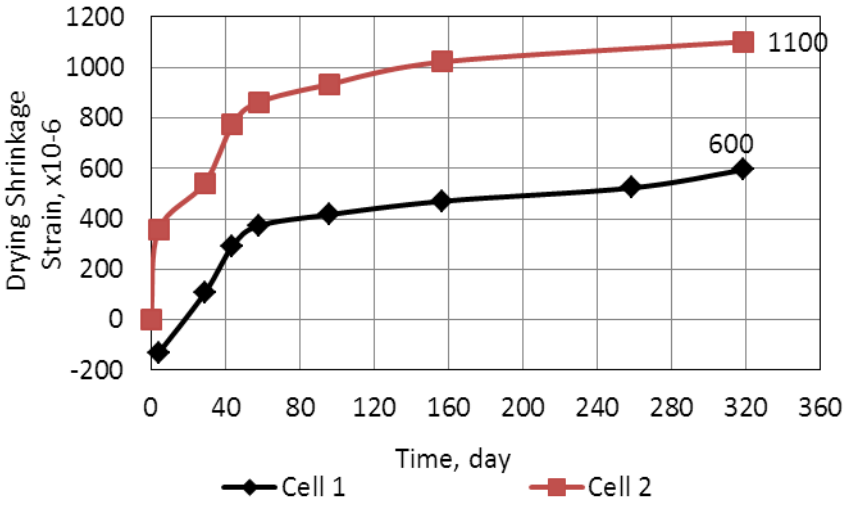

Figure 3-77. PCC drying shrinkage test results for samples wet cured for 28 days, Project 3.

The other three samples cast in the field for Project 3 were used to investigate the effect of the special curing condition advised by the dual standard. These three extra samples were transferred to the drying shrinkage environmental room immediately upon demolding instead of being moist cured for the first 28 days. It is believed that this curing condition is closer (yet not the same) to the field conditions than the curing procedure suggested by the standards, therefore, might be more representative of the actual drying shrinkage that develops in the field.

The drying shrinkage results obtained from these three samples are provided in Figure 3-78. Based on Figure 3-78, the drying shrinkage measured for the samples taken from each of the three cells is very similar, indicating that the PCC mixture is relatively consistent in all three cells. This is consistent with the results obtained from the w/cm ratio microwave oven test. Based on this test, the w/cm ratio was 0.48, 0.5 and 0.48 in Cells 1, 2 and 3, respectively.

It is also interesting to note that no moist curing, Figure 3-78, in comparison to 28 days of moist curing, Figure 3-77, produced an increase of about 130 microstrain, on average.

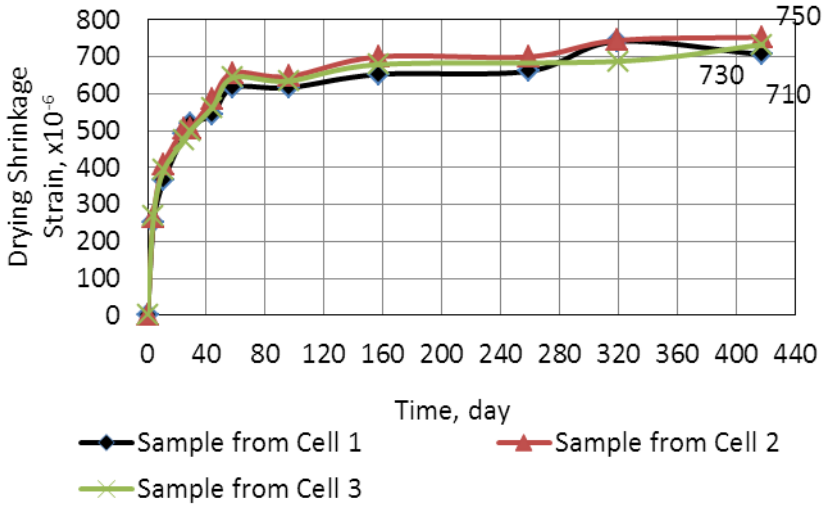

Figure 3-78. PCC drying shrinkage test results for samples without wet curing, Project 3.

3.5.3 Establishing TZ for Project 3

Similar to the previous projects, strain and temperature measurements in the slab were used in this section to establish TZ for Project 3. Strain-temperature graphs were generated based on the measurements obtained using the VW strain gages at the top and bottom of each slab. These graphs are presented in Figure 3-79 to Figure 3-95. A summary of the times of placement, final set and zero-stress is also provided in Table 3-53 to Table 3-58.

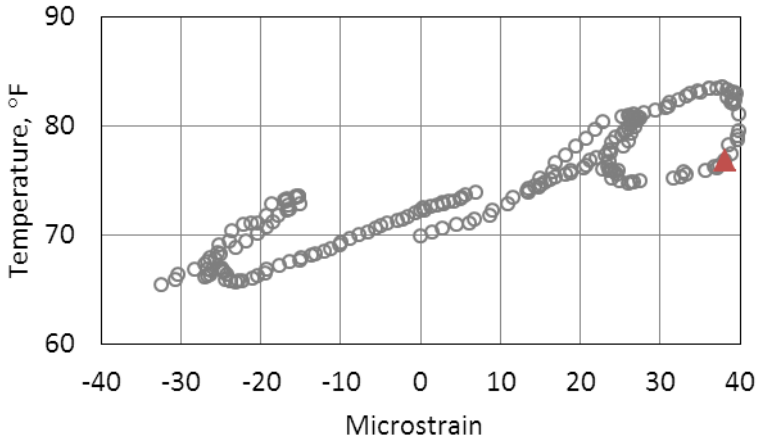

Figure 3-79. Measured strain-temperature at the top of Slab A, Cell 1, Project 3.

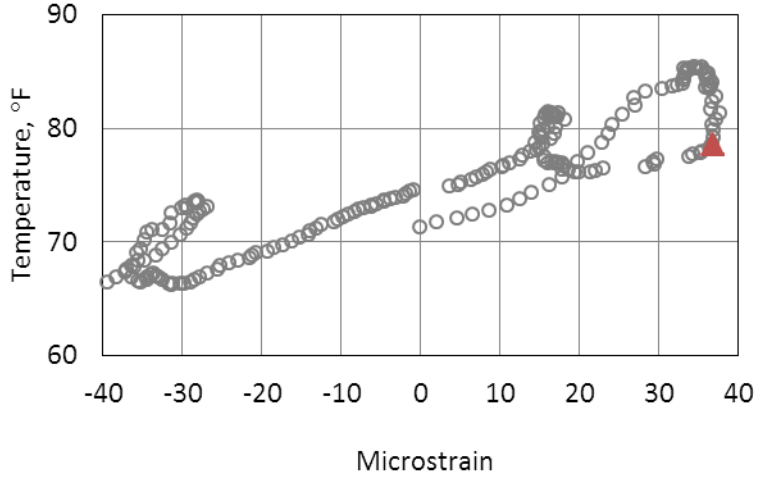

Figure 3-80. Measured strain-temperature at the top of Slab B, Cell 1, Project 3.

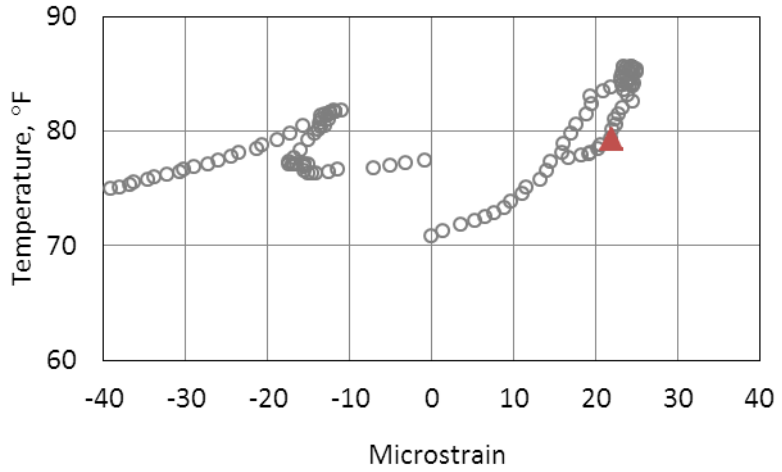

Figure 3-81. Measured strain-temperature at the top of Slab C, Cell 1, Project 3.

Table 3-53. Final set and TZ at the top of Slabs A, B and C, Cell 1, Project 3.

Slab	Time of Placement	Finals Set	TZ
A	8:30 AM	4:15 PM	6:15 AM
B	8:30 AM	4:30 PM	6:15 AM
C	8:30 AM	4:15 PM	6:15 AM

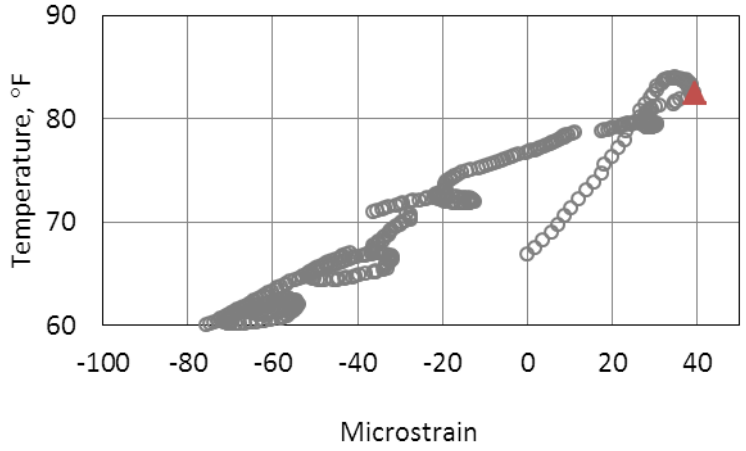

Figure 3-82. Measured strain-temperature at the bottom of Slab A, Cell 1, Project 3.

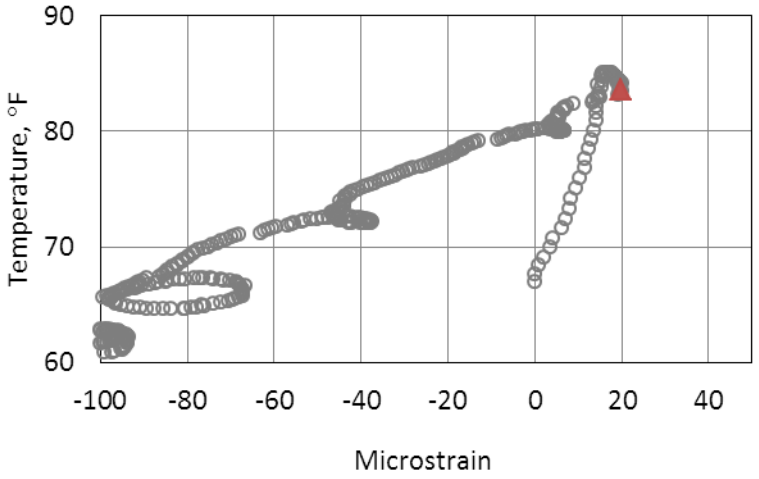

Figure 3-83. Measured strain-temperature at the bottom of Slab B, Cell 1, Project 3.

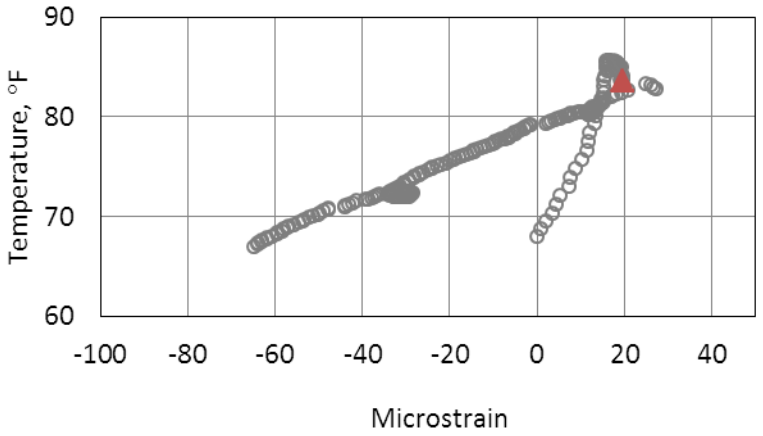

Figure 3-84. Measured strain-temperature at the bottom of Slab C, Cell 1, Project 3.

Table 3-54. Final set and TZ at the bottom of Slabs A, B and C, Cell 1, Project 3.

Slab	Time of Placement	Final Set	TZ
A	8:30 AM	5:30 PM	6:45 AM
B	8:45 AM	5:30 PM	6:45 AM
C	8:45 AM	5:15 PM	7:30 AM

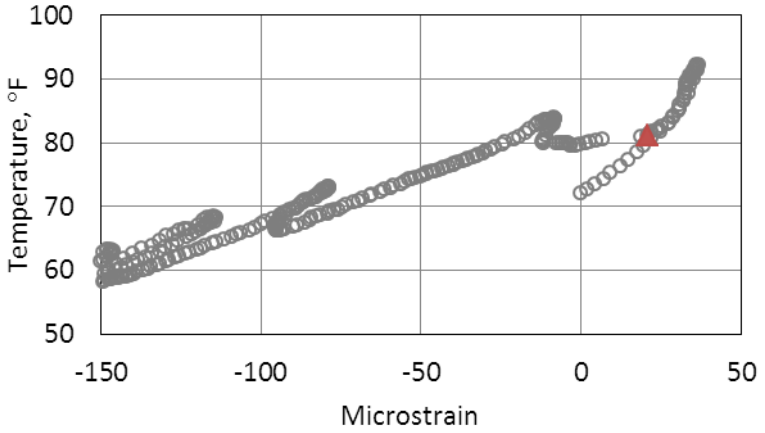

Figure 3-85. Measured strain-temperature at the top of Slab A, Cell 2, Project 3.

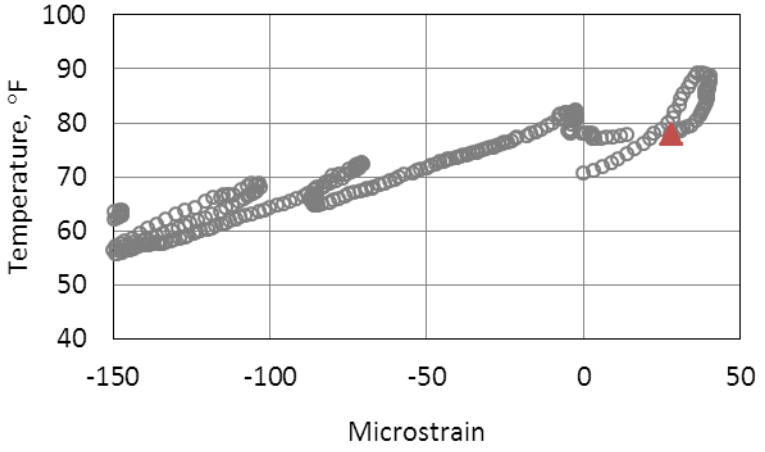

Figure 3-86. Measured strain-temperature at the top of Slab B, Cell 2, Project 3.

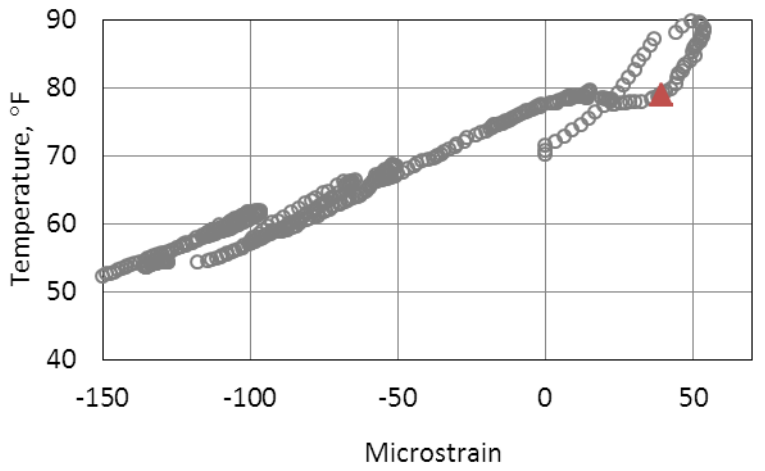

Figure 3-87. Measured strain-temperature at the top of Slab C, Cell 2, Project 3.

Table 3-55. Final set and TZ at the top of Slabs A, B and C, Cell 2, Project 3.

Slab	Time of Placement	Finals Set	TZ
A	12:00 PM	7:15 PM	7:45 AM
B	12:00 PM	7:15 PM	7:45 AM
C	12:00 PM	7:15 PM	7:45 AM

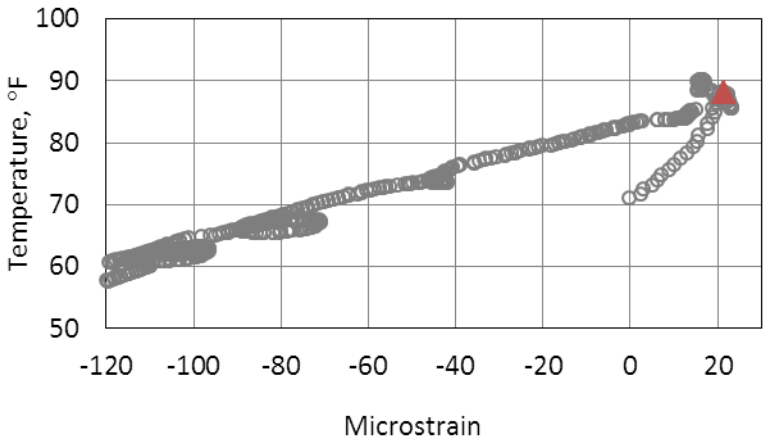

Figure 3-88. Measured strain-temperature at the bottom of Slab A, Cell 2, Project 3.

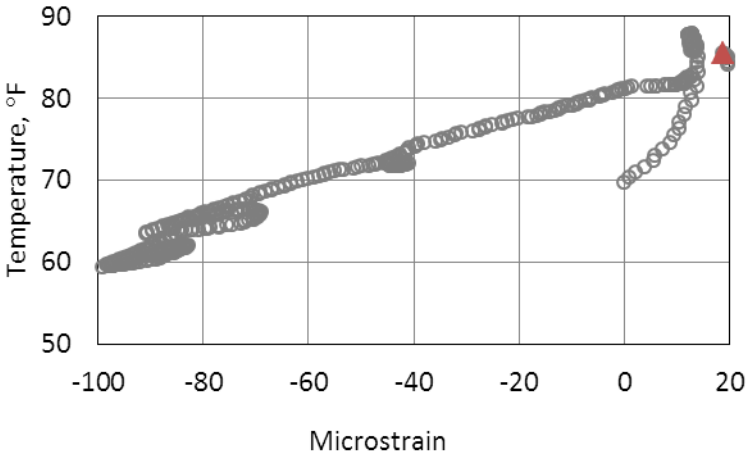

Figure 3-89. Measured strain-temperature at the bottom of Slab B, Cell 2, Project 3.

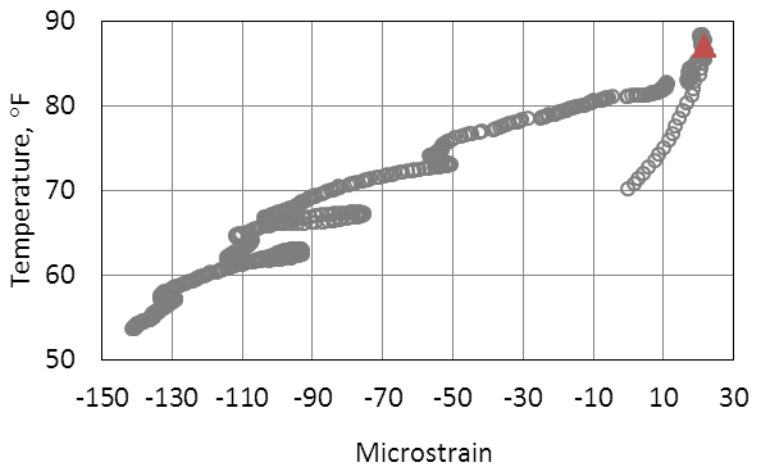

Figure 3-90. Measured strain-temperature at the bottom of Slab C, Cell 2, Project 3.

Table 3-56. Final set and TZ at the bottom of Slabs A, B and C, Cell 2, Project 3.

Slab	Time of Placement	Finals Set	TZ
A	12:00 PM	7:15 PM	8:15 AM
B	12:00 PM	7:15 PM	8:15 AM
C	12:00 PM	7:15 PM	8:15 AM

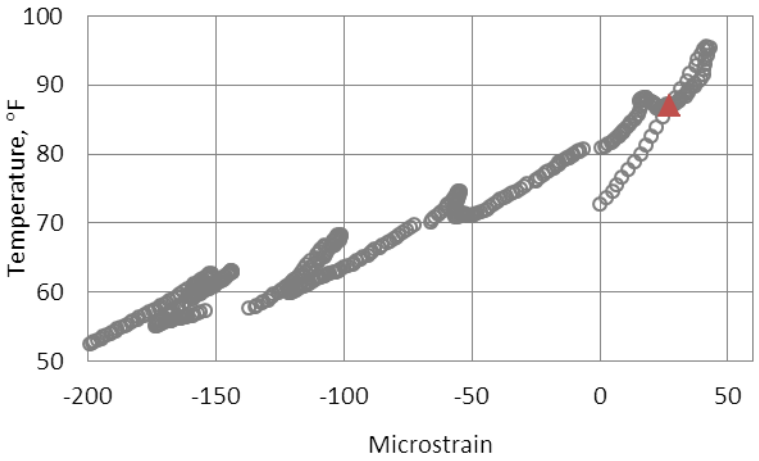

Figure 3-91. Measured strain-temperature at the top of Slab A, Cell 3, Project 3.

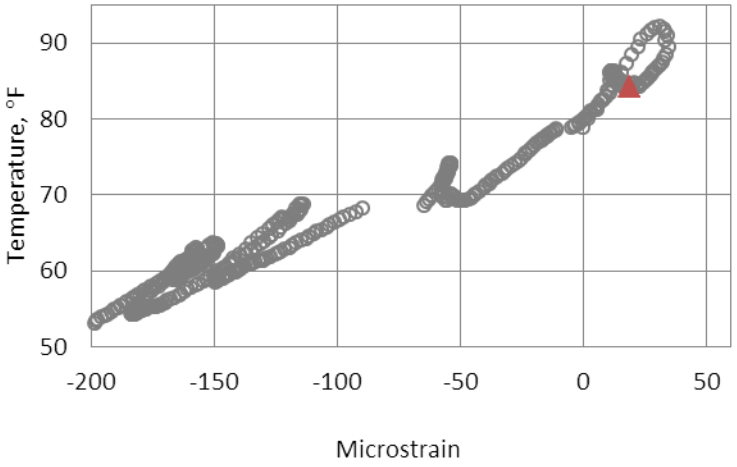

Figure 3-92. Measured strain-temperature at the top of Slab B, Cell 3, Project 3.

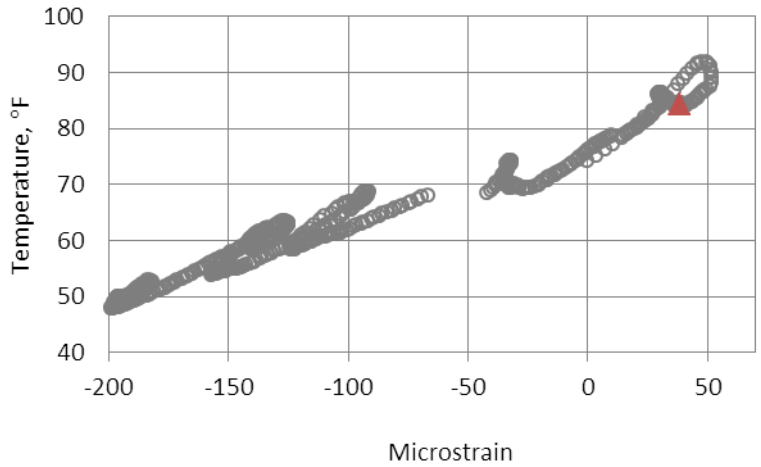

Figure 3-93. Measured strain-temperature at the top of Slab C, Cell 3, Project 3.

Table 3-57. Final set and TZ at the top of Slabs A, B and C, Cell 3, Project 3.

Slab	Time of Placement	Finals Set	TZ
A	3:45 PM	12:00 AM	11:30 AM
B	3:45 PM	12:00 AM	11:30 AM
C	3:45 PM	12:00 AM	11:30 AM

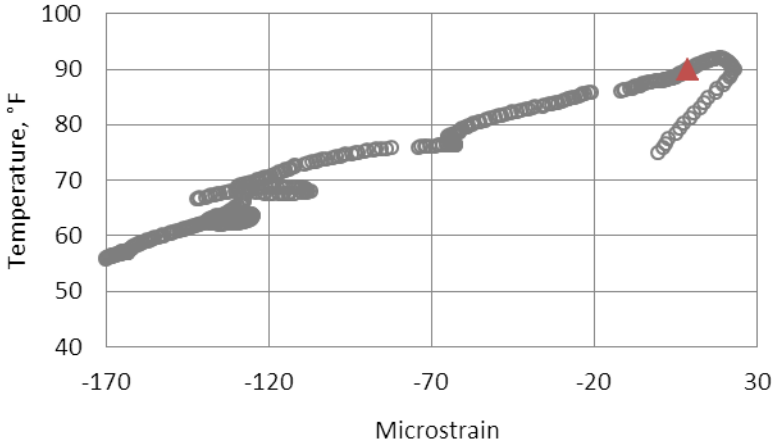

Figure 3-94. Measured strain-temperature at the bottom of Slab A, Cell 3, Project 3.

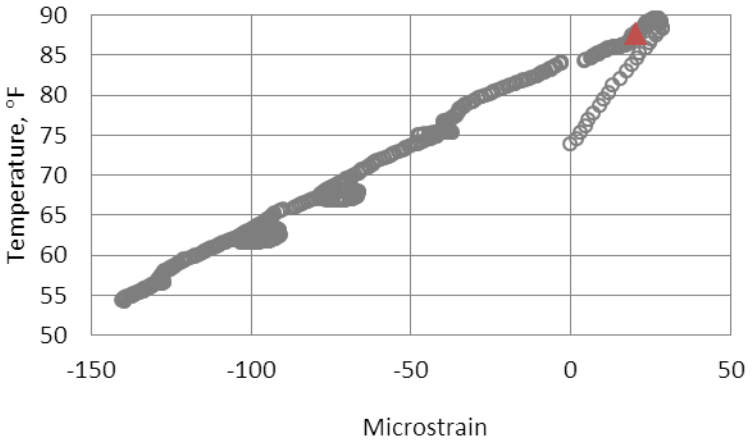

Figure 3-95. Measured strain-temperature at the bottom of Slab B, Cell 3, Project 3.

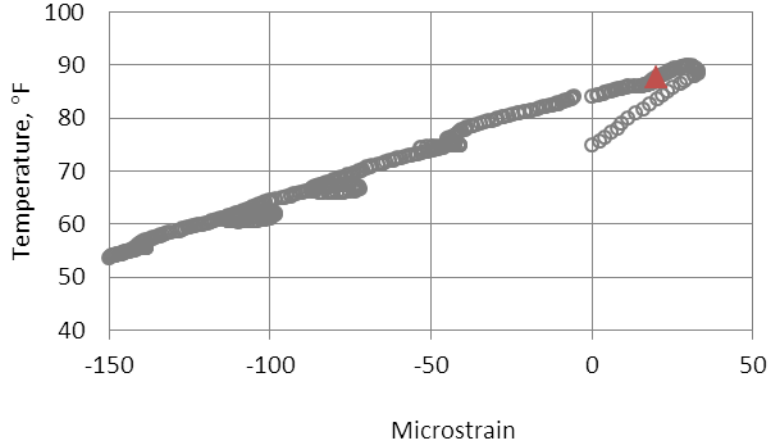

Figure 3-96. Measured strain-temperature at the bottom of Slab C, Cell 3, Project 3.

Table 3-58. Final set and TZ at the bottom of Slabs A, B and C, Cell 2, Project 3.

Slab	Time of Placement	Finals Set	TZ
A	3:45 PM	12:00 AM	12:15 AM
B	3:45 PM	12:00 AM	12:15 AM
C	3:45 PM	12:00 AM	12:15 AM

Based on Table 3-53 to Table 3-58, slabs in Cell 1 reached TZ at between 21.75 and 23 hours after construction; for Cell 2 it was 19.75 to 20.25 hours and for Cell 3 from 19.75 to 20.5 hours. It is noticed that despite the different times of paving for each cell, only a slight variation is seen between TZ established for the cells. This behavior can be explained by considering the overcast conditions, which were present throughout the entire day of paving.

Figure 3-97 presents the temperature variation at the top and the bottom of the slabs in Cells 1, 2 and 3 for a duration of 24 hours following construction. As seen in Figure 3-97 (a), slabs in Cell 1 show a lower temperature peak when compared to the temperature variation for Cells 2 and 3 in Figure 3-97 (b) and (c), respectively. This could be explained by considering the ambient temperature at the time of placement for each cell. The ambient temperature at the time of construction of Cell 1 is as low as 40°F while it is around 60 °F at the time of placement for Cell 2 and 54 °F at the time of placement for Cell 3.

It should also be noted that since it started to rain during the application of the curing compound, slabs in Cells 2 and 3 were covered with plastic sheets at 4:15 PM. Plastic sheets can confine the heat of hydration that generates within the slabs and prevent its loss to the atmosphere thereby accelerating the hydration process.

The overcast conditions and the use of plastic sheets have resulted in a very similar temperature variation at the top and the bottom of the slabs for all three cells.

Final set and TZ are also highlighted in Figure 3-97 with respect to the temperature variation over time in each cell. Based on Figure 3-97, final set occurred prior to the hydration temperature peak and TZ occurred after the hydration temperature peak in three cells.

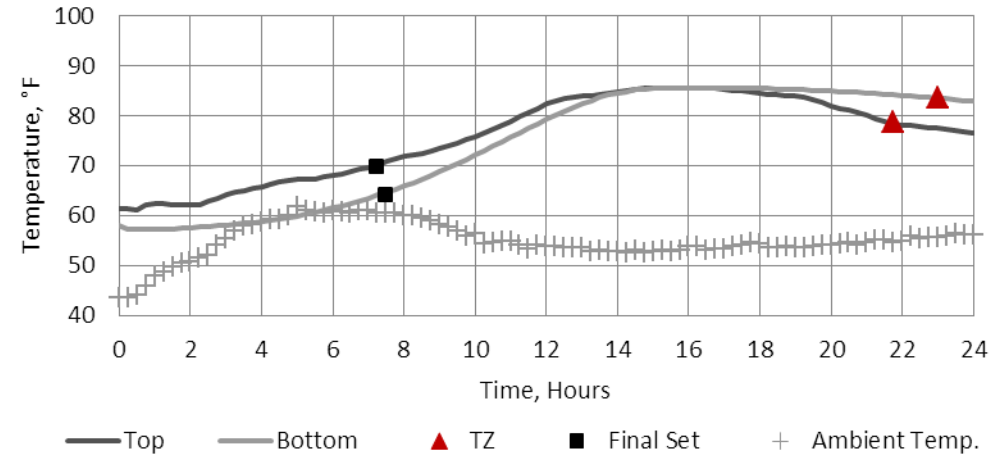

(a)

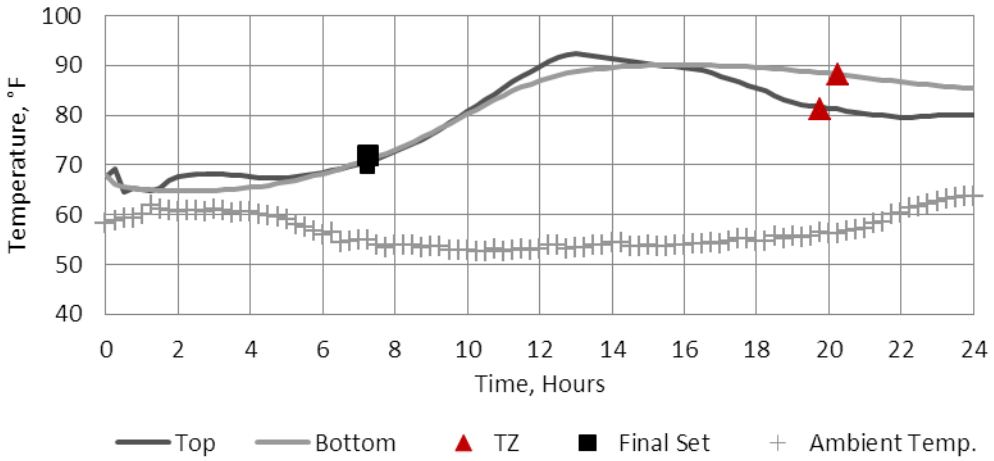

(b)

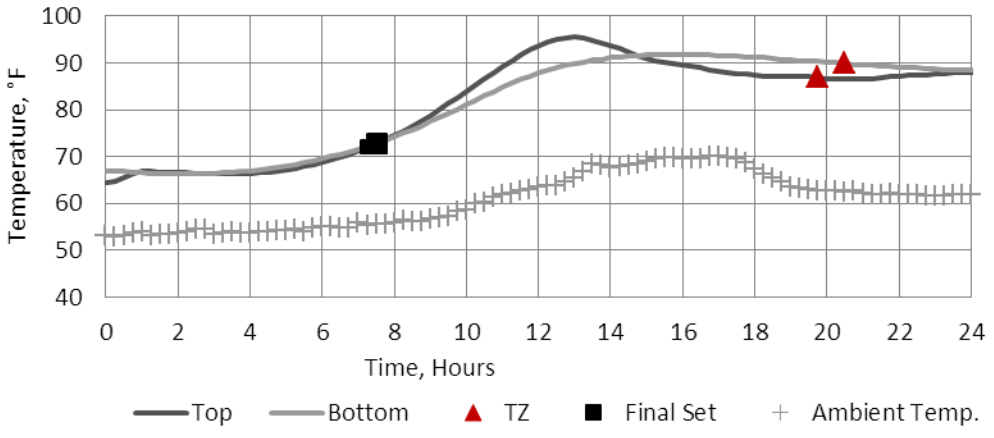

(c)

Figure 3-97. Final and TZ presented with respect to the temperature over time for (a) Cell 1(b) Cell 2 (c) Cell 3

Project 3.

The equivalent age was estimated based on temperature measurements made at the top and bottom of slab by the thermistor in the VW strain gage. The equivalent age at TZ at the top and bottom of slabs is provided in Table 3-59. As expected, the equivalent ages at TZ for all of the instrumented slabs are similar, although slight variation is seen from cell to cell. This could be due to variation in PCC mixture design in different cells. This discussion will be expanded upon in the following section.

Table 3-59. Equivalent age at TZ for all instrumented slabs in Project 3.

	Equivalent Age at TZ (Hours)								
	Cell 1			Cell 2			Cell 3		
	Slab A	Slab B	Slab C	Slab A	Slab B	Slab C	Slab A	Slab B	Slab C
Top Gage	23.2	24.4	25.3	24.9	23.3	23.2	26.4	24.6	24.6
Bottom Gage	22.9	23.6	26.1	25.5	23.9	24.5	27.4	26.1	26.4

The degree of hydration in each instrumented slab was estimated over time. The inputs required by the hydration model and their corresponding values are summarized in Table 3-60. The cement composition was obtained from the cement mill sheet and the w/cm ratio of the PCC mixture was measured in the field by performing the w/cm microwave oven test.

Table 3-60. Inputs used to estimate the degree of hydration, Project 3.

Parameter	Value
P_{C3S} (%)	69
P_{C3A} (%)	7
P_{SO3} (%)	2.9
Blaine (cm^2/g)	4,030
Average w/cm in Cell 1	0.48
Average w/cm in Cell 2	0.5
Average w/cm in Cell 3	0.46

Using the input values from Table 3-60, the hydration shape and time parameters and the ultimate degree of hydration was established for the PCC mix used in each cell. The results are provided in Table 3-61. The hydration parameters from Table 3-61 and the equivalent age established in each slab, are then used to estimate the degree of hydration for each slab. The critical degree of hydration is summarized in Table 3-62. The results are also presented in the form of a bar graph in Figure 3-98. Based on Figure 3-98, the degree of hydration at TZ does not show much variation between cells.

Table 3-61. Hydration parameters and the ultimate degree of hydration, Project 3.

Parameter	Value
T	14.5
B	0.608
Ultimate Degree of Hydration- Cell 1 and 3	0.73
Ultimate Degree of Hydration- Cell 2	0.74

Table 3-62. Critical degree of hydration for all the instrumented slabs in Project 3.

	Critical Degree of Hydration								
	Cell 1			Cell 2			Cell 3		
	Slab A	Slab B	Slab C	Slab A	Slab B	Slab C	Slab A	Slab B	Slab C
Top Gage	0.5	0.51	0.52	0.52	0.51	0.51	0.52	0.51	0.51
Bottom Gage	0.50	0.51	0.54	0.53	0.51	0.52	0.53	0.52	0.52

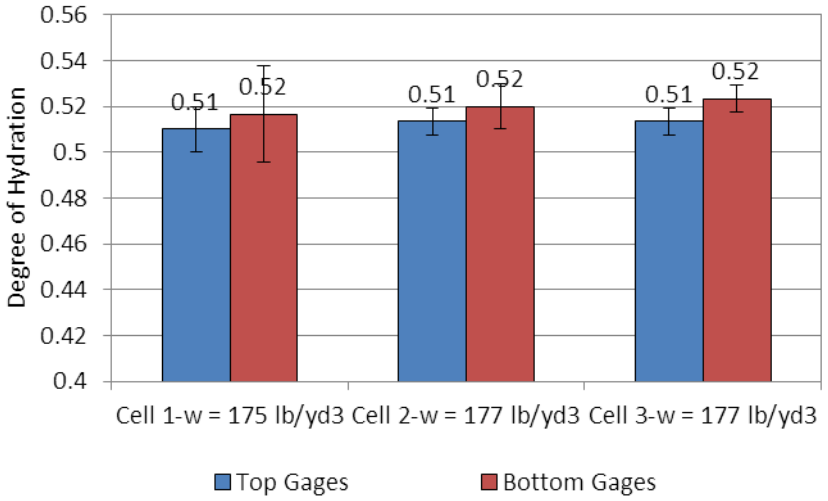

Figure 3-98. Average critical degree of hydration in each cell, Project 3.

3.6 PROJECT 4 ON US 22

3.6.1 Project 4-Location and Characteristics

The last pavement section that was instrumented is located in Clyde County, Pennsylvania. The test section included nine PCC slabs in the westbound lane of US-22. Instrumentation of this section started on April 26, 2010 and was accomplished over a period of two days. The paving of this section of Route 22 started at 8:00 AM (a 2 hour delay occurred due to freezing weather

conditions), Thursday April 29, 2010 at stationing 359+00. Paving on Thursday continued until about 6:30 PM and up to stationing 396+00. Paving started again the next morning at 8:00 AM. Cell 1 was located at stationing 377+96 to 378+35 and Cell 2 was located at 390+31 to 390+76. These two cells were paved during the first day of paving. Cell 3 was constructed at stationing 399+00 to 399+45 and was paved in the morning of the second day of paving.

The new pavement structure is a JPCP with a transverse joint spacing varying from 13 ft at the start to 15 ft at the end. The paving width was 24 ft to accommodate two adjacent 12-ft wide lanes. No. 5 epoxy-coated tie bars, were placed every 30 inch along both the lane/shoulder and centerline joints. Epoxy-coated 1.5-inch diameter, 18-inch long dowel bars were spaced every 12 inch along the transverse joints with the first dowel located 6 inches from each longitudinal joint.

The design thickness for the PCC layer was 10 inch. Pre- and post-construction surveys were performed at each cell to establish the as-built thickness of the PCC layer. The average as-built thicknesses for the slabs in each cell are presented in Figure 3-99.

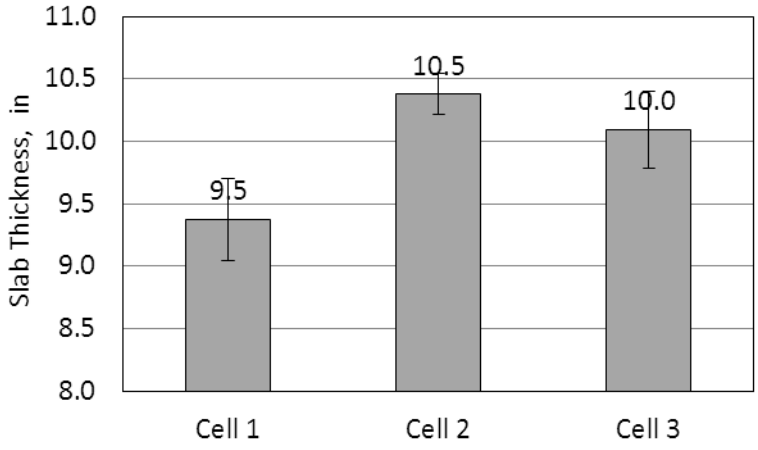

Figure 3-99. As-built PCC slab thickness at each cell based on surveying, Project 4.

A PennDOT Class AA-500 PCC was slip form paved for this project. The cementitious materials include Type I cement manufactured by Cemex Cement, Louisville, KY and Class F fly ash from Headwaters Co.-Hatfield power station. The coarse aggregate met AASHTO No. 57 gradation specifications and consisted primarily of limestone. The fine aggregate met PennDOT Specification Type A sand. Gradations for the fine and coarse aggregates can be found in Table 3-63 and Table 3-64, respectively. The mixture design for the PCC used for each cell can be found in Table 3-65.

Table 3-63. Gradation of fine aggregate used in the PCC for Project 4.

Fine Aggregate	
Sieve Size	Percent Finer
3/8"	100
#4	99
#8	80
#16	62
#30	41
#50	22
#100	6

Table 3-64. Gradation of coarse aggregate used in the PCC for Project 4.

Coarse Aggregate - Limestone	
Sieve Size	Percent Finer
1 ½"	100
1"	98
½"	39
#4	6
#8	3

Table 3-65. PCC mixture design for 3 cells in Project 4.

Material	Specific Gravity	Absorption (%)	Batch Weight (lbs/yd^3)		
			Cell 1	**Cell 2**	**Cell 3**
Type I Cement	3.15	n/a	500	500	500
Fly Ash-Class F	2.89	n/a	88	88	88
Fine Aggregate	2.62	1.24	1166	1166	1166
Coarse Aggregate	2.68	0.52	1840	1840	1840
Water Content	1	n/a	180	194	187
Unit Weight (lb/ft^3)	n/a	n/a	142.6	142.6	142.6

Cement at this project was provided by Cemex Cement, Louisville, KY. The composition of the cement used in the PCC mixture is summarized in Table 3-66. This information was obtained from the mill sheet.

Table 3-66. Composition of the cement used for Project 4.

Chemical Data		
Component	Value (%)	Specification
SiO_2	20.7	-
Al_2O_3	4.5	-
Fe_2O_3	3.2	-
CaO	63.1	-
MgO	2.8	6.0-Max
SO_3	2.7	C-1038-Max
C_3S	59	3.0-Max
C2s	12	
C_3A	6	0.75-Max
Alkalis	0.66	-
Loss of Ignition	1.0	-
Insoluble Res.	0.29	-
Physical Data		
Blaine (cm^2/g)	3909	2800-Min4000-Max

3.6.2 Fresh and Hardened Concrete Properties

During paving, fresh concrete property testing such as slump, w/cm ratio, entrained air and time of final set was performed by the research team on the concrete used in each cell. Table 3-67 provides the results of the fresh PCC tests obtained for each cell.

Table 3-67. Fresh concrete properties measured at the site of Project 4.

Property	Measured								
	Cell 1			Cell 2			Cell 3		
	High	Low	Ave.	High	Low	Ave.	High	Low	Ave.
Slump (in)	1.5			1.75			1	0.75	1.25
Air (%)	6.8			7.2			5.8		
w/cm Ratio	0.48	0.45	0.47	0.47	0.45	0.46	0.48	0.43	0.46
Unit Weight (lbs/ft^3)	150	146	148	150	149	149.5	150	146	148

To establish the time of set by the penetration test, three mortar specimens were prepared according to ASTM C403, from the concrete used to construct Cell 2. The temperature for one of the specimens was recorded during testing using thermocouples so that the final set time of the specimens could be related to the set time of the slabs through maturity. The results for these tests are summarized in Table 3-68 for each sample. Furthermore, the needle penetration resistance pressure readings for each sample is shown in a graph in Figure 3-100. The average final set time for the three samples was estimated as 9 hours and 24 minutes.

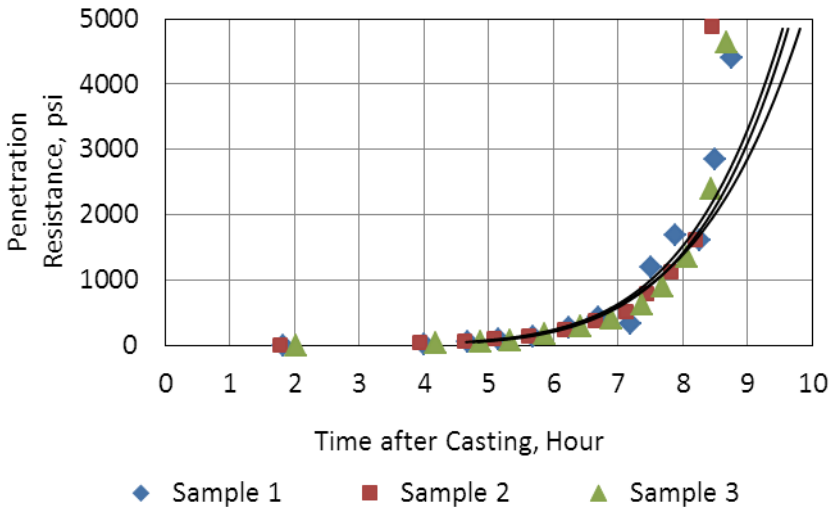

Figure 3-100. Pressure readings from the penetration test for three samples, Project 4.

Table 3-68. The times of initial and final set from the penetration test, Project 4.

Sample Number	Time of Initial Set (Hours)	Time of Final Set (Hours)	Maturity (°F-Hour)
1	6.7	9.3	522.4
2	6.8	9.5	-
3	6.8	9.3	-
Average	6.8	9.4	522.4

Similar to previous projects, the mechanical and thermal properties were established for the PCC used for the construction of Project 4. This was achieved through tests performed in the PMML at the University of Pittsburgh according to the corresponding ASTM standards. The results of only the 28-day testing are provided in this section. More details regarding the results from the testing can be found elsewhere (Nassiri and Vandenbossche 2010).

Table 3-69. Elastic modulus, compressive strength and modulus of rupture established at 28-days in the laboratory for Project 4.

Property	Cell 1	Cell 2	Cell 3	Mean	Standard Deviation
E_c (psi)	4.2E+06	4.45 E+06	4.3 E+06	4.4 E+06	35,000
υ	0.20	0.20	0.21	0.2	0.03
f_c (psi)	4590	5000	5090	4890	160
MR (psi)	850	740	790	790	55

The CTE of the PCC mixture used for Project 4 was measured following the same procedure described fully in Section 3.3.2. One sample was cast from the PCC used to pave each cell. The results of the subsequent tests are summarized in Table 3-70.

Table 3-70. Measured PCC CTE for each cell in Project 4.

Cell Number	CTE (με/ºF)	Mean of CTE (με/ºF)	Standard Deviation (με/ºF)
1	5.4	5.3	0.07
2	5.3		
3	5.2		

The ultimate drying shrinkage for the PCC mixture used for Project 4 was established in the laboratory. Three samples (one at each cell) were cast for measuring the drying shrinkage in accordance with AASHTO T 160/ASTM C 157. The drying shrinkage test results for the samples are presented in Figure 3-101. The results obtained for the ultimate drying shrinkage are very similar between three cells with Cell 3 showing the maximum and Cell 1 the minimum drying shrinkage.

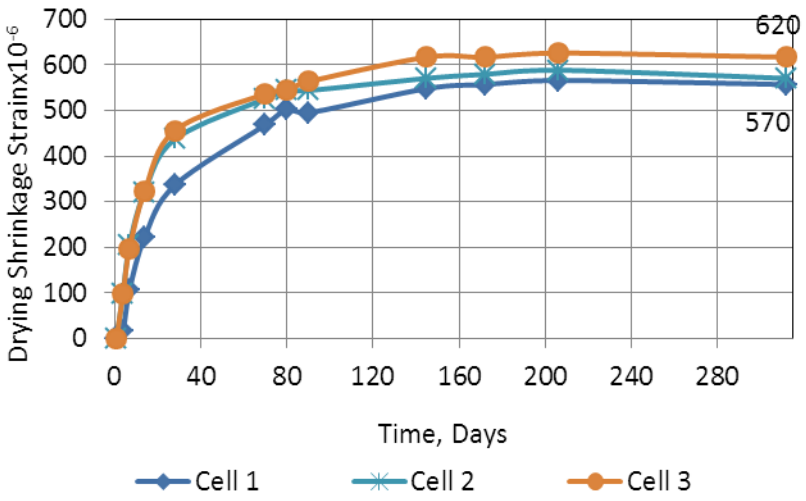

Figure 3-101. Drying shrinkage established in the laboratory for the PCC used for Project 4.

3.6.3 Establishing TZ for Project 4

Similar to the previous projects, strain and temperature measurements in the slab were used to establish TZ for each instrumented slab in Project 4. Strain-temperature graphs were generated for the strain measured in each slab. These graphs are presented in Figure 3-102 to Figure 3-119. A summary of the times of placement, final set and zero-stress is also provided in Table 3-71 to Table 3-76.

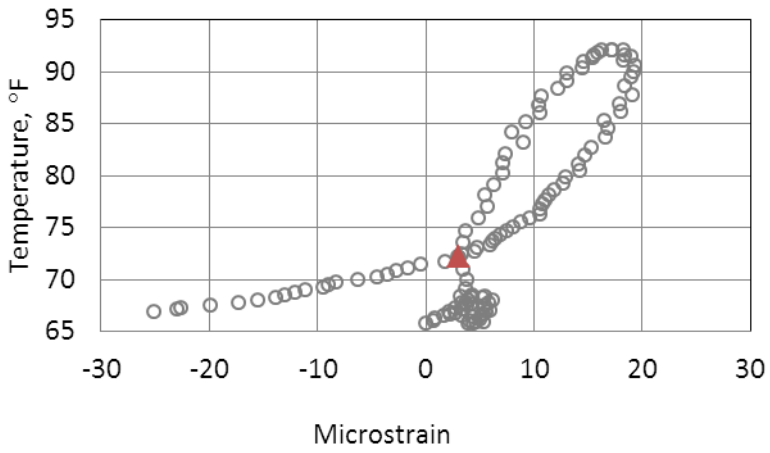

Figure 3-102. Measured Temperature-strain at the top of Slab A, Cell 1, Project 4.

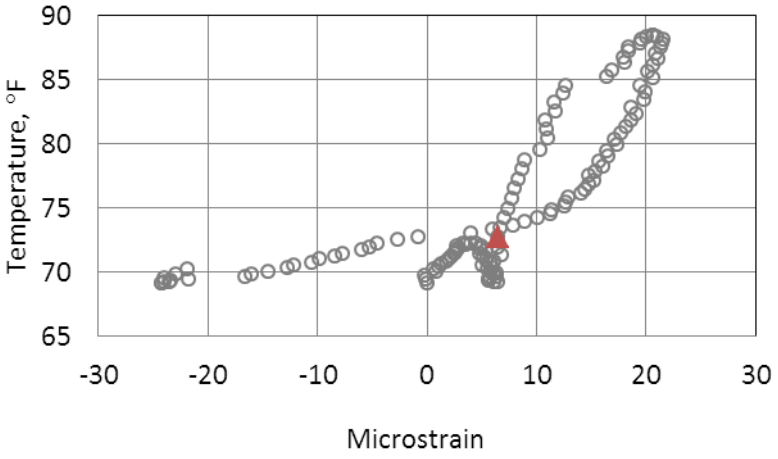

Figure 3-103. Measured temperature-strain at the top of Slab B, Cell 1, Project 4.

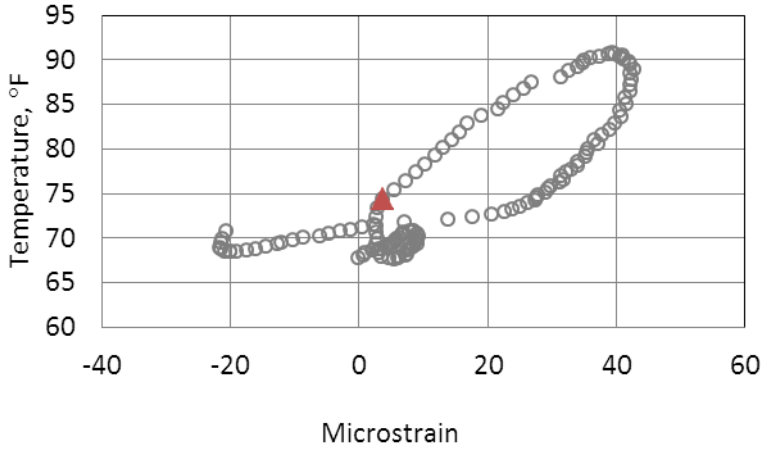

Figure 3-104. Measured temperature-strain at the top of Slab C, Cell 1, Project 4.

Table 3-71. Time of final set and TZ for top of Slabs A, B and C, Cell 1, Project 4.

Slab	Time of Placement	Final Set	TZ
A	2:00 PM	11:45 PM	9:45 AM
B	2:00 PM	11:45 PM	10:15 AM
C	2:00 PM	11:45 PM	10:30 AM

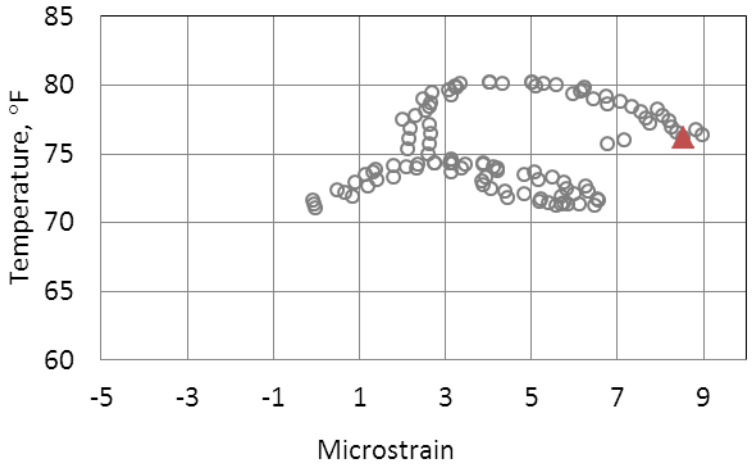

Figure 3-105. Measured temperature-strain at the bottom of Slab A, Cell 1, Project 4.

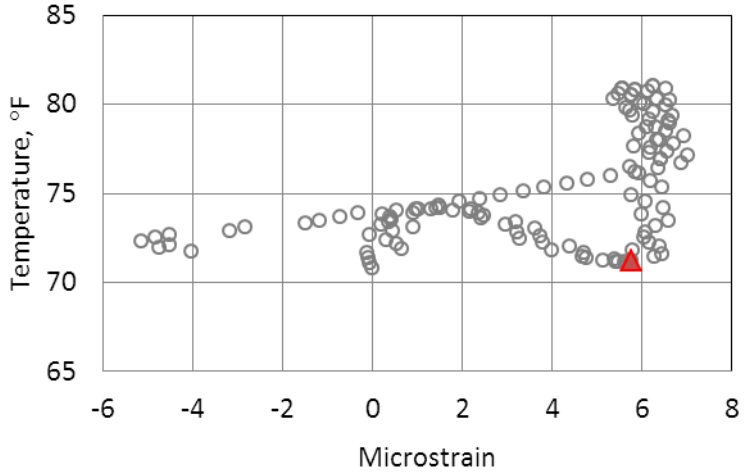

Figure 3-106. Measured temperature-strain at the bottom of Slab B, Cell 1, Project 4.

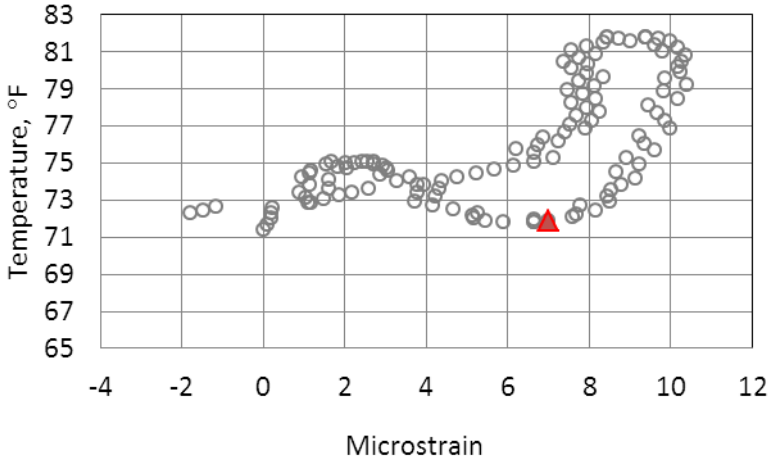

Figure 3-107. Measured temperature-strain at the bottom of Slab C, Cell 1, Project 4.

Table 3-72. Time of final set and TZ for top of Slabs A, B and C, Cell 1, Project 4.

Slab	Time of Placement	Final Set	TZ
A	2:00 PM	11:45 PM	10:30 AM
B	2:00 PM	11:45 PM	10:30 AM
C	2:00 PM	11:45 PM	10:30 AM

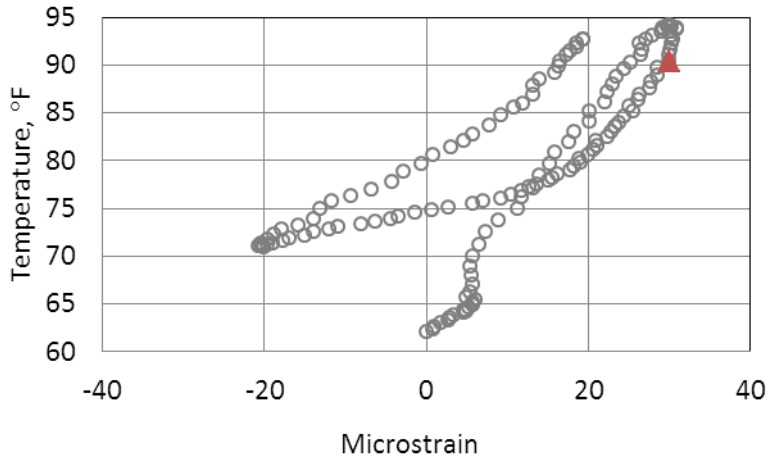

Figure 3-108. Measured temperature-strain at the top of Slab A, Cell 2, Project 4.

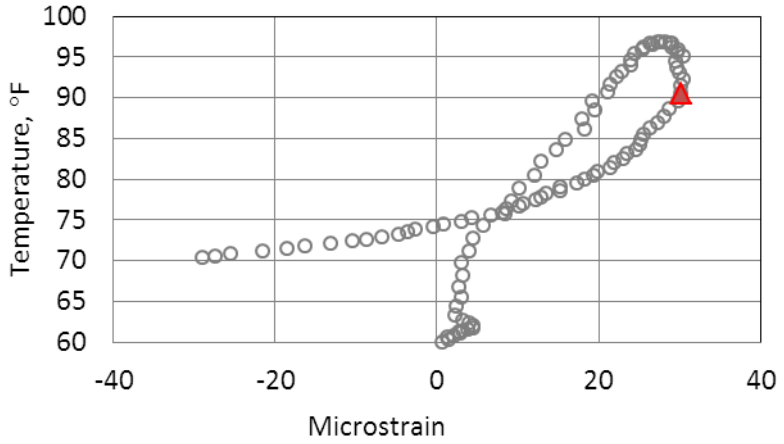

Figure 3-109. Measured temperature-strain at the top of Slab B, Cell 2, Project 4.

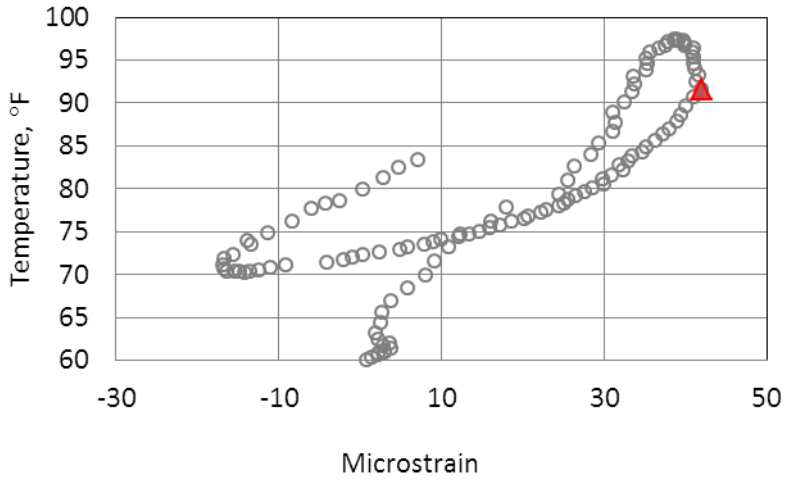

Figure 3-110. Measured temperature-strain at the top of Slab C, Cell 2, Project 4.

Table 3-73. Time of final set and TZ for top of Slabs A, B and C, Cell 2, Project 4.

Slab	Time of Placement	Final Set	TZ
A	5:30 PM	4:45 AM	7:30 PM
B	5:30 PM	4:45 AM	7:30 PM
C	5:30 PM	4:45 AM	7:15 PM

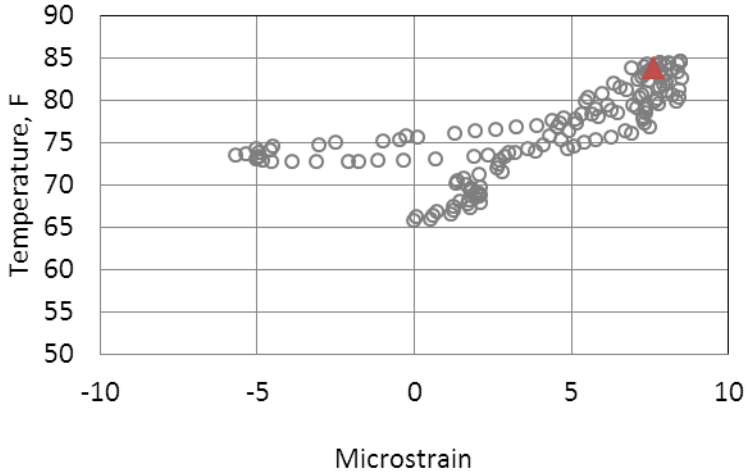

Figure 3-111. Measured temperature-strain at the top of Slab A, Cell 2, Project 4.

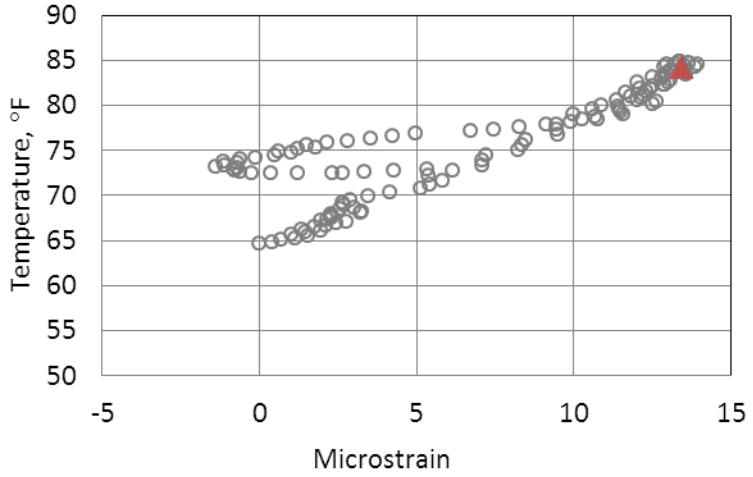

Figure 3-112. Measured temperature-strain at the top of Slab B, Cell 2, Project 4.

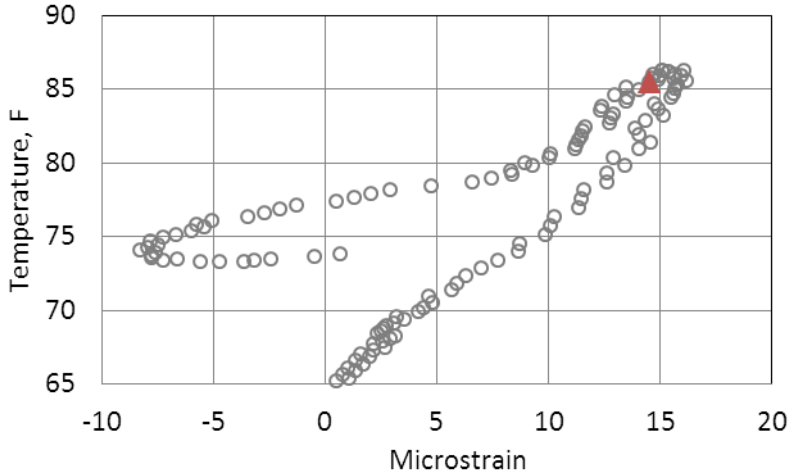

Figure 3-113. Temperature versus strain measured by the top gage in Slab C, Cell 2, Project 4.

Table 3-74. Time of final set and TZ for bottom of Slabs A, B and C, Cell 2, Project 4.

Slab	Time of Placement	Final Set	TZ
A	5:30 PM	4:00 AM	9:15 PM
B	5:30 PM	4:00 AM	9:15 PM
C	5:30 PM	4:00 AM	9:15 PM

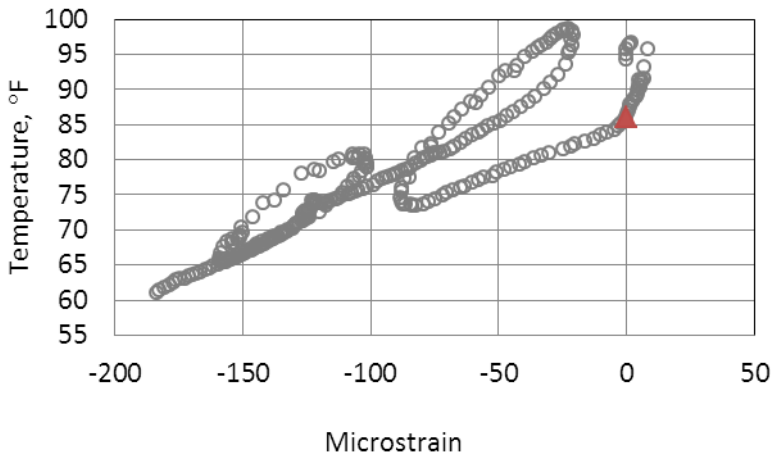

Figure 3-114. Measured temperature-strain at the top of Slab A, Cell 3, Project 4.

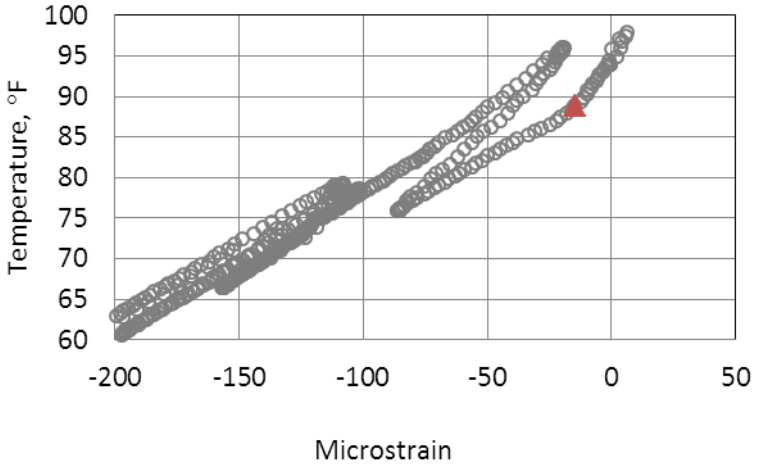

Figure 3-115. Measured temperature-strain at the top of Slab B, Cell 3, Project 4.

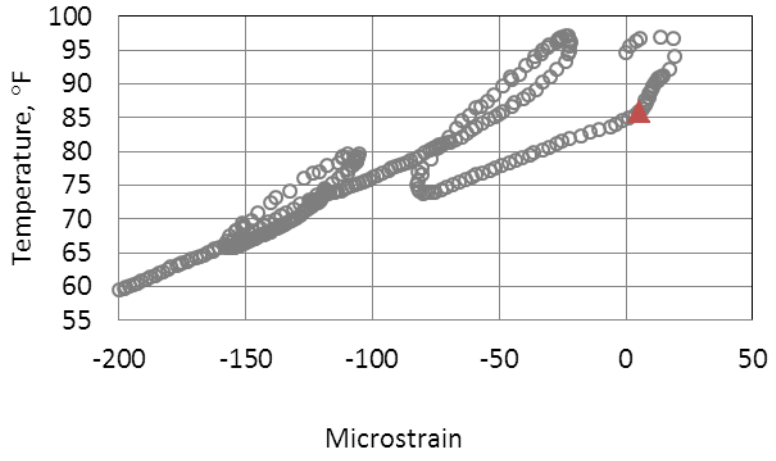

Figure 3-116. Measured temperature-strain at the top of Slab C, Cell 3, Project 4.

Table 3-75. Time of final set and TZ for top of Slabs A, B and C, Cell 3, Project 4.

Slab	Time of Placement	Final Set	TZ
A	8:45 AM	5:00 PM	10:45 PM
B	8:45 AM	5:00 PM	11:15 PM
C	8:45 AM	5:00 PM	11:15 PM

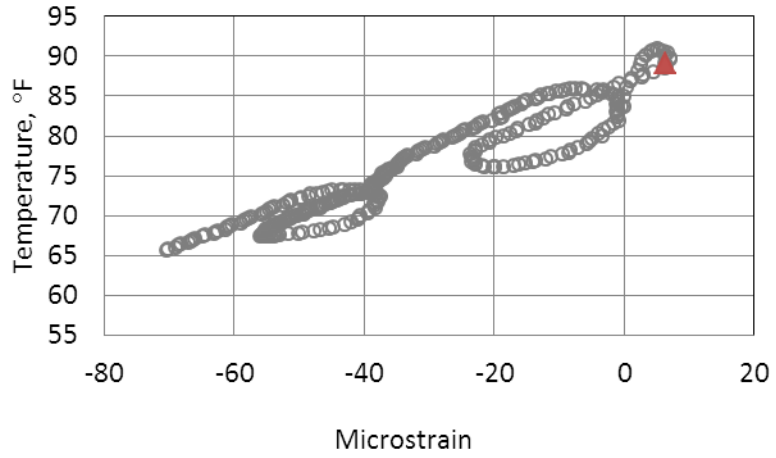

Figure 3-117. Measured temperature-strain at the bottom of Slab A, Cell 3, Project 4.

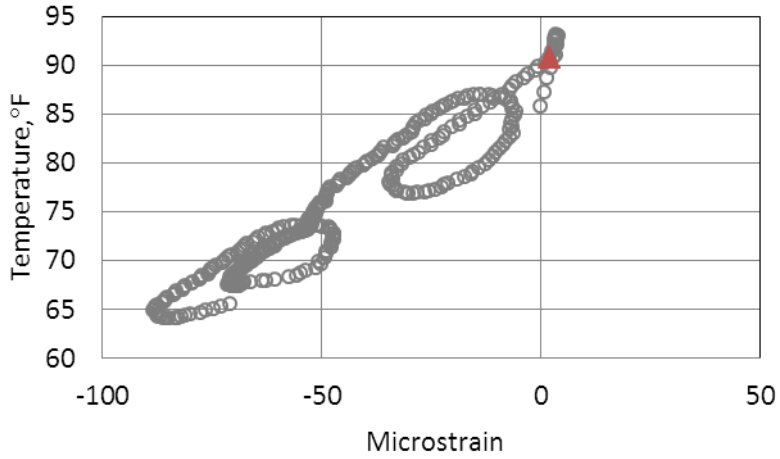

Figure 3-118. Measured temperature-strain at the bottom of Slab B, Cell 3, Project 4.

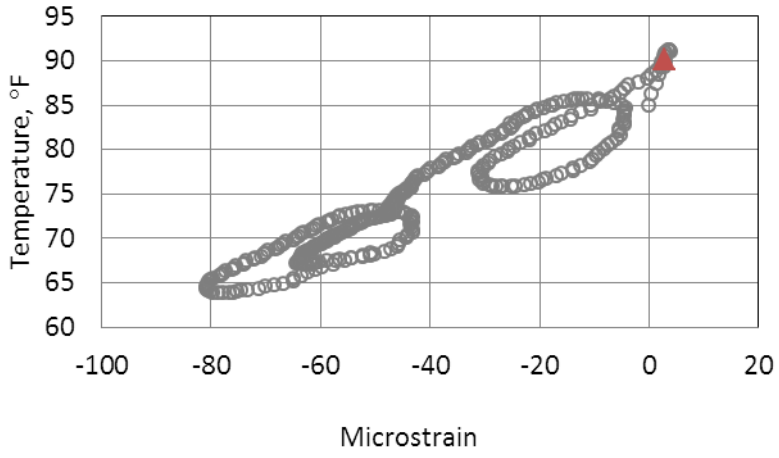

Figure 3-119. Measured temperature-strain at the bottom of Slab C, Cell 3, Project 4.

Table 3-76. Time of final set and TZ for bottom of Slabs A, B and C, Cell 3, Project 4.

Slab	Time of Placement	Final Set	TZ
A	8:45 AM	6:45 PM	11:15 PM
B	8:45 AM	6:30 PM	11:15 PM
C	8:45 AM	6:45 PM	11:15 PM

A summary of the time of placement, final set and TZ was provided in Table 3-71 to Table 3-76 for all the slabs. TZ for the slabs in Cell 1 was reached at 19.75 to 20.5 hours, while this time is equal to at about 25.75 to 28 hours for Cell 2 and for Cell 3 it is from 14 to 14.5 hours.

To investigate the cause of the significant variation seen in TZ across different cells, the temperature variation in slabs is provided in Figure 3-120. It is interesting to note that the ambient temperature is still rising during the construction of the first cell, as seen in Figure 3-120 (a), and is clearly falling at the time of the construction of Cell 2, as seen Figure 3-120 (b). For this reason, the hydration occurred more rapidly in Cell 1 than in Cell 3 during the first day. In other words, the higher ambient temperature accelerated the hydration process for Cell 1 during the first day, while most of the hydration for the slabs in Cell 2 occurred the following day. Therefore, during the second day, the heat of hydration for Cell 2, together with the high daytime ambient temperature, resulted in a higher peak temperature. Cell 3, on the other hand, was paved in the morning of the following day. This cell shows the highest peak temperature as early as 9.5 hours after construction. This is due to the high day-time ambient temperature, which coincided with the peak heat of hydration in this cell.

Also, in Cell 1, the temperature of the slabs is increasing at both the final set and TZ. The temperature of the slab is increasing at the final set and decreasing at TZ for Cells 2 and 3, as was observed for the previous projects.

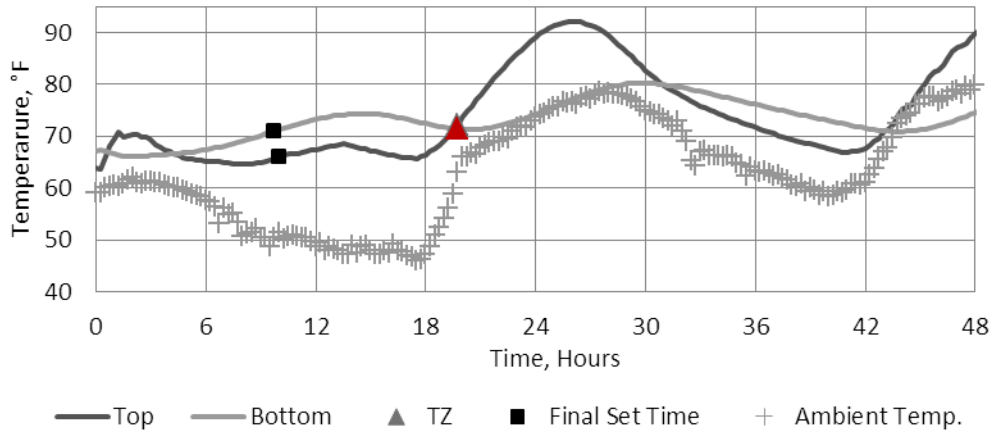

(a)

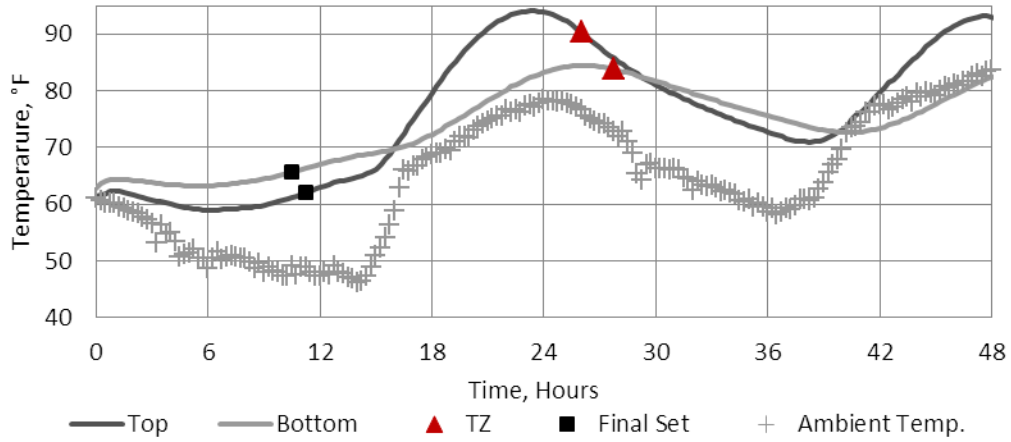

(b)

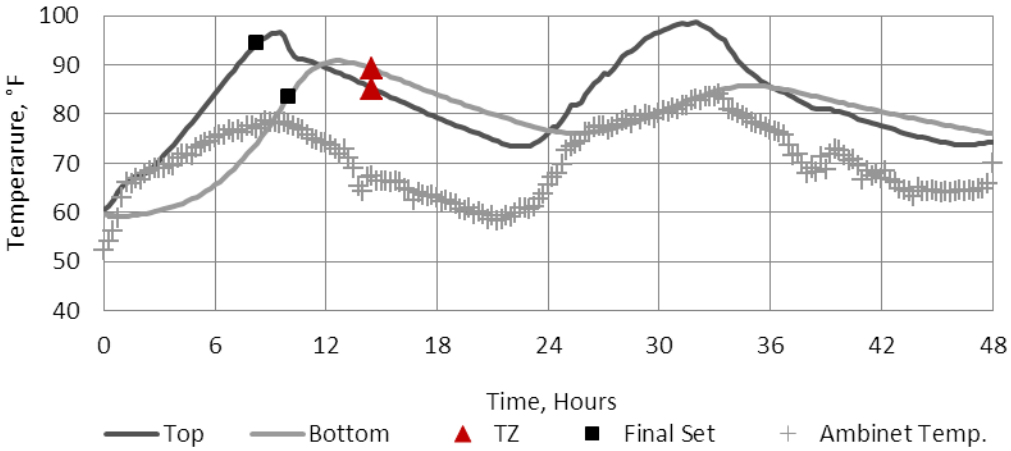

(c)

Figure 3-120. Final and TZ presented with respect to the temperature over time for (a) Cell 1(b) Cell 2 (c) Cell 3

Project 4.

The equivalent age at TZ was estimated for the top and bottom of each slab. This is summarized in Table 3-77. Based on the equivalent age, the degree of hydration was estimated for each instrumented slab. The inputs required by the hydration model are summarized in Table 3-78. The cement composition was obtained from the cement mill sheet and the w/cm ratio of the PCC mixture was measured in the field using the w/cm ratio microwave oven test. Using the input values from Table 3-78, the hydration shape and time parameters and the ultimate degree of hydration was established for the PCC used in each cell. The results are provided in Table 3-77 and Table 3-79.

Table 3-77. Equivalent age at TZ for all the slabs in Project 4.

	Equivalent Age at Tz (Hours)								
	Cell 1			Cell 2			Cell 3		
	Slab A	Slab B	Slab C	Slab A	Slab B	Slab C	Slab A	Slab B	Slab C
Top Gage	17.3	18.9	18.7	27.1	27.1	27.75	19.4	20.1	19.8
Bottom Gage	19.7	19.6	20.3	27.3	27.1	27.7	15.9	16.8	17.0

Table 3-78. Inputs used to estimate the degree of hydration, Project 4.

Parameter	Value
P_{C3S} (%)	59
P_{C3A} (%)	6
P_{SO3} (%)	2.7
Average w/cm Ratio in Cell 1	0.47
Average w/cm Ratio in Cell 2	0.46
Average w/cm Ratio in Cell 3	0.46

Table 3-79. Hydration parameters and the ultimate degree of hydration, Project 4.

Parameter	Value
T	16
B	0.58
Ultimate Degree of Hydration- Cell 1and 2	0.73
Ultimate Degree of Hydration- Cell 3	0.72

Finally, using the input values presented in Table 3-79 and the equivalent ages established for each slab at TZ, the critical degree of hydration was estimated for each slab. This is summarized in Table 3-80 and also presented in the form of a bar graph in Figure 3-121.

Table 3-80. Critical degrees of hydration for all the slabs in Project 4.

	Critical Degree of Hydration								
	Cell 1			Cell 2			Cell 3		
	Slab A	Slab B	Slab C	Slab A	Slab B	Slab C	Slab A	Slab B	Slab C
Top Gage	0.43	0.45	0.44	0.52	0.52	0.52	0.45	0.46	0.45
Bottom Gage	0.46	0.45	0.46	0.52	0.52	0.52	0.41	0.42	0.42

The degree of hydration shows significant variation from cell to cell as seen in Figure 3-121. One factor contributing to this can be the variation in the PCC mixture design used for each cell. The high water content reported for Cell 2 in the batch slip, and also validated by the microwave oven test, could explain the higher degree of hydration reached at TZ in this cell. The water content was report as 180, 194 and 187 lb/yd^3 in Cell 1, 2 and 3, respectively. The measured w/cm ratio was 0.43, 0.52 and 0.45 according to test results performed in the field for Cells 1, 2 and 3, respectively.

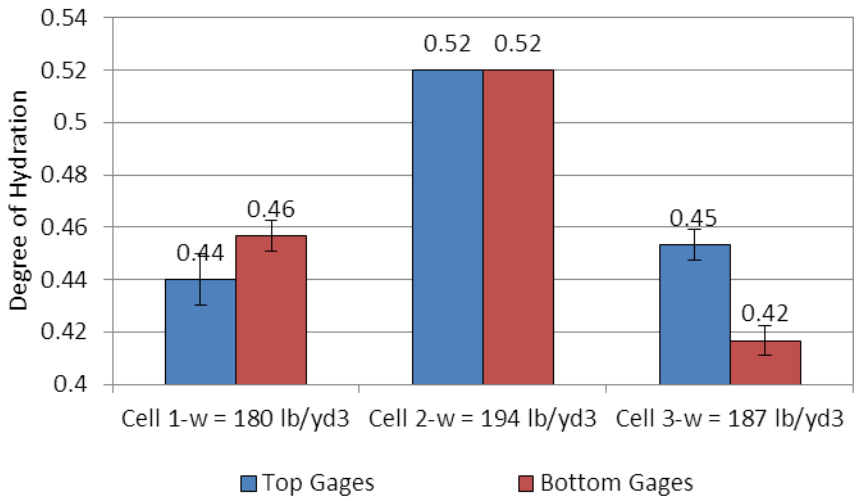

Figure 3-121. Average critical degree of hydration at the top and bottom for each cell, Project 4.

The effect of temperature variation in the sub-layer at TZ was also investigated for the three cells. The base is a CTPB for this project. The stiffness of this material is not expected to fluctuate with changes in temperature as occurs with the ATPB, yet it is beneficial to investigate the trend in temperature of the base with respect to changes in the temperature of the slab. This data is presented in Figure 3-122.

Based on Figure 3-122, temperature changes in the slab in comparison to the base in Cells 1 and 2 show the opposite trend. In these cells, the slab is cooling down while the base is heating up at TZ. In Cell 3, on the other hand, not much variation is noted in the temperature of the base at TZ. This could have contributed to the slabs in this cell to reach TZ earlier at the bottom and later at the top.

Overall the critical degree of hydration is established at between 0.44 and 0.52 at the top of the slabs, while it is established at 0.42 to 0.52 at the bottom of the slabs.

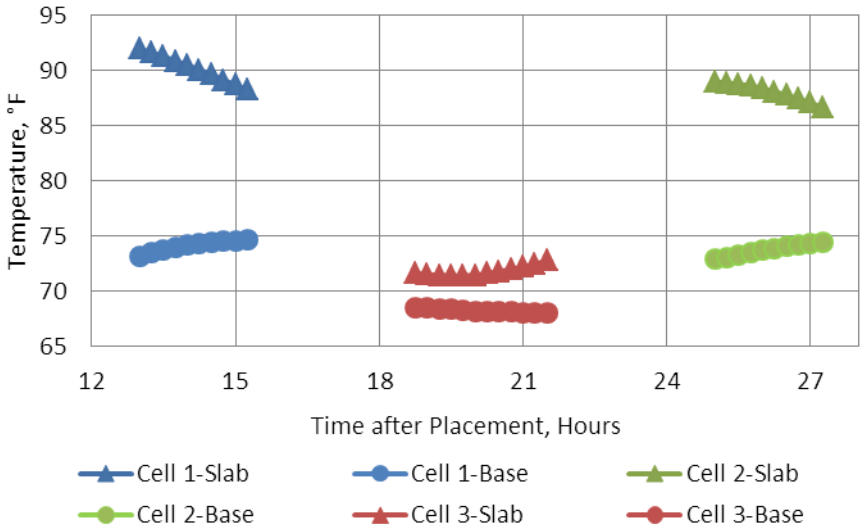

Figure 3-122. Changes in the measured temperature for the slab and the base at TZ in Project 4.

3.7 COMPARISONS OF TZ BETWEEN PROJECTS

Major factors that are significant to the degree of hydration reached in the slabs at TZ include the restraint against slab movement, such as dowel and tie bars, base friction, the PCC mixture and unit weight and slab thickness. Regarding the external restraints, all the four projects had the same dowel and tie bar design. Each pavement structure contained No. 5 epoxy-coated tie bars spaced 30 inch along the longitudinal joints and epoxy-coated 1.5-inch diameter, 18-inch long dowel bars spaced 12 inch on-center along the transverse joint. The base type varied between the projects. Projects 1 and 2 both consisted of ATPB while Projects 3 and 4 both had CTPB layers. The design slab thickness was 12 inch for both Projects 1 and 2, while it was 14 inch for Project 3 and 10 inch for Project 4.

Regarding the PCC mixture, the coarse aggregate was limestone for all of the projects. Fifteen percent of the cement was replaced with Class C fly ash for Projects 1 and 2 and Class F

for Project 3 and 4. Based on the field measurements, the w/cm ratio, varied between projects and also within each project. Furthermore, there was also variation in the type and quantity of chemical admixtures (i.e. air entrainer and water reducer) used between and within projects.

Based on this discussion, since Projects 1 and 2 have a ATPB and Projects 3 and 4 have a CTPB, the critical degree of hydration for Project 1 is compared to that of Project 2. The critical degree of hydration for Project 3 is then evaluated together with that for Project 4. A summary of the major characteristics for all four of the test sections together with the actual time of paving for each cell in each project is provided in Table 3-81. The w/cm ratio in this table is based on the proportioning information provided by the batch slips from the plant. The w/cm ratio established by performing the microwave oven test is provided in parentheses in Table 3-81.

Table 3-81. Pavement characteristics and actual time of construction for each cell, all projects.

Project	Parameter	Cells 1	Cells 2	Cells 3	Base Type	Month of Paving	Slab Thickness (in)
1	w/cm Ratio	0.32 (0.41)	0.35 (0.47)	0.34 (0.48)	ATPB	Sep.	12
	Time of Paving	8:00	10:15	12:00			
	Base Temp. (°F)	100	103	108			
2	w/cm Ratio	0.3 (0.46)	0.32 (-)	0.32 (0.48)	ATPB	May	12
	Time of Paving	8:15	14:45	16:30			
	Base Temp.(°F)	83	89	83			
3	w/c Ratio	0.32 (0.48)	0.32 (0.5)	0.32 (0.48)	CTPB	Oct.	14
	Time of Paving	8:30	12:00	15:45			
	Base Temp.(°F)	83	83	87			
4	w/cm Ratio	0.32 (0.43)	0.35 (0.52)	0.34 (0.45)	CTPB	Apr.	10
	Time of Paving	8:45	14:00	17:30			
	Base Temp. (°F)	83	76	75			

3.7.1 Projects 1 & 2

Within each slab, between the critical degrees of hydration reached at the top versus at the bottom, the lower one was selected as the representative critical degree of hydration for the slab. It is expected that the rest of the slab would follow the portion that has already reached TZ. The results for both projects are presented together in Figure 3-123. According to this figure, Project 1 shows a significantly higher critical degree of hydration than Project 4, especially in Cells 1 and 3. This difference is 7 percent in Cell 1, only 3 percent in Cell 2 and 9 percent in Cell 3. To explain this behavior, the major factors that can influence TZ, and therefore the critical degree of hydration, are reviewed for the two projects.

The first factor that was studied is the PCC mixture design. The w/cm ratio is slightly higher for Cells 1 and 2 for Project 1 than the same cells for Project 2. The w/cm ratio is the same for Cell 3 for Project 1 and Cell 3 for Project 2. This slight difference in the w/cm ratio for the two projects does not explain the trend seen in the degree of hydration. The next factor that was considered was the base temperature. According to Figure 3-48 and Figure 3-72, the base temperature at TZ is about 10 °F lower for Project 2 in comparison to Project 1. This again does not explain the lower critical degree of hydration seen for this project, since the ATPB stiffness increases, thereby providing more frictional restraint.

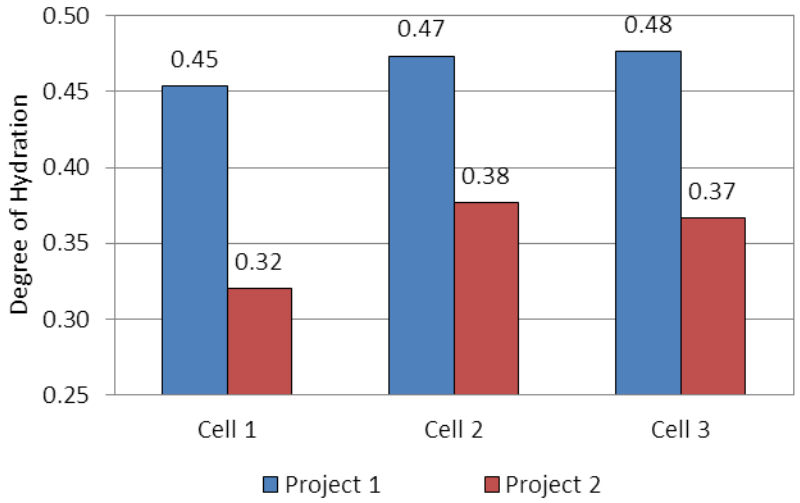

Figure 3-123. Critical degree of hydration for each cell for Project 1 and Project 2.

Another factor that should be considered is slab thickness. The thicker slabs in Cell 2 for Project 2, might overcome the effects of a lower w/cm ratio for this cell as compared to the same cell in Project 1. In the case of Cell 3, the slabs from the two projects had the same w/cm ratio, so the 1-inch increase in slab thickness in Project 1, could have resulted in an increase in the friction at the base interface and therefore a later TZ. Slabs in Cell 1 for both projects had the same thickness.

Self-weight of the slab is another factor that can result in higher levels of friction at the base interface. The PCC mixture used for Project 1 was slightly denser than the one used to pave Project 2. The measured unit weight for Cell 1, 2 and 3 was established as 152 lb/ft^3 for Project 1 while it was established as 146 lb/ft^3, 150 lb/ft^3, and 148 lb/ft^3 in Cell 1, 2 and 3, respectively, for Project 2.

The mortar sample used to establish final set time for Project 1 reached a higher maturity at final set when compared to Project 2 (535 °F-Hour vs. 400 °F-Hour.) Therefore, it appears that the difference in TZ seen for both project should be sought in the PCC mixture properties

rather than structural properties of the two sections. This possible variation in the PCC mixture was not reflected in the PCC mixture design sheets for the projects and therefore the cause cannot be concluded. Overall, the critical degree of hydration varied between an average range of 0.35 and 0.47 for the two projects with the ATPB layer.

In the end, it should be noted that the difference seen between the critical degrees of hydration established for Project 1 in comparison to Project 2 is not expected to result in significant changes in the built-tin temperature gradient and consequently the design slab thickness. This will be investigated in more detail in Chapter 7.

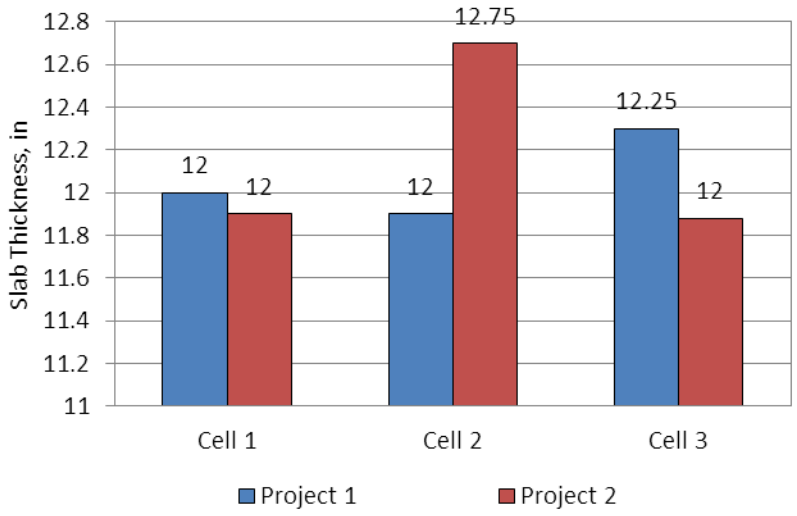

Figure 3-124. As-built slab thickness in each cell for Project 1 and Project 2.

3.7.2 Projects 3 & 4

According to Figure 3-125, Project 3 shows a higher critical degree of hydration than Project 4. This could simply be explained through the fact that the slabs in Project 3 are significantly thicker than the slabs in Project 4. This is summarized in Figure 3-126.

Additionally, according to Table 3-81, the w/cm ratio for the PCC used on Project 3 was higher than that for the PCC used for Project 4. This could be an additional explanation for the trend seen in the critical degree of hydration for the two projects.

Overall, the average critical degree of hydration for 14-inch slabs with a CTPB was established at 0.51. This value was established as 0.45 for the 10-inch slabs with the same base material.

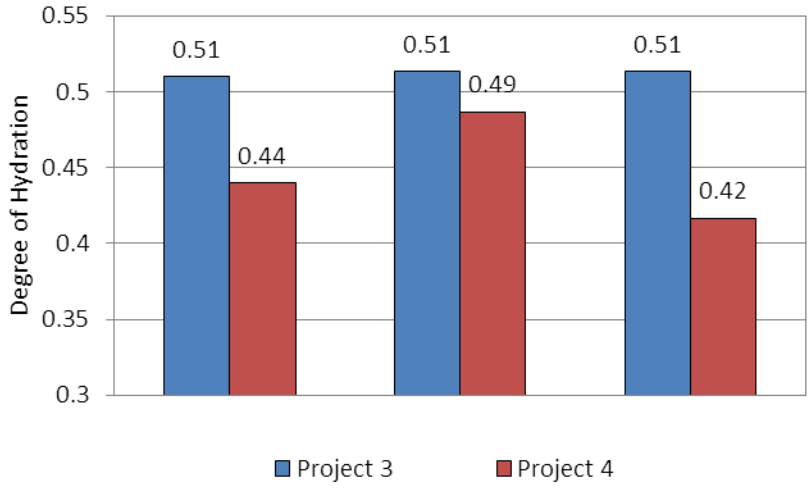

Figure 3-125. Critical degree of hydration in each cell for Project 3 and Project 4.

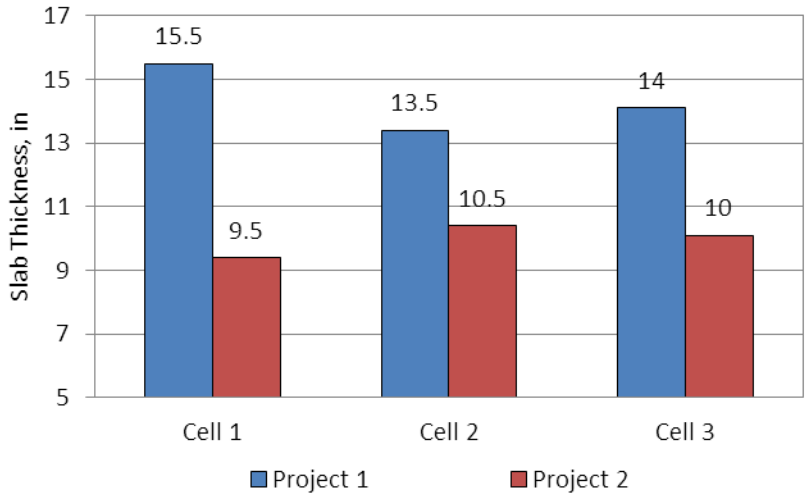

Figure 3-126. As-built slab thickness in each cell for Project 3 and Project 4.

3.8 COMPARISON OF LOCATION OF NEUTRAL AXIS FOR ALL PROJECTS

The neutral axis was established previously in Section 3.3.3, for Cells 1, 2 and 3 on Project 1, based on the strain-temperature behavior in the slab. The location of the neutral axis in terms of percent of slab thickness is provided again in Figure 3-127. The same procedure was followed to identify the location of the neutral axis for the cells in Project 2. The results are superimposed on Figure 3-127 for comparisons. Based on the figure, the location of the neutral axis for the two projects is relatively consistent and varies between 50 and 65 percent of the slab thickness.

The changes in the location of the neutral axis with time can also be investigated for Project 1. The data collection period for Project 2, however, does not provide a sufficient number of strain-temperature loops to investigate the time-dependent behavior of the pavement with respect to the location of the neutral axis. Based on the figure, one can conclude that the location of the neutral axis is relatively consistent with time. A slight upward growth toward the

slab surface is seen in the location of the neutral axis for all cells in Project 1. The possible cause of this behavior could be the growth in the stiffness of the slab over the few days after construction. As the stiffness of the slab increases with time, the governing effects of the stabilized base on the location of the neutral axis can become less influential.

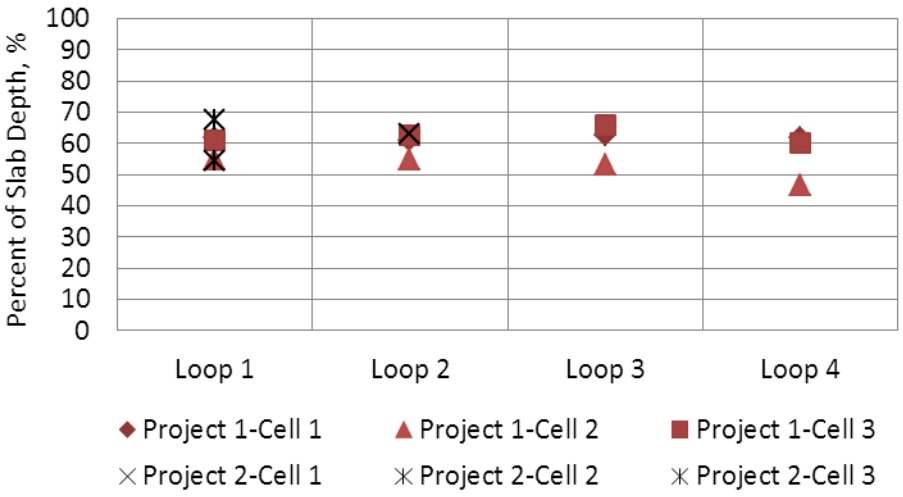

Figure 3-127. Location of neutral axis Projects 1 and 2 with the ATPB.

Following the same procedure, the location of the neutral axis was also established for Projects 3 and 4 with the CTPB layer. The respective results are presented in Figure 3-128 for both projects. It is apparent based on Figure 3-128 that the location of the neutral axis is closer to the bottom of the slab for Project 3 in comparison to Project 4. The only factor between the two projects that can explain this behavior is slab thickness. For Project 3, slab thickness varied between 15 and 16.5 inch while it was between 9 and 10 inch for Project 4. The thicker slabs, resulting in more friction between the slab and the base seem to be pulling the neutral axis closer to the bottom of the slabs in Project 3. Overall, the neutral axis for Project 4, with the thicker slabs, is established very close to the bottom of the slab, while the neutral axis for Project 3, with

the thinner slabs, is established at almost mid-depth. The difference between the effects of the CTPB versus the ATPB layers on the location of the neutral axis cannot be identified, since the slabs are constructed with different thicknesses.

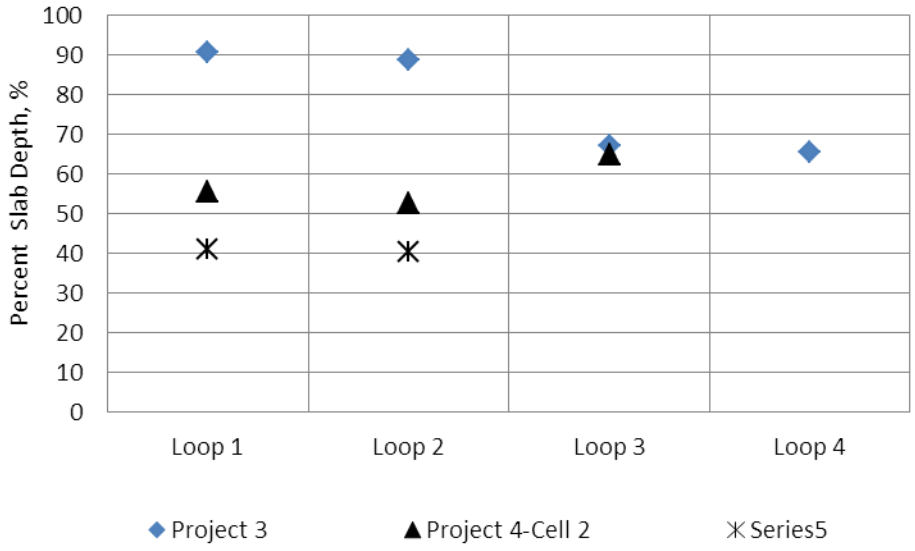

Figure 3-128. Location of neutral axis Projects 3 and 4 with the CTPB.

4.0 CHAPTER 4-ESTABLISHING $\Delta T_{built\text{-}in}$

Zero-stress time was established for each instrumented project in the previous chapter. In this chapter, the temperature measured across the depth of each slab is used to establish the ELTG at TZ. The possibility of occurrence of relaxation in $\Delta T_{built\text{-}in}$ due to creep at early ages will also be investigated in this chapter.

4.1 $\Delta T_{built\text{-}in}$-PROJECT 1

Geographic location, design features and the PCC mixture design for this project were discussed in detail in Section 3.3.1. TZ was established based on the changes in the strain with changes in temperature in the slab. The critical degree of hydration was estimated as 0.45, 0.47 and 0.48 for Cells 1, 2 and 3, respectively. The temperature measured throughout the depth of the slab at midslab for both Slabs A and C will be used in this section to establish the $\Delta T_{built\text{-}in}$. The temperature measured at TZ in Slabs A and C in each of Cells 1, 2 and 3 is presented in Figure 4-1. Temperatures corresponding to the two slabs in the same cell are represented by the same color in this figure. As seen in Figure 4-1, the temperatures for the two slabs in each cell are similar and follow the same trend. These temperature measurements are used to estimate the equivalent linear temperature gradient, (referred to as the ELTG, hereafter.) The Janssen-Snyder method presented previously in Equations 2-12 to 2-14 was used for this purpose. The ELTG at

TZ was estimated using both measurements in Slabs A and C. The subsequent results are provided in Table 4-1. The time of paving for each cell is also included in Table 4-1. The average of the temperatures measured in Slabs A and C were used to estimate the temperatures for Slab B within each cell.

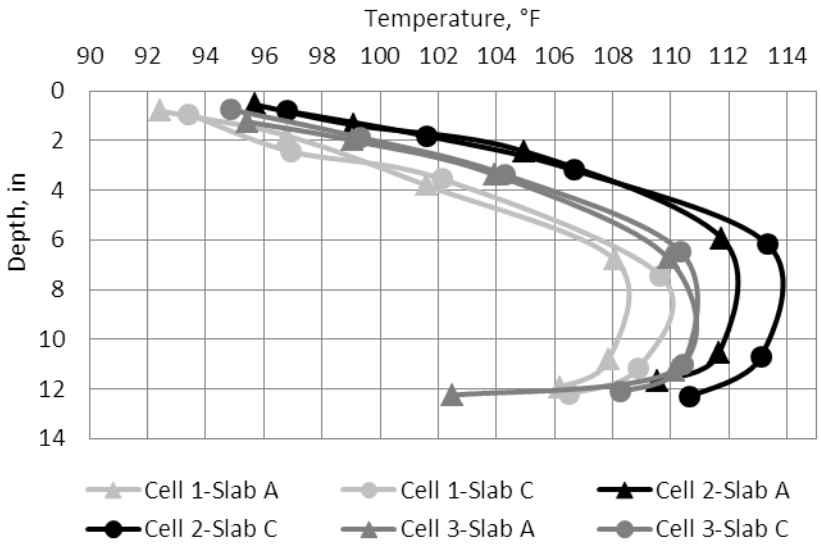

Figure 4-1. Temperature measured at TZ along the depth of the slabs in each cell for Project 1.

Table 4-1. ELTG established at TZ based on measured temperature for each cell for Project 1.

Slab No.	ELTG in each Cell (°F/in)		
	Cell 1- Paved at 8:00 AM	Cell 2- Paved at 10:15 AM	Cell 3- Paved at 11:30 AM
A	-1.0	-1.0	-0.9
C	-1.2	-1.0	-0.9
Average	-1.1	-1.0	-0.9

According to Table 4-1, the $\Delta T_{built\text{-}in}$ established for three cells for Project 1 are quite similar, especially between Cells 1 and 2. This was expected, because the time of paving for the

three cells was exceptionally close in this project. As presented in Table 4-1, Cell 1 was constructed at 8:00 AM, Cell 2 at 10:15 AM and Cell 3 at 11:30 AM.

4.1.1 Evaluation of Possible Effects of Early-Age Creep

As discussed previously, the $\Delta T_{built\text{-}in}$ can be affected by the early-age creep relaxation. To be able to investigate the role of creep in the slabs, the curvature was estimated for each slab using the measured strain at the top and bottom of the slabs. The relation provided in Equation 4-1 was employed to estimate the curvature for the slabs. This equation was derived simply based on the geometry of the curled slab. In this equation, negative curvature represents downward curling and positive curvature represents upward curling.

$$\rho = -\frac{\varepsilon_t - \varepsilon_b}{D(1+\varepsilon_t+\varepsilon_b)} \quad (4\text{-}1)$$

where, ρ = Curvature, 1/ft

ε_t = Strain measured at the top of the slab,

ε_b = Strain measured at the bottom of the slab,

D = Distance between the gage installed at the top and bottom of the slab, established by surveys performed pre- and post-construction of the slabs, ft

The following assumptions were made while deriving the above equation (Asbahan 2009): (a) the slab is elastic, homogenous and isotropic, with temperature-independent material properties; (b) plane sections remain plane after bending; (c) stresses and strains in the vertical direction are zero; (d) the deflection of the slab is small compared to the slab dimensions; and (e)

temperature and shrinkage strains vary in the vertical direction only (Mohamed and Hansen 1997).

When using Equation 4-1, the measured strain was corrected for the difference between the CTE of concrete and the CTE of the steel wire in the gage. The respective relation is provided in Equation 4-2.

$$\varepsilon_{Mechanical} = (R_1 - R_0)\, B + (T_1 - T_0)\,(\alpha_s - \alpha_c) \qquad (4\text{-}2)$$

This strain has been referred to as the "mechanical strain" in literature (Burnham and Koubaa 2001). The mechanical strain is of more interest when studying the effects of environmental loads on the slab. $\varepsilon_{Mechanical}$ is mainly the length-change in the slab due to drying shrinkage and creep. When using Equation 4-2, one should note that, it is assumed that the expansion/contraction of the slab due to temperature changes is equal to the temperature change in the slab multiplied to the CTE of the slab. While this assumption only holds for a free slab. An in-service slab is restrained by the base and is not free to completely deform due to temperature changes. This can result in over- or underestimation of drying shrinkage strains in the slabs.

In this section, the curvature was estimated for all slabs in each of the cells for Project 1. As mentioned earlier, the time of placement was very similar for cells in Project 1, hence the behavior of the slabs, in terms of curvature, was the same in all cells. The drying curvatures, estimated for the three slabs in Cell 2 based on the mechanical strain from Equation 4-2, are presented in Figure 4-2, as examples. Primary point to elaborate about Figure 4-2 is the rather large daily fluctuations seen in the drying curvature. Since moisture diffuses quite slowly in concrete, variation in the daily drying curvature was expected to be negligible. One way to

investigate the significance of the fluctuations seen in the drying curvature in Figure 4-2, is through making comparisons with the thermal curvature in the slab. Thermal curvature is due to different uniform temperature changes at the top with respect to the bottom of the slabs. The estimation of the thermal strain was made using the following relation:

$$\varepsilon_{thermal} = (T_1 - T_0) \times \alpha_c \qquad (4\text{-}3)$$

The resulting thermal curvature together with the ELTG for the slabs on Cell 2 is superimposed to Figure 4-2 for comparisons. Based on this figure, it is apparent that the fluctuations seen in the drying curvatures are significantly smaller than the fluctuations seen in the thermal curvatures.

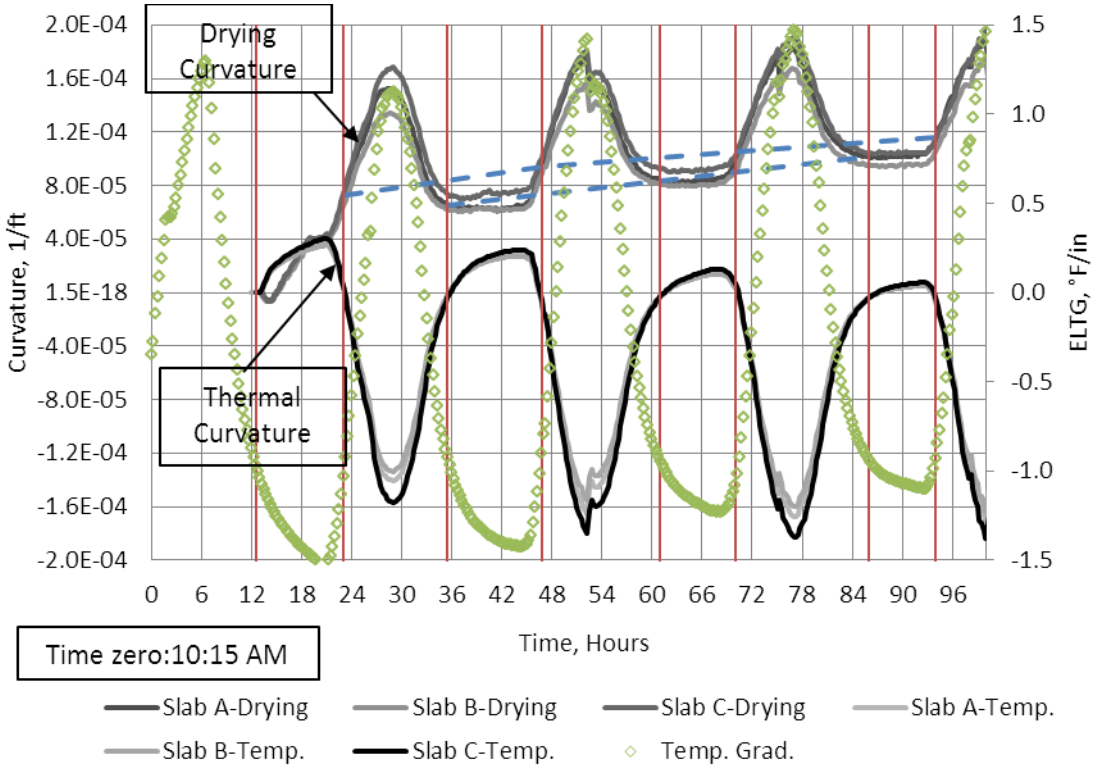

Figure 4-2. Estimated drying and thermal curvatures for slabs in Cell 2, Project 1.

As seen in Figure 4-2, all of the slabs in Cell 2 show an upward curvature over the entire time. This is an indicator of the occurrence of drying shrinkage and rapid evaporation at the surface of the slabs due to the hot and sunny weather conditions. It is also noticed that the slabs are accumulating an upward curvature as the concrete ages.

According to Table 4-1 and Figure 4-2, the built-in temperature gradient established for the slabs on Cell 2 has a negative value, -1.0 °F/in, meaning that a positive built-in curl has locked into the slab. This implies that at any time following TZ, when the transient ELTG in the slab is equal to the built-in temperature gradient (referred to as the "critical times" hereafter,) the slabs will be flat. However, as seen in Figure 4-2, due to drying shrinkage, the slab never becomes flat again after TZ. Since the creep mechanism can relax a portion of the built-in curl in the slab, it is expected that the slabs show a smaller upward curvature at each critical time when compared to the previous critical time.

The critical times for the slabs in Cell 2 are represented by the red vertical lines in Figure 4-2. According to this figure, two critical times occurred during each 24-hour period, one during the day and the other during the night. Two separate lines, the blue dashed lines in Figure 4-2, were used to connect the curvatures at the day critical times and the curvatures at the night critical times. These lines were separated to account for the effects of daily temperature fluctuations on curvature. As seen in Figure 4-2, the upward curvature increases progressively from one red line to the other. This increase in the upward curvature is again attributed to drying shrinkage that occurs in the slabs over time. The effects of creep on the built-in gradient, if any exists, is masked by the ever-increasing drying shrinkage and thereby can not be quantified based on the behavior of the slab presented in Figure 4-2.

General Concerns Regarding Early-Age Creep

It should be mentioned here that the same type of analysis will be followed for the other three instrumentation projects in the later sections of this chapter to investigate the possible effects of creep on the built-in gradient. A comprehensive review was provided in Section 2.4 of this study on the theoretical models that are currently available to estimate the early-age creep in concrete. The model developed originally by Bazant (Bazant and Chern 1985), known as the Triple Power Law, and recalibrated later by Emborg and Westman (Westman 1999) for early-age loading, known as the Extended Triple Power Law, has been very well known as the most robust model available for estimating the early-age creep in concrete.

This model, however, was not able to be utilized in this study due to multiple reasons. First, the state of stress for the Extended Triple Power Law model is compression, while in the case of a pavement, flexural stresses develop in the slab due to moisture and temperature gradients. A few studies that consider tensile creep in concrete at early ages were also discussed in Section 2.4. The number of studies performed on this topic is limited and the results of the studies that have been performed are contradictory.

The second factor that makes estimating the early-age creep in concrete slabs a very challenging task to do is the frequent changes in the level of stress due to changes in the temperature gradients that exist in the slab. The magnitude of the stress also varies at different locations of the slab due to different support and restraint conditions.

The proper way to approach this problem would be an analysis using a step-by-step finite element method that estimates the stress history in the entire slab as a series of discontinuous increments. The creep can then be estimated at every time step and for every space node based on the current stress level to modify the previously estimated strain at that time step. This model

can be validated by the use of strain measurements in the slab, like the ones provided in Figure 4-2 for Project 1.

4.2 $\Delta T_{built\text{-}in}$-PROJECT 2

For Project 2, similar to the previous project, temperature was measured throughout the depth of Slabs A and C in each cell. TZ was established for the slabs in this project in Section 3.4.3. The temperature measured at TZ was used to establish the $\Delta T_{built\text{-}in}$. These temperatures are presented in Figure 4-3 for all three cells. The temperatures for the two slabs in each cell do not completely agree, especially at the top. To select the correct temperature for each cell, the temperatures measured using the thermistor within each VW in Slabs A and C were superimposed in Figure 4-3. Based on Figure 4-3, temperatures for Slab C in Cells 1 and 2 and Slab A in Cell 3 correspond with the strain gage thermistor readings and therefore will be used to establish $\Delta T_{built\text{-}in}$. The temperature measured in Slab C of Cells 1 and 2 will be used to establish the built-in gradient at TZ in Slabs A and B and the temperatures measured in Slab A of Cell 3 is used for Slabs A and B in Cell 3. In doing so, the ELTG at TZ was estimated for each cell using the Janssen-Snyder method. The subsequent results are provided in Table 4-2. According to this table, a distinct difference is noticeable between the $\Delta T_{built\text{-}in}$ established for Cell 1 in comparison to that established for Cells 2 and 3. This difference can be explained by considering the difference in the time of paving for each cell. As seen in Table 4-2, Cell 1 was paved in the morning while the other two cells were paved in the afternoon and within one hour from each other.

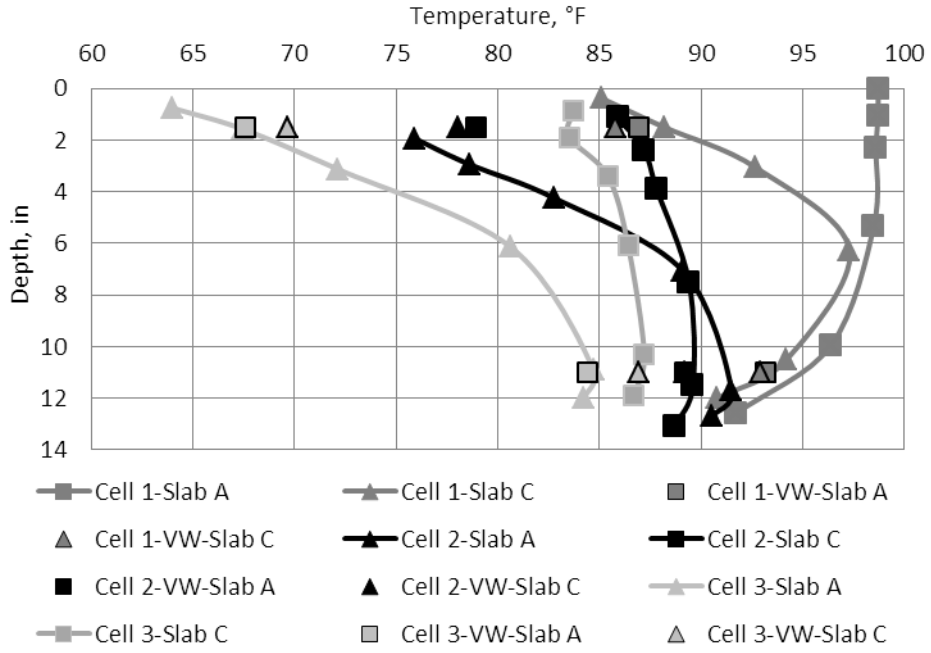

Figure 4-3. Temperature measured along the depth of the slab at TZ in Project 2.

Table 4-2. ELTG estimated at TZ based on measured temperature for each cell in Project 2.

Slab No.	ELTG (°F/in)		
	Cell 1 Paved at 8:15 AM	Cell 2 Paved at 3:00 PM	Cell 3 Paved at 4:30 PM
A	-0.5	-1.0	-1.7
C	-0.5	-1.0	-1.7

The possible relaxing effect of the early-age creep on the permanent curling was investigated for the slabs in Project 2 for the first 72 hours after paving. This was performed by following the same analysis as that used for Project 1. The drying curvature is presented in Figure 4-5, Figure 4-6 and Figure 4-7 for Cells 1, 2 and 3, respectively.

It is interesting to note the magnitude of the curvature for the slabs in Project 2 with respect to the curvatures seen previously for the slabs in Project 1. When comparing Figure 4-5 to Figure 4-2, it is noticed that the magnitude of the curvature seen for the slabs for Project 2 are

almost half of that for the slabs for Project 1. This behavior is easily explained by considering the overcast and humid weather conditions present for Project 2 starting from 24 hours after construction and continuing thereafter. This can be seen in Figure 4-4.

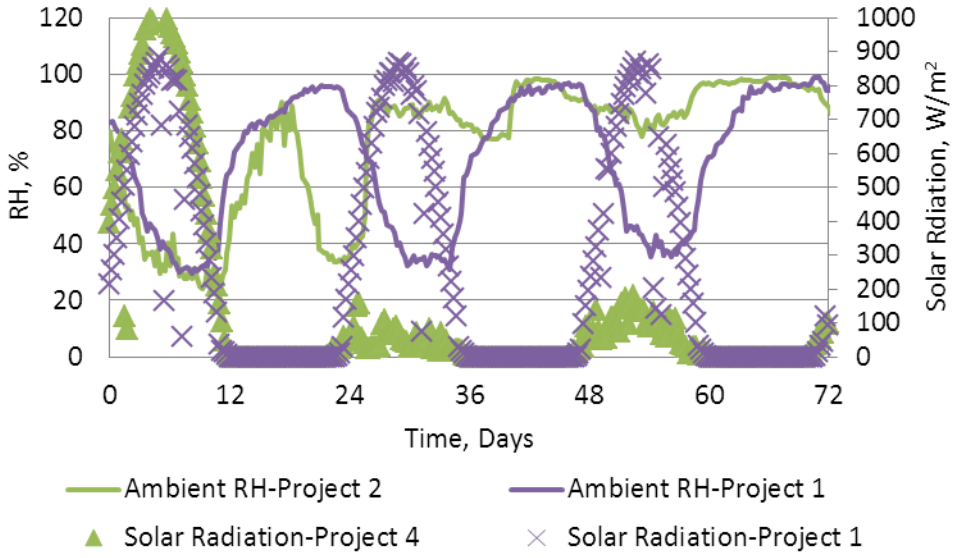

Figure 4-4. Ambient RH and solar radiation for Projects 1 and 2 over the first 3 days after construction.

Furthermore, when comparing the curvatures in between the three cells in Project 2, almost the same magnitude of drying curvature is seen for all cells. It must, however, be mentioned that, the curvature for the slabs on Cell 3 is consistently slightly, 10 to 20 percent, larger than the curvature of the slabs in Cells 1 and 2.

To quantify the magnitude of the drying curvature with respect to the thermal curvature, the thermal curvature was also estimated for the slabs for Cell 1 and is superimposed to Figure 4-5. Based on this figure, during the first 40 hours after construction, the large ELTG present in the slabs resulted in a large upward thermal curvature. At age 40 hours, the thermal and drying curvatures reach the same magnitude. Between ages 40 and 54 hours, the ELTG in the slab

changes by only about 0.4 °F/in. During this period of time, the changes in the thermal curvature and the drying curvatures are almost equal.

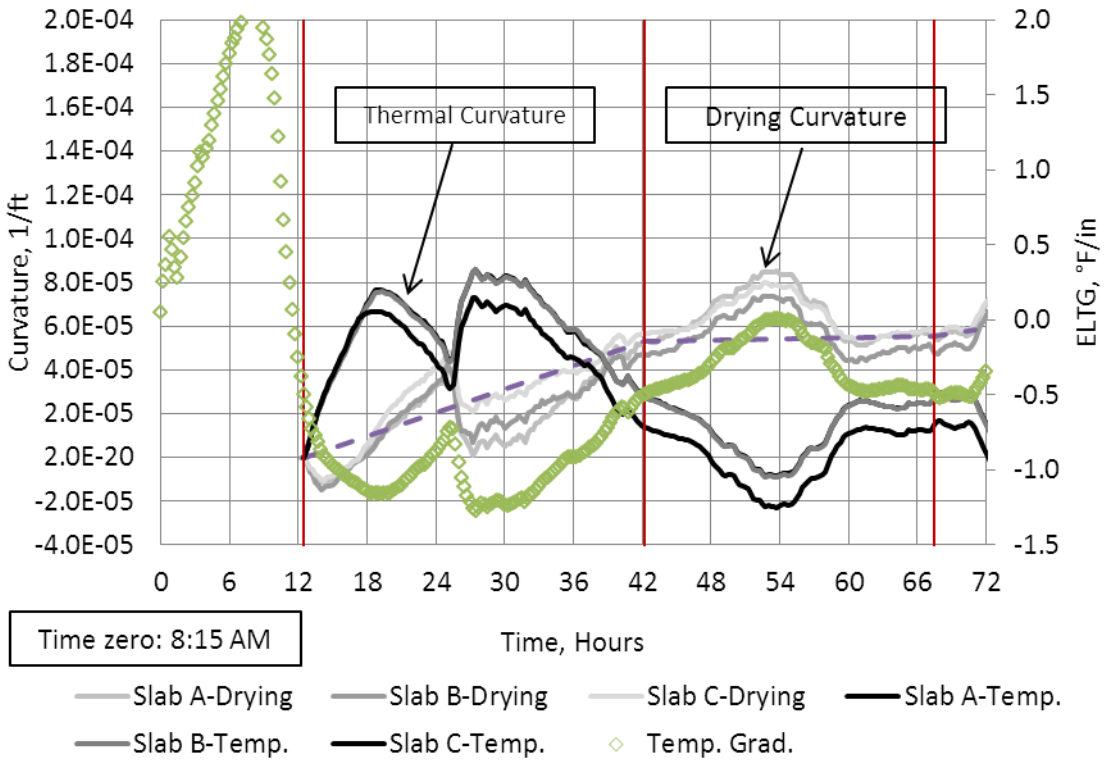

Figure 4-5. Estimated curvature due to drying shrinkage and possible creep for slabs in Cell 1, Project 2.

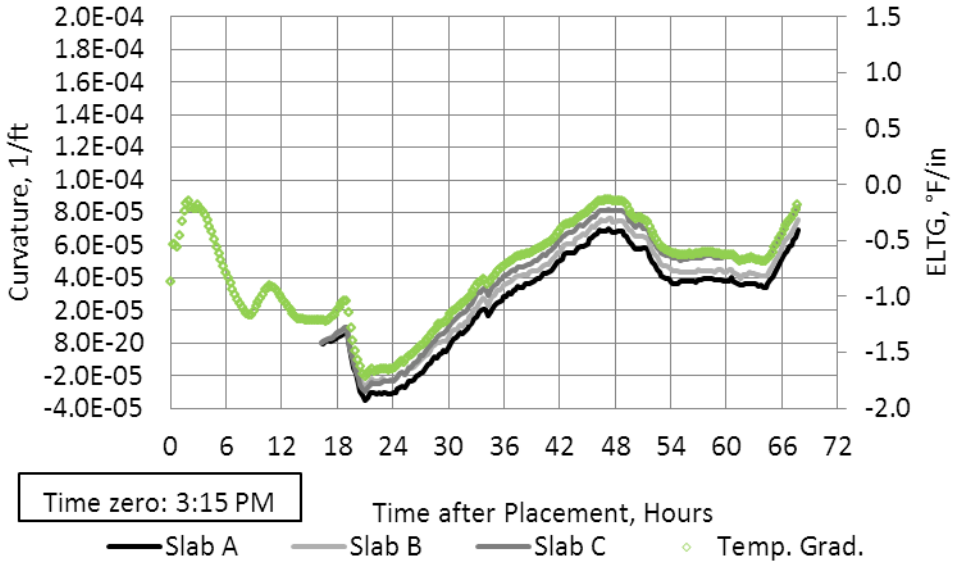

Figure 4-6. Estimated curvature due to drying shrinkage and possible creep for slabs in Cell 2, Project 2.

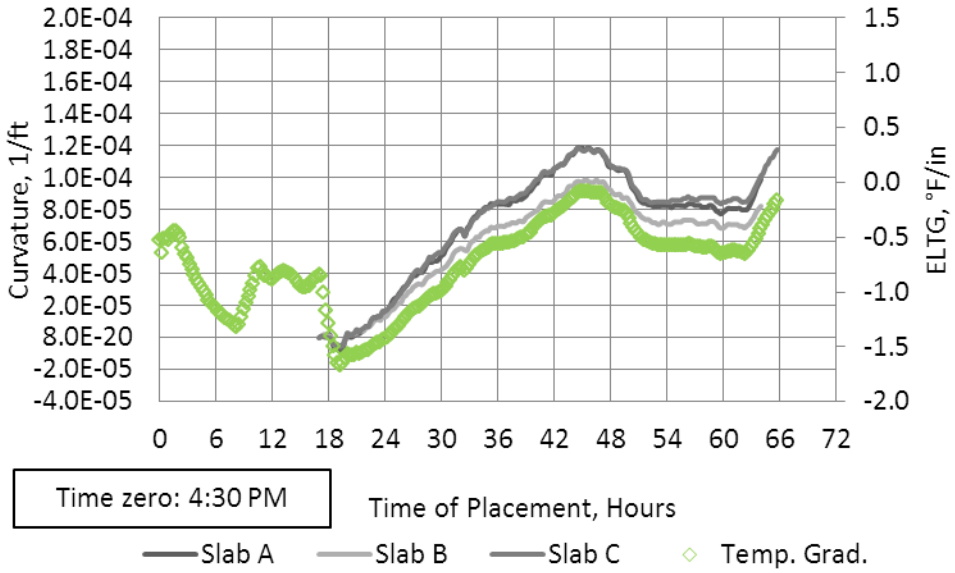

Figure 4-7. Estimated curvature due to drying shrinkage and possible creep for slabs in Cell 3, Project 2.

Based on Figure 4-5, the built-in temperature gradient at TZ, as also seen in Table 4-2, is approximately -0.5 °F/in. It is anticipated that the tensile creep reduces a portion of this positive permanent curling that has locked into the slabs at TZ. Therefore, a reduction is expected in the

upward drying curvature at the critical times as the concrete ages. Drying shrinkage can mask the effects of creep on the built-in gradient. Among the three cells for Project 2, Cell 1 has the least increasing drying curvature over time and was therefore selected for the creep analysis.

In Figure 4-5, similar to Figure 4-2 for Project 1, the critical times are represented by red vertical lines. The slab exhibits an upward curvature at the subsequent times when the ELTG is equal to -0.5 °F/in. As seen in Figure 4-5, the first critical time following TZ occurs at about 42 hours. At this time, the curvature is larger than the curvature at TZ, which can only be attributed to drying shrinkage. The next critical time occurs at age 67 hours. Between the ages 42 hours (the first critical time) and 67 hours (the next critical time,) the curvature remains positive and almost constant. Considering the overcast conditions during this period of time, it is apparent that not much drying shrinkage occurred in the slab. With no drying shrinkage and a constant curvature in the slabs, one can conclude that little to no creep occurred in the slabs during the first 72 hours after construction.

4.3 $\Delta T_{built\text{-}in}$-PROJECT 3

To establish $\Delta T_{built\text{-}in}$ for the slabs in Project 3, the temperature measured in the middle of Slabs A and C on each cell were used. This data is presented in Figure 4-8. The ELTG was estimated based on this data. The subsequent results for the ELTG are provided in Table 4-3. Based on the table, although the time of paving is different for the three cells, the $\Delta T_{built\text{-}in}$ is similar for all three cells. This can be explained by considering the overcast and cold weather conditions present throughout the day of paving. Furthermore, slabs in Cells 2 and 3 were covered with plastic sheets shortly after paving since it started to rain.

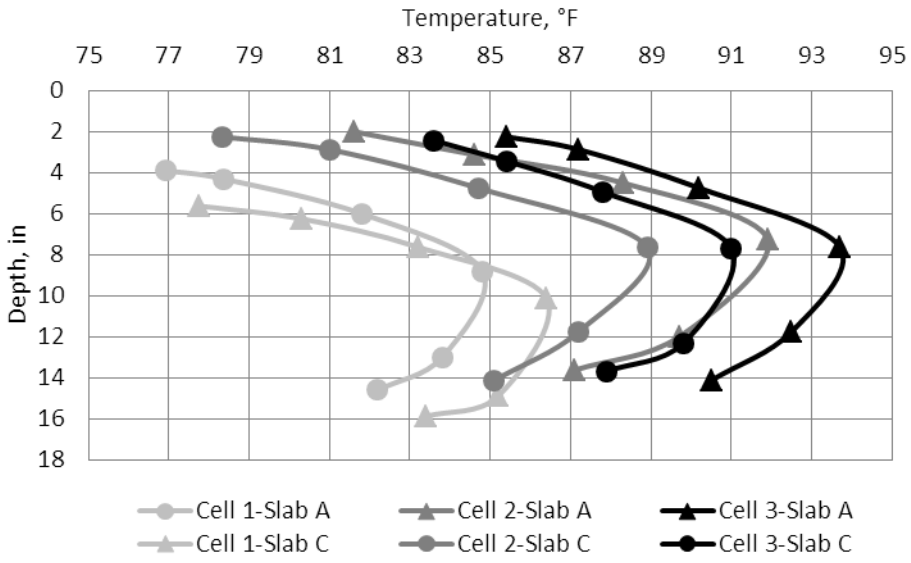

Figure 4-8. Temperature measured across the depth of slab at TZ in Project 3.

Table 4-3. Estimated ELTG based on measured temperature at TZ for each cell in Project 3.

Slab No.	ELTG (°F/in)		
	Cell 1 Paved at 8:30 AM	Cell 2 Paved at 12:00 PM	Cell 3 Paved at 4:00 PM
A	-0.4	-0.4	-0.4
C	-0.4	-0.4	-0.4
Average	-0.4	-0.4	-0.4

The possible effect of creep on the established permanent curl is investigated in this section, by once again studying the changes in the curvature of the slabs over time. The estimated curvature for the slabs is provided in Figure 4-9, Figure 4-10 and Figure 4-11 for Cells 1, 2 and 3, respectively.

The time at which the joints of the slabs cracked is exceptionally noticeable for the slabs in this project. These times for Slabs A and B for Cell 1 are indicated with black circles in Figure 4-9. Slab C did not crack during the first four days after paving.

The built-in temperature gradient was equal to -0.4 °F/in in the slabs for the three cells. To be able to investigate the effects of creep, the slabs with the least amount of drying shrinkage need to be selected for the analysis. This is because the drying shrinkage that occurs in the slabs overshadows the possible effect of creep.

For Cell 1, according to Figure 4-9, Slab A, with the earliest time of cracking, shows the largest drying curvature, while Slab B does not exhibit significant curvature due to drying until hour 63. At this point in time, the joints of this slab crack and the slab starts to show a larger upward curvature. Slab C, on the other hand, does not crack during the first 100 hours presented in Figure 4-9 and exhibits the lowest curvature due to drying shrinkage. Based on this discussion, the effects of creep for Cell 1 can best be investigated for Slab C, with the exhibited the least amount of drying shrinkage.

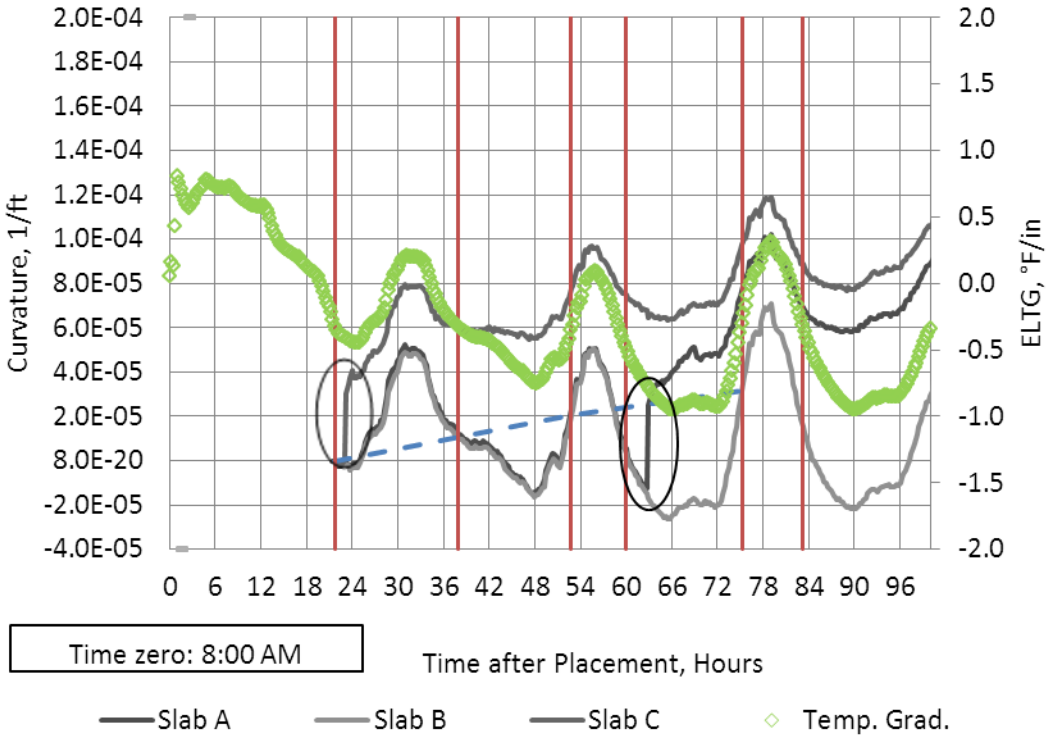

Figure 4-9. Estimated curvature due to drying shrinkage and possible creep for slabs in Cell 1, Project 3.

The blue dashed line in Figure 4-9 connects the curvature of the slab at the critical times. This line shows a positive slope, which implies a constant increase in the curvature in between the red lines as the slab ages. Hence, no decrease is noticed in the value of the built-in gradient over the first 4 days after paving. This again leads to the conclusion that the relaxing effects of creep on the built-in temperature gradient in not reflected in Figure 4-9.

In the case of Cell 2, as presented in Figure 4-10, the time the joints of the slab cracked is noticeable for Slabs A and C. The magnitude and the trend in the drying curvature for the slabs in this cell is very similar to that for the slabs in Cell 1. The least amount of drying shrinkage is seen for Slab C in this cell, therefore the creep analysis can be best performed on this slab. Two blue dashed lines, one connecting the curvatures at the day critical times and the other

corresponding to the curvature at the night critical times, are presented in Figure 4-10. The slope of the line for the day critical times is positive the entire time. The nighttime line, on the other hand, shows a slightly negative slope during the time period of between 36 and 48 hours. This line maintains a slightly positive slope thereafter. This negative slope can be an indication of the creep counteracting the drying shrinkage and relaxing a portion of the built-in gradient in the slabs. One way to explain this behavior in this slab is that in the absence of the contraction joints until hour 90, extra restraints is present against the thermal expansion and contraction or even drying shrinkage in the slab. This can result in higher levels of sustained stress in the slab and thereby more creep.

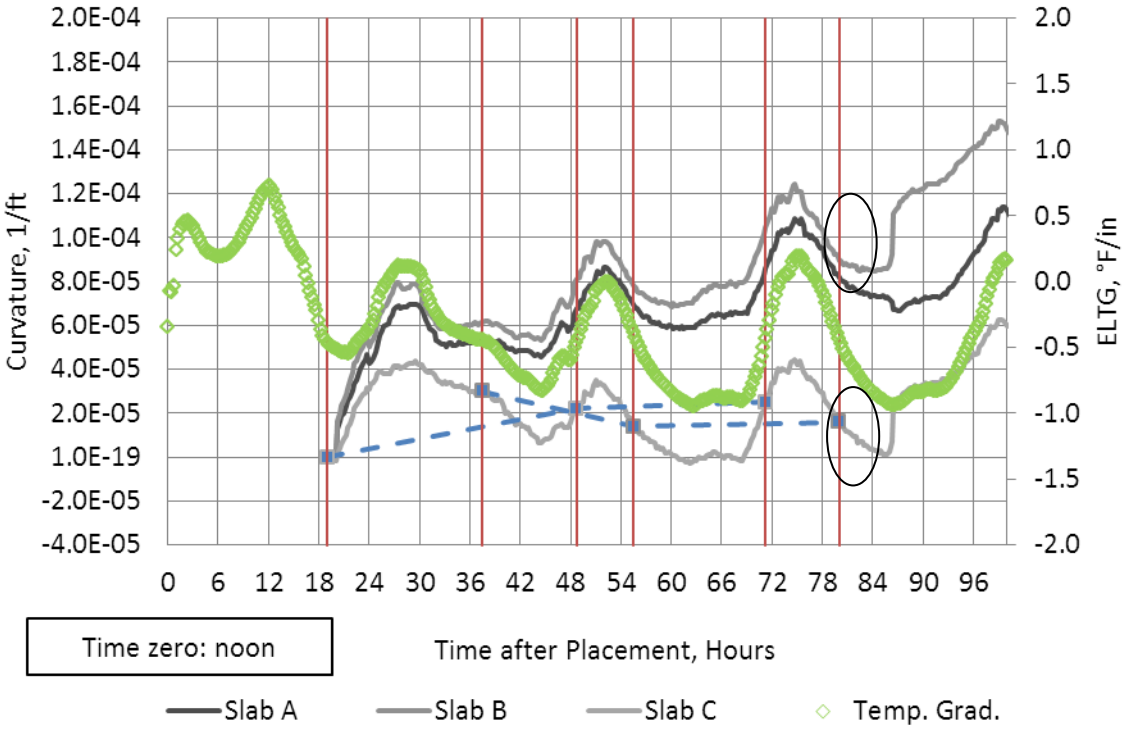

Figure 4-10. Estimated curvature due to drying shrinkage and possible creep for slabs in Cell 2, Project 3.

Figure 4-11 shows the drying curvature estimated for the slabs in Cell 3. The time the joints cracked for the slabs in this cell is noticeable and is highlighted in Figure 4-11 by black circles. Based on Figure 4-11, Slabs A and B cracked at the same time, while Slab C cracked at approximately 30 hours later.

The slabs in Cell 3 show the least amount of curvature of all cells for Project 3. These slabs are almost flat until they crack at an age of 54 hours. This is the smallest curvature observed in the first three projects analyzed. This could be the results of plastic sheets placed over the slabs soon after construction along with the consistent overcast conditions during the two days following construction. The ambient RH and solar radiation measured at the site for the project are presented in Figure 4-12. Since the slabs in this cell show almost no drying shrinkage, they are the best candidates for a creep analysis. The two dashed lines in Figure 4-11 connect the curvatures at the critical times. Both lines show almost constant slopes. This again indicates that either little to no creep has occurred in the slab.

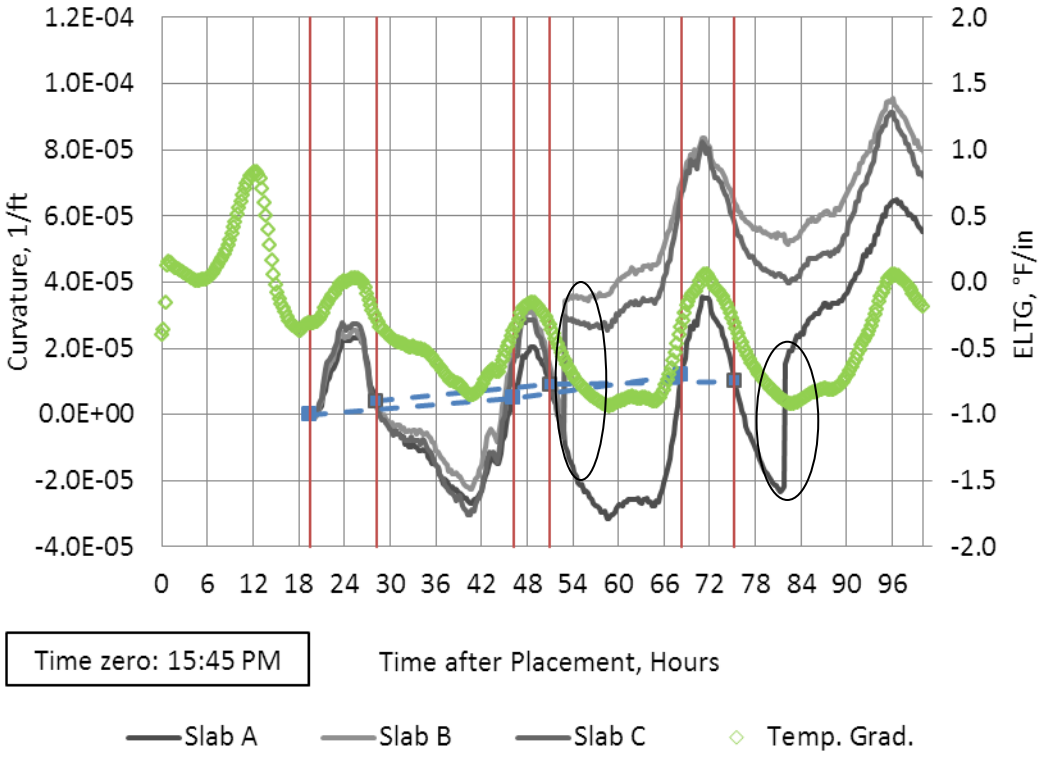

Figure 4-11. Estimated curvature due to drying shrinkage and possible creep for slabs in Cell 3, Project 3.

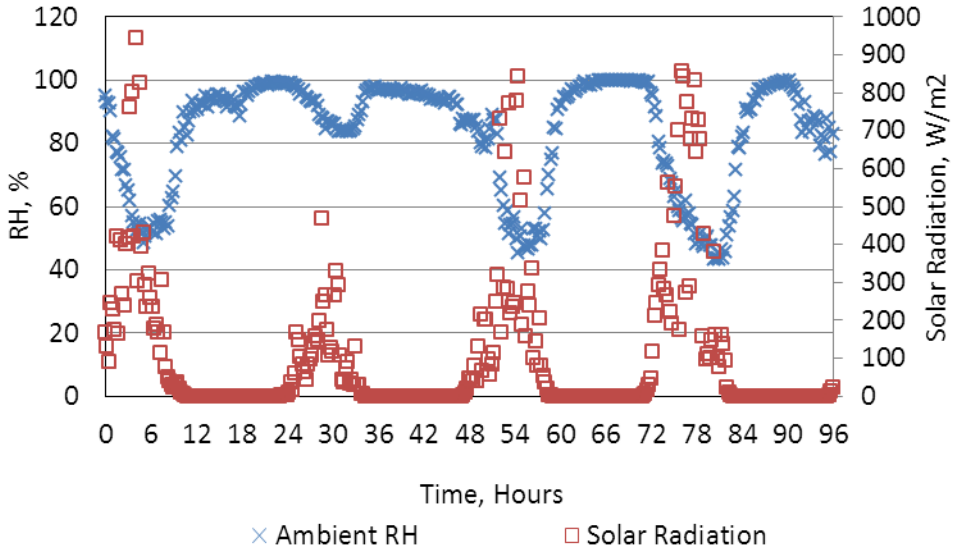

Figure 4-12. Ambient RH and solar radiation measured for the first four days after construction of Project 3.

4.4 $\Delta T_{built\text{-}in}$-PROJECT 4

Temperature measured in Slabs A and C for each cell in Project 4 at TZ are presented in Figure 4-13. The Janssen-Snyder method was employed to estimate the ELTG based on the measured temperatures presented in Figure 4-13. The results are provided in Table 4-4 for the three cells. It is interesting to note the significant difference between the gradients established for the three cells. The built-in temperature gradient is close to zero for Cell 1, around 1 °F/in in Cell 2 and -0.3 °F/in in Cell 3. This is due to the different times of construction for each of the cells. Cell 1 was constructed in the afternoon, Cell 2 in the late afternoon and Cell 3 was constructed in the morning on the following day.

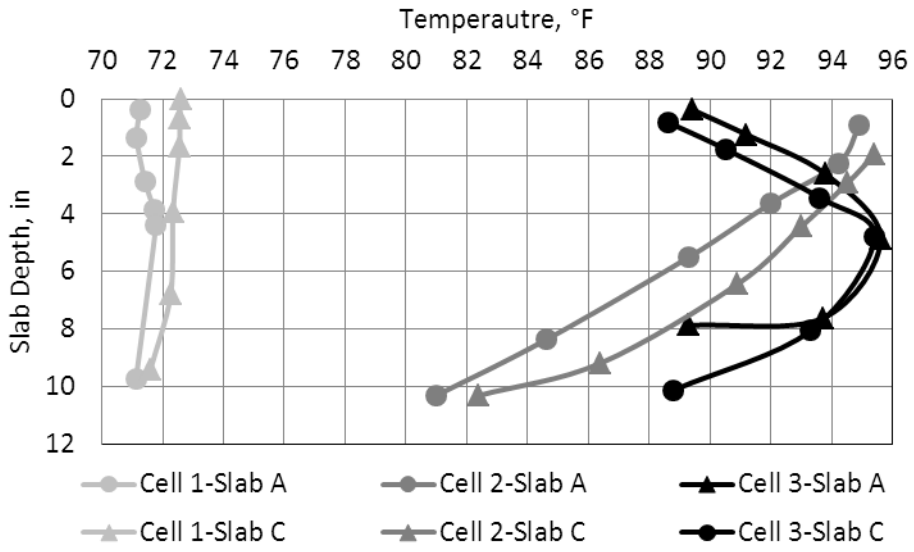

Figure 4-13. Measured temperature at TZ in Slabs A and C in three cells for Project 4.

Table 4-4. Estimated ELTG at TZ based on measured temperature for each cell in Project 4.

Slab No.	ELTG (°F/in)		
	Cell 1 Paved at 2:15 PM- April 29th	Cell 2 Paved at 5:30 PM- April 29th	Cell 3 Paved at 8:45 AM- April 30th
A	0.1	0.9	-0.3
C	0	0.8	-0.3
Average	0	0.8	-0.3

The curvature based on the measured strain at the top and bottom of the slabs in Cells 1, 2 and 3 are provided in Figure 4-14, Figure 4-15 and Figure 4-16, respectively. Again, Cell 1 and 2 were paved in the late afternoon, while Cell 3 was paved in the morning of the following day.

The built-in temperature gradient established for the slabs in Cell 1 is very close to zero as seen in Table 4-4. In Cell 2, on the other hand, a positive temperature gradient was present at TZ in contrast to all the previous projects. Since creep can negate a portion of the permanent curling over time, slabs in Cell 2, are expected to show a larger curvature at the critical times as the slab ages. Based on Figure 4-15, the curvature does show an increase over time, however, this increase in curvature could also be due to drying shrinkage. Since, the ambient conditions maintained during the construction of Cells 1 and 2, the curvature seen for the slabs in Cell 1 in Figure 4-14, with a zero built-in gradient, can be used to isolate the drying curvature from the curvature due to the built-in temperature gradient for the slabs in Cell 2.

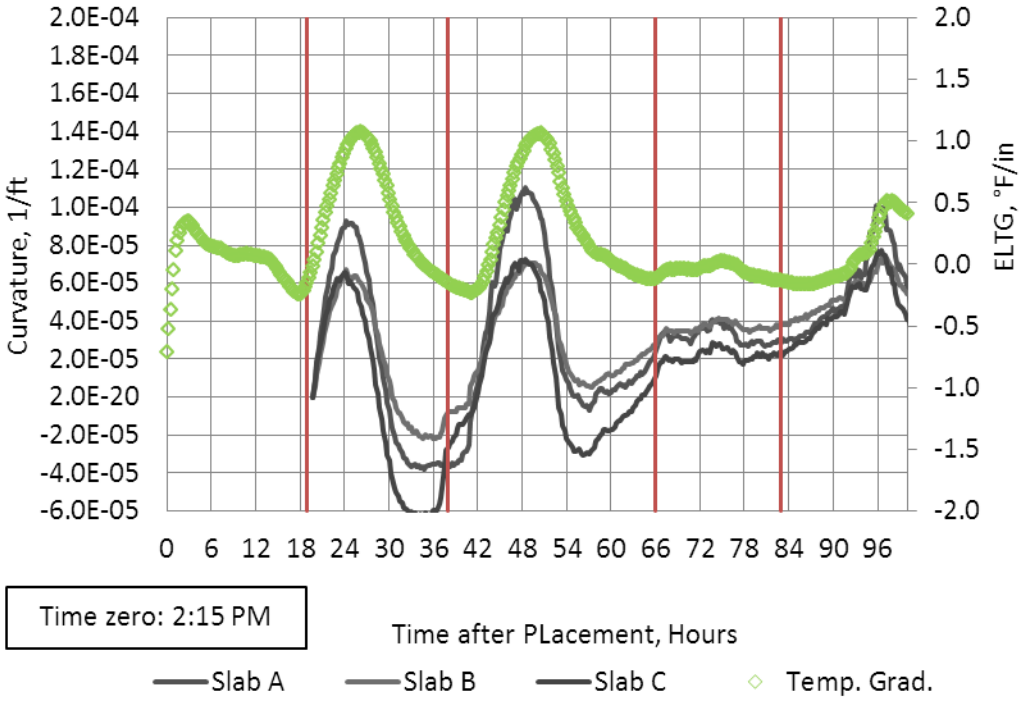

Figure 4-14. Estimated curvature due to drying shrinkage and possible creep for slabs in Cell 1, Project 4.

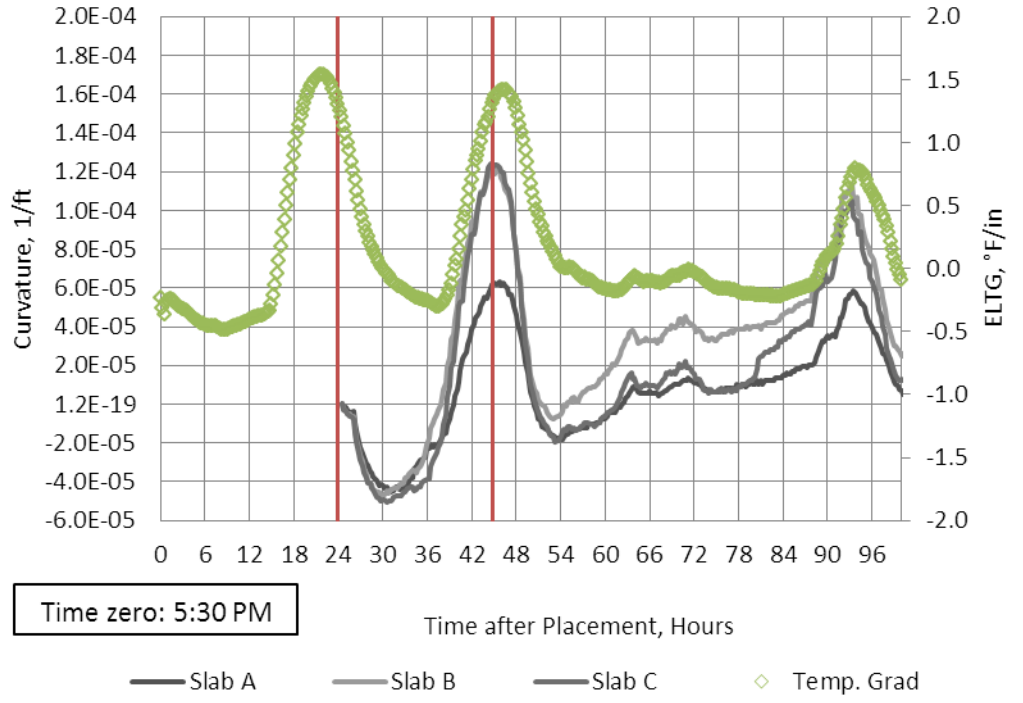

Figure 4-15. Estimated curvature due to drying shrinkage and possible creep for slabs in Cell 2, Project 4.

As seen in Figure 4-15, the transient ELTG reaches the built-in temperature gradient only once during the period of data collection. This time is around 45 hours after the construction of Cell 2. TZ for the slabs in Cell 2 was established as 24 hours after the construction of this cell which is hour 27 on Figure 4-15. At this age, the curvature of the slabs in Cell 1 is equal to -2.0E-5 1/ft based on Figure 4-14. At 45 hours after paving Cell 2 (the critical time,) the curvature for the slabs in Cell 2 is equal to 1.6E-4 1/ft based on Figure 4-15, this corresponds to hour 48 for the slabs in Cell 1. The curvature for these slabs is around 1.0E-4 1/ft as seen in Figure 4-14. This means that, the increase in curvature from the first red line in Figure 4-15 to the second line in the same figure is approximately 1.6E-4 1/ft. The increase in the curvature over the same time period for the slabs in Cell 1 with a zero built-in gradient is around 9.0E-5 1/ft. The larger progress seen in the curvature of the slabs in Cell 2 with respect to Cell 1 can be attributed to the relaxing effects of creep. It should be noted that Cell 1 was constructed in the sunny hours of the day, while during construction of Cell 2 the sun already set. Therefore, it is possible that Cell 1 was more susceptible to drying shrinkage than Cell 2.

The slabs in Cell 1 for Project 4 are different than the slabs in Cells 2 and 3, since Cell 3 was paved during the morning on the second day of paving. The estimated curvature for the three slabs in Cell 3 is presented in Figure 4-16 together with the transient ELTG in the slabs for a duration of about 4 days following paving. The built-in temperature gradient was established as -0.3 °F/in for the slabs in this cell. A similar analogy as the one used for the previous projects with a negative built-in temperature gradient was used in this section to investigate the effects of creep on permanent curling. The black dashed line in Figure 4-16 connects the curvatures corresponding to the critical times. The slope of the black dashed line is close to zero, implying that the effect of creep on the permanent curling is not reflected in Figure 4-16.

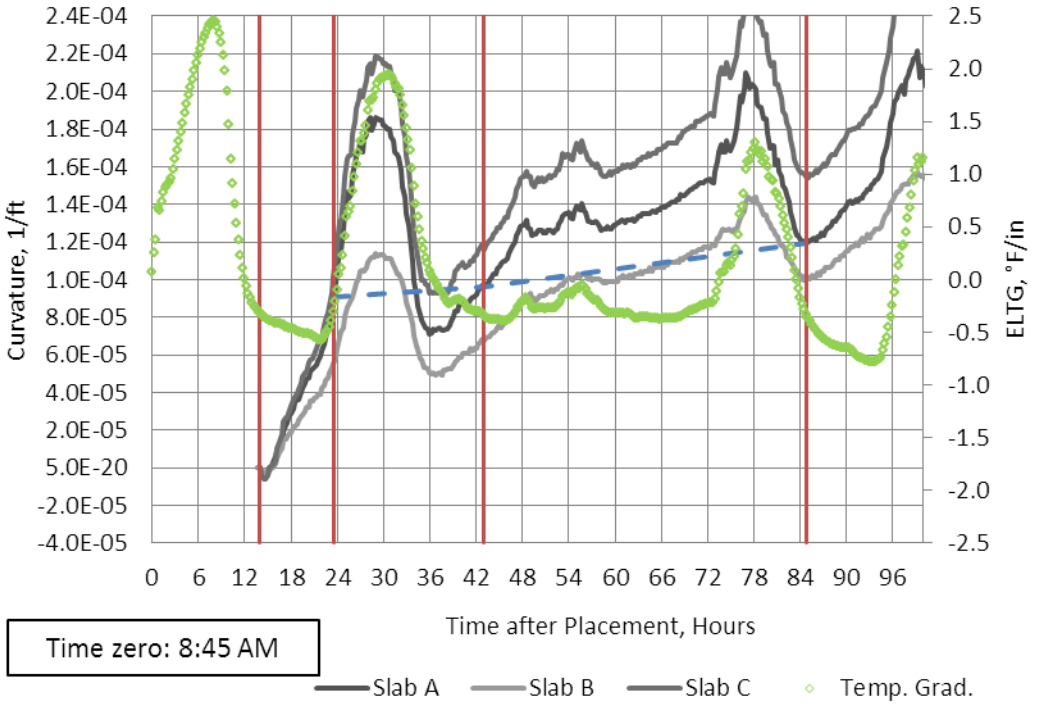

Figure 4-16. Estimated curvature due to drying shrinkage and possible creep for slabs in Cell 3, Project 4.

It is also very interesting to note the larger upward curvature for the slabs in Cell 3 in comparison to the slabs in Cells 1 and 2. This again shows the effects of the conditions at the time of paving on the drying shrinkage that occurs in the slabs during early ages.

4.5 COMPARISONS OF $\Delta T_{built\text{-}in}$ BETWEEN PROJECTS

A comparison of the built-in gradient established for all four projects is provided in this section, in spite of the fact that each of the four projects features a specific PCC mixture, climatic condition and design, which consequently affects the built-in temperature gradient. A summary of the built-in temperature gradient established for the three different cells in all the four projects

is presented in Figure 4-17. In this figure, the cells are grouped based on time of paving. Four groups consisting of morning, noon, afternoon and late afternoon paving were defined.

According to Figure 4-17, the lowest variability is seen in the built-in temperature gradient established for the slabs paved during the morning and at noon. The largest variability, on the other hand, is seen among the slabs paved in late afternoon. This is because in the case of morning/noon paving, similar climatic conditions were present during the day for the months the four projects were constructed. In the case of afternoon and evening paving, the climatic conditions varied depending on the time of paving. Cold conditions present in the afternoon decreased the rate of hydration of the cement. Depending on the rate of hydration, TZ can occur anytime during the night, resulting in a negative built-in gradient, or the next day, resulting in a positive temperature gradient.

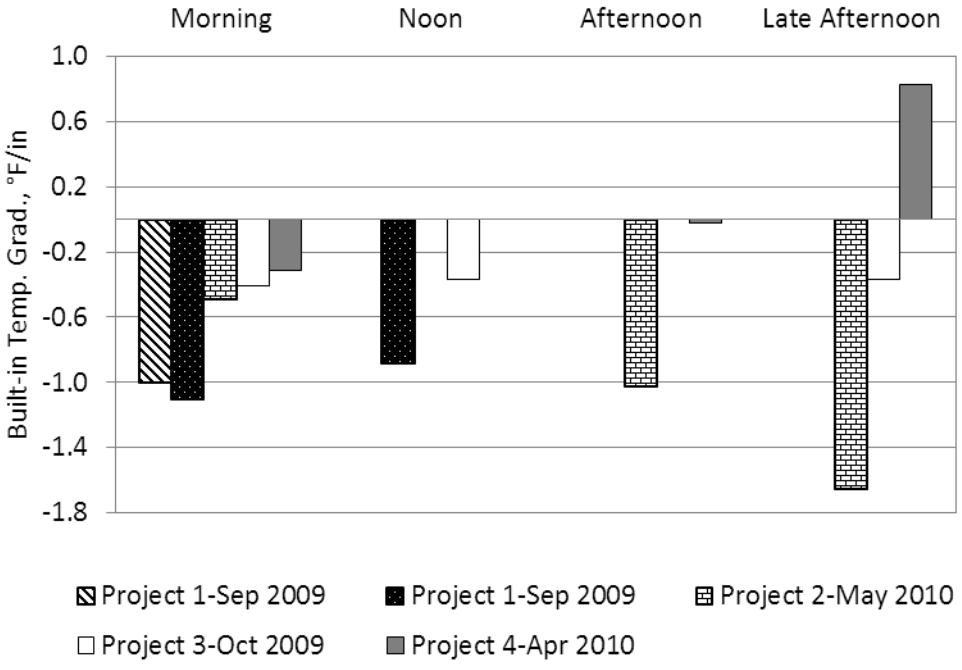

Figure 4-17. Built-in temperature gradients established for the four instrumented projects.

5.0 CHAPTER 5-NUMERICAL MODEL TO PREDICT TEMPERATURE

In order to be able to establish the built-in temperature gradient in the slab, the temperature along the cross section of the pavement structure at TZ is required. It was shown in the previous chapter that temperature can be measured in the pavement by the use of thermocouples. To be able to establish $\Delta T_{built\text{-}in}$ without the need to instrument the slab with thermocouples, a numerical temperature model is developed in this chapter. This chapter focuses on development, implementation and validation of a numerical solution for the heat transfer equation to predict the temperature variation in the pavement structure during the first 48 hours after placement.

5.1 THEORY AND FORMULATION BEHIND TEMPERATURE MODEL

5.1.1 Heat Transfer Equation

The governing equation of heat transfer due to conduction presented in Equation 5-1 in one dimensional domain, can be solved with respect to distance, x, and time, t, to predict temperature changes in a cross section of a pavement structure. The concrete slab in a pavement structure is significantly large in width and length in comparison to depth and therefore it is safe to treat the temperature analysis as a one-dimensional problem.

Equation 5-1 shows, based on the law of the conservation of energy, the rate of change in the stored energy in the control volume, at any point in time, depend on the rate at which the thermal/mechanical energy flows in or out of the control surface. In addition to the inflows and outflows, thermal energy can be generated within the control volume, which is the heat due to hydration of the cement in the case of hardening concrete (Ye 2007).

$$\frac{d}{dx}(k.\frac{dT}{dx}) + Q_H = \rho.C_p.\frac{dT}{dt} \quad (5\text{-}1)$$

where, T = Temperature, °C

t = Time, hours

ρ = Density, kg/m^3

c_p = Specific heat, J/kg/°C

Q_H = Generated heat per unit time and volume, W/m^3

k = Thermal conductivity, W/m/°C

Equation 5-1 is solved easily by using step-by-step integration in time applied by using numerical methods such as finite difference method (FDM) (Thompson, Dempsey et al. 1987; Jeong, Wang et al. 2001; Ruiz, Kim et al. 2001). The FDM is a simple numerical technique that is commonly used to solve partial deferential equations (PDE s), such as the one presented above. With this approach, the temperature across the pavement structure can be predicted at each time step. Boundary conditions need to be chosen properly to satisfy compatibility with the field conditions (Ruiz, Kim et al. 2001). Furthermore, Q_H, the heat generated by the hydration of the cement, in this equation needs to be defined at each increment of time. Therefore, another model needs to be incorporated into the major temperature model to estimate the heat of

hydration that is produced in the slab at each increment of time. This model, together with the corresponding boundary conditions, will be discussed briefly in the following section.

5.1.2 Boundary Conditions

When the PCC slab is placed in the field, heat will be transferred to and from the surroundings. The temperature in the PCC is determined by the balance between the heat generation in the PCC and the heat exchange with the environment. Heat transfer to the surroundings occurs in four different ways: conduction, convection (q_c), irradiation (q_r), and solar absorption (q_s). This is presented schematically in Figure 5-1.

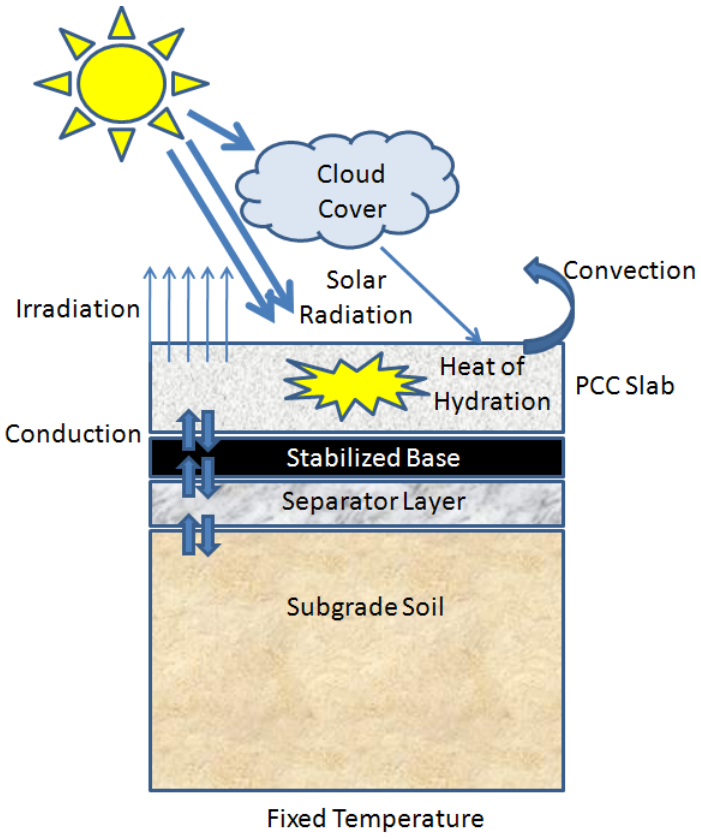

Figure 5-1. Heat transfer mechanisms between the pavement and the environment.

The conditions at the top and the bottom of the pavement structure are provided in Equations 5-2 and 5-3 (Jeong, Wang et al. 2001).

pavement surface: $$-k\nabla T.n + q_c + q_r - q_s = 0 \quad (5\text{-}2)$$

pavement bottom: $$-k\nabla T.n = 0 \quad (5\text{-}3)$$

Models available in literature for defining each of the four heat transfer mechanisms at the boundary conditions are summarized in Table 5-1.

Table 5-1. Models used to define the boundary conditions for the heat transfer model.

Heat Transfer Mechanism	Corresponding Model	Definition of Parameters	Reference
Convection	$q_c = h_c(T_c - T_a)$ (5-4)	q_c = Convection heat flux W/m^{2,} h_c = Surface convection coefficient kJ/m^2/h/°C Tc = Concrete surface temperature, °C T_a = Surrounding air temperature, °C.	(Solaimanian and Kennedy 1998)
	If $w \leq 5$ m/s: $h_c = 20 + 14w$ (5-5) else: $h_c = 25.6*0.78w$ (5-6)	w = Wind velocity, m/s	(Ruiz, Rasmussen et al. 2006)
Solar Absorption	$q_s = \beta.q_{solar}$ (5-7)	q_s = Solar absorption heat flux W/m^2, β = Solar absorptivity, q_{solar} = Instantaneous solar radiation, W/m^2.	(Ruiz, Schindler et al. 2001; Jeong and Zollinger 2006)
Irradiation	$q_r = \varepsilon.\sigma(T_C^4 - T_\infty^4)$ (5-8)	q_r = Heat flux of heat emission from the surface, W/m^2 σ = Stefan-Boltzmann radiation constant = 5.67×10^{-8} W/m^2/°C^4 ε = Surface emissivity of concrete = 0.88	(Hermansson 2001; Jeong and Zollinger 2006)

It should be noted that due to complexities caused by the fourth-degree relation in Equation 5-9 in Table 5-1 for irradiation, this relation was replaced by a simplified empirical relation provided in Equation 5-7 (Branco, Mendes et al. 1992; Ruiz, Schindler et al. 2001).

$$q_r = \varepsilon[4.8 + 0.075.(T_a - 5).(T_c - T_a)] \quad (5\text{-}9)$$

Four layers were included in the model including the PCC slab, the stabilized base, either ATPB or CTPB, the subbase layer and the subgrade soil. The nodes and the finite difference mesh for the pavement structure is presented schematically in Figure 5-4. At the PCC slab/base interface, the boundary conditions were defined as follows:

For the concrete layer, at time step i-1:

$$q_{conc} = \frac{k_{conc}}{\Delta x}.(T_{Int} - T_{conc}) \quad (5\text{-}10)$$

where, q_{conc} = Heat inside the concrete layer, W/m^2

k_{conc} = Thermal conductivity of concrete, W/m/°C

Δx = Element size, m

T_{conc} = Temperature of the first node in the concrete layer next to the interface node, °C

T_{Int} = Temperature of the interface node, °C

For the base layer at time step i-1:

$$q_{base} = \frac{k_{base}}{\Delta x}.(T_{Int} - T_{base}) \quad (5\text{-}11)$$

where, q_{base} = Heat inside the base layer, W/m^2

k_{conc} = Thermal conductivity of the base material, W/m/°C

T_{base} = Temperature of the first node in the base layer next to the interface node, °C

Temperature at the interface at time step i:

$$(T_{Int})_i = (T_{Int})_{i-1} + \frac{(q_{conc} + q_{base})\Delta t}{(\rho_{base}.C_{P_{base}} + \rho_{conc} + C_{P_{conc}})} \quad (5\text{-}12)$$

where, $(T_{Int})_i$= Temperature at the interface at time step i, °C

$(T_{Int})_{i-1}$ = Temperature at the interface at time step i-1, °C

ΔT = Time step, hours

ρ_{base} = Density of the base material, kg/m^3

C_{Pbase} = Specific heat of the base material, J/kg/°C

ρ_{conc} = Density of the concrete, kg/m^3

CP_{conc} = Specific heat of the concrete, J/kg/°C

The same type of boundary condition was defined at the base/subbase interface. At the bottom of the pavement structure, a constant temperature of 12 ºC was assumed at the depth of 100 inches (Hermansson 2001). This was assumed based on the findings from previous studies which have shown the temperature of the earth maintains at an almost constant level at this depth (Dempsey, Herlache et al. 1985).

5.1.3 Heat of Hydration Model

The hydration reaction of Portland cement is an exothermic process. Therefore, when using the general heat transfer equation, presented in Equation 5-1, to predict the temperature variations across the pavement structure, the rate of heat liberation, Q_H, needs to be considered for each time step.

A regression model was developed in 2005 to characterize the formation of hydration products by measuring the heat released during hydration for different concrete mixtures

(Schindler and Folliard 2005). This model was formulated by performing semi-adiabatic calorimeter tests on different concrete mixtures. This model, presented in Equation 5-13, accounts for effects of concrete mixture, cement chemical composition, cement fineness and SCMs and is based on the equivalent age, te.

$$Q_H = H_u C_c (\frac{\tau}{te})^{\beta} (\frac{\beta}{te}) \alpha(te) \exp[\frac{-E}{R}(\frac{1}{273+Tc} + \frac{1}{273+Tr})] \quad (5\text{-}13)$$

where, Q_H = Rate of heat liberation, W/m^3

C_c = Cementitious materials content, kg/m^3

H_u = Total heat of hydration of cementitious materials at 100 percent hydration, J/kg, obtained from the following relation (Ruiz, Rasmussen et al. 2006):

$$H_u = H_{cem} P_{cem} + 461 P_{slag} + 1800 P_{Cao-FA}.P_{FA} \quad (5\text{-}14)$$

where, H_{cem} = Total heat of hydration of cement,

P_{Cao-FA} = Mass ratio of Cao in fly ash to total fly ash content,

H_{cem} = Heat of hydration of cement, defined by the following relation (Bogue 1974):

$$H_{cem} = 500 P_{C3A} + 260 P_{C2S} + 866 P_{C3S} + 420 C_4 AF + 624 P_{So3} + 1186 P_{free-Cao} + 85 P_{Mgo} \quad (5\text{-}15)$$

One of the inputs, for estimating the Q_H, as seen in Equation 5-13, is the slab nodal temperature. Numerical solutions, such as FDM, which solve equations through iterations, make it possible to use the data from the previous time step in the current step. This way Q_H can be estimated at every desired increment of time.

5.1.4 Thermal Properties

Thermal properties including the coefficient of thermal conductivity, k and the specific heat, Cp of the concrete are required by the heat transfer model as seen in Equation 5-1. Thermal conductivity is the uniform flow of heat through a unit of thickness over a unit area of concrete (Zoldners 1971) or in other words, the ratio of the heat flux to temperature gradient (Mindess 2002). Specific capacity of concrete, on the other hand, is the amount of heat required to raise the temperature of concrete by one degree. Thermal conductivity of concrete can be measured in the laboratory by using a guarded-hot-plate apparatus as prescribed by the ASTM C 177 (ASTM C 177 1992).

Thermal conductivity of the concrete depends on variables such as the conductivity of the cement and aggregate, mix proportions and compactness of the placed concrete. Generally speaking, thermal conductivity of the concrete is a function of that of the paste and the aggregate and it greatly depends on the moisture content of the concrete (Zoldners 1971). Different rock types can be used as the aggregate in the mix and affect the overall conductivity of the mix. Rock types such as quartzite, sandstone and other quartzose rocks show the highest conductivity. Rocks such as limestone and dolomite exhibit an intermediate k and basalt and barite are among rock types with low conductivity. Typical values for the k of concrete mixtures made of different rock types are listed in Table 5-2 (Scanlon and McDonald 1994). Thermal conductivity of the concrete also depends on its density. Lightweight concrete, for example, includes high porosity has a very low conductivity (Mindess 2002).

Conductivity of fresh concrete is expressed as a fraction of the degree of hydration. An empirical relation is available that provides a linear relation between the k of concrete and the

degree of hydration (Ruiz, Rasmussen et al. 2006). This relation is provided in Equations 5-16. The following equation suggests that k at the beginning of hydration is 33 percent higher than the final k at the end of hydration.

$$k = k_{\infty}(1.33 - 0.33\alpha) \tag{5-16}$$

where, k = Current thermal conductibity of concrete, W/m/°C,

k_{∞} = Thermal conductivity of mature concrete from Table 5-2, W/m/°C,

α = Degree of hydration,

Other relations are available that suggest k of saturated concrete to be twice the final k of hardened concrete (Yang 1996). Equation 5-16 was incorporated into the temperature model for every node along the depth of the concrete slab by using the currenet degree of hydration corresponding to each node at every time step.

The specific heat of concrete also depends on the proportion and Cp of different constituents in the mix including cement, aggregate and water (RILEM Bulletin 1981). The specific heat of aggregate and cement or any other material can be determined by using a calorimeter. The specific heat of concrete is also strongly affected by the level of moisture and temperature of concrete (Yang 1996). The relation provided in Equation 5-17 includes the effects of proportioning and specific heat of each constituent together with the degree of hydration in establishing the Cp for concrete (Van Breugel 1999; Ruiz, Rasmussen et al. 2006; Ye 2007).

$$Cp = \frac{1}{\rho}(W_c \alpha C_{cef} + W_c(1-\alpha).Cc + Wa.Ca + W_W.C_w) \tag{5-17}$$

where, Cp = Current specific heat of concrete, J/kg/°C,

W_c, W_a, W_w = Amount by weight of cement, aggregate and water, kg/m^3,

C_c, C_a, C_w = Specific heat of cement, aggregate and water from Table 5-3, J/kg/°C,

C_{cef} = Fictious specific heat of the hydrated cement determined as 8.4 Tc+339 where Tc is the current concrete temperature in °C.

Table 5-2. Typical values for thermal conductivity of mature concrete (Scanlon and McDonald 1994).

Aggregate Type	Moist Density of Concrete, lb/ft^3 (kg/m3)	Thermal Conductivity Btu/ft-°F (W/m/°C)
Quartzite	147-153 (2350-2440)	1.8-2.4 (3.1-4.1)
Dolomite	156.25 (2500)	1.9 (3.3)
Limesone	153-152.5 (2450-2440)	1.3-1.9 (2.2-3.2)
Sanstone	150-2130 (2400-2130)	1.7 (2.9)
Granite	151.3 (2420)	1.5 (2.6)
Basalt	158-147 (2520-2350)	1.1-1.7 (1.9-3.0)

Table 5-3. Typical values for Cp for concrete constituents (Ruiz, Rasmussen et al. 2006).

Material	Specific Heat Btu/lb-°F (J/kg/°C)
Cement	0.27 (1140)
Water	1.0 (4187)
Limestone/Dolomite	0.27 (910)
Sandstone	0.18 (770)
Granite/Gneiss	0.19 (780)
Siliceous River Gravel	0.18 (770)
Basalt	0.24 (900)

The thermal properties of other layers in the pavement structure, including the base and the subbase layer are also required for the heat transfer model as seen in Equation 5-1. Typical values are available for thermal properties of the base materials and different soil types. This information is provided in Table 5-4 and Table 5-5.

Table 5-4. Thermal properties of some base materials (Thompson, Dempsey et al. 1987; SHRP-C-321 1993).

Base Material	Density lb/ft^3, (kg/m^3)	Specific Heat, Btu/lb-°F (J/kg/°C)	Thermal Conductivity Btu/ft-°F (W/m/°C)
Dry Gravel	106.4 (1703)	0.20015 (838)	0.3 (0.52)
Wet Gravel	118.6 (1898)	0.25007 (1047)	1.4 (2.42)
Asphalt Concrete	148 (2371)	0.21997 (921)	0.7 (1.21)
Asphalt	144 (2302)	0.25007 (1047)	0.8 (1.38)
Stabilized Base	146 (2339)	0.24004 (1005)	1.92 (3.32)
Cohesive Subgrade	129 (2066)	0.28995 (1214)	0.92 (1.59)

Table 5-5. Thermal properties of different soil types based on AASHTO soil classification (Thompson, Dempsey et al. 1987; SHRP-C-321 1993).

Soil Classification	Density lb/ft^3, (kg/m^3)	Thermal Conductivity Btu/ft-°F (W/m/°C)	Specific Heat, Btu/lb-°F (J/kg/°C)
A-1	74.3 (1188)	0.52 (0.9)	0.17 (712)
A-2	59.4 (950)	0.47 (0.81)	0.17 (712)
A-3	65.3 (1045)	0.59 (1.02)	0.2 (838)
A-4	53.5 (856)	0.59 (1.02)	0.17 (712)
A-5	50.5 (808)	0.26 (0.45)	0.17 (712)
A-6	53.5 (856)	0.35 (0.60)	0.17 (712)
A-7	47.5 (760)	0.17 (0.30)	0.17 (712)

5.1.5 Finite Difference Method

The FDM is one of the several techniques that can be used to obtain numerical solutions to the heat transfer PDE presented in Equation 5-1. In all numerical solutions the continuous PDE is replaced with a discrete approximation. The mesh is used to define the locations where the discrete solution is computed. Two key parameters of the mesh are Δx, the local distance

between adjacent points in space, and Δt, the local distance between adjacent time steps (Recktenwald 2004). This is presented schematically in Figure 5-2.

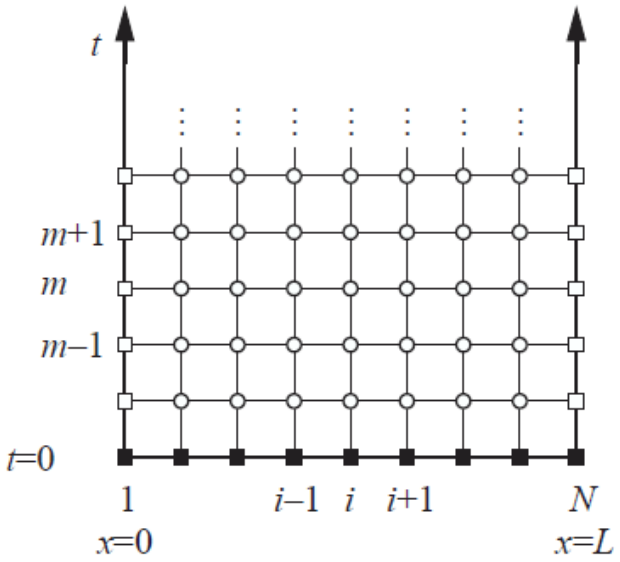

Figure 5-2. The finite difference mesh including time and space (Recktenwald 2004).

A forward finite difference solution was used for the time, m, and a second-order central finite difference solution was applied for the space, i, to solve the heat Equation 5-1, known as forward time, centered space (FTCS) solution. This is presented schematically in Figure 5-3. A simple form of the heat transfer equation with the FTCS solution is presented in Equation 5-18. Alpha in this equation is the thermal property of the material.

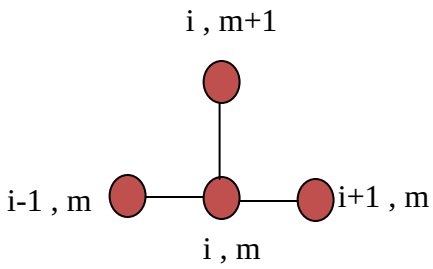

Figure 5-3. Schematic presentation of FTCS in the time-space domain.

$$\frac{u_i^{m+1} - u_i^m}{\Delta t} = \alpha \frac{u_{i+1}^m - 2u_i^m + u_{i-1}^m}{\Delta x^2} \qquad (5\text{-}18)$$

As mentioned earlier, a four-layer structure was modeled. The total depth was assumed as 100 inches for the pavement structure. The thickness of the PCC slab varied between 10- to 15 inches. This is presented schematically in Figure 5-4.

To insure the stability of the model, the maximum allowable time step needs to be established based on the element size and the thermal diffusivity. Since at every time step, the degree of hydration varies with depth, every node in the concrete layer had a different thermal diffusivity in each time step. Δt was defined as the minimum of the amount determined using the relation provided below for every node in for each time step:

$$\Delta t = \frac{\Delta x^2}{4[\frac{k}{\rho Cp}]} \qquad (5\text{-}19)$$

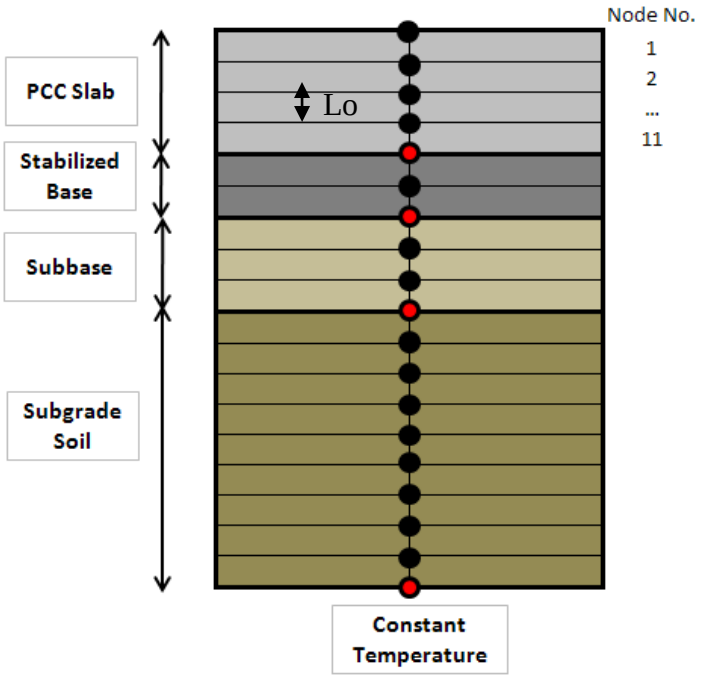

Figure 5-4. The nodes considered in the temperature model for the pavement structure.

5.2 CONCRETE TEMPERATURE PREDICTION MODEL VALIDATION

The validity and accuracy of any numerical model needs to be investigated to make sure the solutions are reliable and realistic. In order to validate the implemented temperature model in this study, the predictions from the model were compared against the actual temperature measurements in the field for the four instrumented projects. Details on the instrumentation of the four projects were presented thoroughly in previous chapters and will not be provided here to avoid repetition. The predicted and measured temperatures in the slabs will be presented for the three different cells in each project.

5.2.1 Model Validation-Project 1-Section B09, Westbound

Project 1 consisted of a 12-inch PCC slab, a 4-inch ATPB layer and a 6-inch subbase placed on the subgrade soil. The PCC mixture design properties and the cement composition for this project are provided in Table 3-2 and Table 3-5, respectively. Additionally, ambient conditions such as solar radiation, wind speed and temperature measured at the site for Project 1 were used to define the boundary conditions at the surface of the pavement. The thermal conductivity of the mature concrete made of limestone was defined as 2.0 W/m/°C based on typical values provided in Table 5-2 for limestone aggregate. The thermal properties of the base layer were defined using Table 5-4 for hot mix asphalt. The subbase material was defined as wet gravel with the corresponding thermal properties from Table 5-4. A summary of the inputs used in the model for this project is provided in Table 5-6.

Table 5-6. Inputs for the temperature model for Project 1.

Category	Parameter	Value
Time and Space Steps	Δx (cm)	3
	Δt (hour)	varies
	Initial Temperature of concrete, °C	17
Nodes	Nodes in PCC Slab (No.)	10
	Nodes in Base Layer (No.)	3
	Nodes in Sub-base Layer (No.)	5
	Nodes in Subgrade Layer (No.)	45
Thermal Conductivity	k_∞ of Concrete (W/m/°C)	2
	k of Base Layer (W/m/°C)	1.38
	k of Sub-base Layer (W/m/°C)	2.42
Weather Data	Temperature, Wind Speed, Precipitation, Solar Radiation	Measured at the Site
Analysis Time	Time (Hours)	66

Temperature predictions were obtained across the slab depth over a period of 48 hours using the model. The predicted temperatures are compared with the temperatures measured in the field. Temperature was measured at different depths of the PCC slab for the 3 cells instrumented in Project 1. The predicted and the measured temperature were compared at the surface, mid-depth and bottom of slabs in Cells 1, 2 and 3 in Figure 5-5 to Figure 5-13.

Based on these figures, the model predictions agrees relatively well with the measured temperature for the PCC slabs in all cells. To be able to evaluate the accuracy of the predictions at TZ, this point in time is represented with the red vertical lines on each graph.

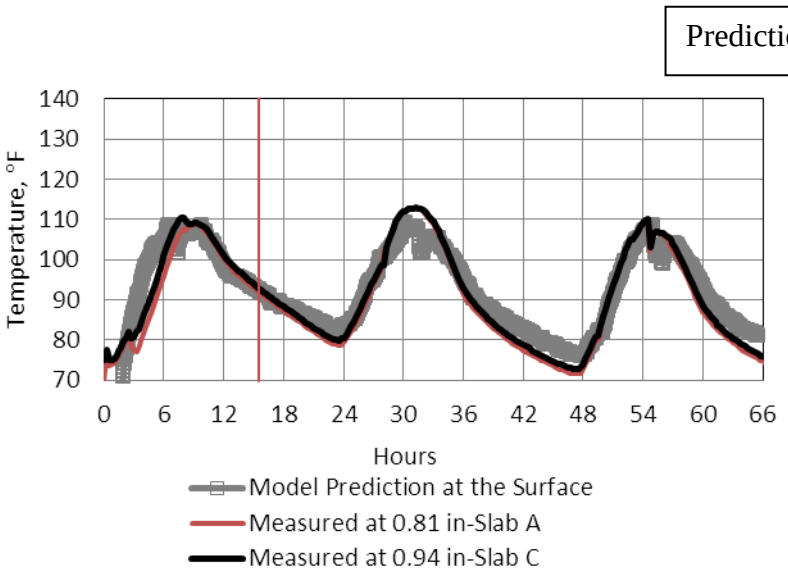

Figure 5-5. Model predictions in comparison to field measurements at the surface of the slab, Cell 1, Project 1.

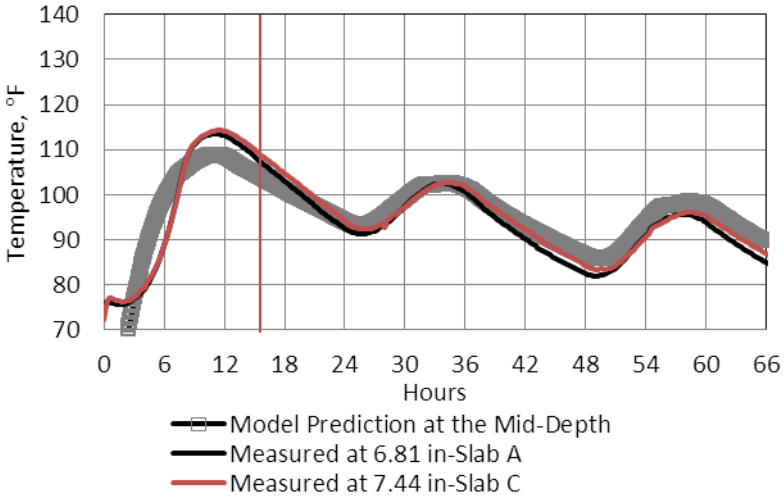

Figure 5-6. Model predictions in comparison to field measurements at the mid-depth of the slab, Cell 1, Project 1.

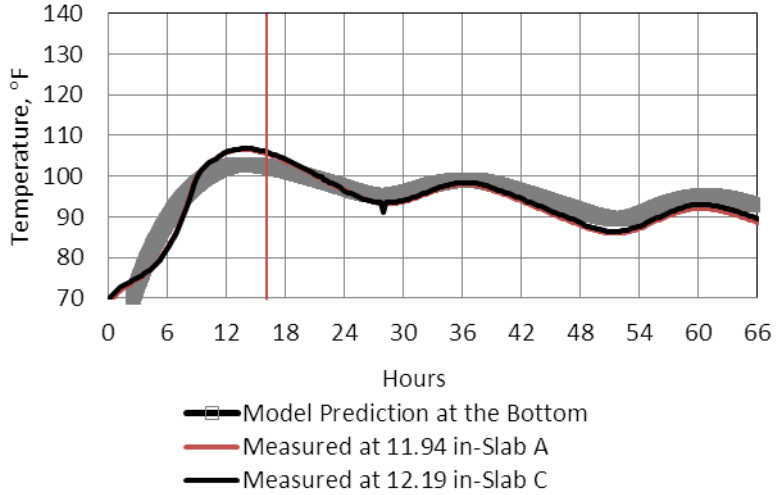

Figure 5-7. Model predictions in comparison to field measurements at the bottom of the slab, Cell 1, Project 1.

Predictions in Cell 2-Project 1

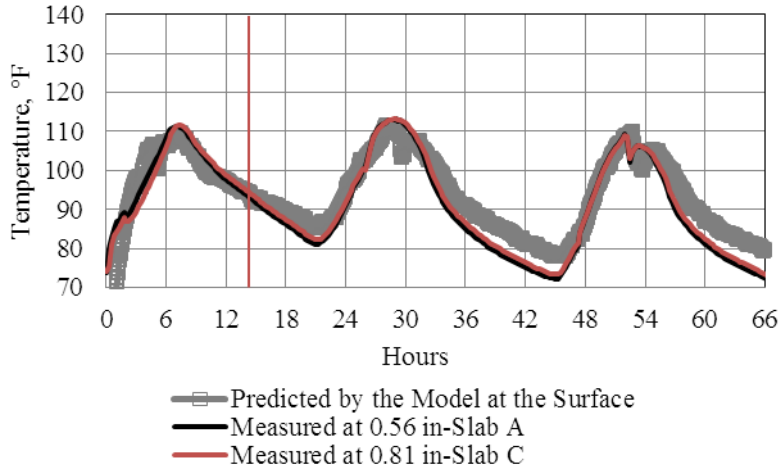

Figure 5-8. Model predictions in comparison to field measurements at the surface of the slab, Cell 2, Project 1.

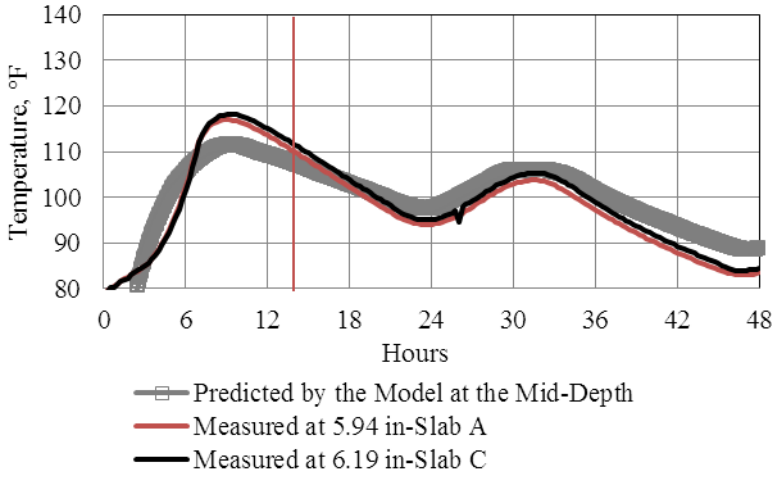

Figure 5-9. Model predictions in comparison to field measurements at the mid-depth of the slab, Cell 2, Project 1.

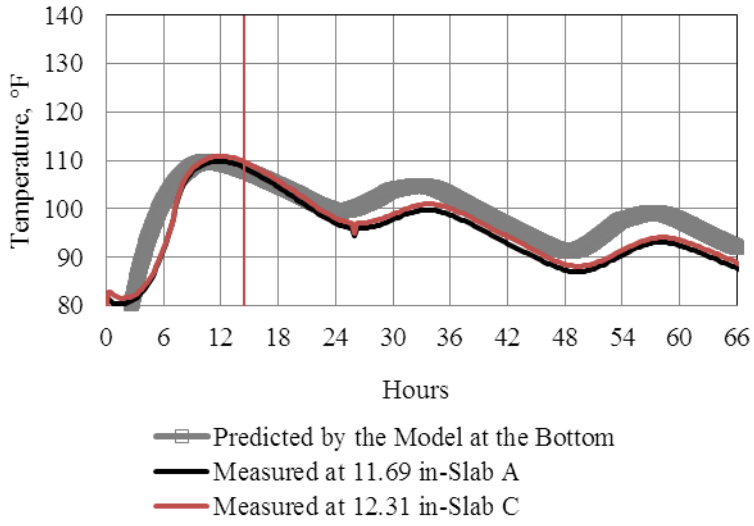

Figure 5-10. Model predictions in comparison to field measurements at the bottom of the slab, Cell 2, Project 1.

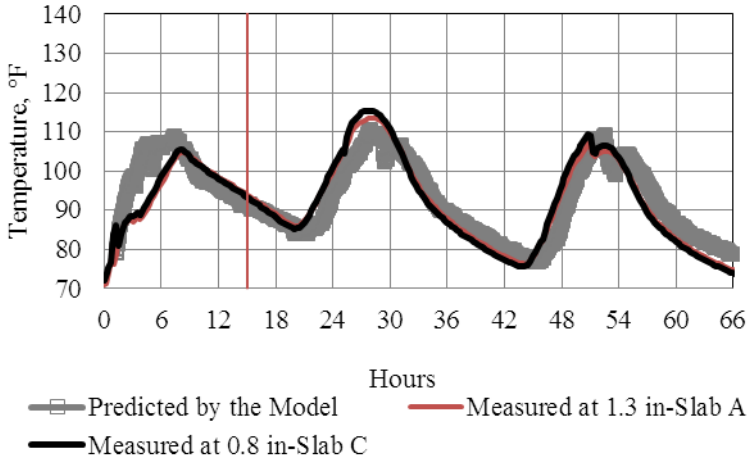

Figure 5-11. Model predictions in comparison to field measurements at the surface of the slab, Cell 3, Project 1.

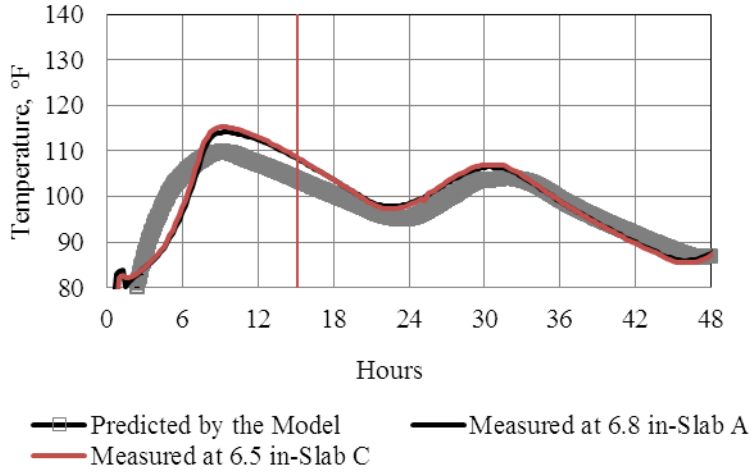

Figure 5-12. Model predictions in comparison to field measurements at the mid-depth of the slab, Cell 3, Project 1.

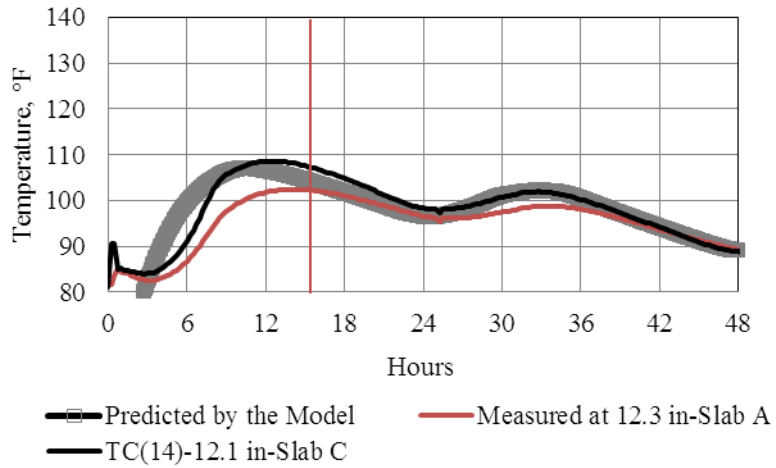

Figure 5-13. Model predictions in comparison to field measurements at the bottom of the slab, Cell 3, Project 1.

Some variation is noticed between the predictions and the measured temperature over approximately the first six hours after placement. These differences could be due to multiple factors. First, the initial temperature of the concrete was defined based on the temperature measurements in the field for the mid-depth of the base layer. However, this temperature is different from the temperature of the concrete at the time it is placed in the field. This is because the concrete batch plant was about four miles from the construction site. During the delivery time, the concrete temperature increases due to the heat of hydration and therefore the zero time for the model, which is the time of placement for the slab does not match with the time water is introduced to the cement. This has resulted in the difference seen between the initial temperature for the model predictions and the measured temperature.

Second, the most accurate method to predict the rate of heat libration for the cement over time is through performing adiabatic caloremetry tests on the cement used in the mixture. The equipment required for performing this test, however, was not within the budget limits of this study. Therefore, existing regerssion models available for predicting the heat libration rate by the hydrating cement was used in this study. This could have resulted in some approximations in predicting the heat of hydration development over time and therefore could contribute to the difference seen between the predicted and measured temperatures.

As seen in Figure 5-5 to Figure 5-13, the errors due to using a regression model for predicting the heat liberation in the concrete dissipate after about six hours. It should be noted that the final objective of the temperature model is to establish the temperature gradient at TZ. TZ is represented in each figure by the red vertical lines. As seen in the figures, at this point in time, the predicted temperatures show acceptable agreement with the measured temperatures.

The w/cm ratio of the mixture is another factor that could be a source of error seen in the predictions during the first five hours after construction. Based on Figure 5-5 to Figure 5-13, the predicted temperatures show the best agreement with the measured temperatures during the first 5 hours for Cells 1 and 2. The poorest agreement observed occurred in Cell 3. The w/cm ratio was established as 0.41 for Cell 1 and 0.47 for Cell 2 and 3. The regression model used to consider the effects of the heat of hydration, Equation 5-13, does not account for the amount of water used in the mix. The effect of a lower w/cm ratio for the PCC mixture used in Cell 1 is noticeable when compared to Cell 3 but not Cell 2. Hence, no judgments can be made on the sensitivity of the temperature predictions to the w/cm ratio of the mixture.

Lastly, the current study does not include the heat loss due to evaporation as one of the heat transfer modes at the surface of the slab. A previous study has shown that cooling due to evaporation can significantly reduce the temperature rise due to hydration at early ages (Ruiz, Rasmussen et al. 2006). This can be another source of the error seen in the predictions for the first few hours following paving.

5.2.1.1 Sensitivity of the Predictions to the Thermal Conductivity

As mentioned earlier, the thermal properties of the mature concrete, the base and the subbase material was defined based on typical values found in literature for the construction materials used. A small sensitivity study was performed in this section to investigate the sensitivity of the temperature prediction in the PCC slab both over time and across the depth of the slab, the base and the subbase layer. Effects of each of these variables on the predicted temperature in the slab will be investigated individually starting with the k of the concrete.

The thermal conductivity of the PCC layer was defined based on the aggregate type used in the mixture. Typical values for PCC mixtures with different aggregate types were provided in Table 5-2. Based on this table, k for the PCC can vary from 1.9- to 4.1 W/m/°C. This range of variation was considered for k in the sensitivity study. Sensitivity of the temperature prediction over time to different values of k is presented in Figure 5-14. The temperature predictions provided in Figure 5-14 correspond to the depth 2.5-inch of the PCC slab.

Based on Figure 5-14, k is quite sensitive to the temperature predictions. According to this figure, higher values for k result in lower temperature predictions for the PCC layer. Additionally, a delay is seen in the time of occurrence of the peak temperature for higher k values. This is as expected since higher k values can result in more and faster heat loss to the surroundings.

It is also interesting to note that the sensitivity of k to the predicted temperature is more noticeable after about 24 hours. This is due to the progress of hydration in the mix. At early ages, k is a function of both the degree of hydration and k of the mature concrete. When the hydration is complete ($\alpha = 1$), k of the concrete is equal to that of the mature concrete.

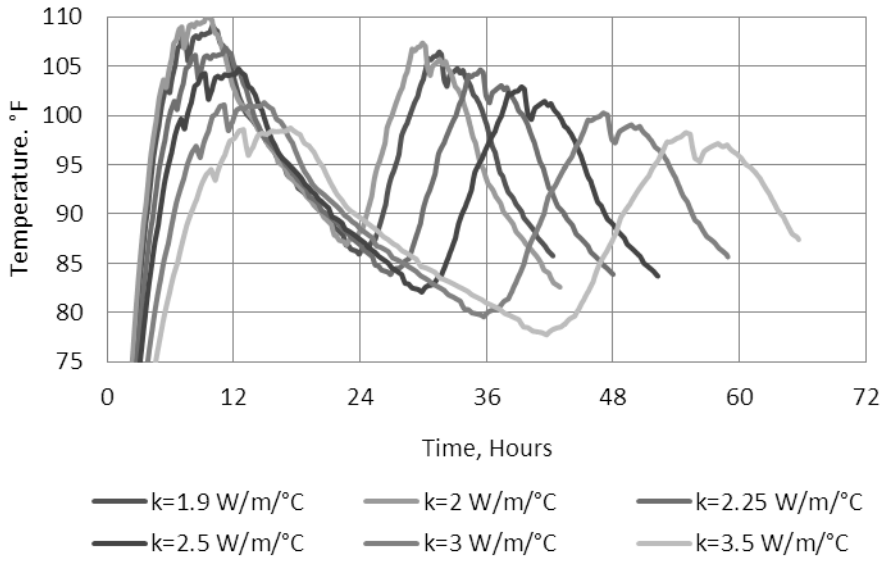

Figure 5-14. Sensitivity of temperature prediction in the upper portion of the PCC layer to thermal conductivity of the PCC.

The effect of k on temperature predictions across the depth of the slab was also investigated. The temperature predictions corresponding to approximately one hour after the placement of the slab is presented in Figure 5-15. It is interesting to note that the temperature predicted for the upper mid-depth of the slab is more sensitive to the thermal conductivity of the PCC than the lower mid-depth of the slab. This agrees with expectations, since the concrete slab with a higher k can lose more heat to the environment at the surface and therefore higher values of k can result in lower surface temperatures.

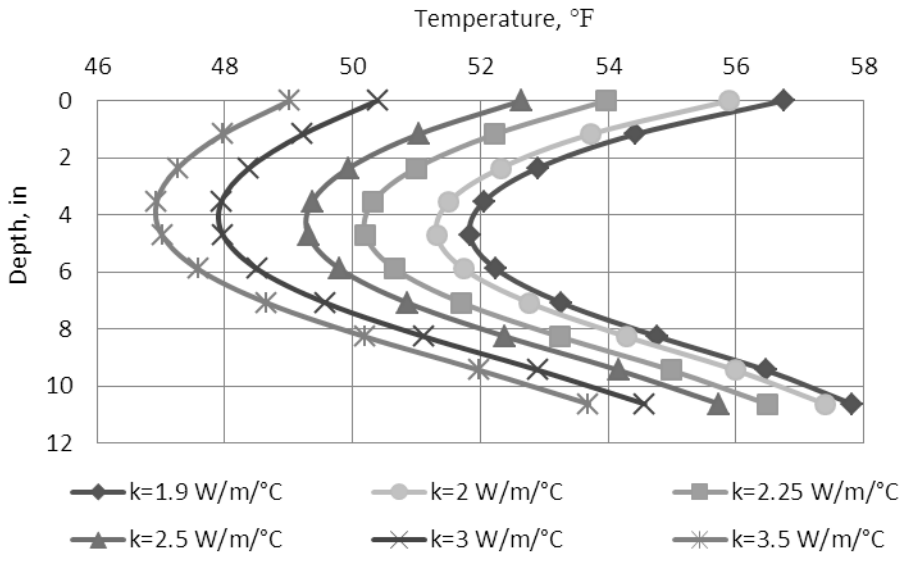

Figure 5-15. Sensitivity of temperature prediction across the depth of the PCC layer to thermal conductivity of the PCC.

The next parameter included in the study is the thermal conductivity of the base material. The range of variation for this parameter was defined based on the typical values available for different base materials in Table 5-4. According to this table, this parameter varies between 0.52 and 3.32 W/m/°C. The effects of changing the k on the temperature predictions are presented in Figure 5-16. Based on this figure, the predicted concrete temperature is not sensitive to the k of the base material.

The effects of the k of the base on the predicted slab temperatures were also investigated over the depth of the slab in Figure 5-17. As expected, this parameter affects the temperature corresponding to only the lower portion of the slab. Based on this graph, the predicted temperature at the bottom of the slab increases as the value of k for the base layer is raised. This agrees with logic, since with higher values of k, the base is able to lose more heat to the slab.

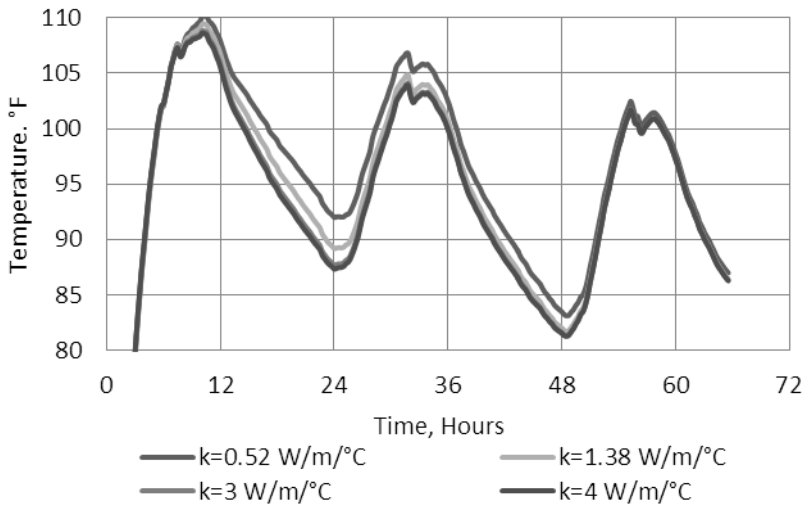

Figure 5-16. Sensitivity of the predicted temperature at the upper portion of the PCC layer to thermal conductivity of the base.

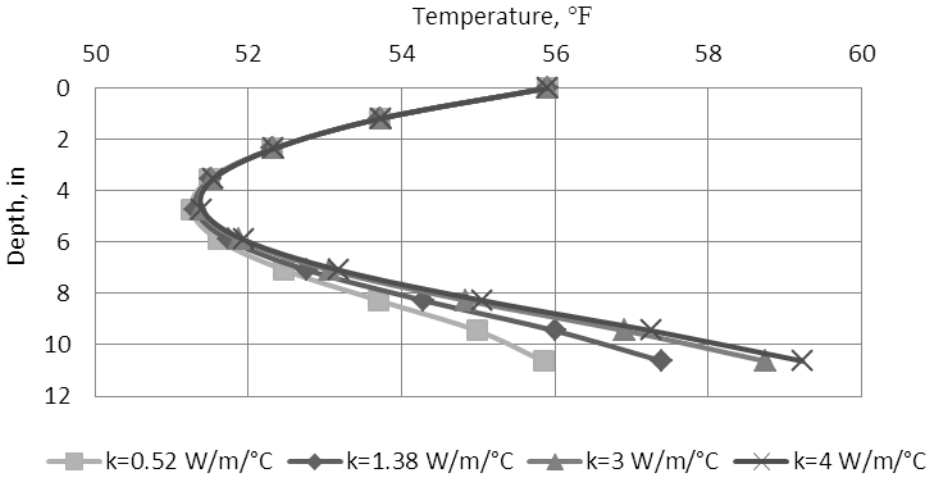

Figure 5-17. Sensitivity of the predicted temperature across the depth of the PCC layer to thermal conductivity of the base.

The next parameter included in the study is the thermal conductivity of the subbase material. Based on Table 5-4, this material can be either dry or wet gravel. The thermal conductivity for these two materials are 0.52 and 2.52 W/m/°C, respectively. This range was included in the study for the k of the subbase. The sensitivity of the k of the subbase to the

temperature predicted in the PCC slab is presented in Figure 5-18. Based on this figure, the temperature in the slab is not affected by the k selected for the subbase material.

The temperature predictions over the depth of the slab one hour after paving are also presented in Figure 5-19. The results presented in both Figure 5-18 and Figure **5-19** reveal that the k of the subbase does not have a significant influence on temperature predictions in the PCC slab.

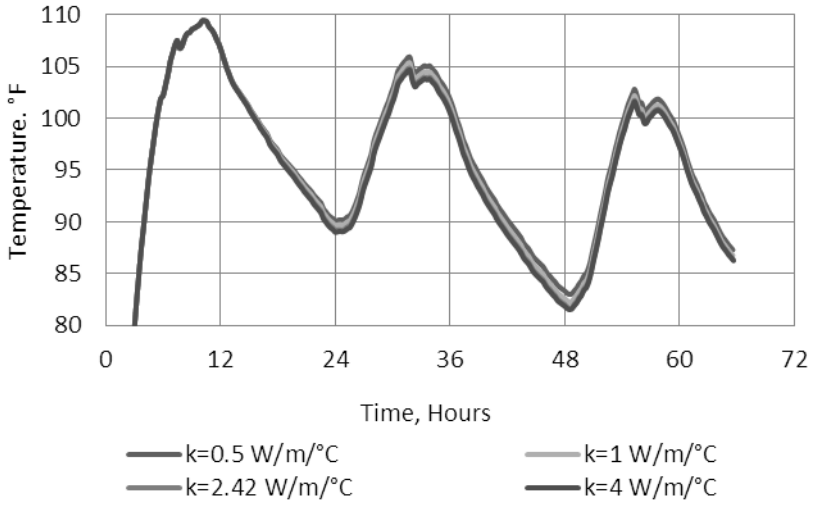

Figure 5-18. Sensitivity of the predicted temperature in the upper portion of the PCC layer to thermal conductivity of the subbase.

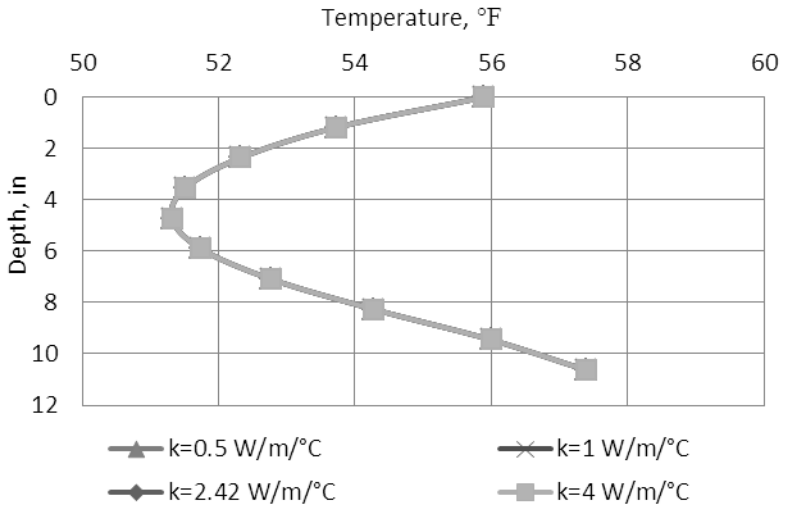

Figure 5-19. Sensitivity of the predicted temperature across the depth of the PCC layer to thermal conductivity of the base.

5.2.2 Model Validation-Project 2-Section B09, Eastbound

Project 2 featured the same structure as that for Project 1. The temperature model was employed to predict the temperature in this pavement structure for the first 48 hours after construction. The concrete mixture design was defined based on the information provided previously in Table 3-24. The cement composition was also provided previously in Table 3-27. The thermal properties for the sub-layers in the pavement structure were defined as the same as the ones used in Project 1.

It is noteworthy that the pavement section instrumented in this project was constructed in the month of May. Three instrumentation cells were constructed at three different times of the day. Cell 1 was constructed at 8:15 AM, Cell 2 at 3:30 PM and Cell 3 at 4:45 PM. The temperature model was implemented to predict the temperature variation over time for slabs in each cell. The predicted temperature at three different depths in the PCC slab are presented in Figure 5-20 to Figure 5-31 together with the measured data at the corresponding depth.

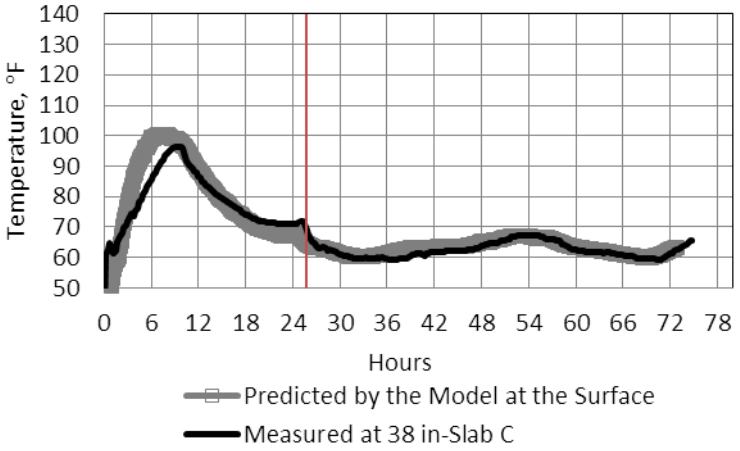

Figure 5-20. Model predictions in comparison to field measurements at the surface of the slab, Cell 1, Project 2.

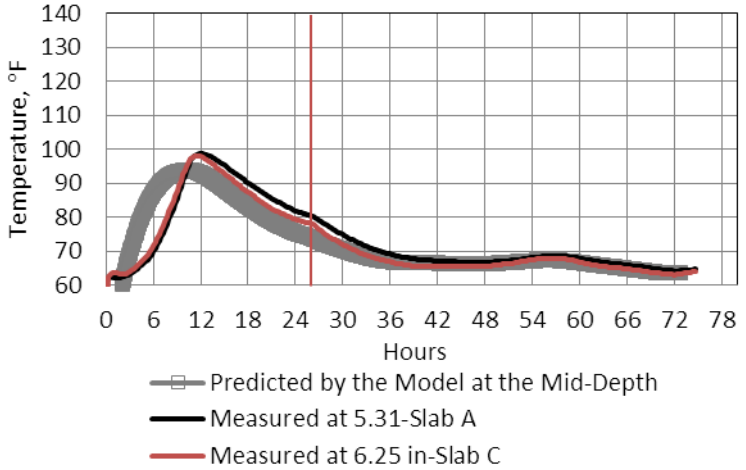

Figure 5-22. Model predictions in comparison to field measurements at the mid-depth of the slab, Cell 1, Project 2.

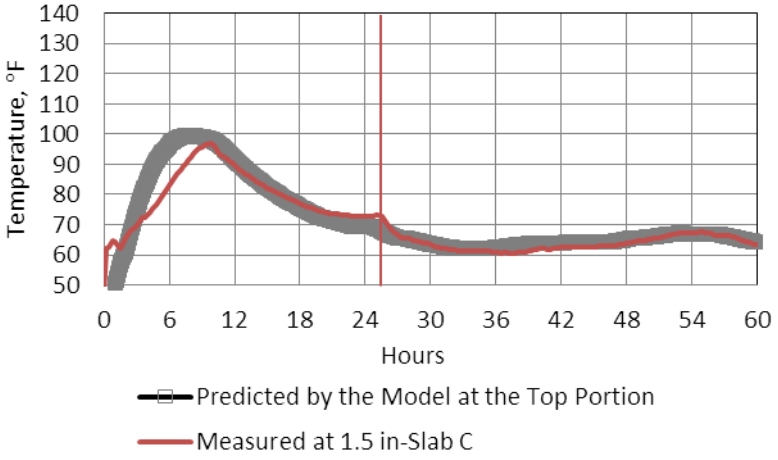

Figure 5-21. Model predictions in comparison to field measurements at the upper portion of the slab, Cell 1, Project 2.

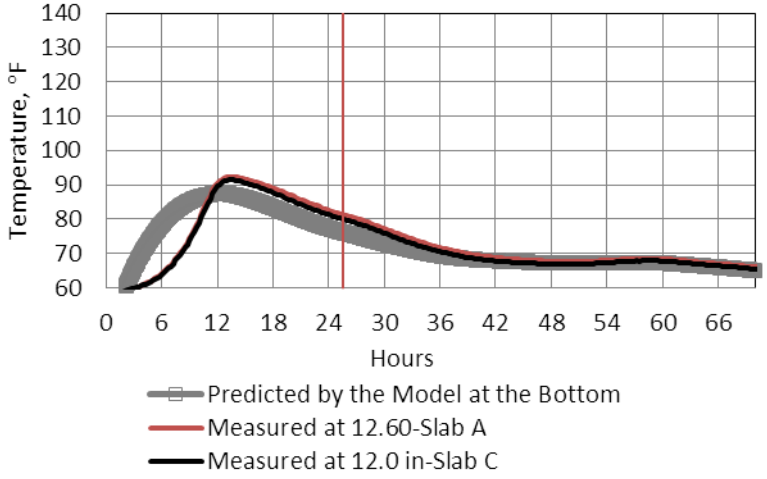

Figure 5-23. Model predictions in comparison to field measurements at the bottom of the slab, Cell 1, Project 2.

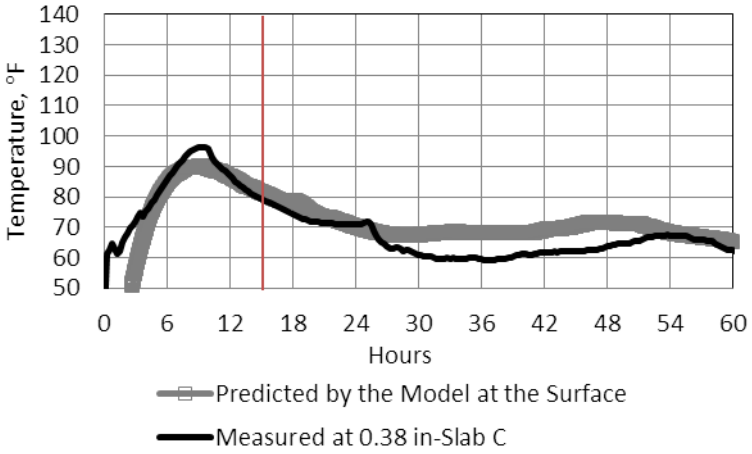

Figure 5-24. Model predictions in comparison to field measurements at the surface of the slab, Cell 2, Project 2.

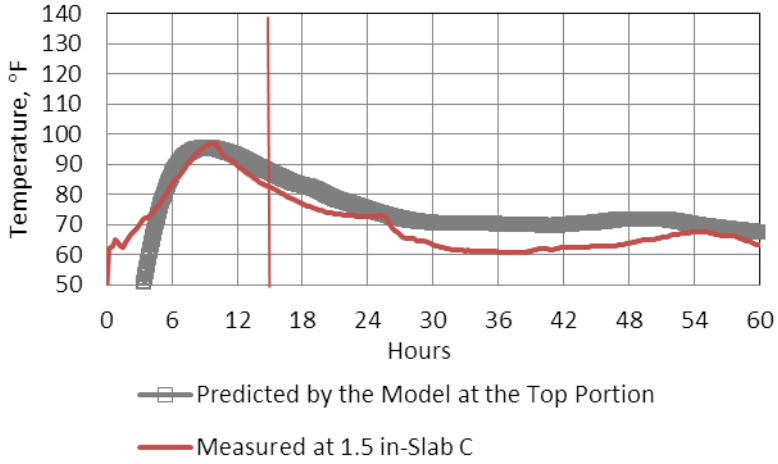

Figure 5-25. Model predictions in comparison to field measurements at the upper portion of the slab, Cell 2, Project 2.

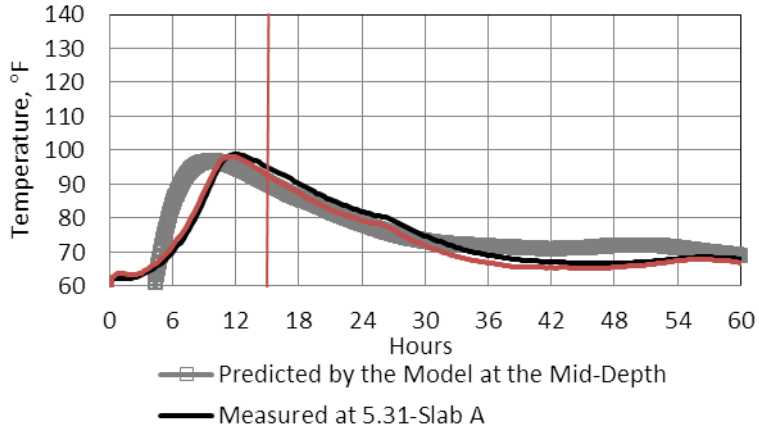

Figure 5-26. Model predictions in comparison to field measurements at the mid-depth of the slab, Cell 2, Project 2.

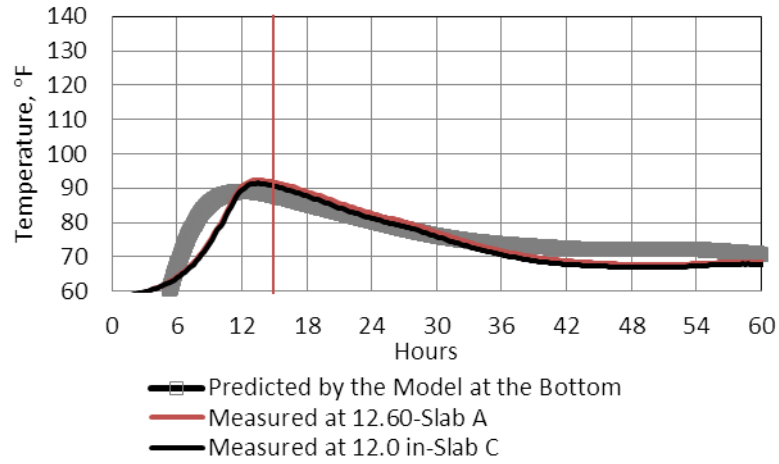

Figure 5-27. Model predictions in comparison to field measurements at the bottom of the slab, Cell 2, Project 2.

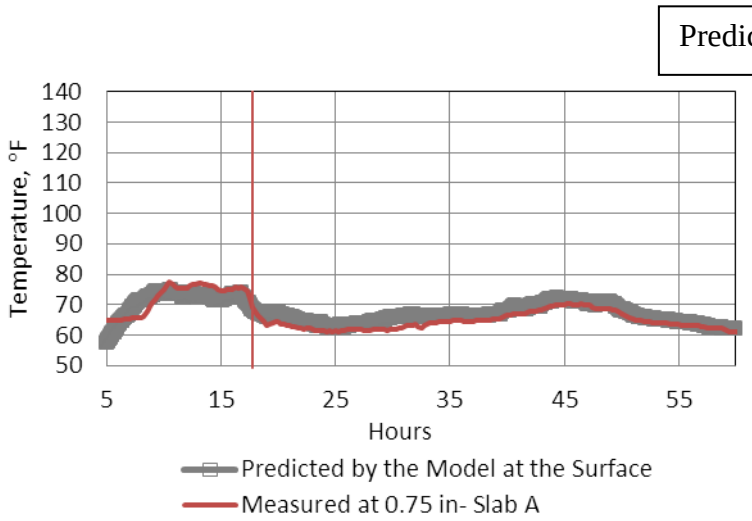

Figure 5-28. Model predictions in comparison to field measurements at the surface of the slab, Cell 3, Project 2.

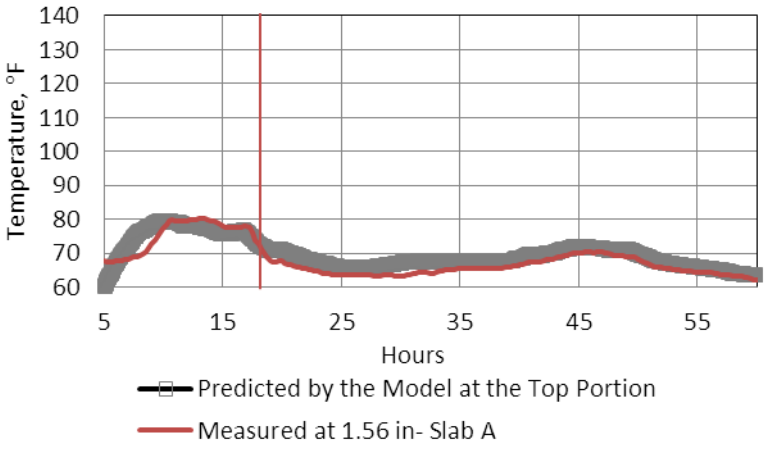

Figure 5-29. Model predictions in comparison to field measurements at the upper portion of the slab, Cell 3, Project 2.

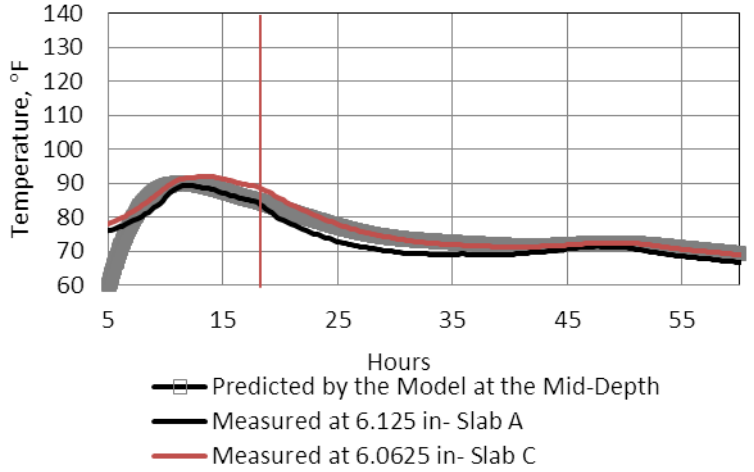

Figure 5-30. Model predictions in comparison to field measurements at the mid-depth of the slab, Cell 3, Project 2.

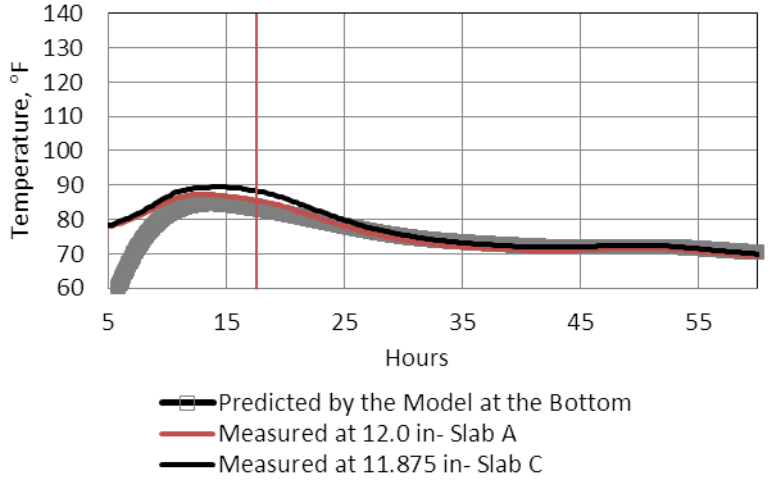

Figure 5-31. Model predictions in comparison to field measurements at the bottom of the slab, Cell 3, Project 2.

5.2.3 Model Validation-Project 3- SR-22, Section B10

The third project instrumented as part of this study included another nine slabs on SR 22 in Westmoreland County, Pennsylvania. Field data from this project was not used in the model validation because the slabs in all three cells were covered with plastic sheets upon placement due to cold weather conditions and rain. The application of plastic sheets on the newly constructed slabs prevented heat exchange between the slabs and the environment, influencing temperature variation in the slabs.

5.2.4. Model Validation-Project 4-US 22

Project 4 was located in Clyde, Pennsylvania. The paving of this section of Route 22 started at 8:00 AM, on April 29th of 2010. Paving on the 29th continued until about 6:30 PM and was started again the next morning at 8:00 AM. Cell 1 and Cell 2 were paved during the first day of paving and in the afternoon while Cell 3 was constructed in the morning of the second day. The new pavement structure is a JPCP with 10-inch thick PCC slabs. More details on the PCC mixture and design features for this project were provided in 3.6.1.

The PCC design mixture, the cement and the fly ash type together with the ambient weather conditions measured at the site for Project 4 were incorporated into the temperature model to predict the slab temperature over the first 48 hours after paving. A summary of the values used to define each input in the model is presented in Table 5-7. The results are presented together with the measured temperature at the top, mid-depth and bottom of slabs in Cells 1, 2 and 3. See Figure 5-32 to Figure 5-43.

Table 5-7. Inputs for the temperature model for Project 4.

Category	Parameter	Value
Time and Space Steps	Δx (cm)	3
	Δt (hour)	varies
	Initial Temperature of concrete in Cell 1, °C	19
	Initial Temperature of concrete in Cell 2, °C	15
	Initial Temperature of concrete in Cell 3, °C	13
Nodes	Nodes in PCC Slab (No.)	8
	Nodes in Base Layer (No.)	3
	Nodes in Sub-base Layer (No.)	5
	Nodes in Subgrade Layer (No.)	45
Thermal Conductivity	k_∞ of Concrete (W/m/°C)	2
	k of Base Layer (W/m/°C)	3.32
	k of Sub-base Layer (W/m/°C)	2.42
Weather Data	Temperature, Wind Speed, Precipitation, Solar Radiation	Measured at the Site
Analysis Time	Time (Hours)	140

According to these figures, the model is able to predict temperature variation in the slabs and the predictions agree relatively well with the measurements in the field. Some variation between the predicted and measured values is seen in Cell 1 and 2 at very early ages. The heat of hydration is predicted too early during the afternoon for the first day in Cell 1. The heat of hydration is also overestimated in Cell 2. This could be because of the hydration time and shape factors that were established by employing regression models. For more accurate results at early ages, these factors need to be established based on the heat signature graphs established using calorimeters.

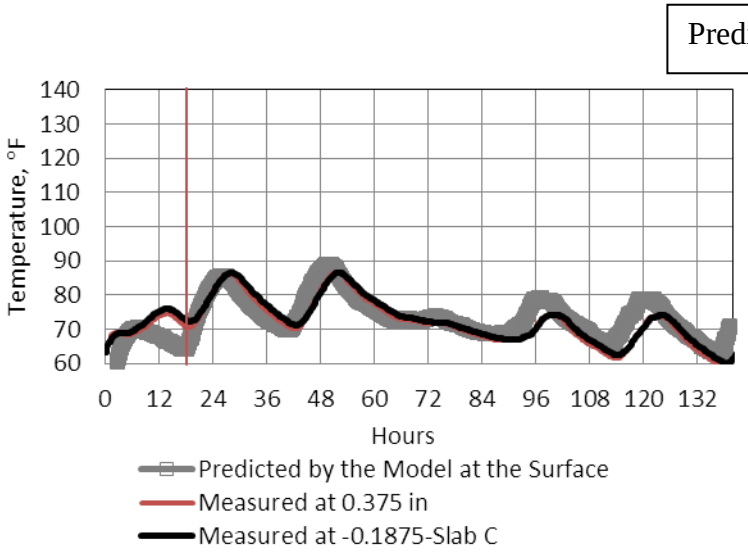

Figure 5-32. Model predictions in comparison to field measurements at the surface of the slab, Cell 1, Project 4.

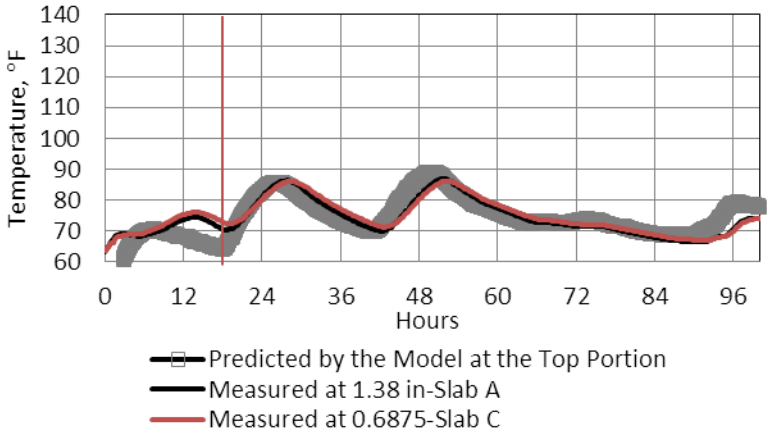

Figure 5-33. Model predictions in comparison to field measurements in the upper portion of the slab, Cell 1, Project 4.

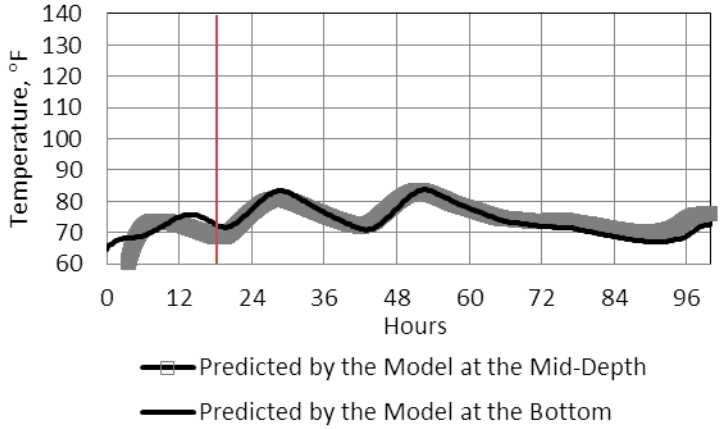

Figure 5-34. Model predictions in comparison to field measurements at the mid-depth of the slab, Cell 1, Project 4.

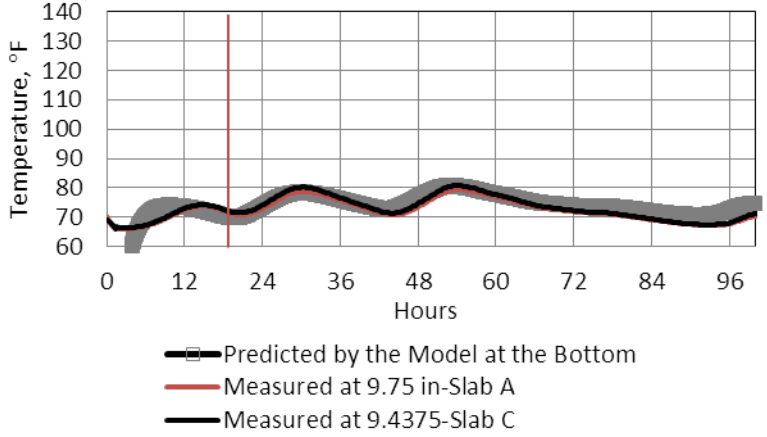

Figure 5-35. Model predictions in comparison to field measurements at the bottom of the slab, Cell 1, Project 4.

Predictions in Cell 2-Project 4

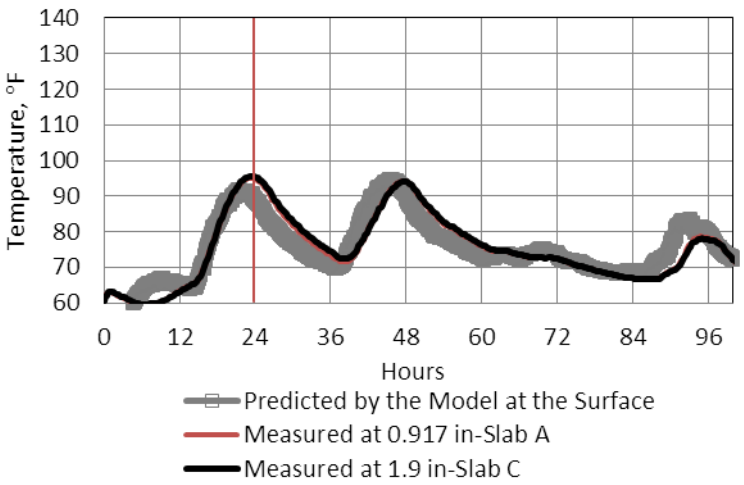

Figure 5-36. Model predictions in comparison to field measurements at the surface of the slab, Cell 2, Project 4.

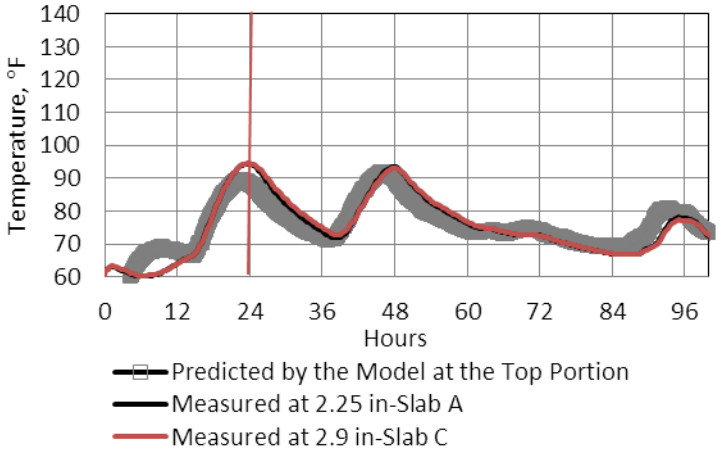

Figure 5-37. Model predictions in comparison to field measurements at the surface of the slab, Cell 2, Project 4.

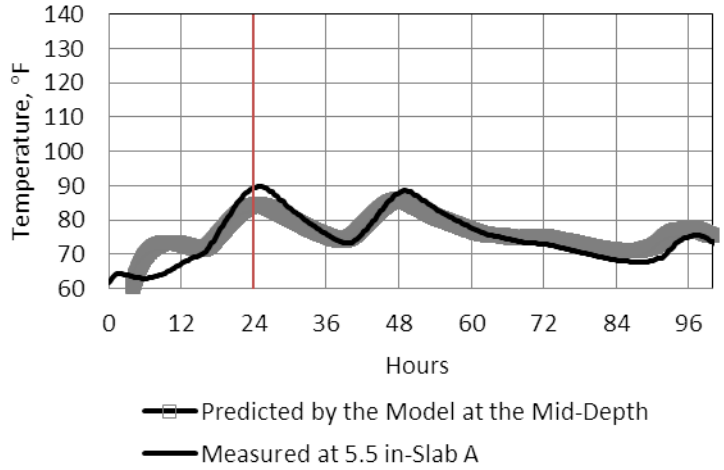

Figure 5-38. Model predictions in comparison to field measurements at the mid-depth of the slab, Cell 2, Project 4.

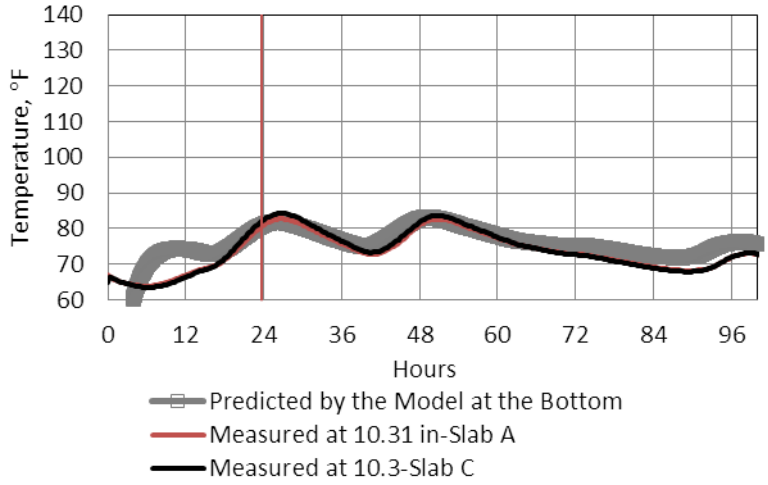

Figure 5-39. Model predictions in comparison to field measurements at the bottom of the slab, Cell 2, Project 4.

Predictions in Cell 3-Project 4

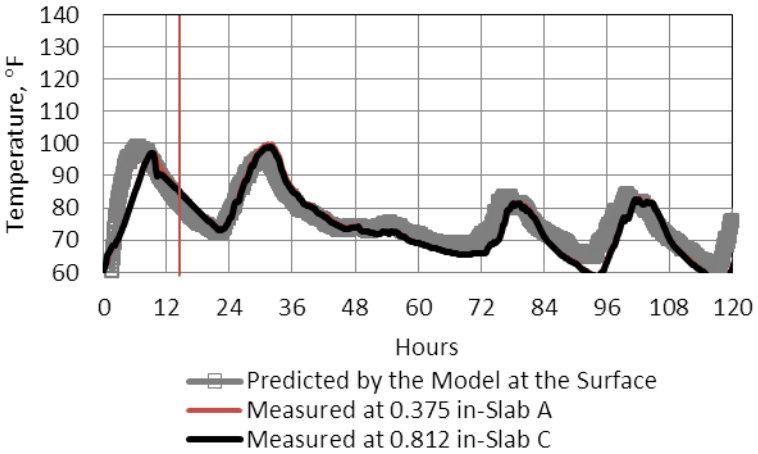

Figure 5-40. Model predictions in comparison to field measurements at the surface of the slab, Cell 3, Project 4.

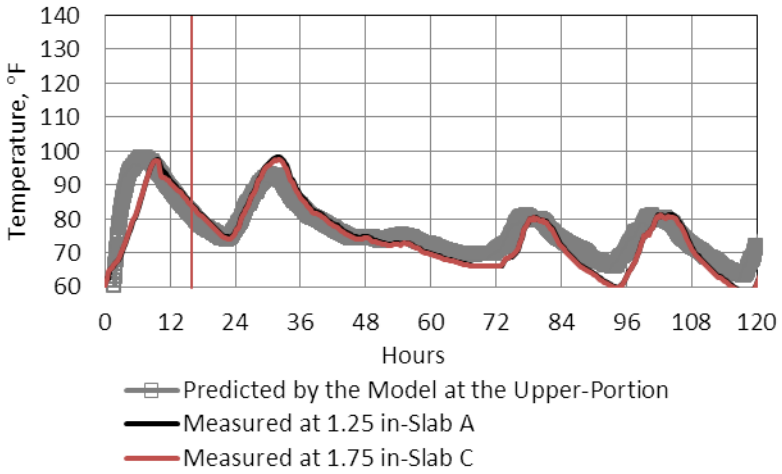

Figure 5-41. Model predictions in comparison to field measurements at the upper portion of the slab, Cell 3, Project 4.

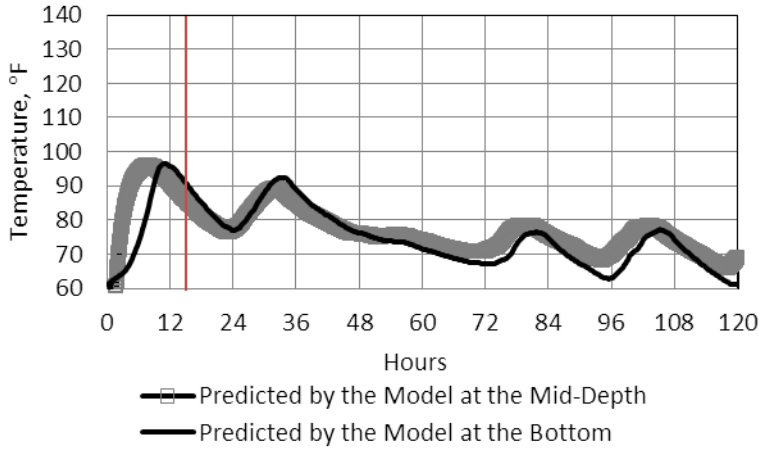

Figure 5-42. Model predictions in comparison to field measurements at the mid-depth of the slab, Cell 3, Project 4.

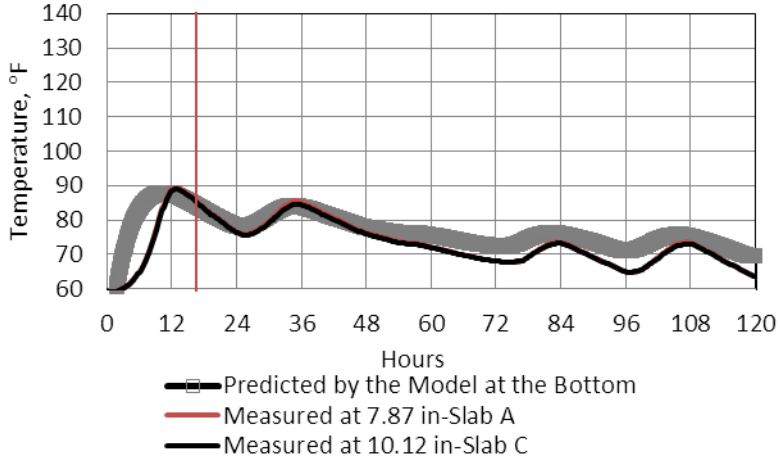

Figure 5-43. Model predictions in comparison to field measurements at the bottom of the slab, Cell 3, Project 4.

6.0 CHAPTER 6-ESTABLISHING PERMANENT WARP GRADIENT

6.1 INTRODUCTION

As discussed previously in Chapters 1 and 2, permanent warping of the slab is the result of the irreversible drying shrinkage gradient in slab. To be able to add together the effects of the permanent warping gradient and the permanent curling in the slab, established earlier in Chapter 4, this parameter needs to be defined in the form of a temperature gradient. This equivalent temperature gradient must produce the same curvature in the slab as that produced by the actual drying shrinkage gradient. Establishing the permanent warping gradient for a concrete slab in the field can be quite challenging. Part of this is due to the restraining effects of variables, such as the dowel/tie bars and the friction between the base and the slab at the interface. In addition to the constraints in the field, the possible creep in the slab can recover a portion of the permanent warping over time. The ultimate goal of this chapter is to put forward a practical and inclusive procedure for estimating equivalent temperature gradient for the permanent warping in JPCPs.

Different methodologies available for establishing a temperature gradient equivalent to the drying shrinkage gradient in the slab were discussed earlier in Section 2.3.2. These procedures include the relation developed by Eisenmann in 1990, the empirical procedure incorporated into the MEPDG design software and lastly, the method developed by Mohamed and Hansen in 1997. The latter method is applied in this study for establishing the equivalent

temperature gradients. In this method, the RH profile throughout the slab depth is used to estimate a humidity difference coefficient. A third-degree polynomial function is then fit through the humidity difference coefficients across the slab depth. The regression coefficients from the polynomial function are used to establish an equivalent linear humidity difference coefficient. The product of the humidity difference coefficient and the ultimate drying shrinkage of the concrete, provides an estimate of the drying shrinkage strain in the slab at the time of interest (Jeong and Zollinger 2005). This strain, when divided by the CTE of concrete, produces an equivalent temperature gradient.

From the brief description of the procedure provided above, it is apparent that this method requires two major pieces of data, the RH profile in the slab and the ultimate drying shrinkage of the PCC mixture. Clearly, the most reliable way to establish the RH profile in the slab is through field measurements. As discussed in Section 2.3.2, several probes, sensors and devices have been developed to measure the internal RH of the concrete. Instrumentation of concrete slabs in-place, however, is extremely extensive and costly. A numerical model that is able to predict the RH variation within the slab that has been validated using measurements can best replace the need for the instrumentation of the slab. Such model will be implemented in the first section of this chapter.

The second piece of information required for establishing permanent warping, when using the Mohamed and Hansen method, is the ultimate drying shrinkage for the concrete mixture. This parameter can be established by measuring the change in length of concrete prisms stored under controlled climatic conditions. Empirical relations are also available that can be employed to predict this property of the mixture. These relations estimate the ultimate drying shrinkage as a function of the PCC mixture design and mechanical properties. The most

widely-used example of these relations (Bazant and Baweja 2000), was introduced in Section 2.3.2. The final product of the ultimate drying shrinkage of the mixture and the equivalent linear humidity difference coefficient is the drying shrinkage strain in the slab, which will be referred to as the "predicted" drying shrinkage strain, hereafter.

One should note that the "in-situ" drying shrinkage in concrete slabs is a structural property that is affected by the constraints in the field and the time-dependent creep, as mentioned earlier. The effect of these factors is not considered in the methodology described above for establishing the predicted drying shrinkage. Therefore, drying shrinkage strains measured in in-service pavements are required to modify the predicted drying shrinkage strains.

A study performed in 2001 (Burnham and Koubaa 2001) introduced a new approach to establishing the time-dependent development of the in-situ drying shrinkage in the slab. This study was performed based on an extensive database of strain measurements available for several pavement structures at MnROAD. In the 2001 study, the in-situ drying shrinkage was established for five different pavement structures. The 2001 study is extended in this chapter to include the data from two more pavement structures at MnROAD. Additionally, the same approach as the 2001 study was followed to establish the development of drying shrinkage in two sets of 6-year old concrete slabs located in Western Pennsylvania, referred to as the SR 22 project, hereafter.

At last, the measured drying shrinkage for the SR 22 and the MnROAD cells is compared to the predicted drying shrinkage, discussed previously. The difference between the two is attributable to the possible effects of the restraining factors existing in the field and also the relaxation due to creep.

This chapter starts with an introduction to the SR 22 test section followed by details on the implementation and validation of a numerical RH model. The chapter continues with establishing the "predicted" drying shrinkage for the cells at SR 22. The "measured" drying shrinkage will also be established for the slabs in both SR 22 and at MnROAD. The last portion of the chapter will focus on developing field correction factors for adjusting the predicted drying shrinkage based on the measured values.

6.2 OVERVIEW OF SR 22 TEST SECTION

Section B01, a 2-mile stretch of SR 22, located in the municipality of Murrysville in Westmoreland County, Pennsylvania was constructed in August of 2004. Prior to the paving of the section, a total of six JPCP slabs were instrumented with Type T thermocouples from Omega Engineering, Model 4200 VW static strain gages from Geokon and SHT75 humidity/temperature sensors from Sensirion. Figure 6-1 presents a schematic layout of the instrumented slabs. These six slabs were divided into two different cells. As seen in Figure 6-1 (a), Cell 1 consisted of three consecutive unrestrained (no dowel or tie bars) PCC slabs. Cell 2 consisted of three restrained PCC slabs. The restrained slabs feature No. 5 epoxy-coated tie bars and 1.5-inch diameter epoxy-coated dowel bars placed at every 12 inches along the transverse joints. Slab Z is a transition slab that separates the two cells. The design features the test section is summarized in Table 6-1.

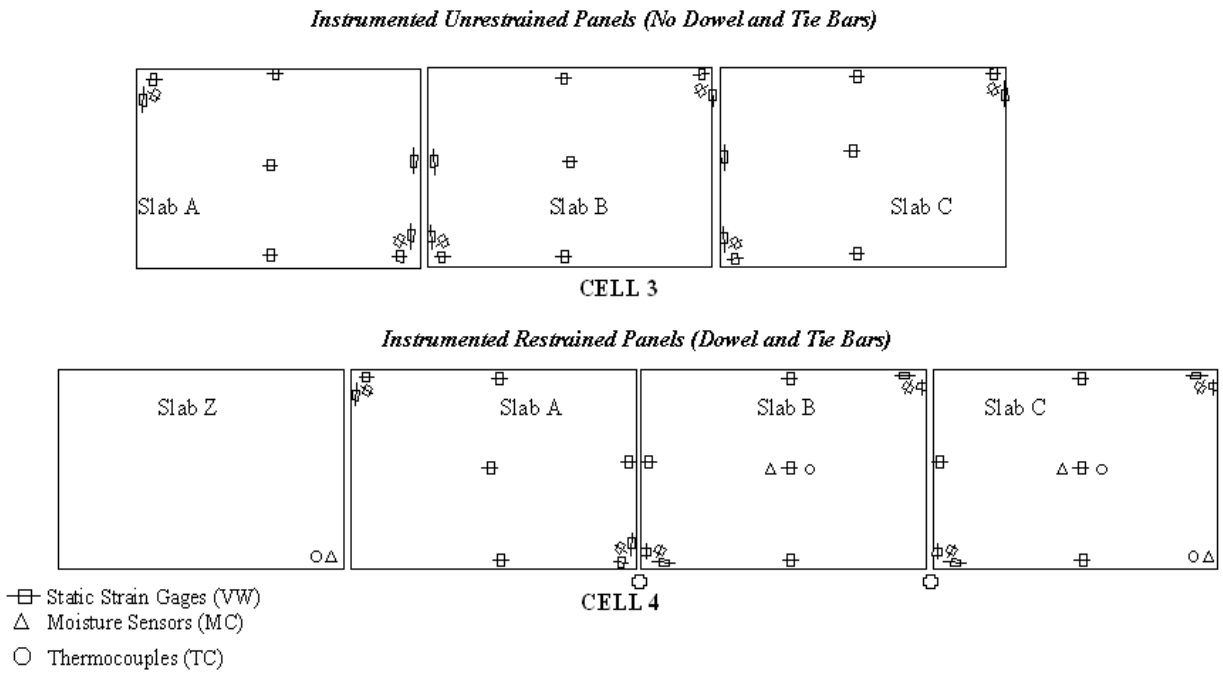

(a)

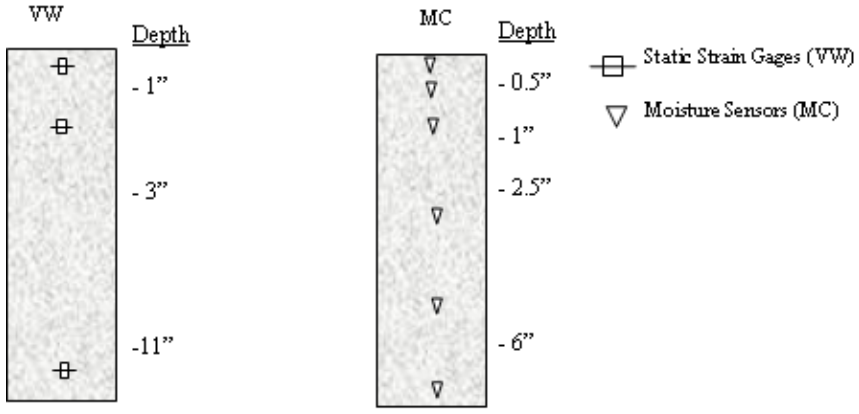

(b)

Figure 6-1. (a) Location and (b) depth of VW gages, moisture and temperature sensors in the test section.

Table 6-1. Design features for the slabs at SR 22 test section.

Cell No.	Construction Date	Slab Thickness (inch)	Base Type	Dowel Diameter (inch)	Slab Width (ft)	Slab Length (ft)
1	8/16/2004	12	ATPB	1.5	12	15
2				None		

The mixture design for the PCC used to pave the section can be found in Table 6-2. The concrete material properties including the CTE, 28-day compressive strength and the ultimate drying shrinkage of the PCC mix for the test section were established in the laboratory. The subsequent results are provided in Table 6-3. This table also includes the ultimate drying shrinkage established using the Bazant empirical relation introduced previously in Section 2.3.2, Equation 2-19.

Table 6-2. Mixture design and fresh concrete properties for the paving PCC for SR 22.

Weight in the Batch (lb/yd^3)				
Cement	Ground Granulated Blast Furnace Slag	Water	Fine Aggregate	Coarse Aggregate
Type I, 382	206	286	1248	1881
Fresh Concrete Properties				
Slump (inch)		Air Content (%)	Unit Weight (lb/ft^3)	
2		5.3	143.3	

Table 6-3. CTE, strength and ultimate drying shrinkage for the PCC used to pave SR 22 test section.

CTE (10^{-6}/°F)	28-day Compressive Strength (psi)	Ultimate Drying Shrinkage (με)			
		Laboratory Test			Bazant Relation
		Sample 1	Sample 2	Sample 3	
5.9	6095	815	1000		700

The slabs in Cell 1 were instrumented with VW static strain gages, while the slabs in Cell 2 were instrumented with thermocouples and RH sensors as well as VW strain gages. The data from the VW gages were collected at 15-minute intervals since the time of paving until present. The RH sensors remained active only over the first two years following the construction of the test section. The nature of the instrumentation and the respective equipment, including VW static strain gages and thermocouples together with the datalogging systems, was the same as

that used in the four test sections instrumented in 2009 and 2010. This was previously discussed in details in Chapter 3, Section 3.2. The RH sensors were not used in the previously discussed test sections, hence a brief description of these sensors is provided below.

6.2.1.1 SHT75 Sensors

The Sensirion SHT75 sensor is a relatively small (approximately 0.75- by 0.25- by 0.125 inch) and cost effective means of measuring RH in the concrete. The module, pictured in Figure 6-2, uses a capacitive polymer sensing element to measure RH and a band gap temperature sensor to measure temperature (Grasley, Lange et al. 2006). Procedures were developed at the University of Illinois at Urbana-Champaign for the use of these sensors in concrete.

Figure 6-2. Sensirion SHT75 humidity and temperature Sensor, (www.sensirion.com, June 2005).

To protect the sensors from direct exposure to the concrete, a sensor housing system was employed. The sensor is inserted into a plastic cylindrical tube for protection. The end of the tube is sealed with a circular GORE-TEX^{TM} membrane vent. These vents act to protect the sensor from exposure to cement particles and excessive water exposure, while allowing the passage of water vapor for accurate humidity readings (Grasley, Lange et al. 2003). The final result, shown in Figure 6-3, is a cost-effective means of measuring the relative humidity in the PCC.

Figure 6-3. Installation of relative humidity sensors in SR 22 test section (Wells, Phillips et al. 2005).

6.3 NUMERICAL MODEL TO PREDICT INTERNAL RH

As discussed previously, a numerical model is implemented in this chapter to predict the internal RH of concrete throughout the slab depth over time. The predictions of the model will be fitted to the measured RH in the slabs at SR 22 test section to achieve the best agreements between the predicted and measured values. The theory and mathematical equations behind the model will be discussed first.

6.3.1 Diffusion Equation

The distribution of the RH in the pores of the concrete can be described using the diffusion theory, based on the Fick's second law, presented in Equation 1 (Bazant and Najjar 1972; Akita, Fujiwara et al. 1997; Jeong, Wang et al. 2001; Oh and Cha. 2003).

$$\frac{\partial H}{\partial t} = (\frac{\partial H}{\partial w})_T \frac{\partial}{\partial x}(C(H)\frac{\partial H}{\partial x}) + (\frac{\partial H}{\partial T})_w \frac{\partial T}{\partial t} + \frac{\partial H_g}{\partial t} \quad (6\text{-}1)$$

The parameter, t, in Equation 6-1 is time, in terms of hour, and the parameter, H, stands for the concrete internal RH. Other parameters in Equation 6-1 are defined individually as follows. The term $(\frac{\partial H}{\partial w})_T$ in Equation 6-1, is the cotangent of the slope of the desorption-adsorption curve, also known as sorption isotherms, at temperature T. The sorption isotherms are largely a function of the pore size of the concrete and therefore the w/cm ratio also the cement content, and the degree of hydration. These isotherms can be established in the laboratory in a relative humidity chamber (RILEM Bulletin 1981; Grasley, Lange et al. 2006). For the sake of simplification, the slope of the desorption isotherm has been previously assumed as constant over a wide range of RH (Bazant and Najjar 1972; Xin, Zollinger et al. 1995). The other factor in Equation 6-1 is the term $(\frac{\partial H}{\partial T})_w$, which defines the effect of temperature change on the concrete RH. In general, it is expected that an increase in temperature result in a decrease in RH. However, typical experimental measurements of temperature and RH inside the concrete has shown that the temperature change can only lead to a very small variation in RH (Zhang, Qi et al. 2009). Similar results were observed in other studies (Akita, Fujiwara et al. 1997; Andrade, Sarria et al. 1999). The term $(\frac{\partial H_g}{\partial t})$ in Equation 6-1, corresponds to the moisture loss

during hydration due to self-desiccation. This study focuses on long-term humidity changes in the slab so variation in the early age humidity is not the concern. It is also noteworthy that, due to the high w/cm ratio for the PCC mixture, higher than the minimum required value of 0.42, the chance of the occurrence of self-desiccation in the concrete during hydration is minimal. The final form of Equation 6-1 used in this study is presented in Equation 6-2:

$$\frac{\partial H}{\partial t} = \frac{\partial}{\partial x}(C(H)\frac{\partial H}{\partial x}) \tag{6-2}$$

Moisture diffusivity, C(H), in Equations 6-1 and 6-2, is a key material parameter which determines the moisture transport "speed" in the concrete (Xu, Ruiz et al. 2009). This parameter is a function of the internal RH, porosity and concrete age (McCullough and Rasmussen 1999). It is almost impossible to directly measure this material property (Xin, Zollinger et al. 1995). Different relations have been historically proposed for the diffusivity by several researchers (Sakata 1983; Ayano and Wittman 2002). The most widely accepted relation for estimating the diffusivity is the one developed by Bazant (Bazant and Najjar 1972). In this relation, diffusivity is defined based on the level of relative humidity in the concrete. This relation is presented in Equation 6-3.

$$C(H) = C_1(\alpha_0 + \frac{1-\alpha_0}{1+(\frac{1-H}{1-H_c})^n}) \tag{6-3}$$

C_1 in this relation is the diffusivity of the saturated mix in $cm^2/hour$. The definition of the other parameters in Equation 6-3 is better described suing Figure 6-4. This figure shows the strong dependence of the diffusivity, C, on the internal RH of concrete. As seen in this figure, α_0 represents the ratio of C_{min}/C_{max}, and n characterizes the spread of the drop in C. H_c is the RH at

which C drops halfway between its maximum and minimum and is namely 0.75 for all concrete mixtures.

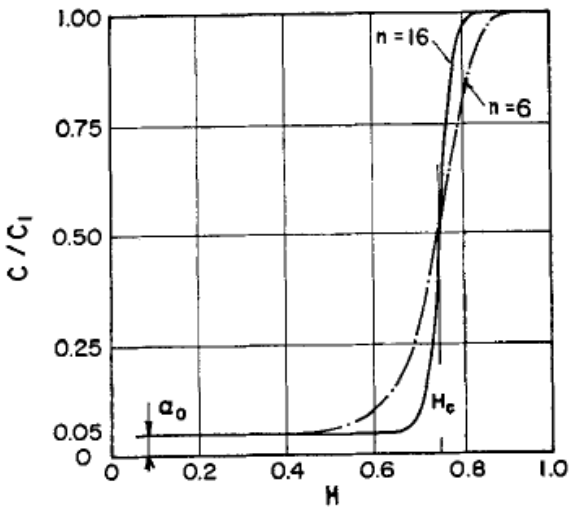

Figure 6-4. Diffusivity, C, versus humidity, H, for n=16, 6 and α_0=0.05 and Hc=0.75 (Bazant and Najjar 1972).

A relation was provided for C_1 by Bazant as part of the Bazant-Panula (BP) drying shrinkage model (Bazant and Panula 1978). In this relation, C_1 is defined based on concrete age, temperature during drying and PCC mixture properties. This relation is provided in Equation 6-4.

$$C_1(t) = C_7 k'_T \, (0.05 + \sqrt{6.3/t}) \qquad (6\text{-}4)$$

C_7 in Equation 6-4 is the assumed or given value of C_1 at age 7 days, obtained from the following relation:

$$C_7 = \frac{1}{8} w/cm \, C - 12 \qquad (6\text{-}5)$$

where, c = Cement content, kg/m^3

if $C_7 < 7$ set $C_7 = 7$, and if $C_7 > 21$ set $C_7 = 21$.

k'_T = Temperature coefficient obtained from the following relation:

$$k'_T = \frac{T}{T_0}\exp\left(\frac{5000}{T_0} - \frac{5000}{T}\right) \quad (6\text{-}6)$$

where, T = Temperature of the environment, Kelvin, T_0 = Reference temperature, Kelvin

Another study in 1997 (Akita, Fujiwara et al. 1997) also developed a relation for the diffusion coefficient, C_1, based on the w/cm ratio of the mixture. This relation is provided below:

$$C_1 = 230/w/cm + 0.25w/cm - 14.7 \quad (6\text{-}7)$$

6.3.2 Numerical Modeling and Boundary Conditions

Equation 6-2 can be solved using a step-by-step integration in time, best applied in conjunction with the finite difference method (Bazant and Najjar 1972). Details on the FDM formulation were previously provided in Section 5.1.5 and will not be provided here to avoid repetition. A total of 15 nodes in space, with Δx equal to 2 cm, were defined for modeling a 12-inch PCC slab. The initial condition of the PCC was defined as fully saturated (H equal to 100 percent.) As seen in Equation 6-3, the diffusivity, C(H), in this relation is highly dependent on the internal RH. C(H) can be estimated easily when using FDM, which solves PDEs at each time step. This way C can be estimated at the current time step based on the humidity estimated at the previous time step.

Proper boundary conditions need to be defined at the top and bottom of the slab. The RH at the slab surface should be in balance with the ambient RH. The rate of moisture exchange between the pavement surface and the environment can be characterized using a simple expression. Based on this expression, provided in Equation 6-8, the moisture exchange between the slab and the environment is relative to the difference between the Gibbs free energies (GFE) per unit mass of water in concrete and in the environment.

$$C(H)\frac{\partial H}{\partial x} = f(H_{ambient} - H_{surface}) \quad (6\text{-}8)$$

The factor f in Equation 6-8 is the surface emissivity coefficient (Akita, Fujiwara et al. 1997) modified based on the curing conditions (Xu, Ruiz et al. 2009). At the bottom (slab/base interface), the PCC slab is considered relatively saturated, based on RH measured in the slabs in the field.

6.4 CONCRETE RELATIVE HUMIDITY MODEL PREDICTED

The best values for the model inputs were established through iterations until the predicted and measured RH converged. Foremost, the ambient RH measured by an onsite weather station at the SR 22 test section was incorporated into the numerical model to predict the RH within the slab over the first two years after construction. The mean monthly ambient RH and temperature measured at the site for SR 22 is presented in Figure 6-5.

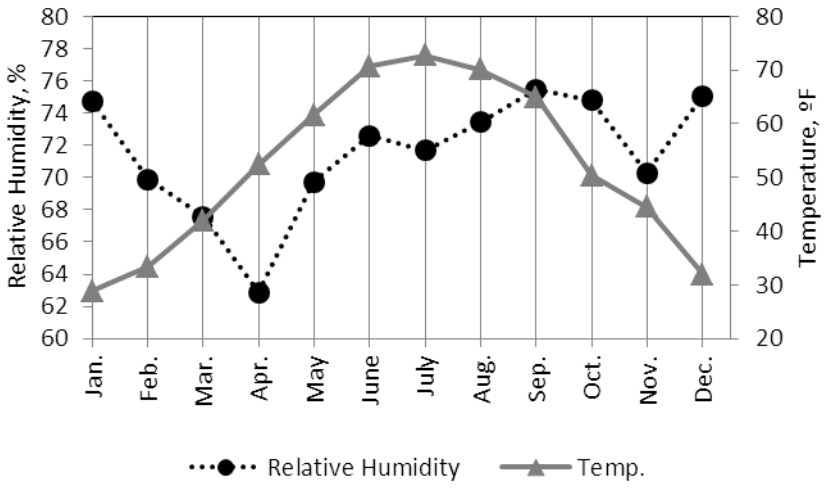

Figure 6-5. Ambient RH and temperature measured at the site for SR 22.

The RH in the slab was measured for the first two years after paving the SR 22 test section. A total of 24 SHT75 RH and temperature sensors were installed at various depths of the slabs in Cell 2 as shown schematically in Figure 6-1. However, out of 24, only the sensors installed at the center of Slab C and at the edge of the transition slab (Slab Z) remained active after the construction of the test section. The active sensors at the center of Slab C include the sensors installed at depths of 0.7-, 1.0- and 10.0 inch. The active sensors at the corner of Slab Z are the sensors installed at depths of 1.55-, 1.6-, 6.6-, and 10.4 inch.

The RH measured at different depths of the slab, at the two aforementioned locations over two years after construction is presented in Figure 6-6. Based on the figure, the measured RH can be analyzed in two ways, first with respect to slab depth in each location and then with respect to location. When considering the RH measured at each location at different depths, it is noticed that, the RH shows variation only in the upper 2 inches of the slabs. The remainder of the slab remains mostly saturated almost the entire time.

When comparing the measurements between locations, it is seen that the variation in RH at the upper portion of the slab is consistent between the two locations over the first year after construction. During the second year, however, the RH measured at the top in the corner of Slab Z deviates from the RH measured at the top in the center of Slab C. The RH at the corner drops down to around 55 percent at age 500 days, while it stays as high as 72 percent at the center of Slab C. This behavior makes sense, since more drying occurs at the corners of the slab in comparison to the center of the slab. The RH measured at the center of the slab will be used in the section for calibrating the model predictions.

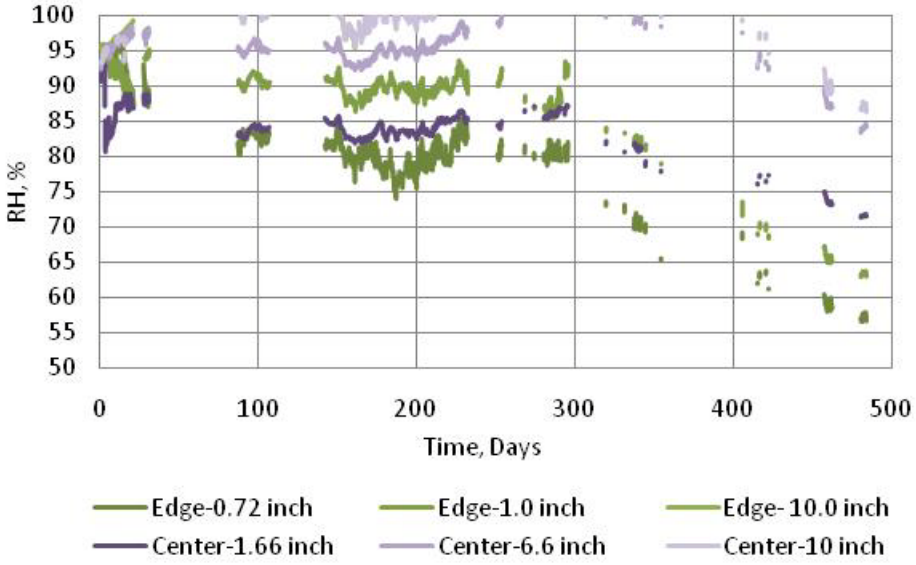

Figure 6-6. RH measured within the slabs at SR 22 over two years at two different locations.

As seen in Equation 6-3, three parameters including, C_1, n and α_0, are involved in defining C. A range of values have been suggested in literature for each of these parameters for different PCC mixtures. A small one-at-a-time sensitivity study including these three variables with a typical range of variation found in literature for each parameter was performed using the

numerical model. Typical values for each parameter involved in the study was used for the base conditions (Bazant and Najjar 1972). Table 6-7 presents a list of the variables used in the sensitivity analysis and their corresponding values.

Table 6-4. Summary of the parameters included in the sensitivity analysis and their corresponding values.

Parameter	C_1(cm^2/day)	n	α_0
Values for the Base Run	0.25	6	0.1
Range of Variation	0.4	1	0.025
	0.6	16	0.04
	0.8	25	0.06
	1.0	35	-
	1.53	-	-

The first variable from Table 6-7 considered in the study is C_1. Based on past laboratory tests on samples from different PCC mixtures, C_1 can range between 0.187 to 1.93 cm^2/day (Bazant, Xi et al. 1993). A typical value for C_1 has been reported as 0.25 cm^2/day (Bazant, Xi et al. 1993). The value of 1.53 cm^2/day in Table 6-7, was established by using the relation provided in Equation 6-7. Figure 6-7 shows the sensitivity of the predictions of the model at depth 1.57 inch to different values of C_1. The measured RH in Slab C at a depth of 1.6 inch is also superimposed on Figure 6-7 for comparison. This depth is selected for comparison since the most variation in the RH is seen in the upper 2-inch of the slab. The proper value for C_1 in Figure 6-7 is selected based on the best match between the predicted and measured data.

Based on Figure 6-7, overall, the RH predicted using the numerical model, decreases with an increase in the value of C_1. According to Figure 6-7, the predictions obtained when using higher values ranging between 0.8 and 1.5 cm^2/day for C_1 show agreement with the measured data for a longer period of time.

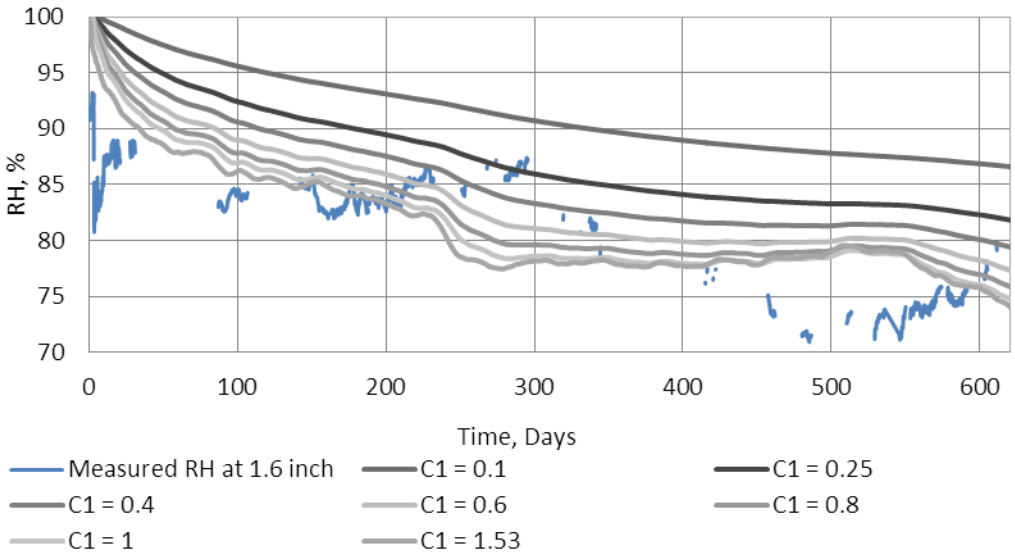

Figure 6-7. Effects of C_1 on the model predicted values at depth 1.6 inches.

The range of values selected for C_1 is quite high in comparison to the typical range of 0.1 to 0.4 cm^2/day suggested by Bazant. However, one should note that according to (Bazant and Najjar 1972) the typical range corresponds to dense concretes, while more porous concrete is expected to have a higher diffusivity. The paving PCC used for SR 22 can be considered a relatively porous mixture considering the high w/cm ratio of 0.48, air content of 5.3 percent and 50 percent ground granulated blast furnace slag (GGBFS.) GGBFS tends to increase the volume of fine pores in the cement hydration products (Mehta 1986). A more porous mixture is expected to show higher levels of diffusivity (Garboczi and Bentz 1992). The effect of GGBFS on the diffusivity of the mixture is somewhat controversial. A study in 1988 (Ozyildirim and Halstead 1988) focused on establishing the effect of fly ash and GGBFS on the permeability of the mixture. The result of this study shows that the samples with 50 percent GGBFS and w/cm ratio of 0.4 and 0.45 show a low to very low 28-day and 90-day permeability, in comparison to the samples with no slag replacement with same w/cm ratio. A mixture with a higher

permeability is expected to also show higher diffusivities. Another study also concluded that the GGBFS in the mixtures decreases the moisture decrement due to moisture diffusion at different ages (Jiang, Sun et al. 2006). Based on this discussion, one can conclude that more field data is required to establish the effect of SCMs on the diffusivity of the concrete.

As seen in Figure 6-7, the model is able to capture the descending trend seen in the RH measured in Slab C over two years. The predictions of the model, however, do not exactly match with the measured data as the result of several factors. The first factor to be considered is the accuracy of the SHT75 sensors. The accuracy of these sensors varies between ± 2 and ± 4 for the RH ranging between 0 and 10 percent and 90 and 100 percent. The accuracy of the sensors is equal to $\pm$ 2 for the RH ranging from 10 to 90 percent.

The second factor that should be considered when evaluating the accuracy of the model is the simplifying assumptions that were made for computational convenience. Material-related moisture properties of concrete (permeability, diffusivity, slope of the moisture isotherm, etc.) play a key role in the mathematical modeling of diffusivity, thereby should be established in the laboratory for more accurate predictions (McCullough and Rasmussen 1999).

The effects of other factors involved with defining C in Equation 6-3, i.e. α_0 and n, was also studied and are presented in Figure 6-8 and Figure 6-9, respectively. Figure 6-8 shows the effects of α_0 on the predicted relative humidity. It should be noted that the value of C_1 was defined as 0.8 cm^2/day based on the previous section. As seen in Figure 6-8, α_0 does not show a significant effect on the predicted results. This agrees with findings by Bazant in that values of α_0 for different concrete mixes are similar and range between 0.05 and 0.1. Based on Figure 6-8, the highest value of 0.1 seems to provide predicted values most similar to those measured.

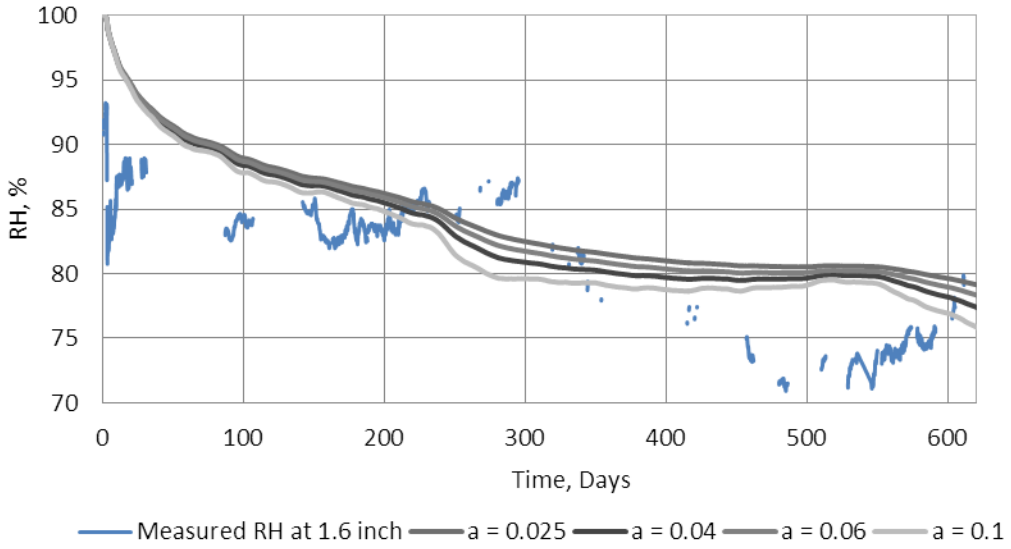

Figure 6-8. Effects of α_0 on the model predicted RH at depth 1.6 inches.

Figure 6-9 shows the influence of n on the predicted RH in the slab. It must be noted that C_1 is defined as 0.8 cm^2/day and α_0 as 0.1 for these runs. Based on Figure 6-9, the parameter n shows a significant influence on the predicted results. Bazant suggested that n varies between 6 and 16 for different PCC mixtures. Based on Figure 6-9, an increase in the value of n results in a decrease in the predicted RH. Furthermore, higher values, such as 16, 25 and 35, result in almost the same RH values. RH values when n=6, shown in Figure 6-9, appear to provide the best estimate of the values measured in the field measurements at both early and later ages.

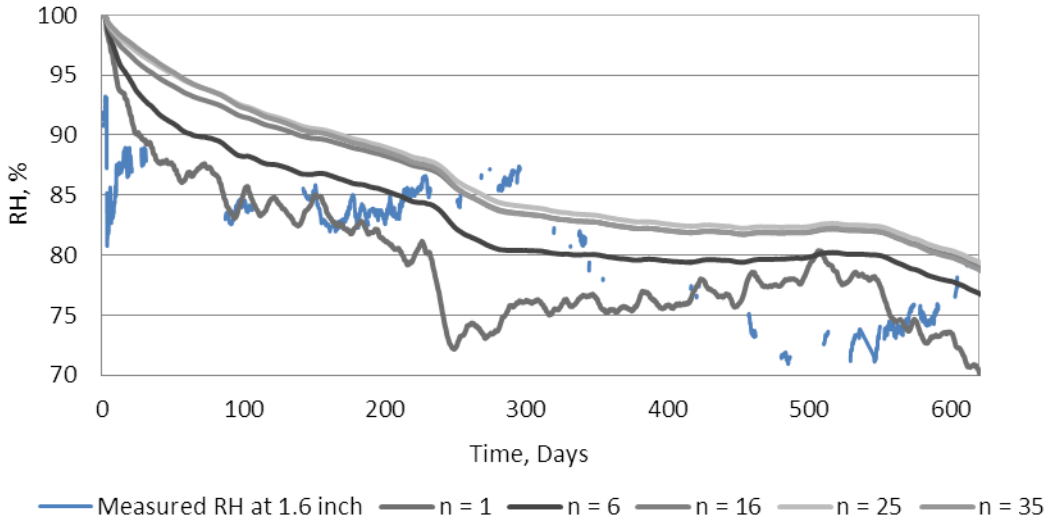

Figure 6-9. Effects of n on the model predicted values at depth 1.6 inches.

The RH predicted using the model with C_1, n and α_0 equal to 0.8, 6 and 0.1, respectively is presented in presented in Figure 6-10 with respect to time for a range of depths in the slab. To evaluate the accuracy of the predictions across the depth of the slab, Figure 6-11 to Figure 6-14 were generated. In these figures, the RH predicted at different depths of the slab is provided in comparison to the measured RH at different depths for both Slabs C and Z. The data corresponding to only four different times throughout the two years following construction is presented herein. These times were selected randomly and based on the availability of field data. As seen in the figures, the model predictions show acceptable agreements with the measured values at the edge and center of the slab.

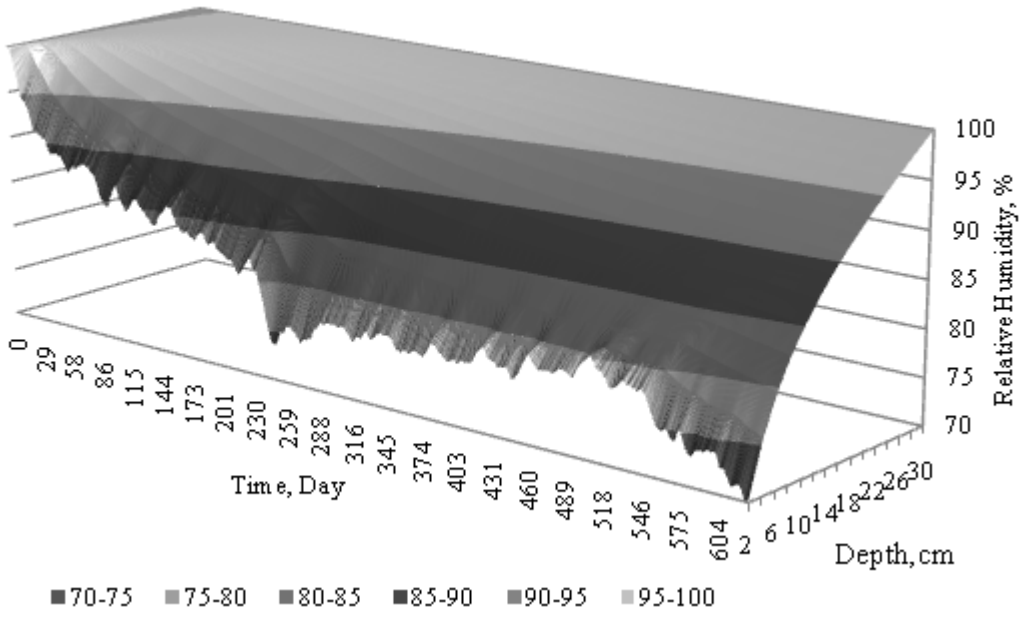

Figure 6-10. Predictions of the model for RH in the slab over two years.

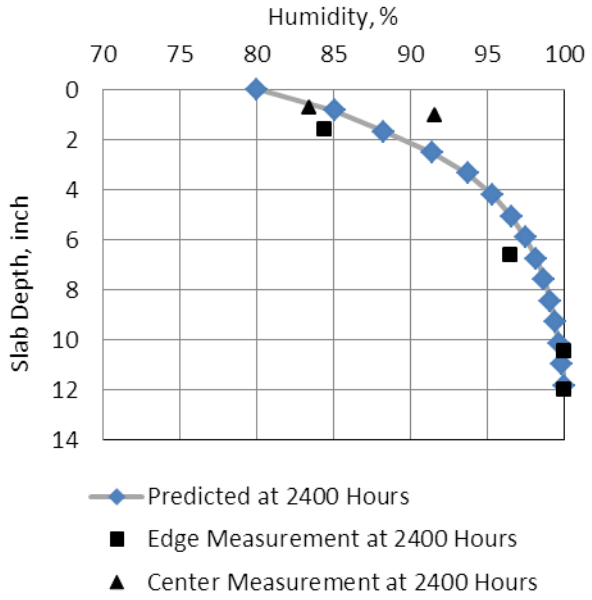

Figure 6-11. Measured vs. predicted RH, 2400 hours after placement.

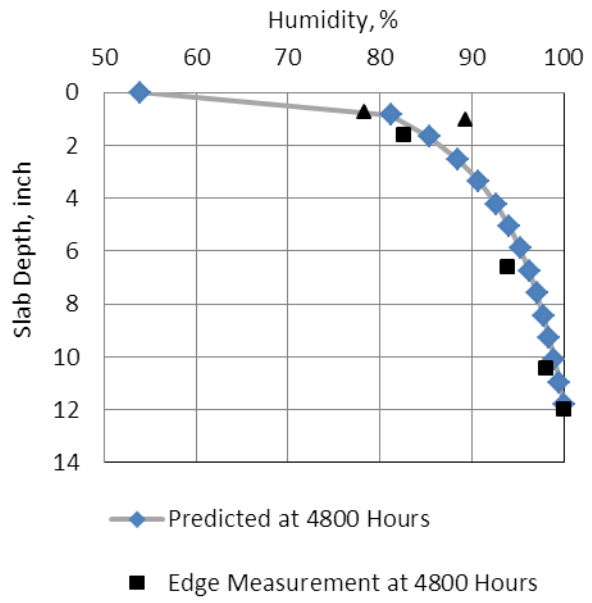

Figure 6-12. Measured vs. predicted RH, 4800 hours after placement.

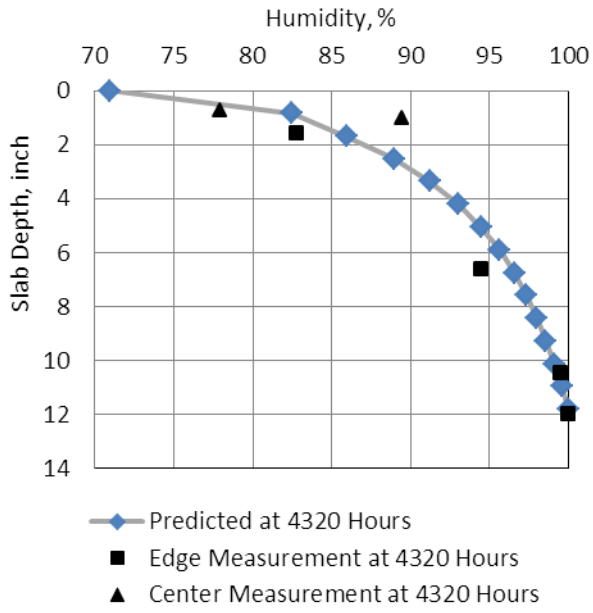

Figure 6-13. Measured vs. predicted RH, 8500 hours after placement.

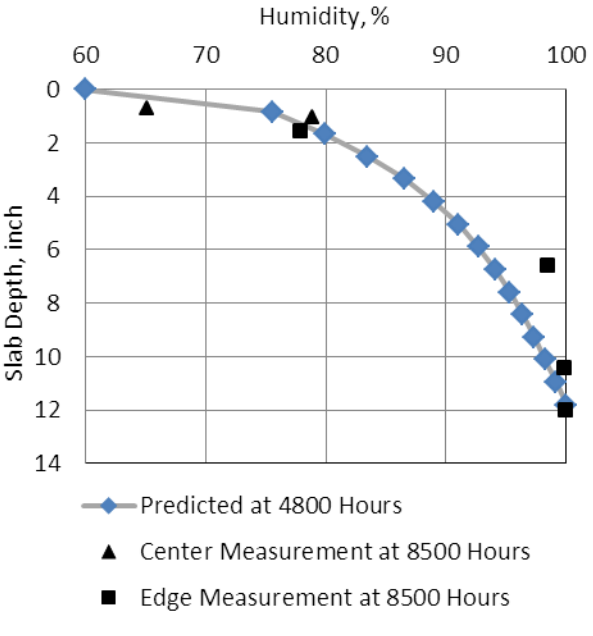

Figure 6-14. Measured vs. predicted RH, 4320 hours after placement

6.5 PREDICTED DRYING SHRINKAGE STRAIN

A numerical model was implemented in the previous section to predict the variation in the RH in the slab with time. A method was developed in the past studies (Mohamed and Hansen 1997) for establishing an equivalent temperature difference based on the regression analysis of the nonlinear temperature profile in the slab. The same method can also be applied to the RH profile in the slab to establish an equivalent temperature difference (Jeong and Zollinger 2005) that would produce the same curvature in the slab as that caused by the non-linear moisture distribution.

Using the RH predictions of the numerical model, the humidity difference coefficient, $\Delta\ [1-(\frac{RH}{100})^3]$, can be established for the slab with time. In doing so (Mohamed and Hansen 1997), a third-degree polynomial is fit into the humidity difference coefficient throughout the slab depth. The regression coefficients from the polynomial function are then used to establish the equivalent linear humidity difference coefficient, $\Delta\ [1-(\frac{RH}{100})^3]_{eq}$ The respective relations for this procedure were presented previously in Section 2.3.2. The RH predictions for SR 22 project in Murrysville were used to establish the humidity difference coefficient, $\Delta\ [1-(\frac{RH}{100})^3]_{eq}$, for a duration of five years. The respective result is provided in Figure 6-15. It should be noted that the discontinuity seen in the predictions between days 1500 and 1600 is because the ambient RH measured at the site using the weather station was unfortunately missing for this time period.

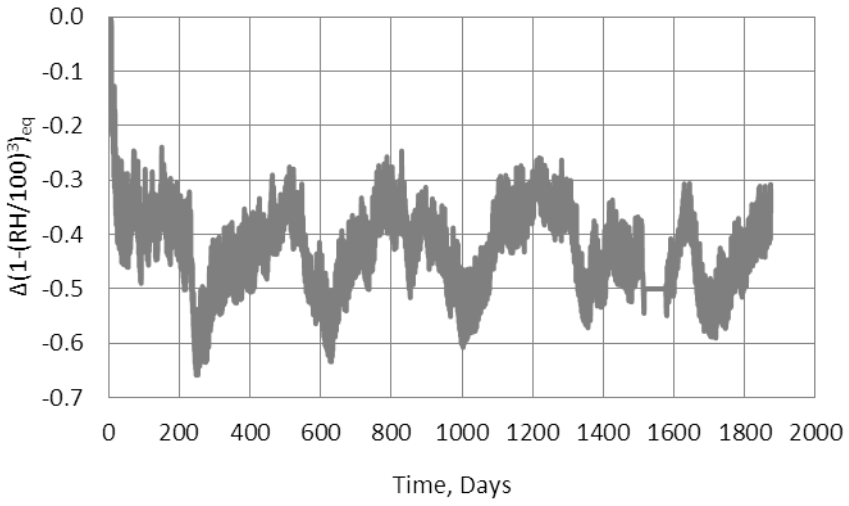

Figure 6-15. $\Delta[1-(\frac{RH}{100})^3]_{eq}$ over five years predicted using the numerical model for the test section.

Based on Equation 2-20, the product of $\Delta[1-(\frac{RH}{100})^3]_{eq}$ and the ultimate drying shrinkage, ε_∞, for the concrete can provide an estimate of the drying shrinkage strain in the slab at the time of interest. As discussed in Section 2.3.2, ε_∞ can be established through laboratory testing, such as the AASHTO T 160 test procedure, or using the Bazant empirical relation provided in Equation 2-17. Both these methods were used to establish ε_∞ for the PCC mixture used for the SR 22 test section.

The AASHTO T 160 test procedure was followed in the laboratory to establish the ultimate drying shrinkage for three prism specimens cast in the field using the paving concrete for the SR 22 test section. It is worth mentioning that the moist curing period of 28 days advised by the standard was not applied to these samples. After the overnight onsite curing, the samples were transferred to the laboratory, demolded and immediately placed in the drying shrinkage environmental room with a constant RH and temperature as advised by the standard. The laboratory test results were provided in Table 6-3. Samples 1 and 2 were cast from one batch of

concrete while Sample 3 was cast from a different batch. As seen in Table 6-3, an average ultimate drying shrinkage of approximately 1000 με can be established for both Samples 1 and 2 and the value of approximately 815 με is obtained for Sample 3. Inconsistencies in the PCC mixture, specifically the w/cm ratio, from different batches used to pave the test section, is believed to be the cause variation between the drying shrinkage measured for Samples 1 and 2 in comparison to Sample 3.

The Bazant empirical model, presented in Equation 2-17, was also employed to establish the ultimate drying shrinkage for the paving for the SR 22 test section. In doing so, the PCC mixture design and mechanical properties provided in Table 6-2 was adopted. The value of 700 με was established for the ultimate drying shrinkage of the concrete. This value is 30 percent lower than the ultimate shrinkage established in the laboratory for Samples 1 and 2; and 15 percent lower than the value established for Sample 3. The three values are very close and the difference seen in the laboratory results and the model prediction are most possibly due to the short period of moist curing applied to the samples. Therefore, the value predicted by the empirical model will be used in the analysis for establishing the empirical long-term drying shrinkage.

The ultimate drying shrinkage established using the Bazant empirical model was multiplied by $\Delta[1-(\frac{RH}{100})^3]_{eq}$, previously established for a five year period of time. The subsequent result is the time-dependent drying shrinkage strain in the slab. See Figure 6-16. To eliminate the seasonal fluctuations in the drying shrinkage, the mean monthly drying shrinkage strain for the month of October in each year was used. The black line in Figure 6-16 connects

these values in every year. Based on Figure 6-16, the long-term (age of 65 months) drying shrinkage can be established as approximately 350 με for the SR 22 test section.

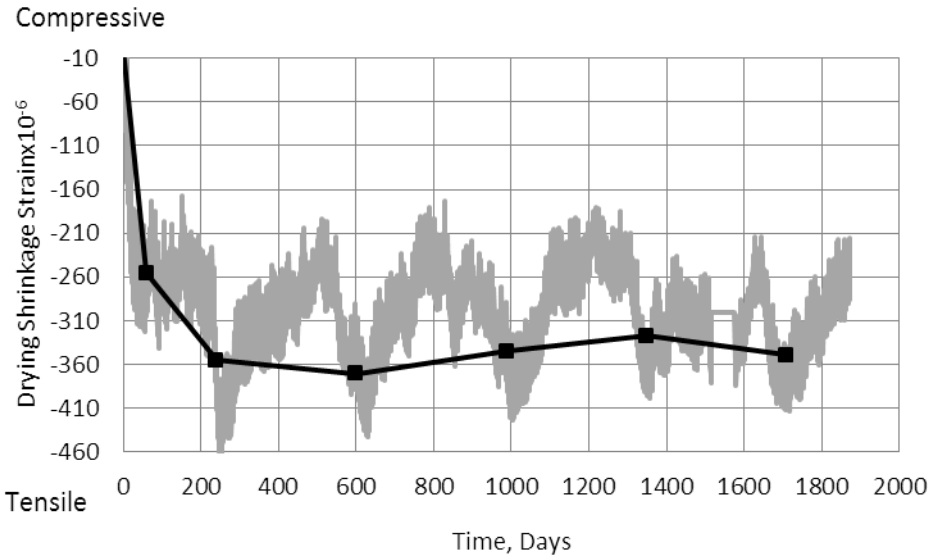

Figure 6-16. Predicted drying shrinkage strain defined as a product of $\Delta[1-(\frac{RH}{100})^3]_{eq}$ and the ε_∞.

6.6 DRYING SHRINKAGE MEASURED IN THE FIELD

6.6.1 SR 22 Test Section

The predicted drying shrinkage established in the previous section considers the effects of ambient weather conditions and the PCC mixture on the development of drying shrinkage. However, it does not account for the effects of the restraining factors and creep on the development of drying shrinkage.

As remarked previously, a study performed in 2001 (Burnham and Koubaa 2001) used the VW static strain data to establish the development of drying shrinkage in concrete slabs over a duration of five years. The same approach is followed in this section to establish the long-term drying shrinkage for the slabs at the SR 22 test section. The data from the VW static strain gages installed in the slabs on SR 22 were used to achieve this goal. The raw readings from the gages need to be corrected for the effects of temperature on the steel wire in the gage using the relation discussed previously in Equation 3-1.

T_0 and R_0 in Equation 3-1 are the temperature and strain corresponding to the zero-stress time in each slab. TZ was established for each individual instrumented slab in a previous study (Wells, Phillips et al. 2006), following the same methodology used in Chapter 3 to establish TZ for the four instrumented projects in 2009 and 2010. The temperature and strain corresponding to TZ in each slab was used to define R_0 and T_0 in Equation 3-1.

The total strain established by Equation 3-1 is a combination of thermal (including temperature gradient and uniform temperature changes), drying shrinkage, creep effects and restraints due to dowel/tie bars and the friction between the base and the slab. The thermal strains due to uniform temperature changes in the slabs can be partially isolated from the total strains by estimating the "mechanical strain" using the relation provided previously in Equation 4-2.

In an effort to isolate the effects of transient temperature gradients on the strains established by Equation 4-2, only the data that corresponded to the time when the slabs were flat was used in the analysis. A concrete slab remains flat when the transient temperature gradient present in the slab is equal to the temperature gradient locked into the slab at TZ. The average

value for this parameter was established as 0.31°F/in for all of the instrumented slabs. More detail on this can be found in the reference Wells, Phillips et al. 2006.

The longitudinal gages in the three consecutive slabs in each of Cells 1 and 2 at the corner location adjacent to the shoulder were selected for characterizing the drying shrinkage strains in the slabs. The reason behind this selection is the fact that the slabs are more prone to drying/wetting at the corner adjacent to the shoulder than in the middle of the slab. The same observation was reported in the 2001 study (Burnham and Koubaa 2001).

The gages at the corner of each slab were installed at three different depths; at the top (between 1 and 2 inches from the slab surface), at mid-depth and at the bottom (approximately 1 inch from the base layer). Since drying occurs in the upper portion of the slab, the data from the top gages were used to characterize the drying shrinkage strain. Additionally, the data from both the top and bottom gages were used to establish the curvature in the slab.

The estimated strain was averaged for the three consecutive slabs to provide more confidence in the results. The average strain due to drying shrinkage at the top of the slabs about 65 months after paving the test section is presented in Figure 6-17 for both the doweled and undoweled slabs. Each data point in Figure 6-17 represents the average of the mean monthly drying shrinkage strain for three consecutive slabs.

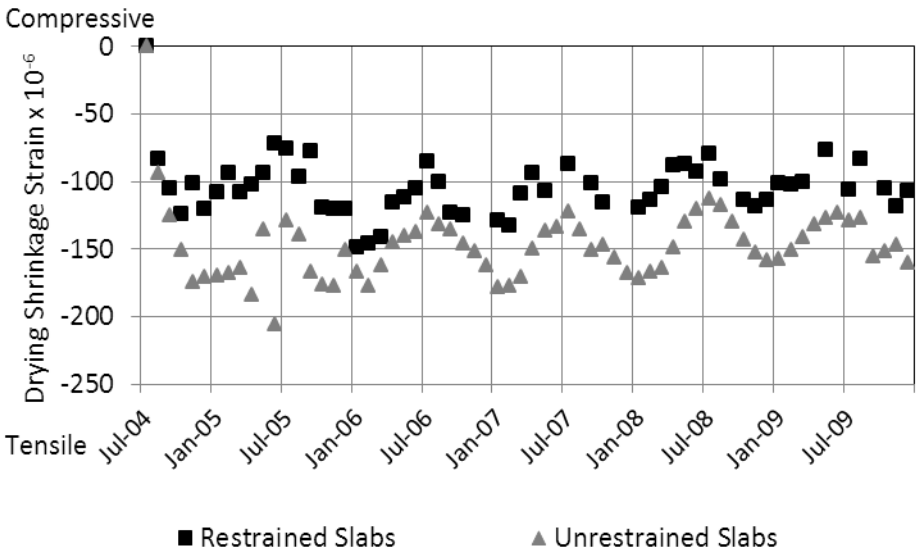

Figure 6-17. Strains due to drying shrinkage at the top of restrained and unrestrained slabs in SR 22 test section.

Based on Figure 6-17, the unrestrained slabs consistently show more drying shrinkage strain in comparison to the restrained slabs. This agrees with logic, since the dowel bars are expected to restrict the shrinkage of the slab in the longitudinal direction. Seasonal variation in the drying shrinkage strain for both restrained and unrestrained slabs is also clearly noticeable in Figure 6-5. The highest level of drying shrinkage is seen during the month of March in every year while the lowest is seen during the month of July. This trend agrees with the trend seen in the ambient RH for the test section presented previously in Figure 6-30.

It is known that the JPCP slabs the joints can lock up during the hottest months of the year due to excessive uniform expansion. The measured strain and temperature in the slabs at the time the joints lock up can be used to provide a check on the drying shrinkage strain established for the slabs in SR 22, presented in Figure 6-17. Studies of strain versus temperature in the slabs in all seasons showed that joint lock up occurs during the spring and the summer of each year for both the restrained and unrestrained slabs in SR 22. Strain-temperature graphs for

the spring and summer of 2006 are provided in Figure 6-18 and Figure 6-19 for the restrained slabs and in Figure 6-19 and Figure 6-26 for the unrestrained slabs as examples.

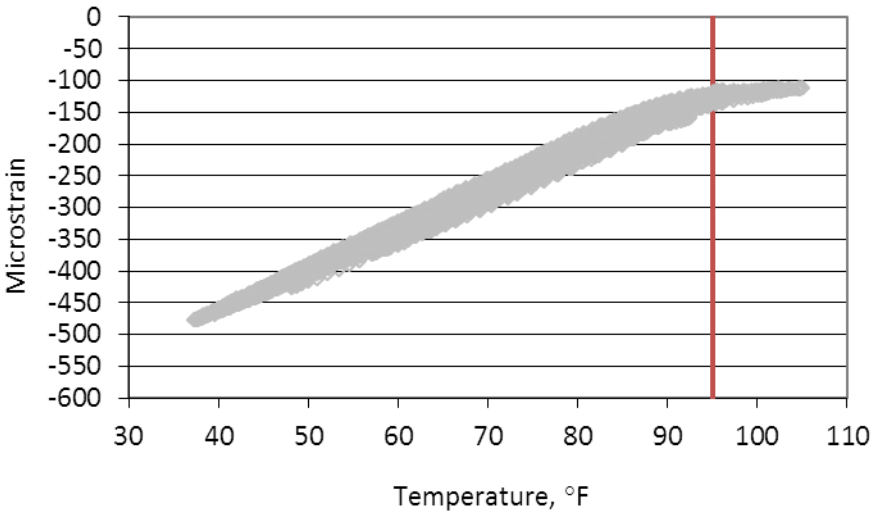

Figure 6-18. Measured strain vs. temperature in the spring of 2006 for restrained slabs in SR 22 test section.

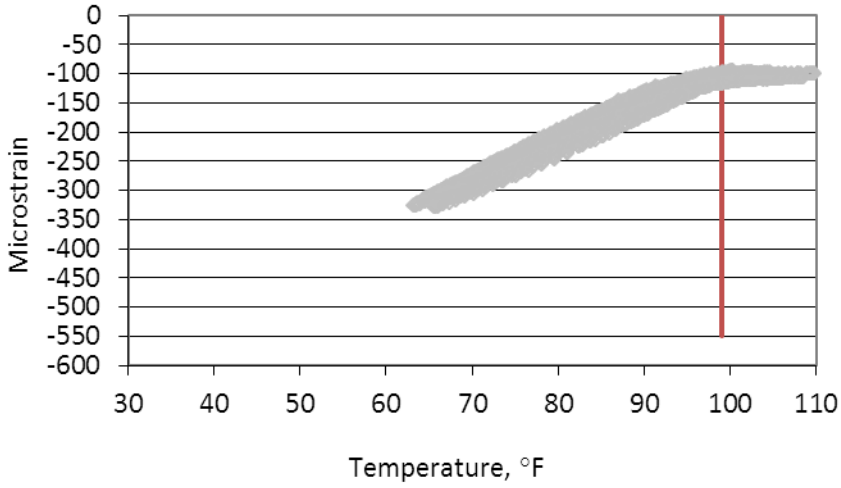

Figure 6-19. Measured strain vs. temperature in the summer of 2006 for restrained slabs in SR 22 test section.

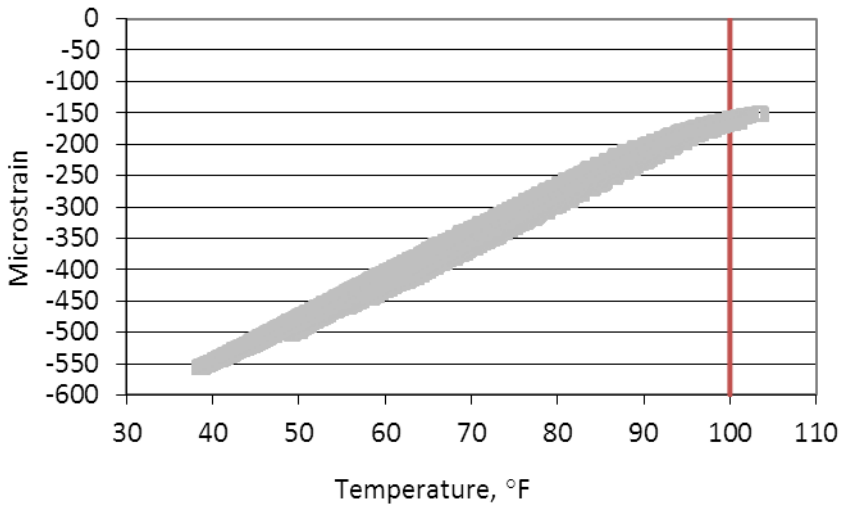

Figure 6-20. Measured strain vs. temperature in the spring of 2006 for unrestrained slabs in SR 22 test section.

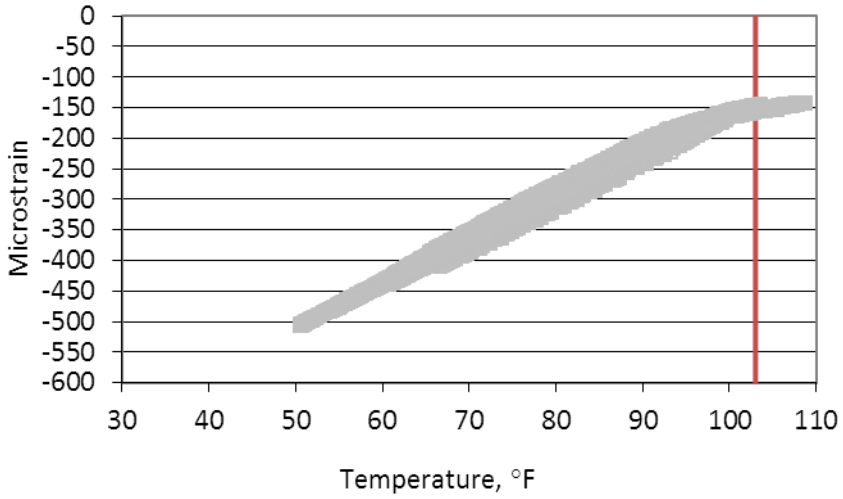

Figure 6-21. Measured strain vs. temperature in the summer of 2006 for unrestrained slabs in SR 22 test section.

Based on Figure 6-18, joint lock up occurred at a total strain equal to approximately 110 με and a temperature equal to 96 °F in the spring of 2006 for restrained slabs. The slab expands uniformly, when its temperature is below the temperature present at TZ. Based on this analogy, the uniform thermal expansions, from Equation 6-9, can be isolated from the total strains at the

time of joint lock up. The remaining strain is due to drying shrinkage and can be compared to the drying shrinkage presented in Figure 6-17.

$$\varepsilon_{thermal} = (T_{lockup} - T_{TZ}) \times \alpha_c \quad (6\text{-}9)$$

This procedure was applied for the strains measured during the spring and summer of 2006 and 2007 for both restrained and unrestrained slabs in SR 22. The results are summarized in Table 6-5. According to Figure 6-17, the drying shrinkage stabilizes in the slabs in year 2006 and remains constant thereafter. This is why the results of the analysis, as seen in Table 6-5, is very similar for both years 2006 and 2007. The same results are expected for years 2008 and 2009 and so the analysis is not repeated for these years.

Table 6-5. Strain and temperature at the time joints lock up for restrained and unrestrained slabs in SR 22.

	Total Strain at Lock-up	Temp. at Lock up	Temp. at Final Set	Thermal Strain	Drying Shrinkage Strain at Lock up
	με	°F	°F	με	με
Restrained Slabs					
Spring 2006	-110	95-96	99	-18	-110-(-20) = -90
Summer 2006	-90	100		6	-90-6= -96
Spring 2007	-120	94		-30	-120-(-30) = -90
Unrestrained Slabs					
Spring 2006	-170	100	107	-40	-170-(-40) = -130
Summer 2006	-150	103		-24	-150-(-24) = -126
Spring 2007	-160	99		-50	-160-(-50) = -110
Summer 2007	-150	100		-40	-150-(-40) = -110

The drying shrinkage strains at joint lock up presented in Table 6-5 agree very well with the drying shrinkage strains established previously in Figure 6-17 for the spring and summer of 2006 and 2007.

To isolate the seasonal variation seen in the drying shrinkage in Figure 6-17, the drying shrinkage strain during October in each year was used to investigate the development of drying shrinkage over the years. This is presented in an individual graph in Figure 6-22 for both the restrained and unrestrained slabs.

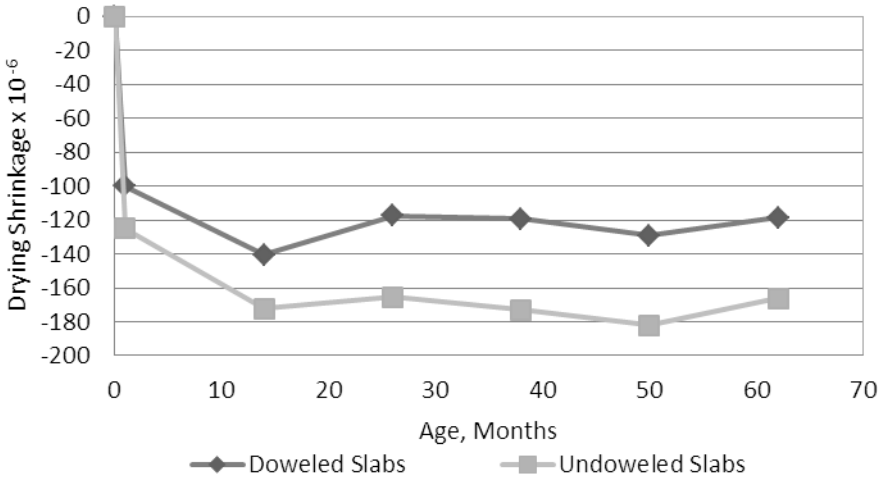

Figure 6-22. Drying shrinkage strains in October of each year at the top of restrained and unrestrained slabs.

According to Figure 6-22, the long-term (age of 65 months) drying shrinkage is equal to approximately 120 με in restrained slabs. For unrestrained slabs this is approximately 160 με showing that the dowel and tie bars present in the restrained slabs reduce the long-term drying shrinkage in the slabs by approximately 25 percent.

The measurements from the VW strain gages installed at the top and the bottom of the slabs were incorporated into Equation 4-1 to estimate the curvature of the slabs. The mean curvature for the month of October in every year is presented in Figure 6-23. The slabs show an upward curvature due to drying shrinkage. A lower upward curvature is seen for the slabs containing dowel and tie bars when compared to the slabs without any dowel and tie bars. This effect is more pronounced in Figure 6-23 in comparison to Figure 6-22, which presents the drying shrinkage strain at the top of the slabs. The curvature 65 months after paving is lower by approximately 30 percent in the slabs with dowels and tie bars.

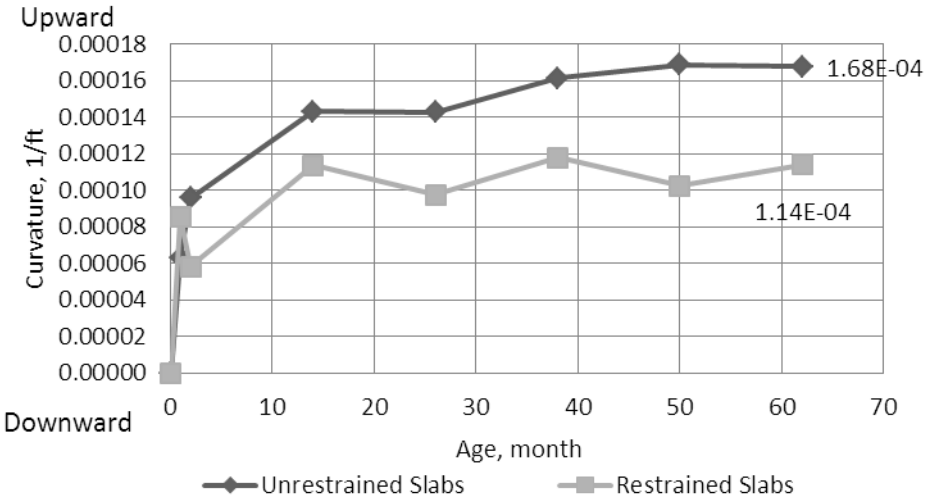

Figure 6-23. Estimated curvature due to drying shrinkage for the doweled and undoweled slabs in SR 22.

6.6.2 MnROAD Study

The development of drying shrinkage strain with time was established in the previous section for both 12-inch doweled and undoweled slabs with a stabilized base layer. To expand this analysis to PCC pavements with a variety of design features, the pavements at MnROAD were also

included in the present study. A study performed in 2001(Burnham and Koubaa 2001), included establishing the development of drying shrinkage over time in Cells 5, 8, 37 and 38 at MnROAD, based on the data from the embedded VW gages. In addition to the analysis for the aforementioned cells, the 2001 study was expanded upon to include gages installed at the top and the bottom of Cells 6 and 9. The drying shrinkage over time was established for each of these two cells following the exact procedure described in the 2001 study. A brief description of MnROAD test section is provided in the following section.

6.6.2.1 MnROAD Section Description

MnROAD is a road research test facility located geographically near Albertville, Minnesota. This test facility is comprised of numerous pavement designs, constructed over the past twenty years. Each test section is heavily instrumented. The layout of MnROAD is presented in Figure 6-24. Of the test sections included in this study, Cells 5, 6, 8, 9 are located on the Westbound I-94 MnROAD mainline and Cells 37 and 38 are located on the low-volume road.

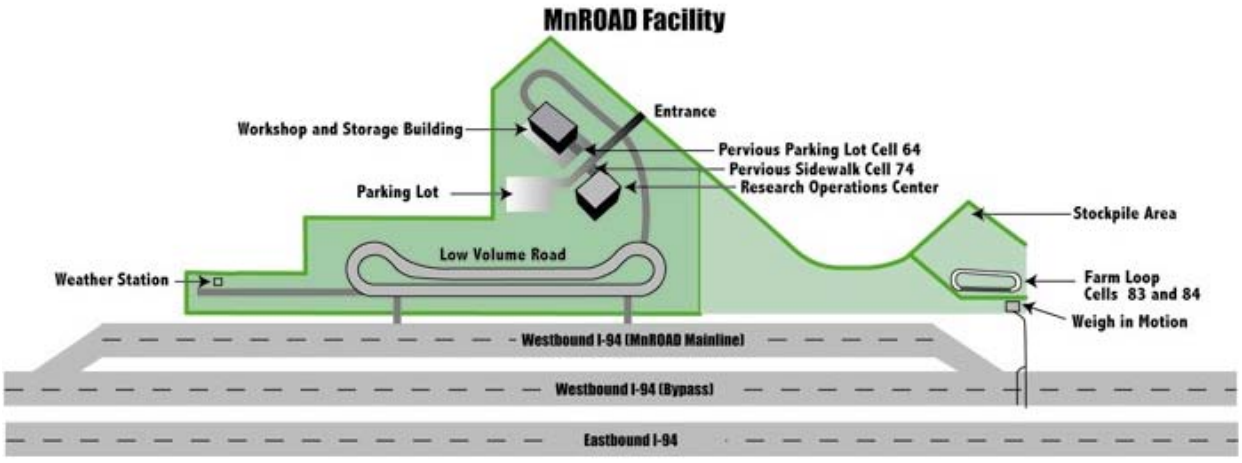

Figure 6-24. MnROAD facility layout (http://www.dot.state.mn.us/mnroad/).

The data used in this study corresponds to the VW static strain gages installed at the top and bottom of slabs in the corner near the transverse joint and adjacent shoulder for Cells 5, 6, 8, 9, 10, 37 and 38. A schematic layout of a typical slab containing VW gages is provided in Figure 6-25. The location of the sensors used in this study is identified by the red circle.

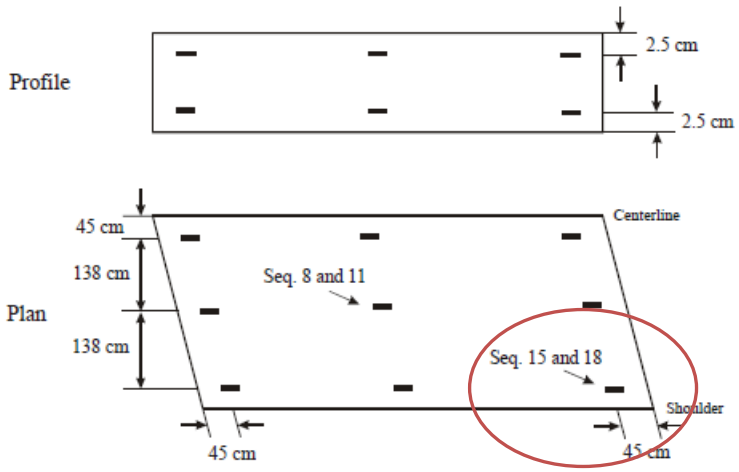

Figure 6-25. Schematic layout of the VW gages for a panel in MnROAD (Burnham and Koubaa 2001).

The design features for each cell are summarized in Table 6-6. The PCC mixture design was the same for all cells and is provided in Table 6-5. The CTE and 28-day compressive strength established in the laboratory for the paving mixture is provided in Table 6-6. The corresponding compressive strength together with the cementitious material content for the mixture in each cell were used to estimate the ultimate drying shrinkage using the Bazant empirical model. The respective result is provided in Table 6-6.

Table 6-6. Design features for the concrete cells at MnROAD.

Test Cell	Construction Date	Slab Thickness (in)	Base Type	Dowel Diameter (inch)	Slab Width (ft)	Slab Length (ft)
5	9/15/1992	7.5	Granular	1 until 9/1995 and none since then	13	20
6				1		15
8	9/16/1992		ATPB	1 until 9/1995 and none since then		
9				1		
10	6/14/1993	9.5	ATPB	1.25	12	20
37	7/19/1993	6	Granular	None		15
38				1		

Table 6-7. PCC mixture design used to pave MnROAD concrete cells.

Weight in the Batch (lb/yd^3)				
Cement	Fly Ash	Water	Fine Aggregate	Coarse Aggregate
Type I, 451	Class C, 79	244	1200	1932

Table 6-8. CTE, drying shrinkage and strength of the concrete used to pave MnROAD.

Test Cell	CTE (10^{-6}/°F)	28-day Compressive Strength (psi)	Ultimate Drying Shrinkage (με)-Bazant Relation
5	4.5	5215	613
6	4.5	5405	610
8	4.7	4790	620
9	5.5	5430	610
10	3.7	5110	614

6.6.3 Analysis of the Results

The mechanical strain determined using VW strain gages located at the top of the slab is provided in Figure 6-26 for each cell at MnROAD. The labeling scheme used to name each

pavement structure in Figure 6-26, from left to right, correspond to: slab thickness-base type (st for stabilized and U for unstabilized)-slab length (ft) -slab width (ft) -dowel diameter (in).

The pavement sections at MnROAD represent a large assortment of design features, which can influence drying shrinkage of slab. In the proceeding section, cells with comparable designs at both MnROAD and SR 22 will be coupled together, to investigate the effect of different design parameters, such as base type, dowel/tie bars and slab thickness, on drying shrinkage.

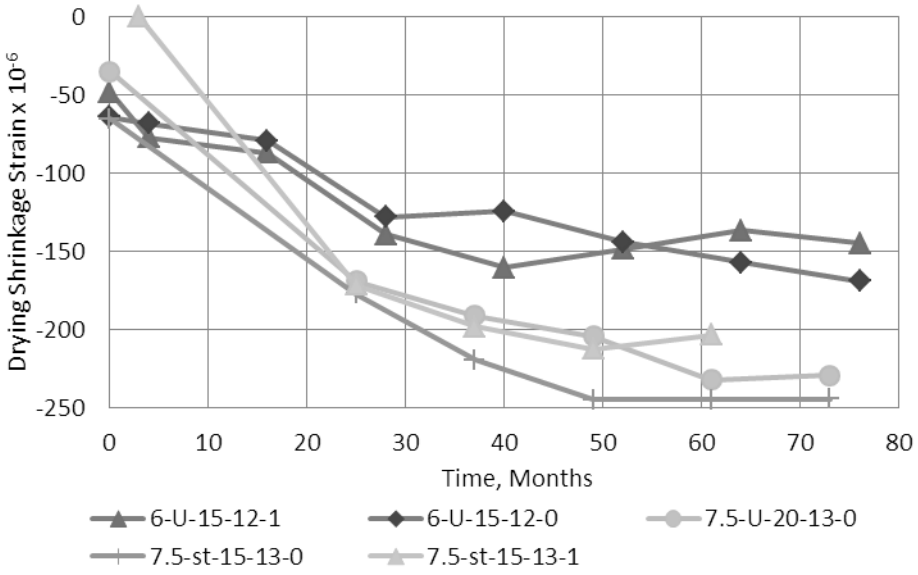

Figure 6-26. Estimated curvature due to drying shrinkage for all the instrumented concrete slabs in MnROAD.

6.6.4 Effect of Pavement Design Features on Slab Drying Shrinkage

6.6.4.1 Dowels and Tie Bars

The effect of 1.5-inch diameter dowels on drying shrinkage was previously investigated in Section 6.6.1 for the SR 22 test section, in Pennsylvania. Based on Figure 6-22, it was concluded that the slabs with 1.5-inch dowels show a lower irreversible drying shrinkage by about 30 percent, when compared to the slabs with no dowel and tie bars. This agrees with expectations, since the dowel provide restraint against the contractions of the slabs due to drying shrinkage in the longitudinal direction.

The effect of 1-inch diameter dowel bars on drying shrinkage can be evaluated for 7.5-inch thick PCC slabs at MnROAD. These pavements both have 15-ft joints spacings and are 14 ft wide and both are on a stabilized base. The drying shrinkage at the top of the pavement is presented in Figure 6-27 for both pavement structures. Based on this figure, the slabs with no dowel and tie bars show a slightly higher drying shrinkage for the majority of the time. The difference at age 60 months is approximately 20 percent.

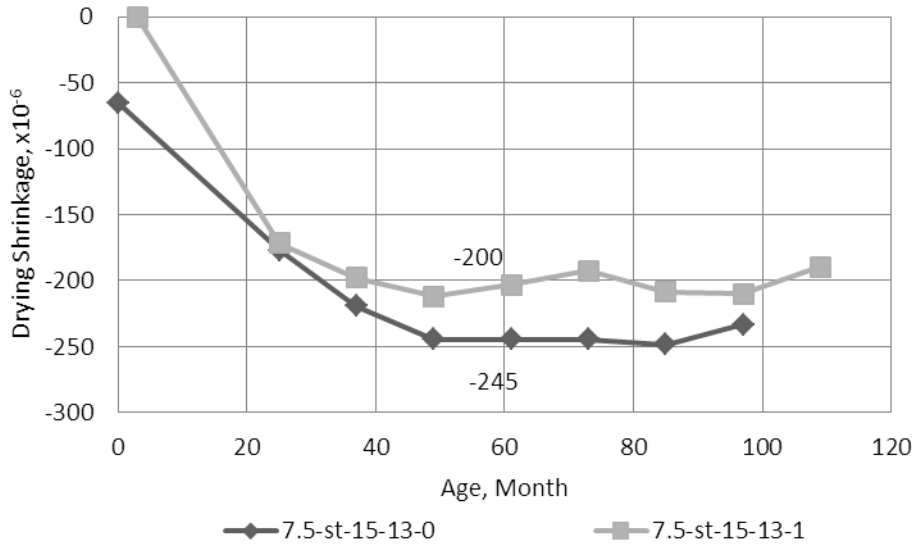

Figure 6-27. Effects of 1-inch dowels on drying shrinkage in stabilized slabs.

6.6.4.2 Slab Thickness

The effect of slab thickness on drying shrinkage is investigated in this section. The development of drying shrinkage for the 12-inch slabs on the SR 22 test section with a stabilized base is compared to that of the 7.5-inch slabs at MnROAD with a similar base material. This is presented in Figure 6-28 for the doweled slabs and in Figure 6-29 for the undoweled slabs.

As seen in Figure 6-28, the thinner slabs include 1-inch dowel bars, while the thicker slabs contain 1.5-inch dowel bars. Based on the discussions in the previous section, 1.5-inch dowels result in a 30 percent reduction in slab drying shrinkage, while the reduction in the drying shrinkage by the 1-inch dowels is about 20 percent. Therefore, the larger dowel diameter in the 12-inch slabs can provide more restraint against warping in these slabs than the 1-inch dowels in the 7.5-inch slabs. This can increase the true effect of slab thickness on slab drying shrinkage and therefore the exact effect of slab thickness cannot be quantified with this data.

.

It should also be pointed out that, as seen in Figure 6-28 and Figure 6-29, the slabs at MnROAD are about 1 ft wider than SR 22. Since the gages in the longitudinal direction were used to establish the drying shrinkage for both SR 22 and MnROAD sections, the width of the slab is not expected to significantly affect the drying shrinkage of the slabs.

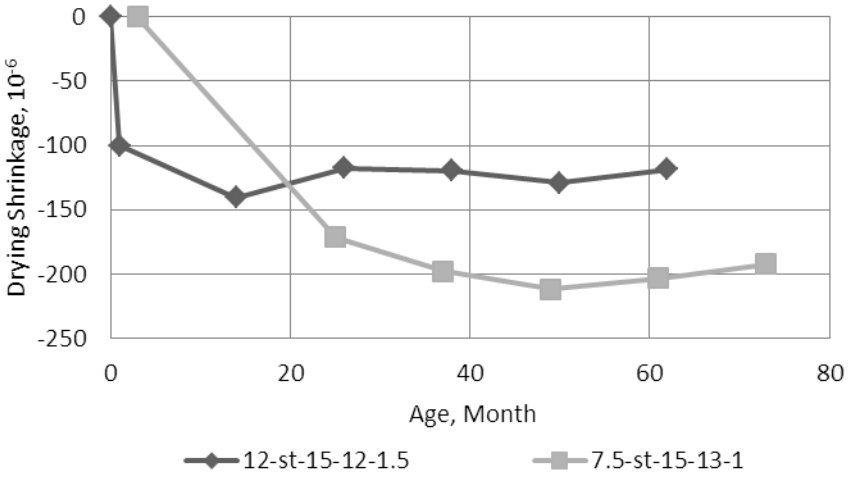

Figure 6-28. Effects of slab thickness on drying shrinkage for doweled slabs.

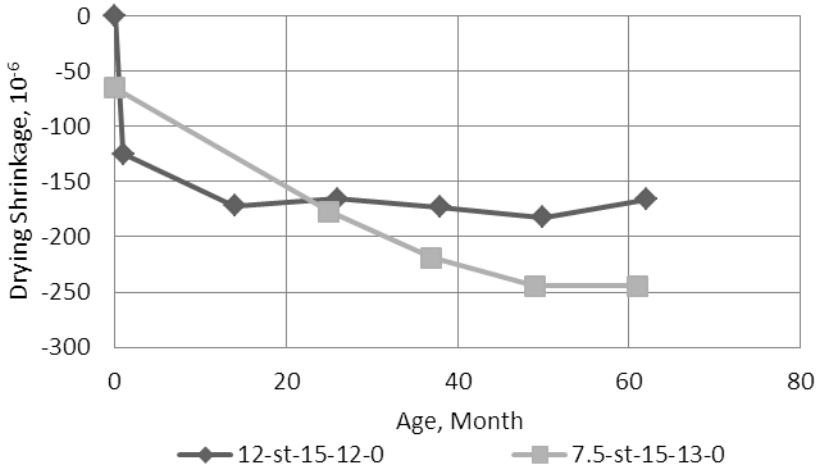

Figure 6-29. Effects of slab thickness on drying shrinkage for undoweled slabs.

Another factor that needs to be considered when comparing drying shrinkage development for the cells at MnROAD to the cells at SR 22, is the climatic differences between the two sites. To provide an overview of the ambient weather conditions at the two sites, the climatic database available in the MEPDG design software for the Allegheny County Airport and the climatic database from the Minneapolis International Airport were used for SR 22 and MnROAD, respectively. The hourly ambient data was available in each database from 1996 to 2003. First, the mean monthly temperature and RH records were generated for each database, the record was then averaged over eight years. The result is provided in Figure 6-30. Based on this figure, the two climatic stations show very similar ambient weather conditions. A slightly drier and warmer condition is noted for Minnesota over the summer when compared to Pennsylvania. The drier conditions in Minnesota can enhance the difference seen between drying shrinkage for the thinner slabs in this project when compared to that of the thicker slabs in SR 22 project.

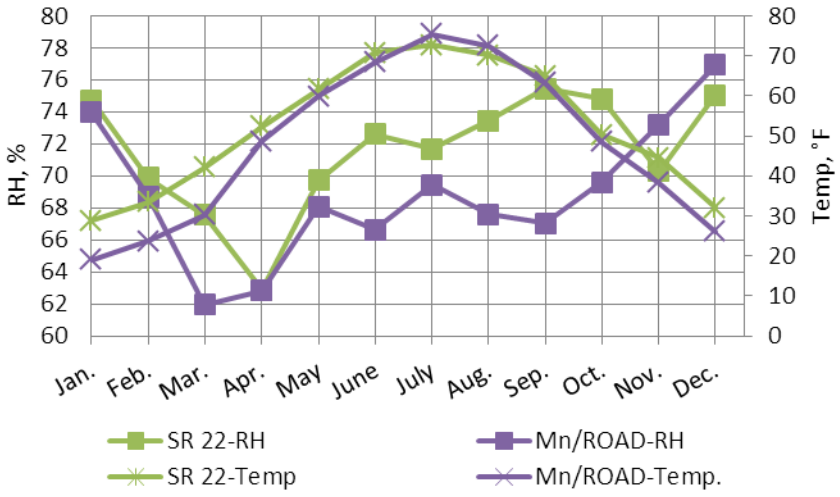

Figure 6-30. Mean monthly temperature and RH for both PA and MN test sections.

PCC mixture design used to the cells at the SR 22 and MnROAD is another factor that can influence drying shrinkage. Based on Table 6-2 and Table 6-7, one can note that the w/cm ratios for both mixtures are relatively similar. Also the ultimate drying shrinkage predicted using the Bazant model is approximately 700 με for the SR 22 mixture and 610 με for the MnROAD mixture, which are very similar. Therefore, one can conclude that variation in drying shrinkage due to differences in the PCC mixture design between the two test sections are minimal.

Since the higher self-weight for the thicker slabs provide more restraint against warping, lower drying shrinkage strain is expected for the thicker slabs at the top. As seen in Figure 6-28, the behavior of the slabs at MnROAD for the first 25 months after construction could not be established due to a lack of data. During the period between 25 and 60 months though, thinner slabs show lower drying shrinkage, as expected.

6.6.4.3 Base Type

The effect of base type, stabilized vs. unstabilized, on drying shrinkage development is investigated in this section. Figure 6-31 shows drying shrinkage over time for two cells with two different base types at MnROAD. Based on Figure 6-31, the slabs placed on an unstabilized base layer start to show a higher level of drying shrinkage beginning 40 months after construction.

One reason for this could be that the stabilized base bonds to the PCC slab resulting in a composite slab with a higher self-weight. A higher self-weight can provide more restraint against warping. Also the stiffer base results in a larger portion of the slab being unsupported when curled, since the slab is unable to "sink" into the base, as occurs with a granular base with a lower stiffness.

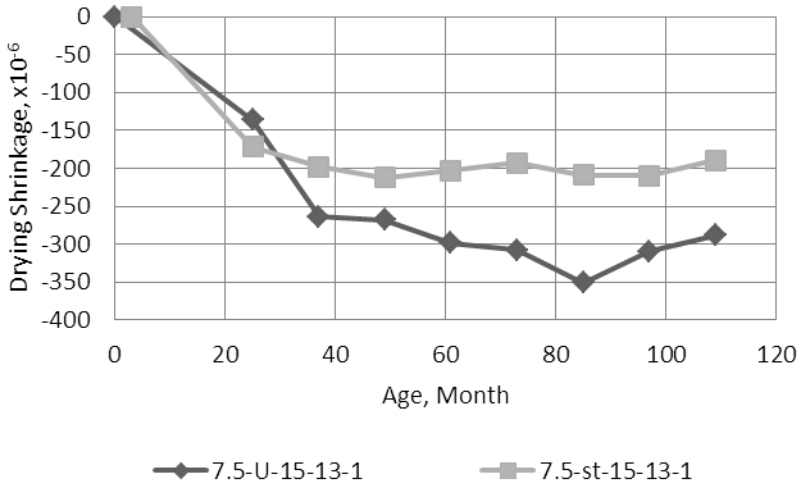

Figure 6-31. Effects of base type, stabilized vs. unstabilized, on drying shrinkage.

It should be pointed out that, close consideration of measured strains for all cells, presented in Figure 6-26, with regards to the pavement design features, reveals that the data corresponding to Cells 37 and 38 (low-volume roads at MnROAD) do not follow logic. It is expected to observe the highest level of drying shrinkage in these slabs when compared to the higher-volume traffic cells at MnROAD. However, these two cells show the opposite behavior. Therefore, it was decided against using the data corresponding to these two cells in the analysis. Potential factors resulting in this behavior, such as time of paving, initial strain and temperature and effects of restraint conditions on the determination of strains were considered however, the reason behind this anomaly remains inconclusive.

6.7 LONG-TERM CREEP AND BASE/SLAB FRICTION

The development of the "predicted" drying shrinkage strain with time, established using the numerical RH model, as a function of the ultimate drying shrinkage of the PCC mixture for both SR 22 and MnROAD projects are compared in this section to the "measured" drying shrinkage strain that developed in the same slabs (established based on the embedded VW strain gages at the top of the slabs in the longitudinal direction.) The difference between the two (predicted and measured drying shrinkage) is introduced as field correction factors at different ages. These correction factors can be applied to the predicted drying shrinkage for any slab with the same design as SR 22 or the MnROAD sections to establish the in-situ drying shrinkage. In other words, the field correction factors allow the predicted drying shrinkage to be corrected for two factors. One of these factors is the possible effects of relaxation with time due to the creep. Among other factors are the friction between the base and the slab and also the dowels/tie bars on the development of drying shrinkage with time.

The comparison between the measured and predicted drying shrinkage is presented graphically in Figure 6-32, for the cells at SR 22. The variation in the measured drying shrinkage and the predicted one at different ages is presented in Table 6-9 in percent difference for the doweled and undoweled slabs separately.

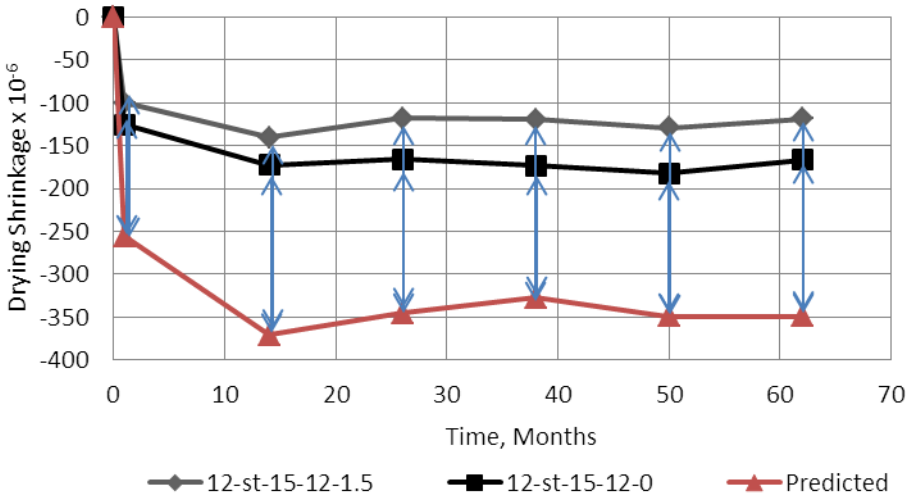

Figure 6-32. Comparison of the measured and predicted drying shrinkage for two cells at SR 22.

Table 6-9. Percent difference between the predicted and measured drying shrinkage for SR 22.

Age (Month)	Percent Difference (%)	
	Restrained Slabs	Unrestrained Slabs
0	0	0
1	48	34
2	62	53
14	62	54
26	66	52
38	63	47
50	63	48
62	66	52

The field correction factors were also established for Cells 8 and 9 at MnROAD. Cells 8 and 9 both consist of 7.5-inch slabs with a stabilized base, while only the slabs in Cell 8 include dowel and tie bars.

First, the time-dependent drying shrinkage strain development was predicted for each cell, using the numerical RH model. In doing so, the climatic database available in the MEPDG for MnROAD was adopted. This compromise was inevitable, since the ambient data collected using the weather station at MnROAD showed discontinuities. The ultimate drying shrinkage for the MnROAD paving mixture was established employing the Bazant empirical relation. The respective results were presented previously in Table 6-6. Based on this table, the average ultimate drying shrinkage for the mixture used to pave the concrete cells at MnROAD is approximately 610 με. As discussed previously, a product of this value and the linear equivalent humidity difference coefficient established for each cell, using the RH numerical model provides the drying shrinkage strain for each cell. Both predicted and measured drying shrinkage strains are presented in Figure 6-33 for Cells 8 and 9. The field correction factors at different ages for both cells are summarized in Table 6-10 in percent difference.

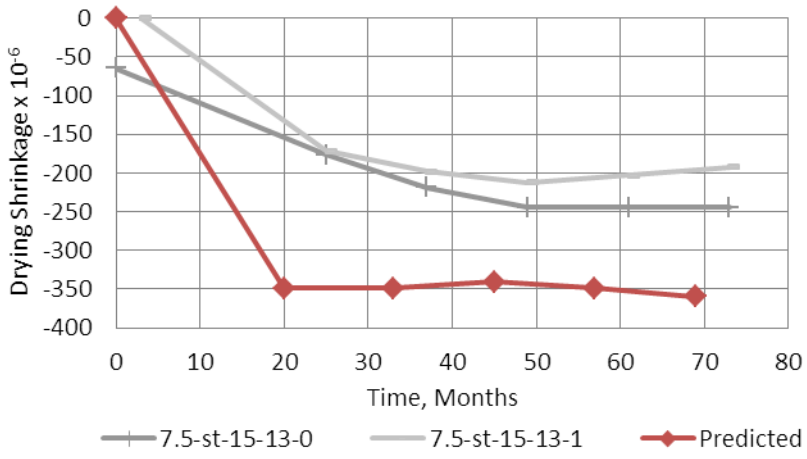

Figure 6-33. Comparison of the measured and predicted drying shrinkage for Cells 8 and 9 at MnROAD.

Table 6-10. Field correction factors for Cells 8 and 9 at MnROAD.

Age (Month)	Percent Difference	
	Restrained -Cell 9	Unrestrained -Cell 8
0	0	0
25	51	49
37	43	37
49	38	28
61	42	30
73	46	32
85	42	31

Considering Figure 6-32 and Figure 6-33 together, one can note that the 12-inch slabs with the ATPB layer at SR 22 show the lowest drying shrinkage of all slabs. At between 60 and 65 months after paving, the age that drying shrinkage is stabilized in most pavements, the correction factor is 32 and 46 percent for the unrestrained and restrained 7.5-inch slabs, respectively. These values are 52 and 66 percent for the unrestrained and restrained 12-inch slabs, respectively. It is very interesting to note that the effect of dowel bars on the field factors for both sets of slabs is almost the same, even though the dowel diameter for the 12-inch slab is a 0.5 inch larger.

The effect of slab thickness is almost consistent between the doweled and undoweled slabs. An increase of 4.5 inches in slab thickness has resulted in a 30 percent increase in the field factors for the restrained slabs. This value is equal to 38 percent for the unrestrained slabs. The field factors established in this section can be interpolated to be used for doweled and

undoweled PCC slabs with a stabilized base and a slab thickness ranging between 7.5 and 12 inches.

It must be noted that the proposed method although innovative, is empirical has its own limitations. For instance, the field factors were not able to be established for sections with granular base layers due to lack of quality data.

Lastly, the field factors were established using the data from slabs that were constructed in the months of August and October. Construction of the slabs in other months during the construction season can result in changes in the field factors. Also, although the analysis performed in this section serves the final aim of this study, which is establishing permanent curl/warp for JPCPs in Pennsylvania, the construction of the pavements in other geographical locations with extremely different climatic condition than Pennsylvania or Minnesota can require adjustments in these field factors.

7.0 CHAPTER 7- PERMANENT CURL/WARP FOR JPCPS IN PENNSYLVANIA

Previous chapters of this study aimed at developing separate methods to establish permanent curling and permanent warping gradients in the slab. In this chapter the two methods are compiled and used to establish the permanent curl/warp temperature gradient for the slabs constructed in Pennsylvania. The procedure includes the following steps and can be used for JPCPs constructed in any geographical location.

TASK 1: compiling an hourly climatic database averaged over at least five years, including major climatic factors such as ambient temperature, relative humidity, wind speed and solar radiation (also available in the MEPDG design software,) that best represents the climatic conditions of the site for the pavement under study.

TASK 2: incorporating the climatic database into the numerical temperature model, developed in Chapter 5, to predict the temperature and degree of hydration profile in the slab over the first 48 hours after paving.

TASK 3: establishing the permanent curling temperature gradient at the time when the slab reaches the critical degree of hydration. The critical degree of hydration was established in Chapter 3 for sections with 10-, 12-, and 14-inch PCC slabs and the stabilized base layer.

TASK 4: incorporating the ambient RH from the climatic database complied previously for the section into the numerical RH model, developed in Chapter 6, to obtain the RH variation in the test section over at least five years.

TASK 5: correcting the predicted drying shrinkage strain using the field correction factors established in Chapter 6, Section 6.7, for different pavement structures. Using the corrected drying shrinkage strain and the estimated CTE of the PCC mixture to establish the permanent warping at different times over five years.

TASK 6: adding together the values of permanent curling and warping gradients

7.1 ESTABLISHING PERMANENT CURLING GRADIENT

7.1.1 Climatic Regions in Pennsylvania

In an effort to establish the built-in temperature gradient for the pavement sections constructed at different locations in Pennsylvania, the entire state was divided into different climatic regions.

The climatic regions were defined mainly based on the variations in elevation, freezing index (FI) and the annual ambient air temperature. The climatic databases available for Pennsylvania in the MEPDG software were exploited to establish the major climatic indices, such as annual air temperature, rainfall, wind speed, RH and FI for each database. The FI for each climatic station together with their elevations are presented in Figure 7-1. The mean annual air temperature for each climatic station together with the elevation is presented in Figure 7-2 As

seen in these two figures, the stations with similar elevations, FI and mean annual air temperature were grouped together.

Five different climatic regions were established for the state. The different climatic regions are shown with the red circles in Figure 7-1 and Figure 7-2. The five different regions were also presented on a county map for the state in Figure 7-3. It is noteworthy that the climatic database for the Pocono Mountains, marked as Region VI in Figure 7-3, suffered from frequent discontinuities in the recorded data and was therefore not included in the study. The same climatic properties as that for Region II, Allegheny Mountains, can be assumed for Region VI until more climatic data is available for this region. The range for the FI, mean annual air temperature and elevation in each climatic region is summarized in Table 7-1.

The five climatic regions established in this section do not include all the counties in the state as seen in Figure 7-3. The proper climatic region needs to be assigned to each county based on the ranges provided in Table 7-1 for FI, mean annual temperature and elevation and based for each region. The FI is available for each county in Pennsylvania in the PennDOT Pavement Policy Manual, Publication 242, Appendix D. The mean annual temperature for each county can also be extracted from the National Oceanic and Atmospheric Administration (NOAA) website.

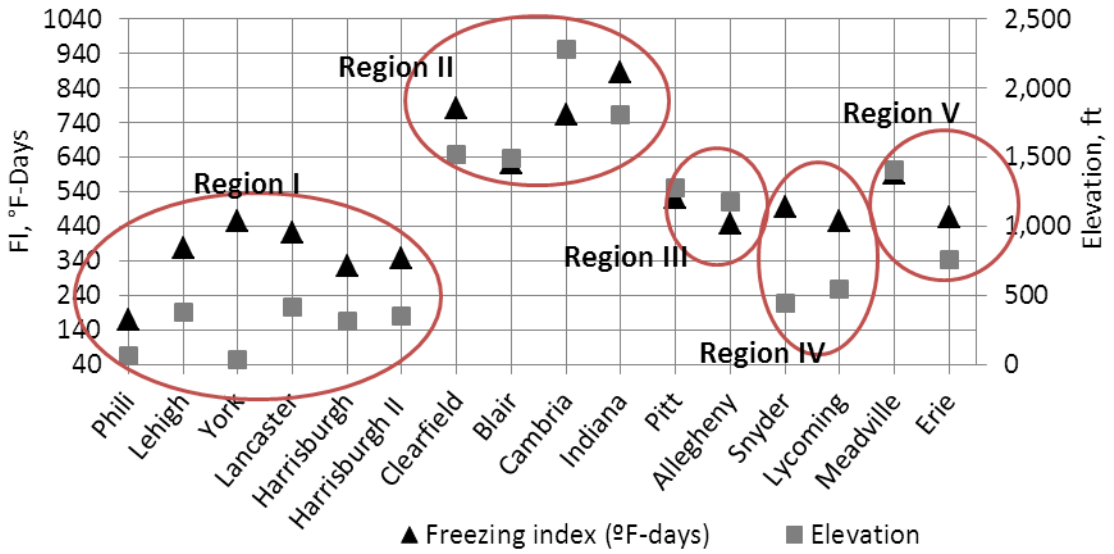

Figure 7-1. Five climatic regions based on the FI and elevation of the climatic stations available in the MEPDG.

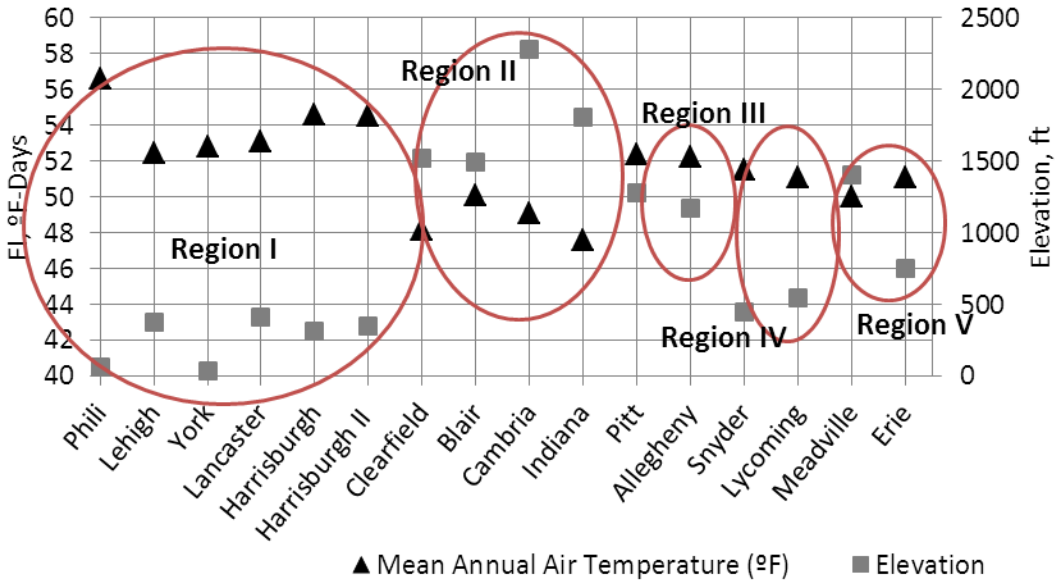

Figure 7-2. Climatic regions based on the mean annual air temperature and elevation of the climatic stations available in the MEPDG.

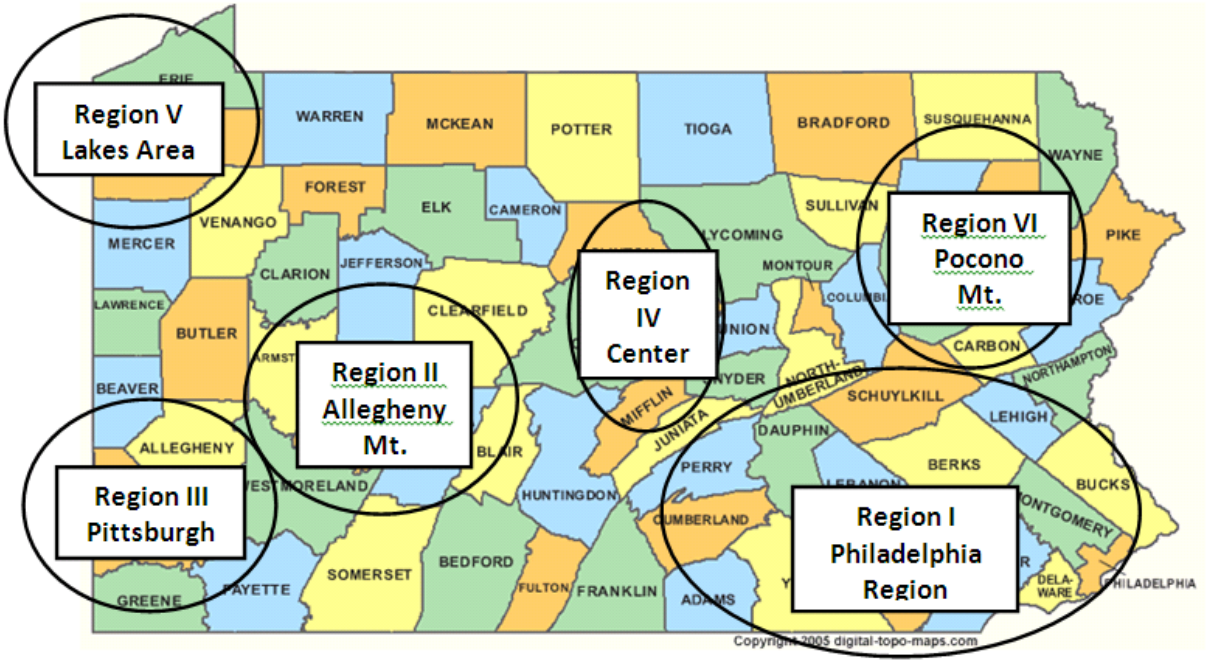

Figure 7-3. Climatic regions on the county map for Pennsylvania, source: www.*Digital-Topo-Maps.com*.

Table 7-1. Ranges for FI, mean annual air temperature and elevation for each climatic region.

Region/Range	Region I		Region II		Region III		Region IV		Region V	
	Min	Max	Min	Max	Min	Max	Min	Max	Min	Max
Mean Annual Air Temperature (ºF)	52	57	48	50	50	52	50	52	50	51
Freezing Index (ºF-days)	150	500	600	1000	400	550	400	500	400	600
Elevation (ft)	0	500	1500	2500	1100	1300	500	500	700	1500

A climatic database was compiled for each of the five climatic regions discussed above. This was accomplished by taking the average of the hourly climatic data for the stations in each region over one year. The one year average data was then averaged over the years that the data was available (minimum of five years). The subsequent results are presented in the form of

average monthly temperature, relative humidity, percent sunshine, wind speed and rainfall in Figure 7-4 through Figure 7-8 for each region.

The established climatic database for each region can then be incorporated into the validated numerical temperature model discussed earlier to predict the temperature gradient at TZ in the slabs constructed in different locations in Pennsylvania.

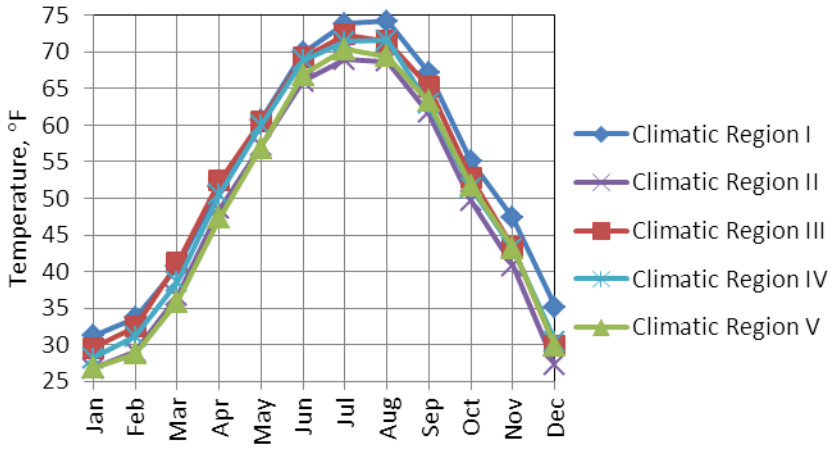

Figure 7-4. Average monthly temperature for each climatic region in the state.

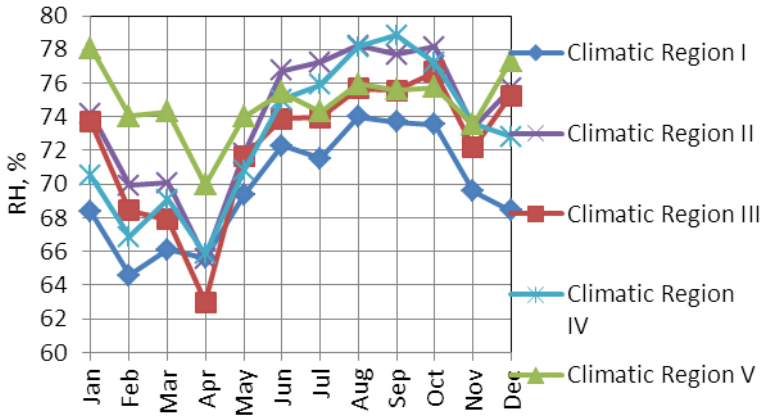

Figure 7-5. Average monthly relative humidity for each climatic region in the state.

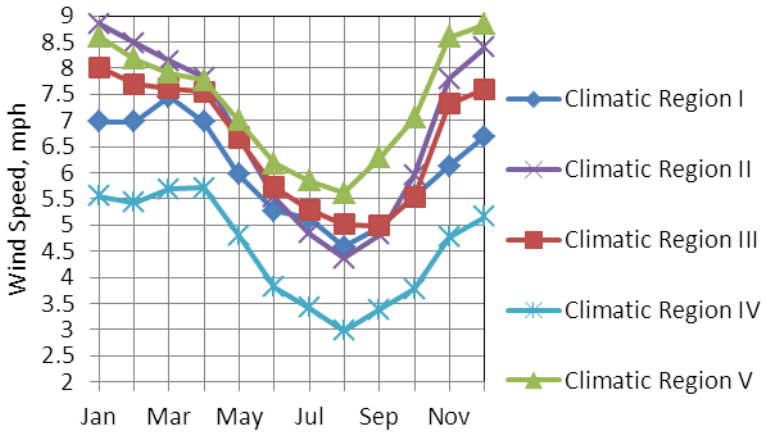

Figure 7-6. Average monthly wind speed for each climatic region in the state.

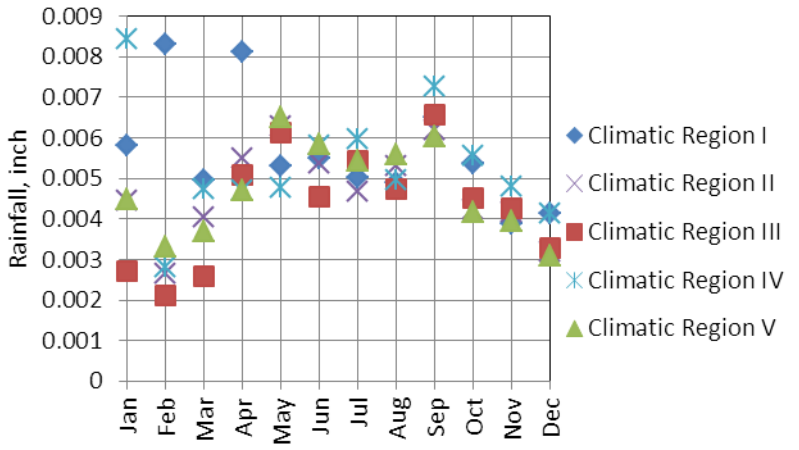

Figure 7-7. Average monthly rainfall for each climatic region in the state.

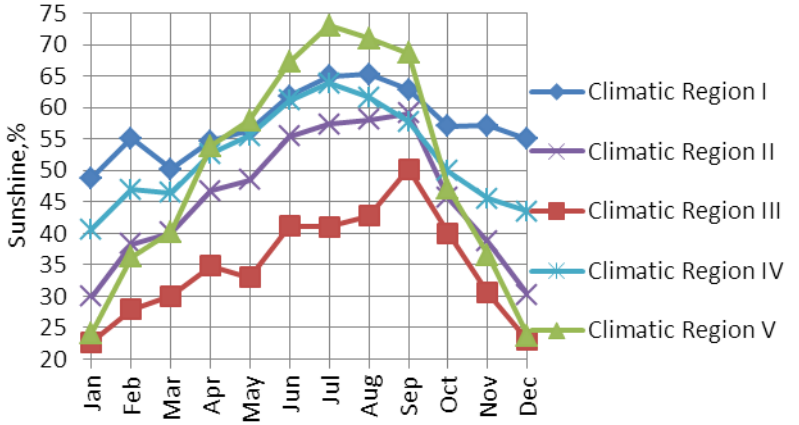

Figure 7-8. Average monthly percent sunshine for each climatic region in the state.

7.1.2 Establishing $\Delta T_{built\text{-}in}$

7.1.2.1 Critical Degree of Hydration

The final goal of this section of the study is to establish the built-in temperature gradient for any pavement structure that consists of a PCC slab with a thickness ranging between 9 and 15 inches including either an ATPB or a CTPB layer. This pavement structure could also be constructed in any of the five climatic regions defined in the previous section and at any time of the day.

As discussed previously, the built-in temperature gradient is the temperature gradient that exists in the slab at TZ. Therefore, in order to establish the built-in temperature gradient, TZ must be defined. Establishing TZ was the main focus of Chapter 3. In this chapter, TZ was established in four instrumented pavement projects based on the strain and temperature changes in the PCC slabs during hardening. Based on the findings in Chapter 3 for Projects 1, TZ is reached in the slabs when the degree of hydration equals 47 percent, while this value was established as 36 percent for Project 2. The variables that are likely to be responsible for the difference in the critical degrees of hydration for the two projects were elaborated upon in Section 3.7. The effects of the variation of 10 percent in the critical degree of hydration on the built-in temperature gradient will be investigated in this section.

The numerical temperature model was employed for performing the analysis. The temperature history for a pavement section with a design similar to that in Project 1 was established. The climatic database generated for Region 1 was used in this small study. The analysis was repeated seven times to include paving of the section in seven different months

throughout the duration of the construction season in Pennsylvania. The time and the day of paving were assumed as 8:00 AM on the first day of every month. The numerical temperature model was used to establish the built-in temperature gradient for both critical degrees of hydration of 0.47 (based on the results for Project 1) and 0.36 (based on the results for Project 2) for every construction month. The subsequent results are presented in Figure 7-9.

Based on the figure, the range of variation in the predicted built-in temperature gradient for the two different critical degrees of hydration is between a minimum of 0.01 °F/in in March and a maximum of 0.35 °F/in in November. This level of variation in the built-in temperature gradient is not expected to have any impact on the design thickness established using the MEPDG. Therefore, it is safe to use the average value of 0.41 as the critical degree of hydration for 12-inch slabs constructed on a stabilized base.

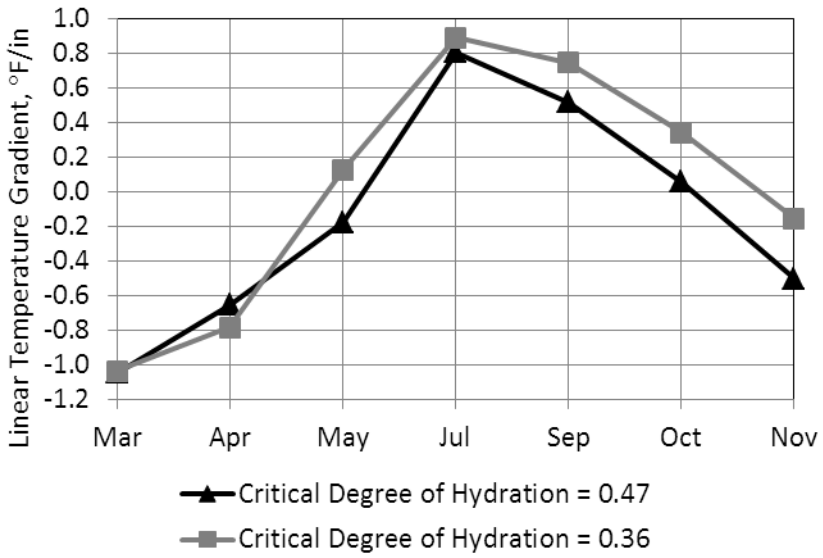

Figure 7-9. Sensitivity of the critical degree of hydration to the predicted built-in temperature gradient.

Chapter 3 also included establishing TZ for Projects 3 and 4, which featured 9 to 15 inch slabs on a CTPB. The critical degree of hydration was established as 51percent for Project 3 and 45 percent for Project 4. The difference between the two was attributed to slab thickness. The slab design thickness for Project 3 was 14 inch, while it was 10 inch for Project 4. Again, a difference of 6 percent in the critical degree of hydration is not expected to affect the design thickness.

Overall, it can be stated that the three critical degrees of hydration established for 12-inch slabs with the ATPB and 10- and 14-inch slabs with the CTPB are very similar. Based on this observation, it can be concluded that the average critical degree of hydration of 45 percent can be used for slabs ranging between 9 and 15 inch with a stabilized base.

7.1.2.2 Month, Day and Time of Paving

Since the designer can only guess the month of construction of the section based on previous experiments in the region, this parameter is very unlikely to be defined accurately at the time of design of the section. Therefore, the sensitivity of the month of construction to the predicted built-in temperature gradient is investigated in this section.

The built-in temperature gradient was established for the slabs constructed on the first day of every month over the construction season, using the climatic database for Region 1 and the average critical degree of hydration of 0.45. The respective results are presented in Figure 7-10 in the form of seasonal averages. The error bars in this figure show the variability in the built-in temperature gradient within each season.

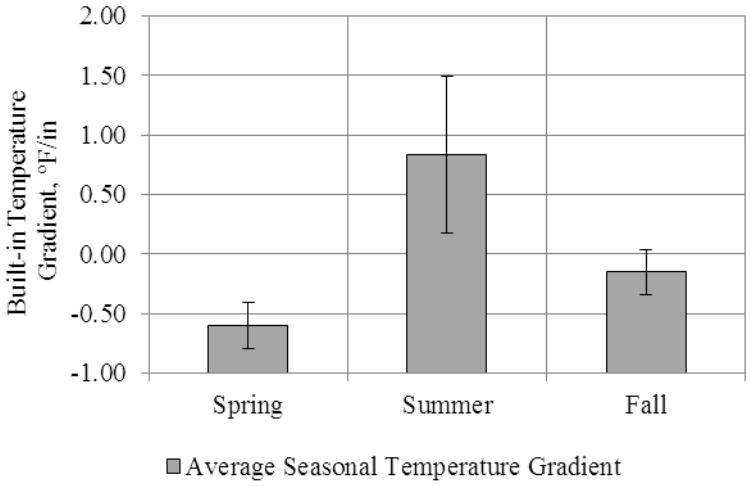

Figure 7-10. Average seasonal built-in temperature gradient for different seasons.

Since the construction season does not start until the warm days in March, the months in winter were not included in the study. It is also noteworthy that spring was defined to include the months of March, April and June. Based on Figure 7-10, the largest positive gradient is seen during the summer. This agrees with expectations, since the high ambient temperatures and solar radiation in the summer result in an increase in the rate of hydration of the cement in comparison to paving in the colder days during the fall or spring. Therefore, the slab which was paved at 8:00 AM, reaches TZ sometime in the hot summer afternoon and thereby a large positive built-in temperature gradient lock into the slab. During the fall or spring, on the other hand, a slab paved in the morning would reach TZ at the cooler time of the day and therefore, the built-in temperature gradient can be negative and the magnitude is relatively small.

Furthermore, a high variability is seen in the built-in temperature gradient for the months in the spring and the fall, as expected, while a very low variability is seen over the summer.

Therefore, the built-in temperature gradient needs to be established for only one month during the seasons with a low variability. This parameter will be established for all the three months in the seasons with high variability (spring and fall).

Sensitivity of the time of paving to the built-in temperature gradient is the next factor that was investigated. To address this issue, three different times of paving during the day were selected; 8:00 AM, 2:00 PM and 5:00 PM. These times were selected based on the changes in the weather conditions during the day. The built-in temperature gradient was established for slabs paved at three different times of the day and on the first day of each month over the construction season. Again, the climatic database for Region I was used for these simulations. The results are presented in Figure 7-11.

Based on the figure, the two paving times of 2:00 PM and 5:00 PM show similar values, however, variability is observed between the morning and the afternoon paving times during the fall and spring. This variability is minimal during the summer.

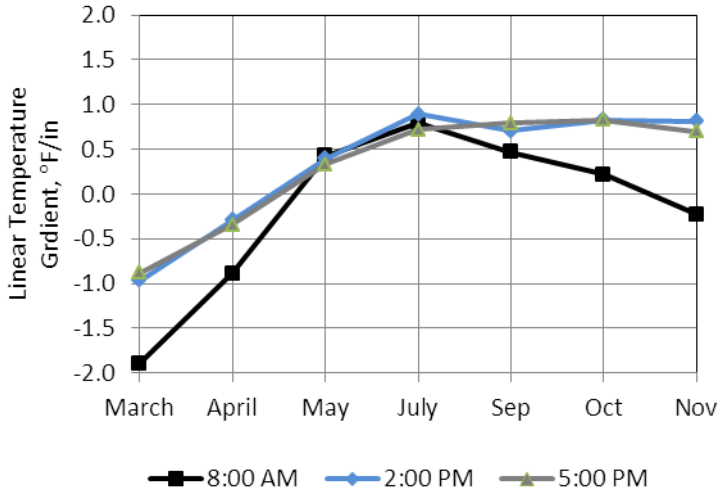

Figure 7-11. Effects of the time of paving on the built-in temperature gradient.

The two months of March and April that appear to show the highest variability in the built-in temperature gradient with respect to the time of paving were selected for further investigation. The built-in temperature gradient was established for sections paved during one day in April and one day in March at different times of the day. Each paving day was defined from 8:00 AM to 8:00 PM and the times of paving were defined one hour apart during each day. The third day of April and the third day of March (since the first day of March included some hours with freezing temperatures) were selected as the paving day. The predicted built-in temperature gradients are presented in Figure 7-12 for all 11 cases during each day.

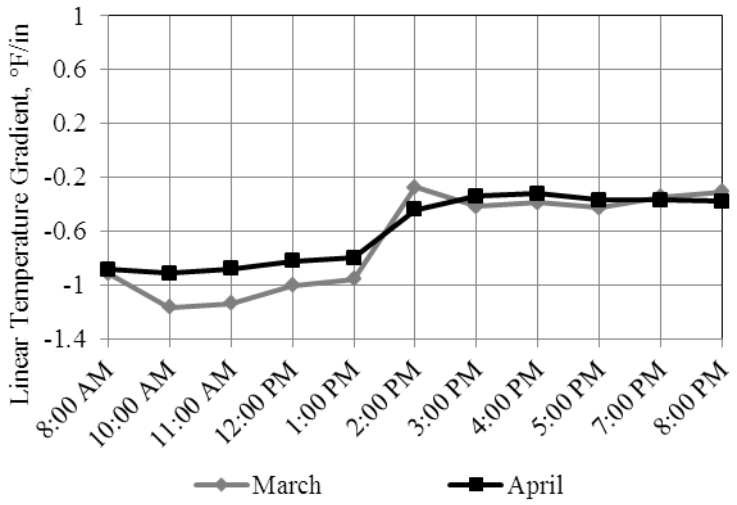

Figure 7-12. Effects of time of paving on the built-in temperature gradient for March and April.

From Figure 7-12, it can be seen that the built-in temperature gradient is relatively constant when the time of paving varies between 8:00 AM and 1:00 PM and also from 2:00 PM to 8:00 PM. Based on this and the results from the previous section, the built-in temperature gradient is established for pavement sections constricted in Pennsylvania in different months during the construction season and at two times of 8:00 AM and 5:00 PM. The average of these two values is suggested to be used in design. The built-in temperature gradient for the slabs paved in the morning and the ones paved in the afternoon are presented in Figure 7-13 and Figure 7-14, respectively. The average of the gradients in Figure 7-13 and Figure 7-14 is presented in Figure 7-15. A summary of the results for all the regions is also provided in Table 7-2.

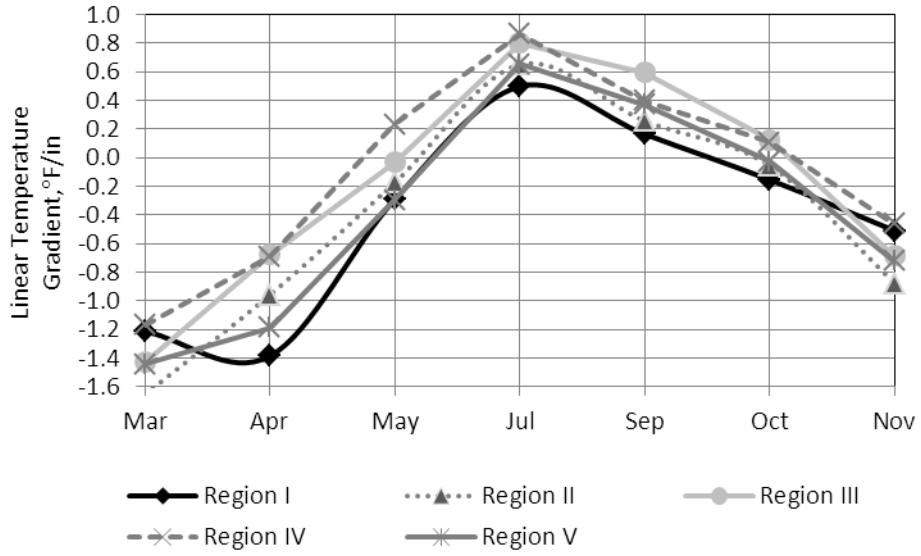

Figure 7-13. Built-in temperature gradient for five different regions in PA, for different construction month and time of paving of 8:00 AM.

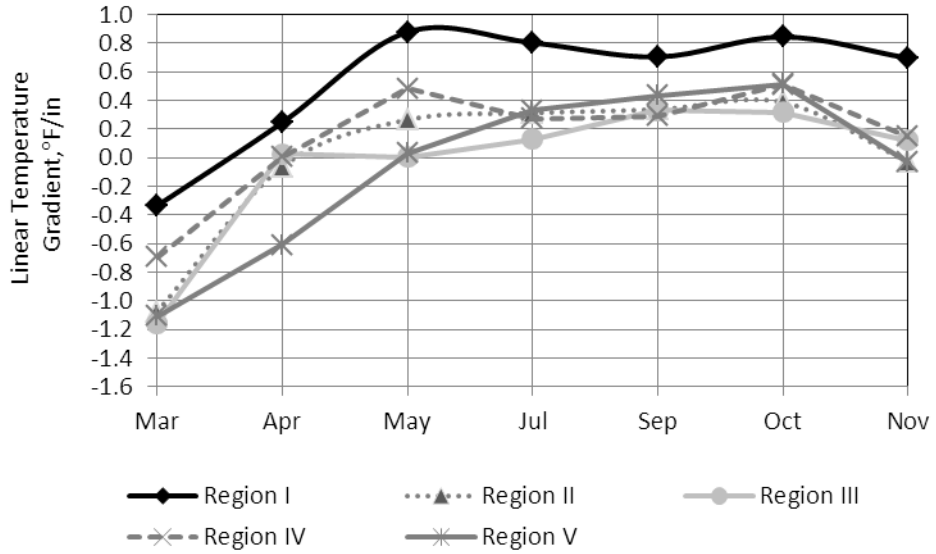

Figure 7-14. Built-in temperature gradient for five different regions in PA, for different construction month and time of paving of 5:00 PM.

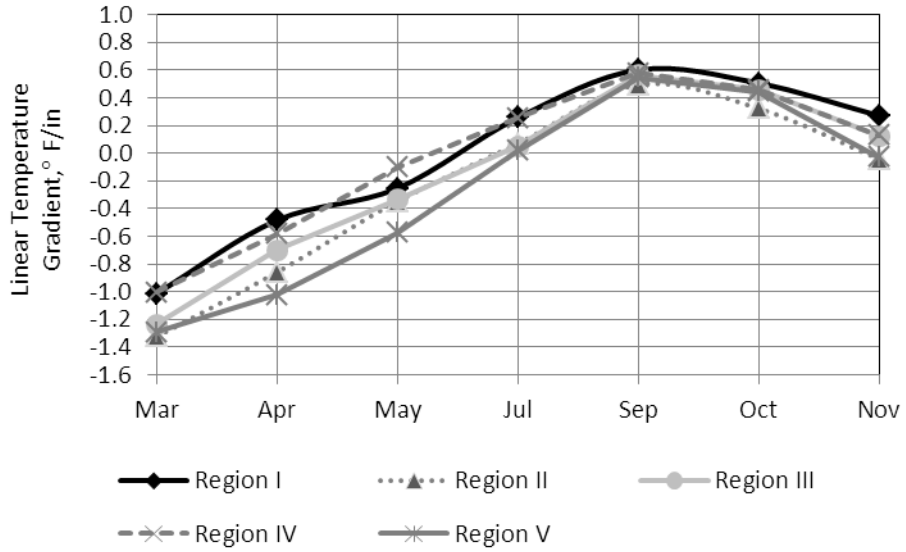

Figure 7-15. Average of the built-in temperature gradient for the morning and afternoon paving times.

Table 7-2. Built-in temperature gradient for the five climatic regions in the state.

Month of Construction/ Climatic Region	March	April	May	July	Sep.	Oct.	Nov.
Region I	-0.8	-0.6	0.3	0.7	0.4	0.3	0.1
Region II	-1.4	-0.5	0.0	0.5	0.3	0.2	-0.5
Region III	-1.3	-0.3	0.0	0.5	0.5	0.2	-0.3
Region IV	-0.9	-0.3	0.4	0.6	0.3	0.3	-0.2
Region V	-1.3	-0.9	-0.1	0.5	0.4	0.2	-0.4

Based on the data from Table 7-2, the built-in temperature gradients for Region I are similar to the ones established for Region IV in all months. These two regions are two neighboring regions on the county map in Figure 7-3 and can be combined into one climatic region, named as Climatic Region A. Furthermore, based on the data from Table 7-2, Regions II

and III show similar values for the built-in temperature gradient in almost all months. These two regions are again neighboring regions on the county map presented in Figure 7-3 and can be combined into one climatic region, named Climatic Region B. Region V, or the lake region, is referred to as Climatic Region C. The final average built-in temperature gradients are summarized in Table 7-3 for Climatic Regions A, B and C.

Table 7-3. Built-in temperature gradient for the three final climatic regions in the state.

Month of Construction/ Climatic Region	March	April	May	July	Sep.	Oct.	Nov.
Region A	-0.9	-0.5	0.3	0.6	0.4	0.3	0.0
Region B	-1.3	-0.4	0.0	0.5	0.4	0.2	-0.4
Region C	-1.3	-0.9	-0.1	0.5	0.4	0.2	-0.4

7.2 PREDICTING DRYING SHRINKAGE STRAIN

The ambient RH for each climatic region was incorporated into the numerical RH model, developed in Chapter 6, to establish $\Delta[1-(\frac{RH}{100})^3]_{eq}$ for a 12-inch slab constructed in each of the five climatic regions in the state. For this purpose, the average hourly climatic database that was generated previously for each region and for a duration of one year was repeated five times to establish the linear temperature gradient equivalent to the 5-year irreversible nonlinear drying shrinkage gradient. The ultimate drying shrinkage of the concrete mix is another variable that is required to estimate the drying shrinkage strain in the slab.

The paving mix commonly used in Pennsylvania is PennDOT Class AA 500 slip form concrete. This mix includes 500 lb/yd^3 cementitious material content plus 88 lb/yd^3 fly ash. Based on laboratory tests performed on samples from the concrete for Projects 1 and 2 and also the SR 22 section, in Sections 3.3 and 3.4 and 6.2.1., the ultimate drying shrinkage for PennDOT Class AA 500 slip form concrete can be assumed as approximately 600 με.

The product of $\Delta[1-(\frac{RH}{100})^3]_{eq}$ predicted using the RH numerical model for each climatic region and the ultimate drying shrinkage of the mixture provides an estimate of the drying shrinkage in the slabs. The mean monthly data corresponding to only one month in every year was selected for each case to eliminate the effects of seasonal fluctuations on the drying shrinkage. The result is presented in Figure 7-16 for all the five climatic regions in Pennsylvania.

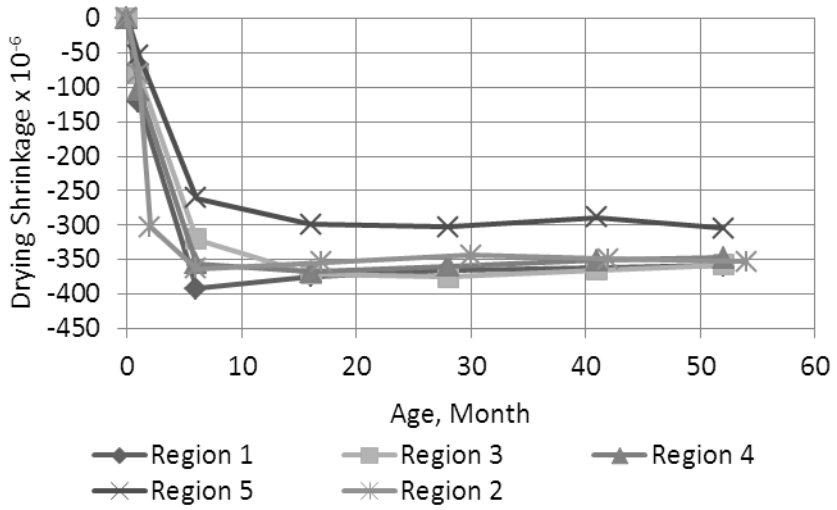

Figure 7-16. Predicted drying shrinkage for slabs in the five climatic regions in Pennsylvania.

7.3 FIELD CORRECTION FACTORS

The predicted drying shrinkage should be corrected for the effects of the restraining factors in the field, such as the friction between the base and the slabs and the dowel and tie bars. The counteracting effects of long-term creep should also be considered. This was achieved by using the field correction factors established for the doweled and undoweled, 12-inch slabs in the SR 22 project. This information was previously provided in Section 6.7, Table 6-9. The CTE of the concrete mix was used to establish the equivalent temperature gradient for the permanent warping, in the slabs. A summary of the adjusted permanent warping gradients over five years is presented in Table 7-4 for the five regions for both doweled and undoweled slabs.

Table 7-4. Predicted drying shrinkage corrected for the field effects for the five climatic regions in Pennsylvania.

Age (Month)		Permanent Warping Equiv. Temperature Gradient, °F/in						
		0	2	6	16	28	41	52
Region I	Doweled	0	-0.5	-2.0	-2.0	-2.0	-2.0	-2.0
	Undoweled	0	-1.0	-3.0	-3.0	-3.0	-3.0	-3.0
Region II	Doweled	0	-0.5	-2.0	-2.0	-2.0	-2.0	-2.0
	Undoweled	0	-1.0	-2.5	-3.0	-3.0	-3.0	-3.0
Region III	Doweled	0	-1.0	-2.0	-2.0	-2.0	-2.0	-2.0
	Undoweled	0	-1.0	-2.5	-3.0	-3.0	-3.0	-3.0
Region IV	Doweled	0	-1.0	-2.0	-2.0	-2.0	-2.0	-2.0
	Undoweled	0	-1.0	-3.0	-3.0	-3.0	-3.0	-3.0
Region V	Doweled	0	-0.5	-1.5	-1.5	-2.0	-2.0	-2.0
	Undoweled	0	-0.5	-2.0	-2.0	-2.0	-2.5	-2.5
Average	Doweled	0	-0.5	-2.0	-2.0	-2.0	-2.0	-2.0
	Undoweled	0	-1.0	-2.5	-3.0	-3.0	-3.0	-3.0

The results in Table 7-4 are very similar for all the five regions at all ages and therefore the average values of all regions at different ages can be used for permanent warping gradient for 12-inch slabs. To establish the permanent effective curl/warp temperature gradient, the permanent curling temperature gradient established previously for each region should be added to the permanent warping gradient in Table 7-4. This is performed for Regions A, B and C. The final result for the doweled and undoweled pavement sections constructed in different months of the year in Pennsylvania is provided separately in Table 7-5 and Table 7-6. ***It is noted that the***

values from Table 7-5 and Table 7-6, need to be multiplied by the slab thickness (10.6 inches) and also a negative sign when used in the MEPDG.

Based on Table 7-5, Region A shows the largest values for the permanent curl/warp gradient in all months and Region C shows the smallest values for this parameter. Values established for the month of July should be used for June and August as well, since minimal variability was seen in the built-in temperature gradient, when the construction occurred during the summer.

The same procedure can be followed to establish the permanent curl/warp effective temperature gradients for pavements structures constructed in other states. In doing so, it is important to establish proper values for the material properties of the concrete, including the 28-day compressive strength, ultimate drying shrinkage and CTE. An accurate climatic database for the site of the pavement section, that has been populated with climatic data over, preferably, a minimum of 10 years, can result in better predictions for both permanent curling and warping in the slab.

It should be noted that currently, the MEPDG uses a default value of -10 °F for the permanent curl/warp effective temperature difference. This value was determined based on an optimization of the cracking model incorporated into the MEPDG. This optimization is performed based on the percent cracking observed in the LTPP sections. The default value used in the MEPDG for the permanent curl/warp equates to a built-in gradient of +0.83 °F/in for a 12-inch slab. This does not agree with the findings in this study. It has been shown here that the drying shrinkage gradient is actually the primary component contributing to the permanent

curl/warp gradient, regardless of the month of construction. It is hoped that the findings from this study help with defining this parameter more accurately in the MEPDG.

Table 7-5. Magnitude of the permanent curl/warp temperature gradient for three climatic regions in Pennsylvania for doweled slabs.

Age (Month)/ Month of Construction	0	2	6	16	28	41	52
Region A							
March	-1.0	-1.5	-3.0	-3.0	-3.0	-3.0	-3.0
April	-0.5	-1.0	-2.5	-2.5	-2.5	-2.5	-2.5
May	0.5	-0.5	-1.5	-1.5	-1.5	-1.5	-1.5
July	1.0	0.0	-1.5	-1.5	-1.5	-1.5	-1.5
Sep.	0.5	0.5	-1.5	-1.5	-1.5	-1.5	-1.5
Oct.	0.0	-0.5	-1.5	-1.5	-1.5	-1.5	-1.5
Nov.	0.0	-1.0	-2.0	-2.0	-2.0	-2.0	-2.0
Region B							
March	-1.0	-1.5	-3.0	-3.0	-3.0	-3.0	-3.0
April	-0.5	-1.0	-2.5	-2.5	-2.5	-2.5	-2.5
May	0.5	-0.5	-1.5	-2.0	-2.0	-2.0	-2.0
July	1.0	0	-1.5	-1.5	-1.5	-1.5	-1.5
Sep.	0.5	0.0	-1.5	-1.5	-1.5	-1.5	-1.5
Oct.	0.0	-1.0	-2.0	-2.5	-2.5	-2.5	-2.5
Nov.	0.0	-1.0	-2.5	-3.0	-3.0	-3.0	-3.0
Region C							
March	-1.0	-1.5	-3.0	-3.0	-3.0	-3.0	-3.0
April	-0.5	-1.0	-2.5	-2.5	-2.5	-2.5	-2.5
May	0.5	0.0	-1.5	-2.0	-2.0	-2.0	-2.0
July	1.0	0.0	-1.5	-1.5	-1.5	-1.5	-1.5
Sep.	0.5	0.0	-1.5	-1.5	-1.5	-1.5	-1.5
Oct.	0.0	-0.5	-1.5	-2.0	-2.0	-2.0	-2.0
Nov.	0.0	-1.0	-2.0	-2.0	-2.0	-2.0	-2.0

Table 7-6. Magnitude of the permanent curl/warp temperature gradient for three climatic regions in Pennsylvania for undoweled slabs.

Age (Month)/ Month of Construction	0	2	6	16	28	41	52
Region A							
March	-1.0	-2.0	-3.5	-3.5	-4.0	-4.0	-4.0
April	-0.5	-1.5	-3.0	-3.0	-3.5	-3.5	-3.5
May	0.5	-0.5	-2.0	-2.5	-2.5	-2.5	-2.5
July	1.0	-0.5	-2.0	-2.0	-2.5	-2.5	-2.5
Sep.	0.5	-0.5	-2.0	-2.5	-2.5	-2.5	-2.5
Oct.	0.0	-1.0	-2.0	-2.5	-2.5	-2.5	-2.5
Nov.	0.0	-1.0	-2.5	-3.0	-3.0	-3.0	-3.0
Region B							
March	-1.0	-2.0	-3.5	-3.5	-4.0	-4.0	-4.0
April	-0.5	-1.5	-3.0	-3.0	-3.5	-3.5	-3.5
May	0.5	-1.0	-2.0	-2.5	-2.5	-2.5	-2.5
July	1.0	-0.5	-2.0	-2.0	-2.0	-2.5	-2.5
Sep.	0.5	-0.5	-2.0	-2.5	-2.5	-2.5	-2.5
Oct.	0.0	-1.0	-2.0	-2.5	-2.5	-2.5	-2.5
Nov.	0.0	-1.0	-2.5	-3.0	-3.0	-3.0	-3.0
Region C							
March	-1.0	-2.0	-3.5	-3.5	-4.0	-4.0	-4.0
April	-0.5	-1.5	-3.0	-3.5	-3.5	-3.5	-3.5
May	0.5	-1.0	-2.0	-2.5	-2.5	-2.5	-2.5
July	1.0	-0.5	-2.0	-2.0	-2.5	-2.5	-2.5
Sep.	0.5	-0.5	-2.0	-2.3	-2.4	-2.5	-2.4
Oct.	0.0	-1.0	-2.1	-2.5	-2.5	-2.5	-2.5
Nov.	0.0	-1.0	-3.0	-3.0	-3.0	-3.0	-3.0

8.0 CONCLUSIONS AND SUGGESTED FUTURE WORK

8.1 MAJOR FINDINGS

The primary objective of this doctoral study was to provide a procedure for establishing practical values for the permanent effective curl/warp temperature gradient. The complete procedure was established through different chapters of the dissertation and the preceding chapter provided an example of utilizing the developed procedure for slabs constructed in Pennsylvania. Significant conclusions drawn in each chapter of the study will be provided in a bulleted list as follows:

- The degree of hydration at TZ, established based on strain-temperature measurements, can be used in other slabs with the same design to identify TZ.
- The average critical degree of hydration was established as 0.41 for 12-inch slabs with an ATPB, 0.51 for 14-inch slabs with a CTPB and 0.45 for 10-inch slabs with CTPB layer. It was concluded that slab thickness and base type do not appear to significantly influence TZ. An average value of 0.45 can be used for slabs with 9 to 15 inch thickness and a stabilized base.
- A negative built-in temperature gradient was established for all the slabs paved in the morning and at noon. The months of paving included September and October of 2009 and May and April of 2010.

- The built-in temperature gradient varied for the slabs that were paved late in the afternoon. Both positive and negative values were obtained for the slabs paved between 2:00 PM and 5:00 PM.
- VW static strain gages can be used to establish the drying shrinkage strain in the slabs over the years. The measured values at the age of five years can be lower than the predicted values by up to 70 percent, for 12-inch doweled slabs, and by 60 percent, for 12-inch non-doweled slabs. This was attributed to the restraint provided by the base and also relaxation due to creep.

8.2 RECOMMENDATIONS FOR FUTURE RESEARCH

Limitations of the procedure developed in the present study for establishing permanent curl/warp together with proposed future researches that can be performed to complete and improve this research are listed as follows:

1. The critical degree of hydration was established in this study for slabs with an ATPB and a CTPB. This research can be extended to include pavement structures with granular bases.
2. The possible effect of the w/cm ratio on the rate of heat liberation during hydration of cement needs to be incorporated into the existing models available for estimating the rate of heat of hydration.

3. A numerical temperature model was implemented in this study to predict the temperature variation in the pavement structure over the first 48 hours after paving. To improve the predictions of the model at early ages, evaporation should also be considered as a mode of heat exchange at the surface of the slab.
4. Possibility of the occurrence of early-age creep was studied in this work based on strain measurements in the field for a duration of 4 days following the construction. A finite-element model can better capture the effects of creep over a longer period of throughout the service life of the pavement. This model should estimate creep at every time step based on the transient stress levels. It is essential for this model to be validated based on strain measurements in the field.
5. Currently, the MEPDG uses a default value of -10 °F for the permanent curl/warp effective temperature difference. This value was defined based on an optimization of the cracking model in the MEPDG. It is anticipated that the findings from the current study will help with defining this parameter more accurately in the MEPDG. It should be noted that changing the values of permanent curl/warp in the MEPDG from the default value requires local calibration of the MEPDG performance models.

APPENDIX A

EARLY-AGE MEASURED TEMPERATURE IN INSTRUMENTED PROJECTS

Project 1

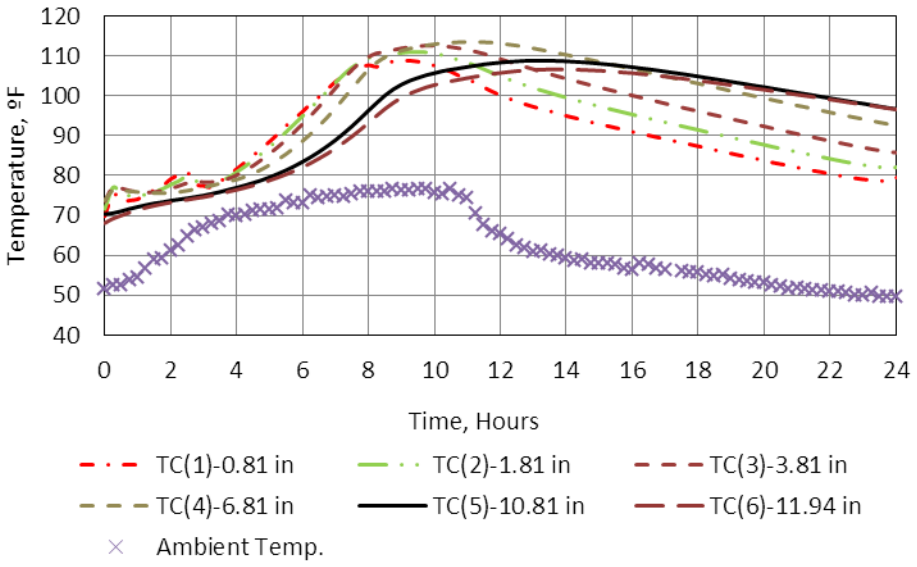

Figure A 1. Temperature measured over the first 24 hours along the depth of Slab A, Cell 1, Project 1.

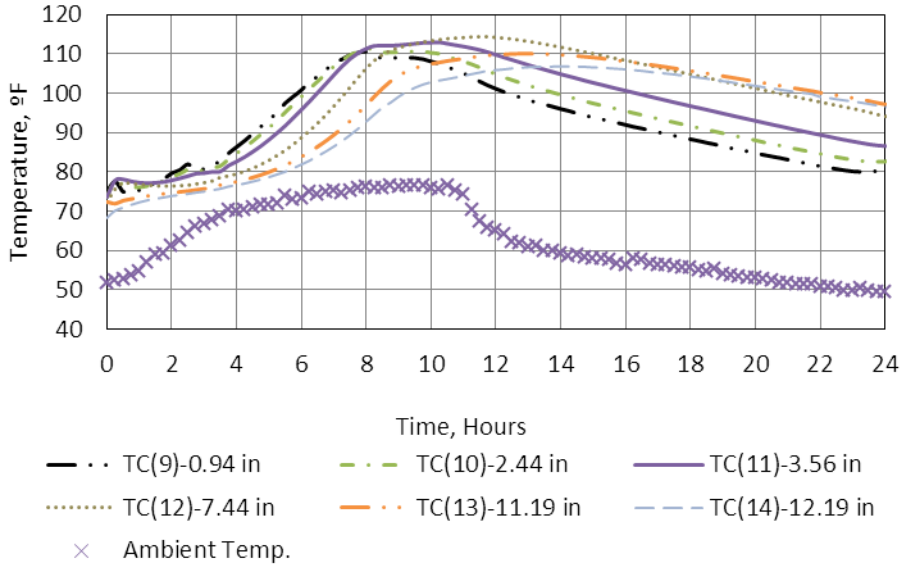

Figure A 2. Temperature measured over the first 24 hours along the depth of Slab C, Cell 1, Project 1.

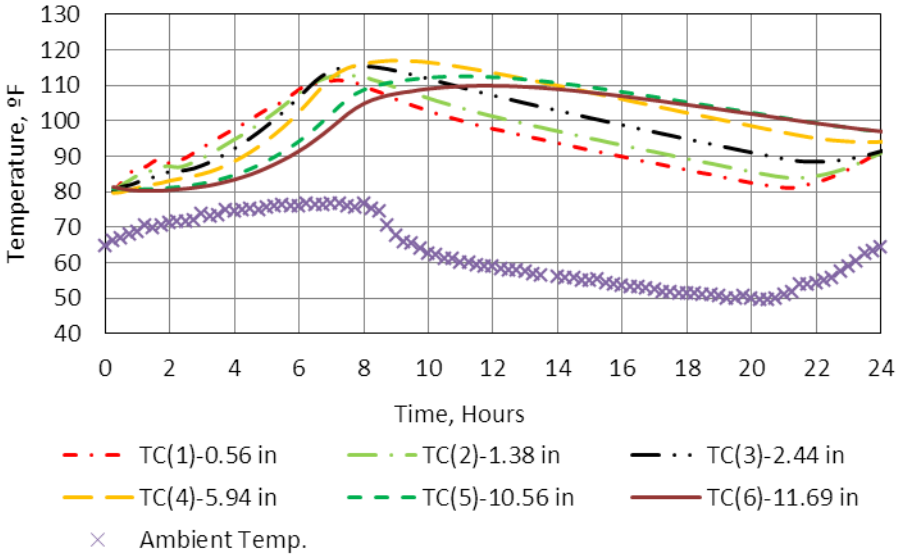

Figure A 3. Temperature measured over the first 24 hours along the depth of Slab A, Cell 2, Project 1.

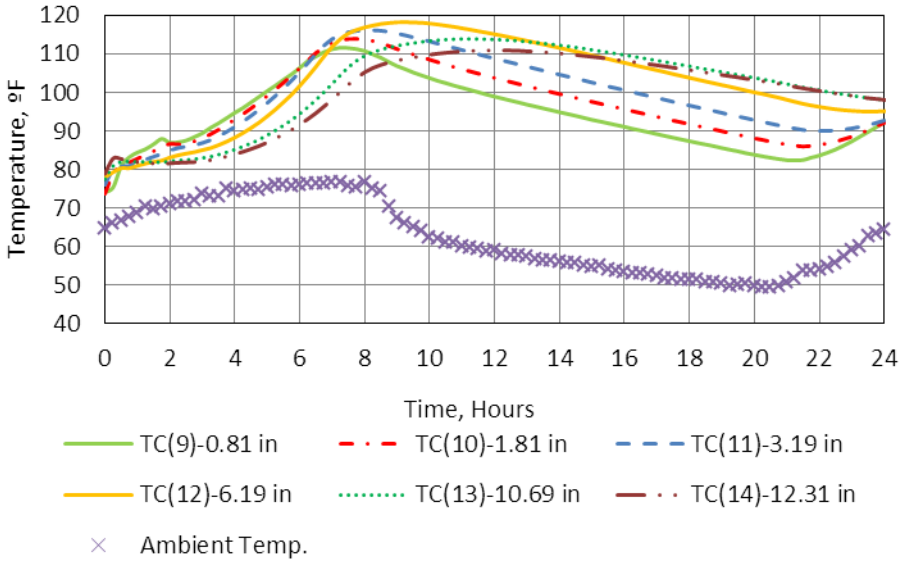

Figure A 4. Temperature measured over the first 24 hours along the depth of Slab C, Cell 2, Project 1.

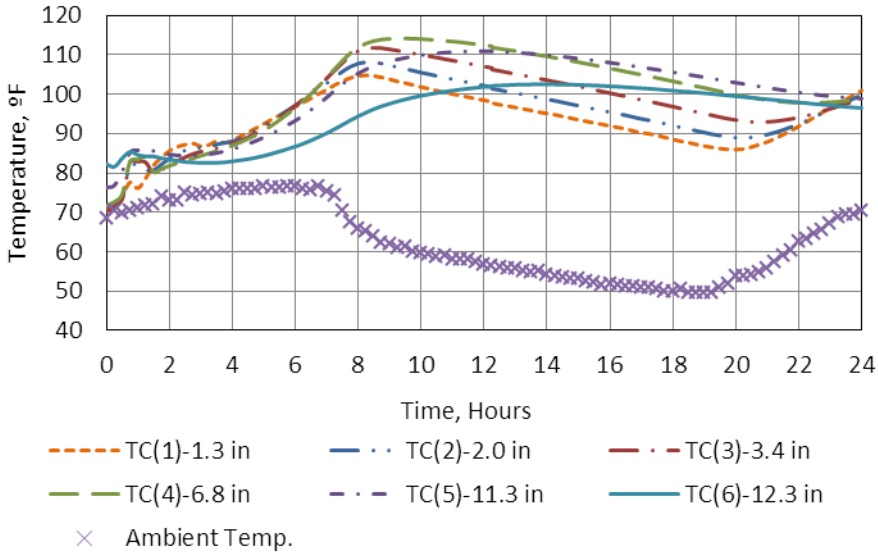

Figure A 5. Temperature measured over the first 24 hours along the depth of Slab A, Cell 3, Project 1.

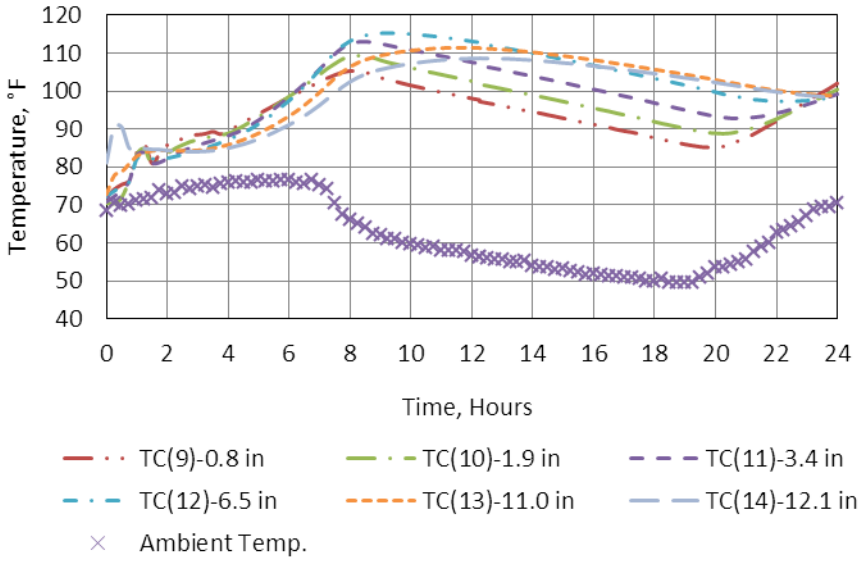

Figure A 6. Temperature measured over the first 24 hours along the depth of Slab C, Cell 3, Project 1.

Project 2

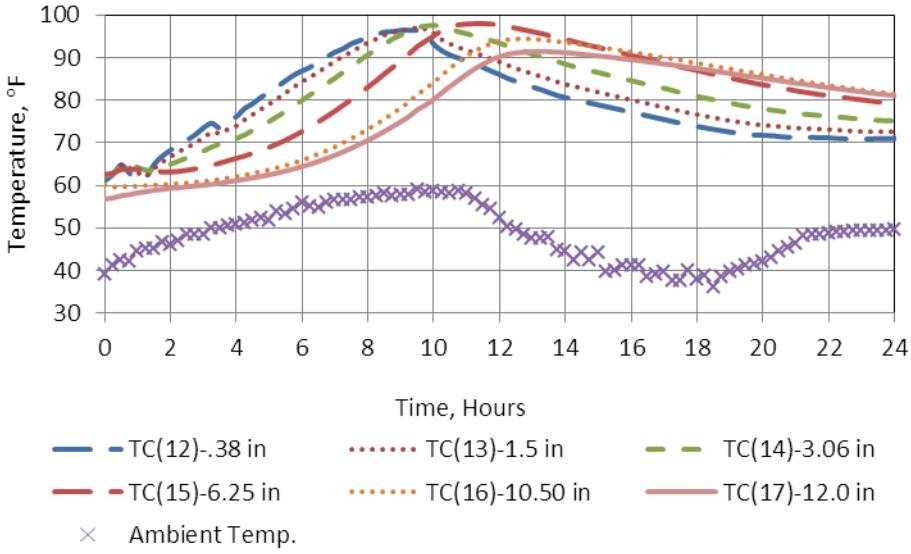

Figure A 7. Temperature measured over the first 24 hours along the depth of Slab C, Cell 1, Project 2.

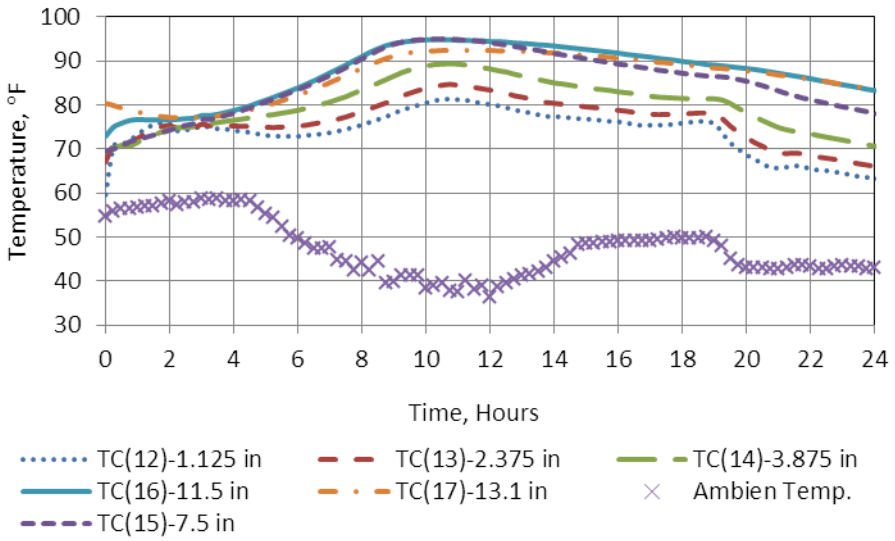

Figure A 8. Temperature measured over the first 24 hours along the depth of Slab C, Cell 2, Project 2.

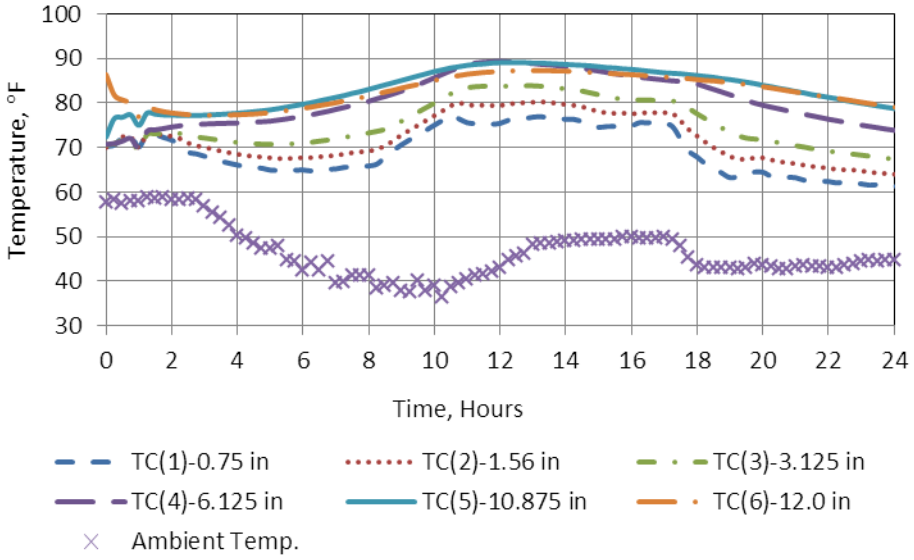

Figure A 9. Temperature measured over the first 24 hours along the depth of Slab A, Cell 3, Project 2.

Project 3

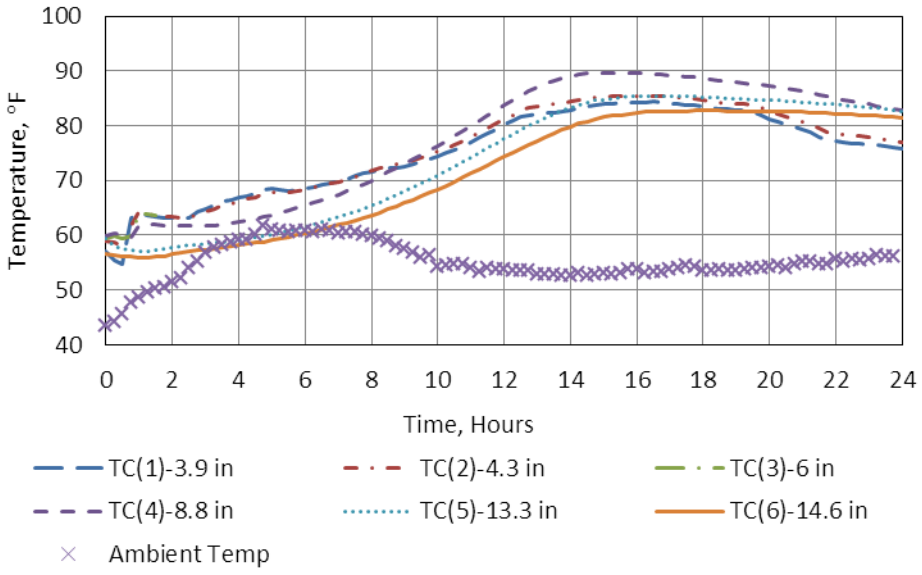

Figure A 10. Temperature measured over the first 24 hours along the depth of Slab A, Cell 1, Project 3.

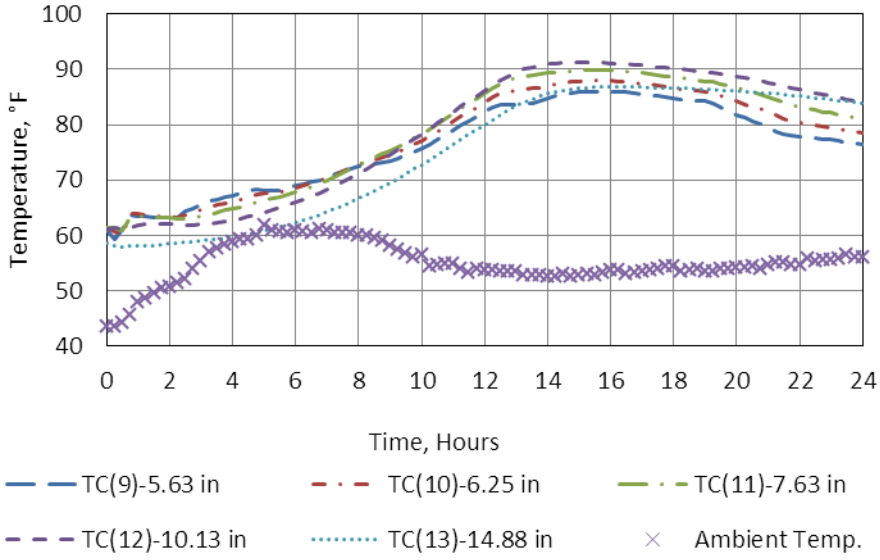

Figure A 11. Temperature measured over the first 24 hours along the depth of Slab C, Cell 1, Project 3.

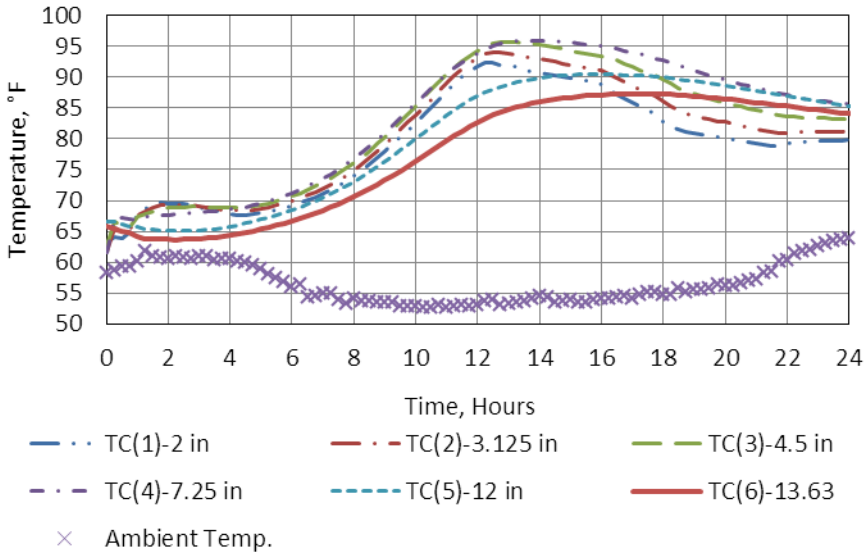

Figure A 12. Temperature measured over the first 24 hours along the depth of Slab A, Cell 2, Project 3.

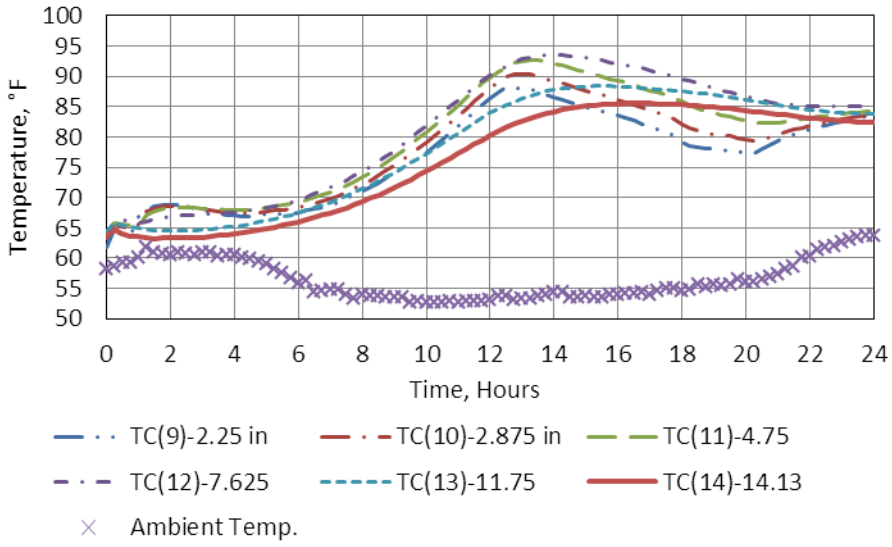

Figure A 13. Temperature measured over the first 24 hours along the depth of Slab C, Cell 2, Project 3.

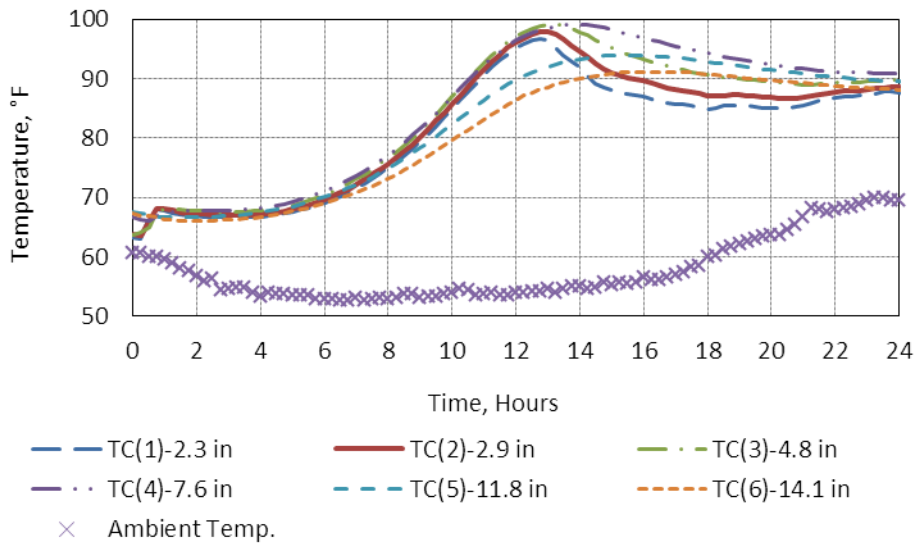

Figure A 14. Temperature measured over the first 24 hours along the depth of Slab A, Cell 3, Project 3.

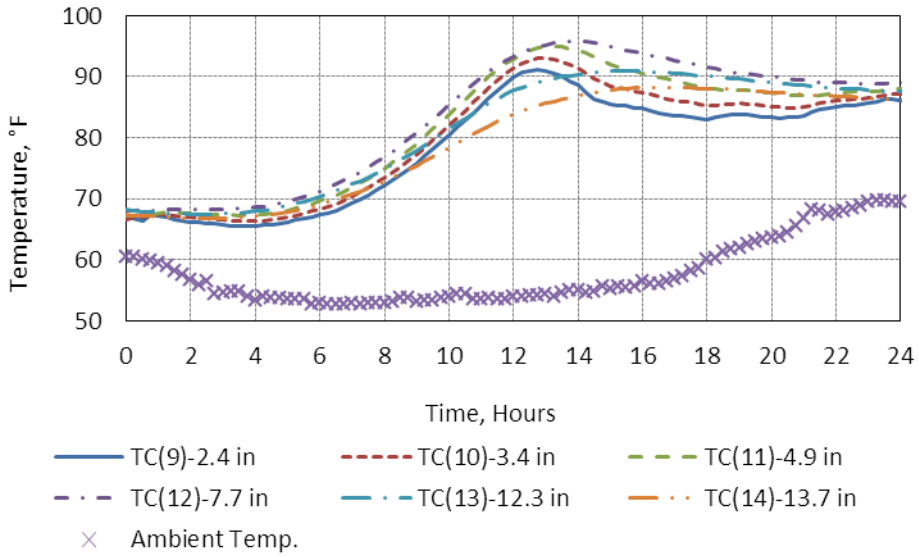

Figure A 15. Temperature measured over the first 24 hours along the depth of Slab C, Cell 3, Project 3.

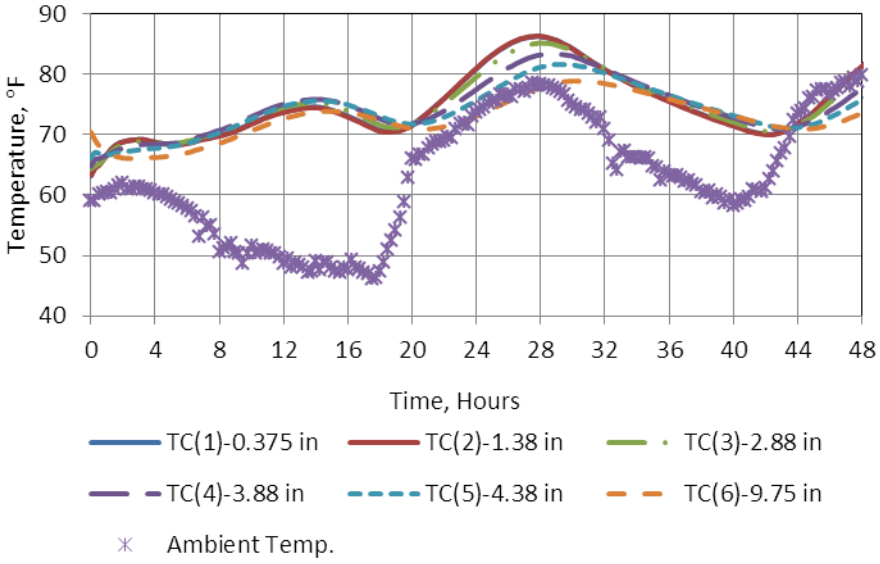

Figure A 16. Temperature measured over the first 24 hours along the depth of Slab A, Cell 1, Project 4.

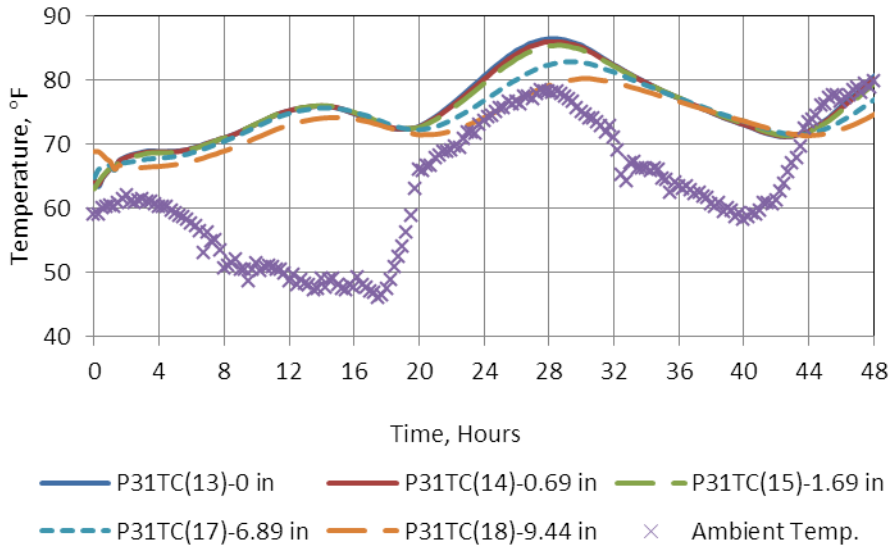

Figure A 17. Temperature measured over the first 24 hours along the depth of Slab C, Cell 1, Project 4.

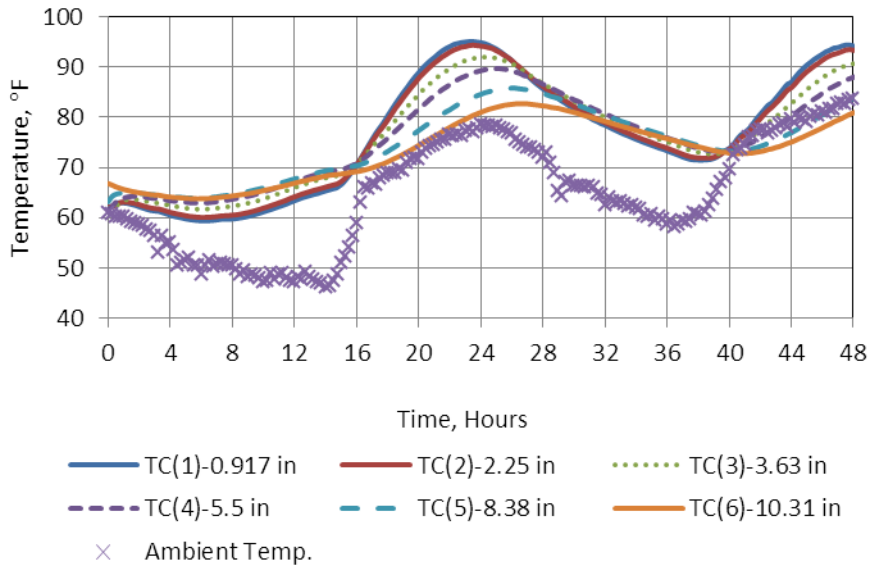

Figure A 18. Temperature measured over the first 24 hours along the depth of Slab A, Cell 2, Project 4.

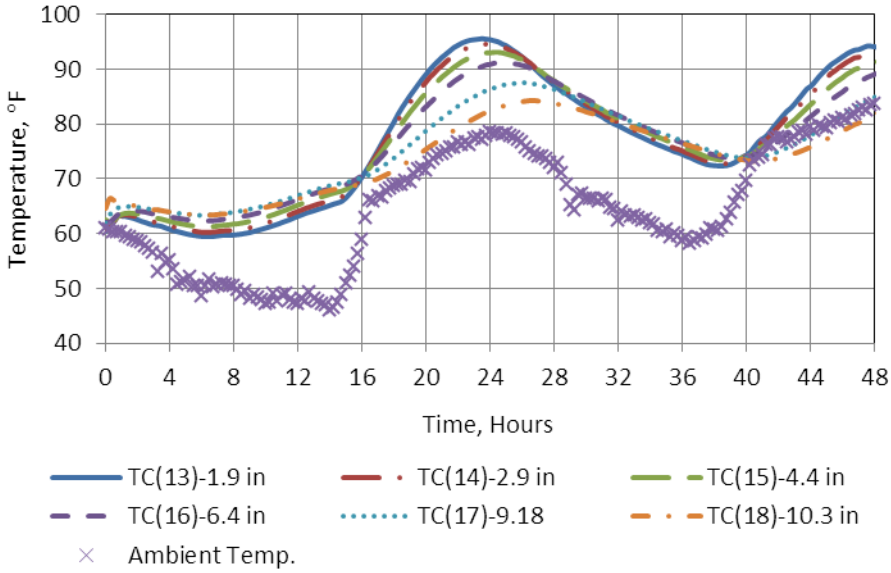

Figure A 19. Temperature measured over the first 24 hours along the depth of Slab C, Cell 2, Project 4.

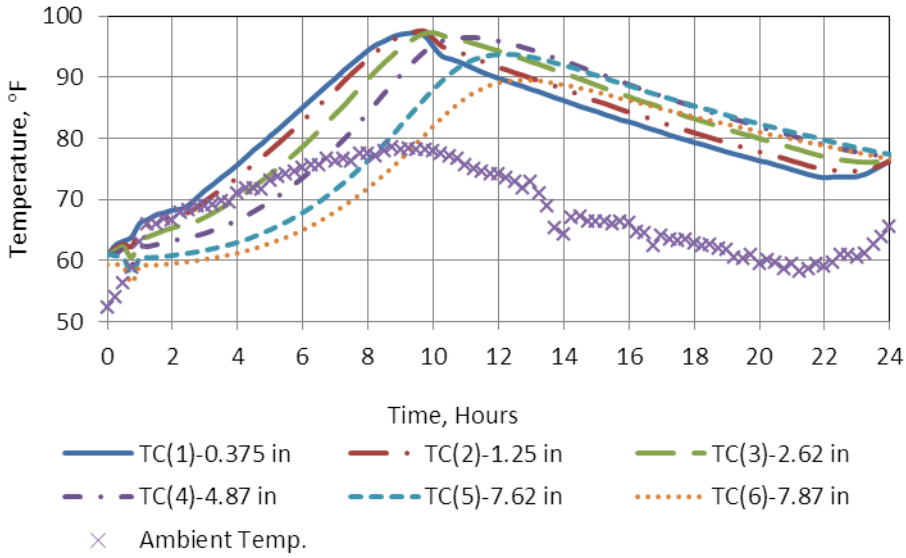

Figure A 20. Temperature measured over the first 24 hours along the depth of Slab A, Cell 3, Project 4.

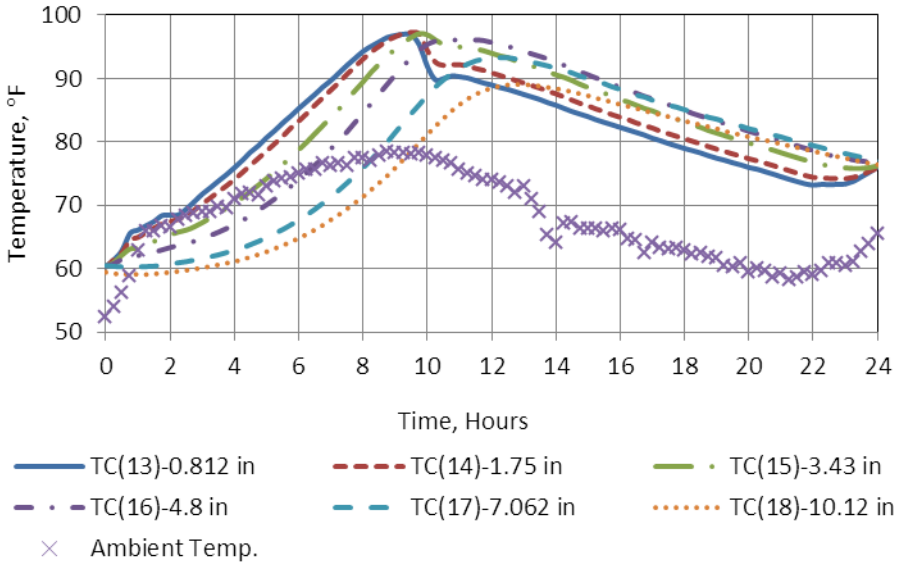

Figure A 21. Temperature measured over the first 24 hours along the depth of Slab C, Cell 3, Project 4.

APPENDIX B

EARLY-AGE MEASURED STRAIN IN INSTRUMENTED PROJECTS

Project 1

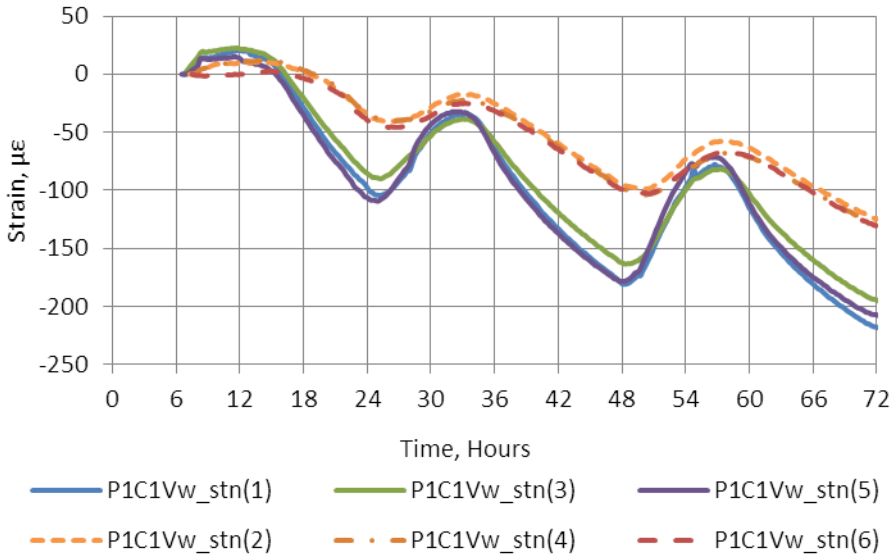

Figure B 1. Strain measured at the top and bottom of Slab A, B and C in Cell 1, Project 1.

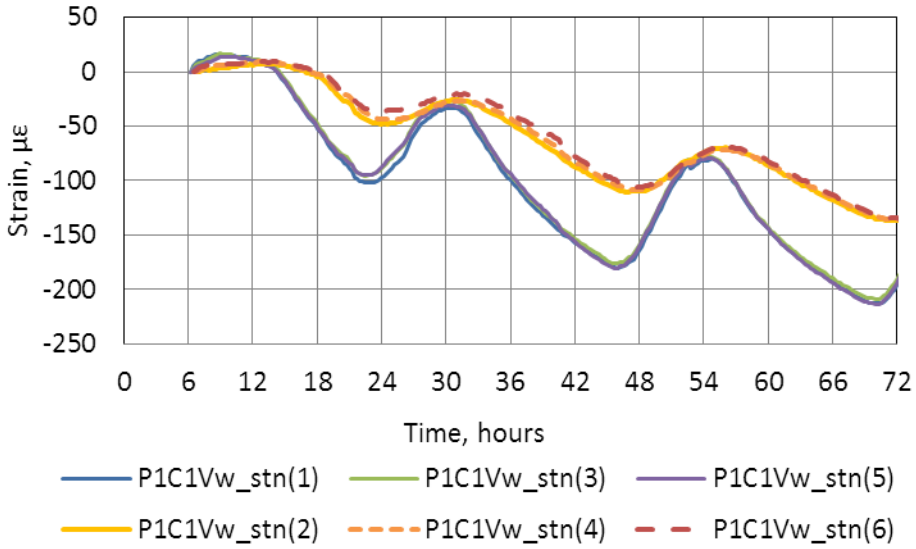

Figure B 2. Strain measured at the top and bottom of Slab A, B and C in Cell 2, Project 1.

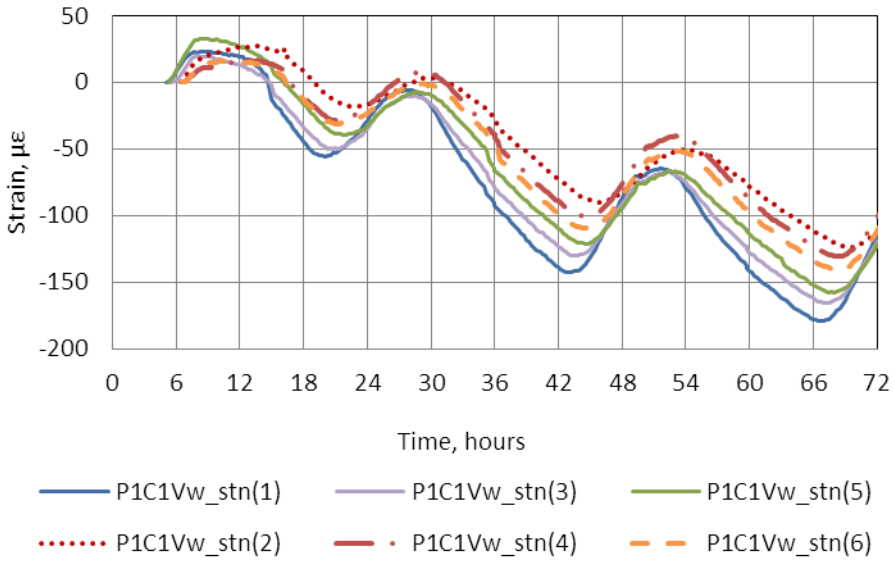

Figure B 3. Strain measured at the top and bottom of Slab A, B and C in Cell 3, Project 1.

Project 2

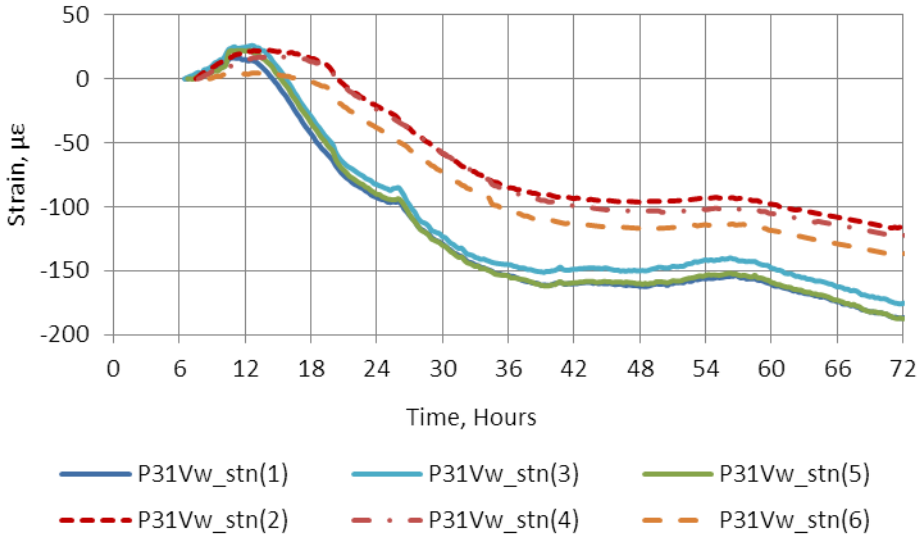

Figure B 4. Strain measured at the top and bottom of Slab A, B and C in Cell 1, Project 2.

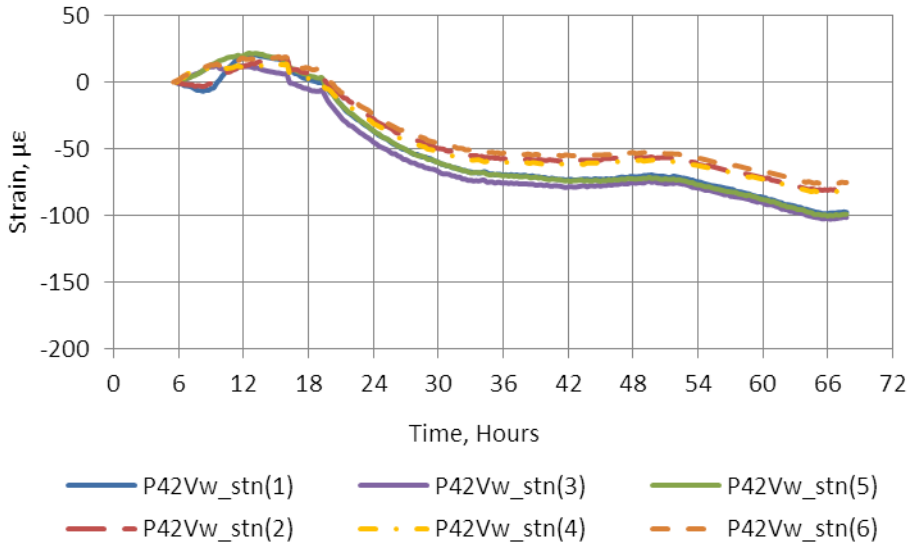

Figure B 5. Strain measured at the top and bottom of Slab A, B and C in Cell 2, Project 2.

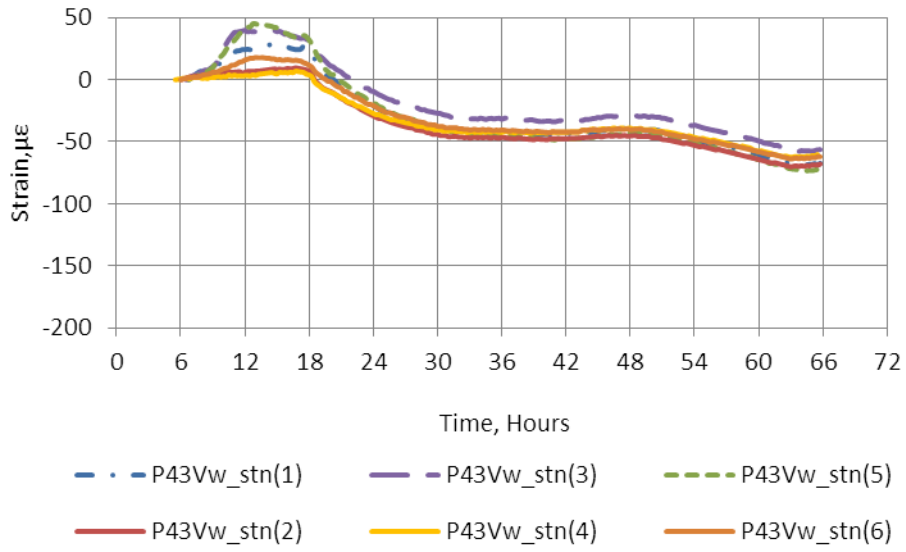

Figure B 6. Strain measured at the top and bottom of Slab A, B and C in Cell 3, Project 2.

Project 3

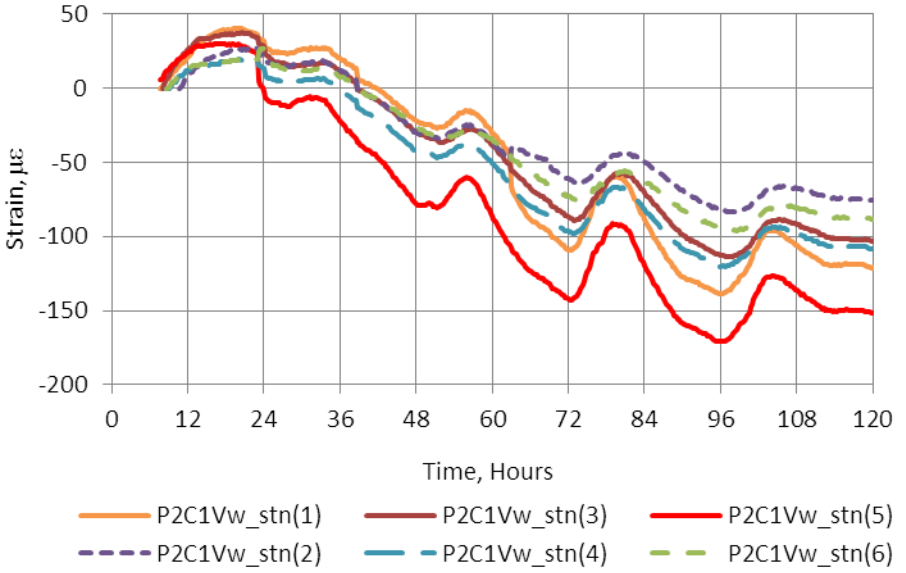

Figure B 7. Strain measured at the top and bottom of Slab A, B and C in Cell 1, Project 3.

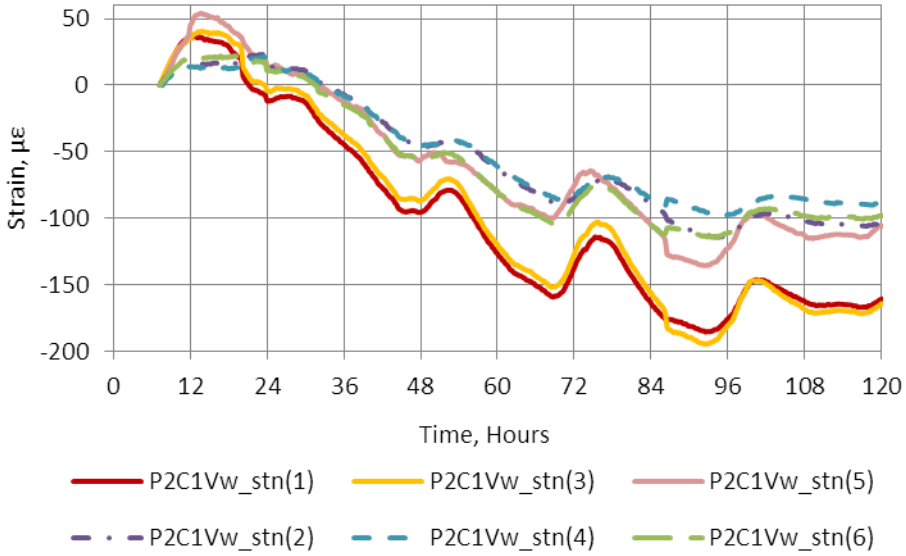

Figure B 8. Strain measured at the top and bottom of Slab A, B and C in Cell 2, Project 3.

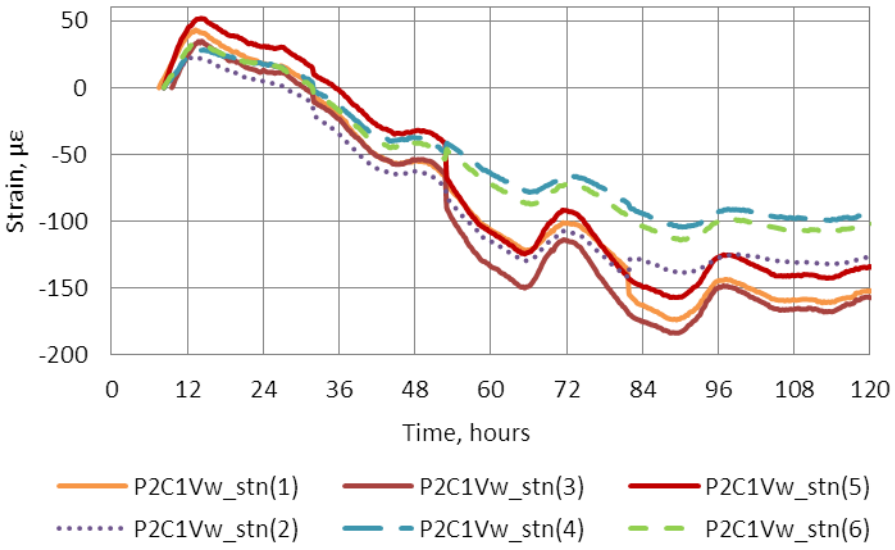

Figure B 9. Strain measured at the top and bottom of Slab A, B and C in Cell 3, Project 3.

Project 4

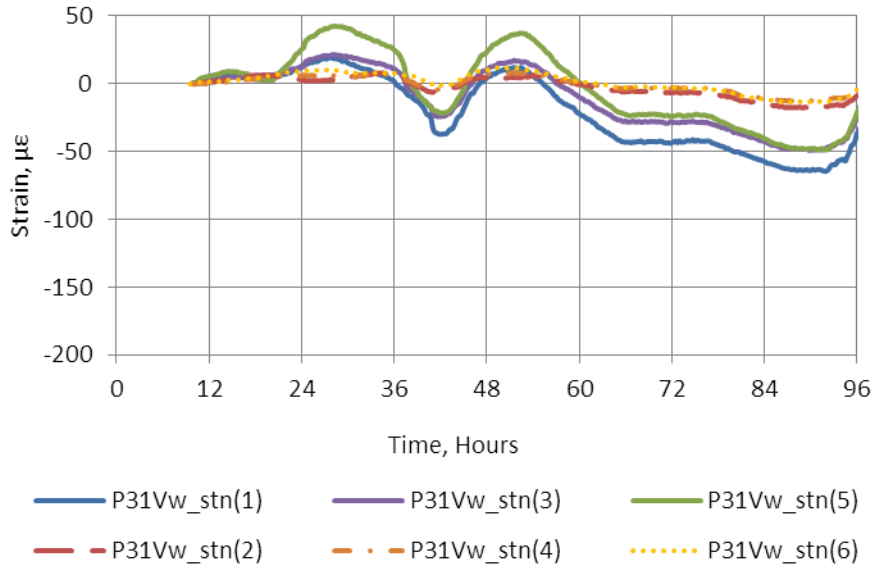

Figure B 10. Strain measured at the top and bottom of Slab A, B and C in Cell 1, Project 4.

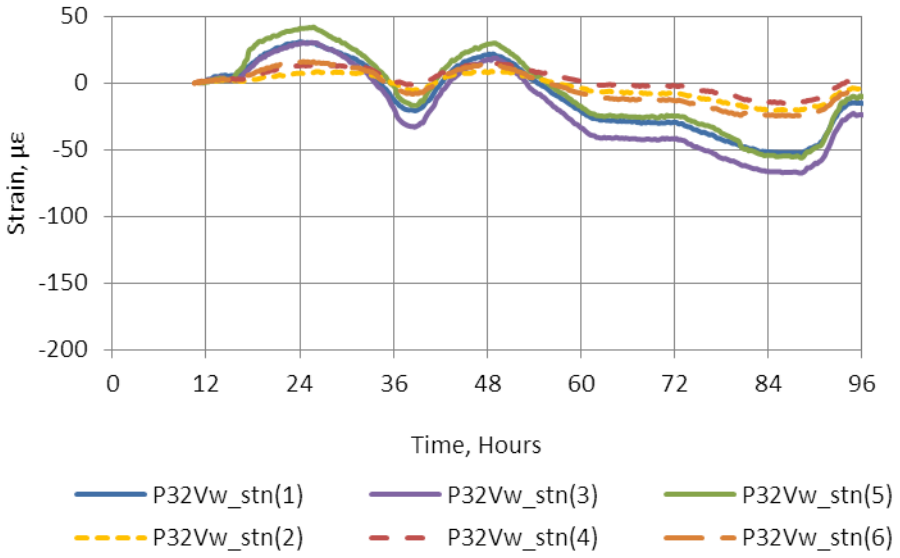

Figure B 11. Strain measured at the top and bottom of Slab A, B and C in Cell 2, Project 4.

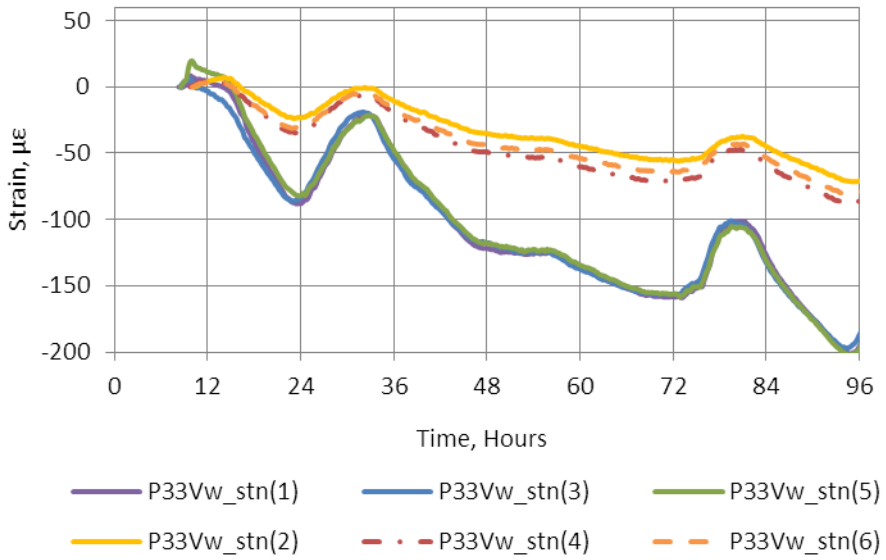

Figure B 12. Strain measured at the top and bottom of Slab A, B and C in Cell 3, Project 4.

BIBLIOGRAPHY

AASHTO (1993). "Guide for Design of Pavement Structures." American Association of State Highway and Transportation Officials, Washington, DC.

Akita, H., T. Fujiwara and Y. Ozaka (1997). "A Practical Procedure for the analysis of Moisture Transfer in Concrete Due to Drying." Magezine of Concrete Research **49**(179): 129-137.

Altoubat, S. A. (2000). Early Age Stresses and Creep-Shrinkage Interaction of Restrained Concrete. Urbana, IL, University of Illinois at Urbana-Champaign. **PhD**.

Altoubat, S. A. and D. A. Lange (2001). "Tensile Basic Creep:Measurements and Behaviour at Early-Age." ACI Materials Journal **98**(5): 386-393.

Andrade, C., J. Sarria and C. Alonso (1999). "Relative Humidity in the Interior of Concrete Exposed to Natural and Artificial Weathering." Cement and Concrete Composites **29**(8): 1249-1259.

Andrade, C., J. Sarría and C. Alonso (1999). "Relative Humidity in the Interior of Concrete Exposed to Natural and Artificial Weathering." Cement and Concrete Composites **1259**.

ARA Inc. ERES Consultants Division (2004). Guide for Mechanistic-Empirical Design of New and Rehabilitated Pavement Structures. National Cooperative Highway Research Program,. Transportation Research Board. Champaign, IL.

Armaghani, J. M., T. J. Larsen and L. Smith (1987). "Temperature Response of Concrete Pavements." Transportation Research Board(1121).

Asbahan, R. (2009). Effects of the Built-in Construction Gradient and Environmental Conditions on Jointed Plain Concrete Pavements. Civil Engineering. Pittsburgh, University of Pittsburgh. **PhD:** 534.

ASTM C 177 (1992). Standard Test Method for Steady-State Thermal Transmission Properties by Means of the Gaurded-Hot-Plate Apparatus Philadelphia, PA**:** 1495-1506.

ASTM C 403 (1999). Standard Test Method for Time of Setting of Concrete Mixtures by Penetration Resistance. American Society for Testing and Materials. Philadelphia, PA.

Ayano, T. and F. H. Wittman (2002). "Drying, Moisture Distribution, and Shrinkage of Cement-Based Materials." Materials and Structures **35**: 134-140.

Bazant, Z., P. , Y. Xi and S. Baweja (1993). "Improved prediction model for time-dependent deformations of concrete:part 7-Short form of BP-KX model, statistics and extrapolation of short-time data." Materials and Structures **26**: 567-574.

Bazant, Z. P. and S. Baweja (2000). "Creep and shrinkage prediction model for analysis and designof concrete structures: Model B3." Adam Neville Symposium: Creep and Shrinkage—Structural Design Effects, ACI SP-194.

Bazant, Z. P. and J. C. Chern (1985). "Triple Power Law for Concrete Creep." American Society of Civil Engineers **111**(1): 63-83.

Bazant, Z. P. and L. J. Najjar (1972). "Nonlinear Water Diffusion in Non-Saturated Concrete." Materials and Construction **5**(25).

Bazant, Z. P. and L. Panula (1978). "Practical prediction of time-dependent deformations of concrete Part I: Shrinkage." Materials and Structures **11**(5): 307-316.

Beckemeyer, C. A., L. Khazanovich and H. T. Yu (2002). "Determining Amount of Built-in Curling in Jointed Plain Concrete Pavement." Transportation Research Record(1809).

Bissonnette, B., P. Pierre and M. Pigeon (1999). "Influence of Key Parameters on Drying Shrinkage of Cementitious Materials." Cement and Concrete Research **29**.

Bogue, R. H. (1974). The Chemistry of Portland Cement. New York, Reinold Publishing Corp.

Branco, F. A., R. A. Mendes and R. A. Mirabell (1992). "Heat of Hydration Effects in Concrete Structures." ACI Materials Journal **89**(2): 139-145.

Burnham, T. and A. Koubaa (2001). A New Approach to Estimate the In-situ Thermal Coefecient and Drying Shrinkage for Jointed Concrete Pavements. 7th International Conference on Concrete Pavements, Orlando, FL.

Byfors, J. (1980). "Plain Concrete at Early Ages." Swedish Cement and Concrete Research Institute.

Carino, N. J., Malhotra, V.M. (1991). The Maturity Method, CRC Handbook on Nondestructive Testing of Concrete, CRC Press, Inc.

Choubane, B. and M. and Tia (1992). "Nonlinear Temperature Gradient Effect on Maximum Warping Stresses in Rigid Pavements." Transportation Research Board **1370**: 11-19.

Coree, B., Halil, C., and Harrington, D. (2005). "Implementing the Mechanistic-Empirical Pavement Design Guide: Implementation Plan." Report No. IHRB Project TR-509.

Dempsey, B. J., W. A. Herlache and A. J. Patel (1985). Environmental Effects on Pavements-Theory Manual. U.S. Department of Transportation, Federal Highway Administration. Contract No. DTFH 61-80-c-0013. Washington, D.C., University of Illinois, Urbana, IL.

Eisenmann, J. and G. Leykauf (1990). "Simplified Calculation Method of Slab Curling Caused by Surface Shrinkage." Proceedings, 2nd International Workshop on Theoretical Design of Concrete Pavements: 185-197 **Madrid, Spain**.

Emborg, M. (1989). Thermal Stresses in Concrete Structures at Early Ages. Devision of Structural Engineering, Lulea University of Technology.

Freiesleben Hansen, P. and E. J. Pederson (1977). "Maturity Computer for Controlled Curing and Hrdening of Concrete." Nordisk Beton **1**(19).

Garboczi, E. J. and D. P. Bentz (1992). "Computer Simulation of the Diffusivity of Cement-Based Materials." Journal of Materials Science **27**: 2083-2092.

Geokon (2010). Instruction Manual-Model 4200/4202/4204/4210 Vibrating Wire Strain Gages.

Gilbert, R. I. (1988). Time Effects in Concrete Structures. Amsterdam, Elsevier.

Grasley, Z. C. (2003). Internal Relative Humidity, Drying Stress Gradients, and Hygrothermal Dilation of Concrete. Civil and Environmental Engineering, University of Illinois at Urbana-Champaign. **PhD**.

Grasley, Z. C. and D. A. Lange (2004). "Modeling Drying Shrinkage Gradient in Concrete " Cement, Concerete and Aggregates (ASTM)(26).

Grasley, Z. C., D. A. Lange, M. D. D'Ambrosia and S. Villalobos-Chapa (2006). Relative Humidity in Concrete. A Contribution from ACI Commitee 236, Concrete International.

Grasley, Z. C., D. A. Lange and M. D. D'Ambrosia (2003). Internal Relative Humidity and Drying Stress gradients in Concrete. Engineering Conferences International, Advances in Cement and Concrete IX, Copper Mountain.

Gutierrez, J. J. (2003). Testing the JPCP Cracking Model of the Mechanistic-Empirical Pavement Design Guide. Civil and Environmental Engineering. Pittsburgh, Pennsylvania, University of Pittsburgh. **MS.**

Hansen, W., Y. Wei, D. L. Smiley, Y. Peng and A. Jensen (2006). "Effects of Paving Conditions on Built-in Curling and Pavement Performance." International Jouranal of Pavement Engineering **7**(4): 291-296.

Hermansson, A. (2001). "Mathematical Model for Calculation of Pavement Tempatures." Transportation Research Record **1764**: 180-188.

Janssen, D. J. (1986). "Moisture in Portland Cement Concrete." Transportation Research Board **1121**: 40-44.

Janssen, D. J. and M. B. Snyder (2000). "The Temperature-Moment Concept for Evaluating Pavement Temperature Data." Journal of Infrastructure Engineering **6**(2): 81-83.

Jeong, J. H., L. Wang and D. G. Zollinger (2001). A Temperature and Moisture for Hydration Portland Cement Concrete Pavements. International Conference on Concrete Pavements, Orlando, FL.

Jeong, J. H. and D. Zollinger (2004). "Early-Age Curling and Warping Behavior Insights from a Fully Instrumented Test-Slab System." Transportation Research Record **1896**: 66-74.

Jeong, J. H. and D. Zollinger (2006). "Finite-Element Modeling and Calibration of Temperature Prediction of Hydrating Portland Cement Concrete Pavements." Journal of Materials in Civil Engineering © ASCE **18**(3): 317-324.

Jeong, J. H. and D. G. Zollinger (2005). "Environmental Effects on the Behavior of Jointed Plain Concrete Pavements." Journal of Transportation Engineerg., ASCE **131**(2): 140-148.

Jiang, Z., Z. Sun and P. Wang (2006). "Internal Relative Humidity Distribution in High-Performance Cement Paste due to Moisture Diffusion and Self-Desiccation." Cement and Concrete Research **36**: 320-325.

Khazanovich, L. (1994). Structural Analysis of Multi-Layered Concrete Pavement Systems. Urbana, IL, University of Illinois at Urbana-Champaign. **PhD**.

Kjellsen, K. O., R. J. Detwiler and O. E. Gjorv (1991). "Developement of Microstructure in Plain Concrete Cement Pastes at Different Temperatures." Cement and Concrete Research **21**(1): 179-189.

L' Hermite, R. (1962). Volume Changes of Concrete. Proceeding of Fourth International Symposium on Chemistry of Cements, Washington, D.C.

Loukili, A., A. Khelidj and P. Richard (1999). "Hydration Kinetics, Change of Relative Humidity, and Autogenous Shrinkage of Ultra-High-Strength Concrete." Cement and Concrete Composites **29**: 577-584.

Mahboub, K. C., Y. Liu and L. D. Allen (2004). "Evaluation of Temperature Reponses in Concrete Pavement." Journal of Transportation Engineerg, ASCE **130**(3).

Martinez, E. E. (1998). Curling Deformations in Cement Paste Slabs and Effects of Shrinkage Reducing Admixtures. Civil and Environmental Engineering, Massachussetts Institute of Technology. **MS**.

Mccarter, W. J., D. W. Watson and T. M. Chrisp (2001). "Surface Zone Concrete: Drying, Absorption, and Moisture Distribution." Journal of Materials in Civil Engineering © ASCE **50**.

McCullough, F. B. and R. O. Rasmussen (1999). Fast-Track Paving: Concrete Temperature Control and Traffic Opening Criteria for Bonded Concrete Overlays. McLean, VA, Technical Report FHWA-RD-98-167.

Mehta, P. K. (1986). Concrete Structure, Properties and Materials. Englewood Cliffs, NJ.
Mindess, S. (2002). Concrete, Pearson Education Inc.

Mirambell, E. (1990). "Temperature and Stress Distributions in Plain Concrete Pavements Under Thermal and Mechanical Loads." Proceedings, Second International Workshop on the Design and Rehabilitation of Concrete Pavements **Sigüenza, Spain**.

Mohamed, A. R. and W. Hansen (1997). "Effect of Nonlinear Temperature Gradient on Curling Stress in Concrete Pavements." Transportation Research Record **1568**: 65-71.

Nasser, K. W. and A. M. Neville (1966). "Creep of Concrete at Temperatures above Normal." Nuclear Engineering and Design **4**(1): 90-96.

Nassiri, S., L. C. Ramirez and J. M. Vandenbossche (2009). Establishing Appropriate Inputs When Using the MEPDG To Design Rigid Pavements in Pennsylvania-Task 3-Field Study Plan. Draft Report Prepared for Pennsylvania Department of Transportation. Pittsburgh, PA, University of Pittsburgh.

Nassiri, S. and J. M. Vandenbossche (2010). Establishing Appropriate Inputs When Using the MEPDG to Design Rigid Pavements in Pennsylvania-Task 5-Establishing the Built-in Gradient. Prepared for Pennsylvania Department of Transportation. Pittsburgh, PA, University of Pittsburgh.

Nassiri, S., J. M. Vandenbossche and K. A. Gatti (2009). Establishing Appropriate Inputs When Using the MEPDG To Design Rigid Pavements in Pennsylvania-Task 2-Sensitivity Analysis. Prepared for Pennsylvania Department of Transportation. Pittsburgh, PA, University of Pittsburgh.

Neville, A. M. (1964). "Creep of Concrete as a Function of Its Cement Paste Content " Magezine of Concrete Research **16**(46): 21-36.

Neville, A. M. (1970). Creep of Concrete: Plain, Reinforced, and Prestressed. Amsterdam, North-Holland Pub. Co.

Neville, A. M. (1996). Properties of Concrete. New York, John Wiley and Sons, Inc.

Oh, H. B. and S. W. Cha. (2003). "Nonlinear Analysis of Temperature and Moisture Distributions in Early-Age Concrete Structures Based on Degree of Hydration." ACI Materials Journal **100**: 361-369.

Ostergaard, L., D. A. Lange, S. A. Altoubat and H. Stang (2001). "Tensile basic creep of early-age concrete under constant load." Cement and Concrete Research **31**: 1895-1899.

Ozyildirim, C. and W. Halstead (1988). "Resistance to Chloride Ion Penetration of Concretes Containing Fly Ash, Silica Fume, or Slag." American Concrete Institude **108**: 35-62.

Parrott, L. J. (1988). "Moisture Profiles in Drying Concrete." Cement and Concrete Research **1**(3): 164-170.

Persson, B. (1998). "Experimental Studies on Shrinkage of High Performance Concrete." Cement and Concrete Research **28**(7): 1023-1036.

Pfeiffer, P. and T. A. Tanabe (1993). Time-Dependent Behaviour. International Workshop on Finite Element Analysis of Reinforced Concrete,, Columbia University, NY.

Pinto, R. C. A., and Hover, K.C. (1999). "Application of Maturity Approach to Setting Times." ACI Materials Journal **96**(6): 686-691.

Pinto, R. C. A. and A. K. Schindler (2010). "Unified Modeling of Setting and Strength Development." Cement and Concrete Research **40**: 58-65.

Rao, C., E. J. Barenberg, M. B. Snyder and S. Schmidt (2001). Effects of Temperature and Moisture on the Response of Jointed Concrete Pavements. 7th International Conference on Pavements, Orlando, FL.

Rao, C. and J. R. Roessler (2005). "Characterizing Effective Built-In Curling from Concrete Pavement Field Measurements." Journal of Transportation Engineerg., ASCE **131**(4): 320-327.

Rao, S. P. (2005). Charcterizing Effective Built-in Curling and its Effect on Concrete Pavement Cracking, University of Illinois at Urbana-Champaign. **PhD**.

Recktenwald, G. W. (2004). Finite-Difference Approximations to the Heat Equation. Portland, OR, Mechanical Engineering Department Portland State University,.

Richardson, J. M. and J. M. Armaghani (1987). "Stress caused by temperature gradient in Portland cement concrete pavements." Transportation Research Board **1121**: 7-13.

RILEM Bulletin (1981). "Properties of Set Concrete at Early Ages-State of the Art Report." Materials and Construction **14**(84).

Ruiz, J., M., P. J. Kim and A. K. Schindler (2001). "Validation of HIPERPAV for Prediction of Early-Aage Jointed Concrete Pavement Behavior." Transportation Research Board **1778**: 17-25.

Ruiz, J. M., R. O. Rasmussen, G. K. Chang, J. C. Dick, P. K. Nelson, A. K. Schindler, D. J. Turner and W. J. Wilde (2006). Computer-Based Guidelines for Concrete Pavements, Volume III: Technical Appendices, FHWA-HRT-04-127.

Ruiz, J. M., A. K. Schindler, R. O. Rasmussen, P. K. Nelson and G. K. Chang (2001). Concrete Temperature Modeling and Strength Prediction Using Maturity Concepts in the FHWA HIPERPAV Software. 7th International Conference on Concrete Pavements, Orlando, FL.

Sakata, K. (1983). "A study on moisture diffusion in drying and drying shrinkage of concrete " Cement and Concrete Research **13**(2): 216-224.

Scanlon, J. M. and J. E. McDonald (1994). Thermal Properties Significance of Tests and Properties of Concrete and Concrete Making Materials. ASTM Special Technical Publication No. 169C,. Philadelphia, PA.

Schindler, A. K. (2004). "Effect of Temperature on Hydration of Cementitious Materials." ACI Materials Journal **101**(1): 72-81.

Schindler, A. K. (2004). Prediction of Concrete Setting. Proceedings of the RILEM Conference on Advances in Concrete through Science and Engineering, Evanston, IL.

Schindler, A. K. and K. J. Folliard (2005). "Heat of Hydration Models for Cementitious Materials." ACI Materials Journal **102**(1): 24-33.

Schindler, A. K., McCullough, B. F. (2002). "The Importance of Concrete Temperature Control During Concrete Pavement Construction in Hot Weather Conditions." Transportation Research Board **1813**: 3-10.

Schindler, A. K., J. M. Ruiz, R. O. Rasmussen, G. K. Chang and L. G. Wathne (2003). "Concrete pavement temperature prediction and case studies with the FHWA HIPERPAV models." Cement and Concrete Composites **26**(5): 463-471.

Schmidt, S. (2001). Analysis of "Built-in" Curling and Warping in PCC Pavements. Civil and Environmental Engineering, University of Minnesota. **MS.**

SHRP-C-321 (1993). A Guide to Evaluating Thermal Effects in Concrete Pavements. Washington, D.C., Stretigic Highway Research Program, National Research Counsil.

Solaimanian, M. and T. W. Kennedy (1998). "Predicting Maximum Pavement Surface Temperature Using Maximum Air Temperature and Hourly Solar Radiation " Transportation Research Record **1417**: 1-11.

Soroka, I. (1979). Portland Cement Paste and Concrete. London, MacMillian Press LTD.

Springenschmid, R., R. Breitenbücher and M. Mangold (1995). Development of the Cracking Frame and theTemperature-Stress Testing Machine. London, Spingenschmid, E & EF Spon.

Taflin, J. W. (2001). Strength, Elastic Deformation and Short-Term Creep Properties of Thermally and Mechanically Loaded Plain Concrete Beams Loaded In Flexure. Department of Civil and Environmental Engineering, University of Washington. **MS.**

Thompson, M. R., B. J. Dempsey, H. Hill and J. Vogel (1987). "Characterizing Temperature Effects for Pavement Analysis and Design." Transportation Research Board **1121**: 14-22.

Umehara, H., T. Uehara, T. Iisaka and A. Sugiyama (1994). Effect of Creep in Concrete at Early Ages on the Thermal Stresses. Proceedings of the International RILEM Symposium, Munich, Germany.

Van Breugel, K. (1999). Simulation of Hydration and Formation of Structure in Hardening Cement-Based Materials. Netherlands, Delft University Press, .

Vandenbossche, J. M. (2003). Interpreting Falling Weight Deflectometer Results for Curled and Warped Portland Cement Concrete Pavements. Civil and Environmental Engineering, University of Minnesota. **PhD**.

Vandenbossche, J. M., F. Mu, J. J. Gutierrez and J. Sherwood (2010). "An Evaluation of the Built-in Temperature Difference Input Parameter in the Jointed Plain Concrete Pavement Cracking Model of the Mechaninstic-Empirical Pavement Design Guide." International Jouranal of Pavement Engineering.

Wade, S. A., J. M. Nixon, A. K. Schindler and R. W. Barnes (2010). "Effect of Temperature on the Setting Behavior of Concrete." Journal of Materials in Civil Engineering © ASCE **22**(3).

Wells, S. A., B. M. Phillips and J. M. Vandenbossche (2005). S.R.-22 Smart Pavement Phase I: Early-Age Material Properties and Pavement Response Characteristics for Jointed Plain Concrete Pavements. Pennsylvania Department of Transportation and the Federal Highway Administration. Pittsburgh, Pennsylvania, University of Pittsburgh, Department of Civil and Environmental Engineering.

Wells, S. A., B. M. Phillips and J. M. Vandenbossche (2006). "Quantifying Built-In Construction Gradients and Early-Age Slab Deformation Caused by Environmental Loads in a Jointed Plain Concrete Pavement." International Jouranal of Pavement Eng. **7**(4).

Westman, G. (1999). Concrete Creep and Thermal Stresses. Division of Structural Engineering, Luleå University of Technology. **PhD**.

Xin, D., D. G. Zollinger and G. D. Allent (1995). "An Approach to Determine Diffusivity in Hardening Concrete Based on Measured Humidity Profiles." Advanced Cement Based Materials **2**: 138-144.

Xu, Q., M. Ruiz, G. K. Change, R. O. Rasmussen and D. K. Rozycki (2009). "A Moisture Transport Model for Enhancing the FHWA HIPERPAV Predictions." Transportation Research Board.

Yang, Q. (1999). "Inner relative humidity and degree of saturation in high-performance concrete stored in water or salt solution for 2 years." Cement and Concrete Research **29**: 45-53.

Yang, S. (1996). A Temperature Prediction Model in New Concrete Pavement and New Test Method for Concrete Fracture Parameters. Civil Engineering, Texas A&M University. **PhD**.

Ye, D. (2007). Early-Age Concrete Temperature and Moisture Relative to Curing Effectiveness and Projected Effects on Selected Aspects of Slab Behavior. Civil Engineering, Texas A&M University. **Ph.D.**

Yu, H., T. and L. Khazanovich (2001). Effects of Construction Curling on Concrete Pavement Bahaviour. 7th International Conference on Concrete Pavements, Orlando, FL.

Yu, H. T., L. Khazanovich, M. I. Darter and A. Ardani (1998). "Analysis of Concrete Pavement Responses to Temperature ans Wheel Loads Measured from Instrumented Slabs." Transportation Research Board(1639).

Zhang, J., K. Qi and Y. Haung (2009). "Calculation of Moisture Distribution in Early-Age Concrete." Journal of Engineering Mechanics: 871-880.

Zhang, J. T., F. Fwa, K. H. Tan and X. P. Shi (2003). "Model for Nonlinear Thermal Effect on Pavement Warping Stresses." Journal of Transportation Engineering (ASCE) **129**: 695-702.

Zoldners, N. G. (1971). "Thermal Properties of Concrete at Sustained Elevated Temperatures." American Concrete Institute **SP-25**(Detroit, MI): 1-32.